Cosmogenic Cl-36 in Ca and K rich minerals: analytical developments, production rate calibrations and cross calibration with He-3 and Ne-21

Irene Schimmelpfennig

UNIVERSITE PAUL CEZANNE AIX-MARSEILLE III
CEREGE

N° 2009AIX30032

Cosmogenic ^{36}Cl in Ca and K rich minerals: analytical developments, production rate calibrations and cross calibration with ^{3}He and ^{21}Ne

L'isotope cosmogénique ^{36}Cl dans les minéraux riches en Ca et en K : développements analytiques, calibrations des taux de production et inter-calibration avec le ^{3}He et le ^{21}Ne

T H E S E

Pour obtenir le grade de

DOCTEUR DE L'UNIVERSITE Paul CEZANNE

Faculté des Sciences et Techniques
Discipline : Géosciences de l'Environnement

Présentée et soutenue publiquement par

Irene SCHIMMELPFENNIG

Le 8 Décembre 2009 au CEREGE

Les Directeurs de thèse
Lucilla BENEDETTI et Didier BOURLES

Ecole doctorale : Sciences de l'Environnement

J U R Y

Pr. John STONE, University of Washington, USA	Rapporteur
Pr. Keith FIFIELD, ANU, Australia	Rapporteur
Pr. Bernard MARTY, CRPG, Nancy	Examinateur
Pr. Bruno HAMELIN, CEREGE, Aix en Provence	Examinateur
Dr. Tibor DUNAI, University of Edinburgh, UK	Examinateur
Dr. Lucilla BENEDETTI, CEREGE, Aix en Provence	Directrice
Pr. Didier BOURLES, CEREGE, Aix en Provence	Co-Directeur
Dr. Raphaël PIK, CRPG, Nancy	Invité

ANNEE : 2009

Résumé en français

Les taux de production du nucléide cosmogénique ^{36}Cl par spallation du Ca et du K (SLHL) proposés actuellement dans la littérature montrent des divergences allant jusqu'à 50% (e.g. Gosse and Phillips, 2001). Nous avons pu montrer que des fortes teneurs en Cl dans les roches utilisées pour les calibrations précédentes entraînent une surestimation de ces taux de production, lié à la production de ^{36}Cl à partir du ^{35}Cl qui est peu contrainte.

Nous avons entrepris une nouvelle calibration à partir de laves datées indépendamment entre 0.4 et 32 ka situées au Mt Etna (38°N, Italie) et au Payun Matru (36°S, Argentine). Le ^{36}Cl a été mesuré dans des feldspaths riches en Ca et en K, mais faibles en Cl. A partir d'une approche bayesienne incluant toutes les incertitudes, les taux de production obtenus sont de 42.2 ± 4.8 atomes ^{36}Cl (g Ca)$^{-1}$ an^{-1} pour la spallation du Ca et de 124.9 ± 8.1 atomes ^{36}Cl (g K)$^{-1}$ an^{-1} pour la spallation du K, avec les facteurs d'échelle calculés selon Stone (2000). Quatre autres modèles de facteurs d'échelle sont également proposés avec des résultats très semblables. Ces nouveaux taux de production sont en accord avec les valeurs précédemment obtenues par d'autres auteurs avec des échantillons faibles en Cl.

Finalement, les concentrations en ^{36}Cl, ^{3}He et ^{21}Ne ont été mesurées dans des pyroxènes prélevés entre 1000 et 4300 m dans des laves du Kilimandjaro (3°S). Les rapports entre ces nucléides ne montrent pas de dépendance altitudinale, ce qui suggère que les taux de production ne varient pas d'un nucléide à l'autre avec l'altitude.

Mots clés : *Datation par isotopes cosmogéniques, ^{36}Cl in situ, minéraux silicatés, roche totale basaltique, Mt. Etna, feuille de calcul ^{36}Cl, calibration de taux de production, méthodes de facteurs d'échelle, gaz rares cosmogéniques, inter-calibration*

Abstract in English

Published cosmogenic ^{36}Cl SLHL production rates from Ca and K spallation differ by almost 50% (e.g. Gosse and Phillips, 2001). The main difficulty in calibrating ^{36}Cl production rates is to constrain the relative contribution of the various production pathways, which depend on the chemical composition of the rock, particularly on the Cl content.

Whole rock ^{36}Cl exposure ages were compared with ^{36}Cl exposure ages evaluated in Ca-rich plagioclases in the same independently dated 10 ± 3 ka lava sample taken from Mt. Etna (Sicily, 38° N). Sequential dissolution experiments showed that high Cl concentrations in plagioclase grains could be significantly reduced after 16% dissolution yielding ^{36}Cl exposure ages in agreement with the independent age. Stepwise dissolution of whole rock grains, on the other hand, is not as effective in reducing high Cl concentrations as it is for the plagioclase. 330 ppm Cl still remains after 85% dissolution. The ^{36}Cl exposure ages are systematically about 30% higher than the ages calculated from the plagioclase. We could exclude contamination by atmospheric or magmatic ^{36}Cl as an explanation for this overestimate. High Cl contents in the calibration samples used for several previous production rate studies are most probably the reason for overestimated spallation production rates from Ca and K. This is due to a poorly constrained nature of ^{36}Cl production from low-energy neutrons.

We used separated minerals, very low in Cl, to calibrate the production rates from Ca and K. ^{36}Cl was measured in Ca-plagioclases collected from 4 lava flows at Mt. Etna (38°N, Italy, altitudes between 500 and 2000 m), and in K-feldspars from one flow at Payun Matru

volcano (36°S, Argentina, altitudes 2300 and 2500 m). The flows were independently dated between 0.4 and 32 ka. Scaling factors were calculated using five different published scaling models resulting in five calibration data sets. Using a Bayesian statistical model allowed including the major inherent uncertainties. The inferred SLHL spallation production rates from Ca and K are 42.2 ± 4.8 atoms ^{36}Cl (g Ca)$^{-1}$ a^{-1} and 124.9 ± 8.1 atoms ^{36}Cl (g K)$^{-1}$ a^{-1} scaled with Stone (2000). Using the other scaling methods results in very similar values. These results are in agreement with previous production rate estimations both for Ca and K calibrated with low Cl samples. Moreover, although the exposure durations of our samples are very different and the altitude range is large, the ages recalculated with our production rates are mostly in agreement, within uncertainties, with the independent ages no matter which scaling method is used.

However, scaling factors derived from the various scaling methods differ significantly. Cosmic ray flux is sensitive to elevation and its energy spectrum increases considerably with increasing altitude and latitude. To evaluate whether various TCN production rates change differently with altitude and latitude and if nuclide-specific or even target-element-specific scaling factors are required, cosmogenic ^{36}Cl, ^{3}He and ^{21}Ne concentration were determined in pyroxenes over an altitude transect between 1000 and 4300 m at Kilimanjaro volcano (3°S). No altitude-dependency of the nuclide ratios could be observed, suggesting that no nuclide-specific scaling factors be needed for the studied nuclides.

Key words: *Cosmogenic-nuclide exposure dating, in situ ^{36}Cl, silicate minerals, basaltic whole rock, Mt. Etna, ^{36}Cl calculator, production rate calibration, scaling methods, cosmogenic noble gases, cross-calibration*

Discipline: Géosciences de l'Environnement

Centre Européen de Recherche et d'Enseignement en Géosciences de l'Environnement
Europôle Méditerranéen de l'Arbois
13545 Aix en Provence
France

Remerciements - Acknowledgement

L'aventure internationale de ma thèse a commencé au printemps 2005 avec un voyage de Göttingen, ma ville d'étude en Allemagne, à Amsterdam où j'ai passé un entretien devant 5 PI's (principle investigators) de CRONUS-EU qui devaient décider de mon avenir... J'ai eu la chance d'avoir été acceptée et - comme j'ai appris plus tard - que Pete Burnard se soit battu pour que je fasse partie de l'équipe française. Merci Pete! Cette décision m'a permis de vivre 4 ans et demi en Provence - là où les gens originaires du grand nord passent souvent leurs vacances - et d'apprendre la belle langue française. I also would like to thank Tibor Dunai, the founder and head of CRONUS-EU, that I got the chance to take part in this excellent European Marie-Curie research network. This made it possible for me to learn so many things and to travel to many great parts of Europe for meetings, conferences and fieldtrips.

Je tiens beaucoup à remercier Lucilla Benedetti pour son formidable encadrement, de m'avoir toujours laissé la liberté de développer mes propres idées, et aussi d'avoir su me motiver aux moments où j'en avais le plus besoin. Un grand merci chaleureux à Raphaël Pik, qui m'a fait découvrir l'Etna et le monde de la spectrométrie de masse à gaz rares. Je remercie aussi Didier Bourlès de m'avoir toujours soutenue quand j'en avais besoin. I wish to gratefully acknowledge Bob Finkel especially for his patience during the numerous fruitful discussions and for correcting so many times my written English.

For the evaluation of my work I am very grateful to John Stone and Keith Fifield, the "rapporteurs" of this thesis manuscript, and to Bruno Hamelin, Bernard Marty and Tibor Dunai, my "examinateurs".

Thanks to all members of the CRONUS-EU network, those I worked and/or had a great time with during the meetings and conferences, just to mention some names: Silke Merchel, Finlay Stuart, Alice Williams, Jurgen Foeken, Luigia DiNicola, Jérôme Chmeleff, Katja Ammon, and all the others. I am also grateful to the members of the CRONUS-Earth network, especially Fred Phillips, Nat Lifton and Devendra Lal who always answered promptly my numerous questions per mail.

Je tiens à remercier Vincent Garreta, P.H. Blard et Aloé Schlagenhauf, de très bons amis pour moi, qui étaient ìmpliqués de façon importante dans mon travail et qui étaient aussi confrontés au défi de terminer une thèse. Merci également du fond du coeur à toutes les personnes du CEREGE qui, de temps en temps, m'ont fait penser à autre chose qu'à mon travail: mes camarades de bureau, Esmaeil Shabanian, la personne la plus gentille que je n'aie jamais rencontrée, Julie Gatacceca, ma première vraie copine au CEREGE, et Fabienne Régoli, la fabuleuse Fabi, puis mes super copine Fatim Hankard, Lucie Ménabréaz und Anne-Lise Develle et tous les autres avec qui j'ai partagé des moments agréables en pause, à la cantine, à la bière du vendredi ou en soirée ailleurs (la liste serait trop longue et j'oublierais certainement quelqu'un...).

Ein grosses Danke auch an Angela Landgraf, mit der ich neben unserer Zusammenarbeit waehrend ihrer Aufenthalte am CEREGE angenehme Gespraeche auf deutsch (!) fuehren und schoene Feierabendausfluege ans Meer machen konnte. Quisiera decir gracias a mis super amigos y amigas con quienes podía vivir mi pasión por el idioma español y compartir tantos momentos alegres, Adrian, Georgette, Belén, Emilio, Pancho, Millarca, Francisca y todos los demás. Je souhaite remercier aussi mes colocataires Nicole, Claudine, Yohan, Xavier et David d'avoir partagé avec moi un endroit tellement agréable et d'avoir supporté de me voir collée devant mon ordi pendant autant de temps, même le soir et le week-end.

Als letztes möchte ich meiner Familie danken für ihre moralische Unterstützung, besonders meiner Schwester Kathrin, die trotz der Distanz (Skype sei dank) jeder Zeit ein offenes Ohr für mich hatte.

Version abrégée en français - Abridged version in French

Introduction

Les applications des isotopes cosmogéniques produits in situ à la quantification des processus superficiels sont en plein essor et encore dans une phase de validation (e.g. Gosse and Phillips, 2001). Elles reposent sur la mesure de la concentration en nucléides comme ^{3}He, ^{10}Be, ^{26}Al, ^{21}Ne, ^{14}C ou ^{36}Cl, qui se forment essentiellement à la surface lors du bombardement par les rayons cosmiques des éléments cibles tels que le silicium ou l'oxygène, contenus dans les minéraux de la roche. La concentration d'un nucléide cosmogénique dans une roche augmente en fonction de son temps d'exposition ce qui permet de l'utiliser pour déterminer depuis combien de temps un échantillon a été exposé au rayonnement cosmique et donc depuis combien de temps il est à la surface terrestre. Le développement de la spectrométrie de masse par accélérateur (SMA) et l'amélioration continuelle de sa sensibilité ont rendu possible la mesure de très petites concentrations de ces nucléides dont le taux de production est faible à la surface de la Terre ($\sim$ 10-50 atomes /(g de roche)/an) (e.g. Elmore and Phillips, 1987; Finkel and Suter, 1993).

Cette thèse porte essentiellement sur le radionucléide ^{36}Cl. Quatre types de réaction entraînent la production de ^{36}Cl in situ dans une roche (e.g. Gosse and Phillips, 2001; Schimmelpfennig et al., 2009, Fig. 1):

1. A la surface, le ^{36}Cl est principalement produit par des réactions de spallation entre des neutrons de haute énergie et des éléments cibles, Ca, K, Ti et Fe.

2. La capture des muons négatifs lents par le ^{40}Ca et le ^{39}K entraîne une production de ^{36}Cl qui devient prédominante en profondeur.

3. La capture de neutrons de faible énergie (thermique et épithermique) par le ^{35}Cl entraîne la formation de ^{36}Cl.

4. Une production du ^{36}Cl non-cosmogénique est dûe à la capture de neutrons radiogéniques de faible énergie par le ^{35}Cl formés suite à la fission de ^{238}U et à la décroissance radioactive de l'U et du Th.

L'occurrence de ces réactions dépend 1- du flux de particules cosmiques qui atteint la surface terrestre et 2- de la composition chimique de l'échantillon, c'est-à-dire de sa concentration en éléments cibles. Or, le rayonnement cosmique est variable dans l'espace et dans le temps. La production de ^{36}Cl varie donc en fonction de la latitude, de l'altitude et également en fonction des variations temporelles du champ magnétique. Pour intégrer ces variations dans le taux de production correspondant au site étudié, on calcule pour chaque site un facteur d'échelle ("scaling factor"). Les modèles qui prédisent ces variations et sur lesquels se basent ces calculs (e.g. Stone, 2000; Dunai, 2001; Lifton et al., 2005; Desilets et al., 2006b) sont encore en discussion. Par ailleurs, la production in situ décroît exponentiellement avec la profondeur avec une production maximale dans le premier mètre (e.g. Fig. 1.12).

En l'absence d'érosion et de pré-exposition, la concentration du ^{36}Cl s'accumule en suivant cette équation:

$$N_{36}(z,t) = P_{total}(z)\ (1 - exp^{-\lambda_{36}t})/\lambda_{36} \tag{1}$$

Avec P_{total} le taux de production total intégrant toutes les réactions, et qui dépend de la profondeur z, t le temps d'exposition et λ_{36} la constante de désintégration ($\ln 2/\lambda_{36} = t_{1/2}$ avec $t_{1/2}$ la demie-vie 301 ka). Cette concentration augmente avec le temps d'exposition jusqu'à atteindre l'état stationnaire, en général après une exposition d'environ 3 à 4 demie-vie (Fig. 1.1). Cet état est atteint lorsque la production du ^{36}Cl est contrebalancée par sa perte par décroissance radioactive. Lorsqu'on tient compte des différents processus qui influent sur l'accumulation du ^{36}Cl dans un échantillon, le taux de production total en nombre d'atomes par gramme de roche par an sur une épaisseur connue et situé à une profondeur connue est :

$$P_{total}(z) = S_{el,s}\ F_s\ Q_s\ P_s(z) + S_{el,s}\ F_n\ (Q_{eth}\ P_{eth}(z) + Q_{th}\ P_{th}(z)) + S_{el,\mu}\ F_{\mu-}\ Q_{\mu-}\ P_{\mu-}(z) + P_r \tag{2}$$

Les indices correspondent au type de réaction, s pour spallation, n pour capture des neutrons de faible énergie, eth pour capture des neutrons épithermaux, th capture des

neutrons thermaux, $\mu-$ pour la capture des muons négatifs lents, et r pour la production radiogénique. P_x est la production de ^{36}Cl résultant du type de réaction x et dépendant de la composition chimique de l'échantillon. Q_x est le facteur intégrant la production sur l'épaisseur de l'échantillon. $S_{el,s}$ et $S_{el,\mu-}$ sont les facteurs d'échelle qui intègrent les effets sur l'altitude et la latitude ainsi que les variations temporelles du champ magnétique pour les réactions de spallation (s) et la capture muonique ($\mu-$). F_x intègre les corrections liées à tout effet d'écrantage (topographie, géométrie, couverture neigeuse, ect. avec $0 < F_x < 1$ et si $F_x = 1$ pas d'écrantage).

Les équations 1 et 2 peuvent donc permettre de calculer un âge d'exposition d'un échantillon dont on connaît la latitude, l'altitude, les facteurs d'écrantage, son épaisseur, sa profondeur et dont on a mesuré très précisément la concentration en ^{36}Cl et en éléments cibles (^{35}Cl, Ca, K, Ti et Fe). L'âge apparent, c'est-à-dire en considérant une érosion nulle et sans pré-exposition, est donc :

$$t_{expo} = \frac{-ln(1 - N_{meas}\ \lambda_{36}/P_{total})}{\lambda_{36}} \tag{3}$$

Afin d'obtenir un âge d'exposition exact, il est donc essentiel de bien contraindre les taux de production de référence. Ces taux de production sont traditionnellement normalisés à un point géographique de référence qui est le niveau de la mer et les hautes latitudes (SLHL). Or, les taux de production proposés actuellement dans la littérature pour le ^{36}Cl montrent des divergences importantes. Celui par spallation du Ca diverge jusqu'à 46% (Stone et al., 1996; Swanson and Caffee, 2001), et celui par spallation du K diverge jusqu'à 53% (Zreda et al., 1991; Swanson and Caffee, 2001).

Le projet CRONUS-Europe - Marie Curie Research Training Networks a pour but de contraindre les taux de production et autres paramètres essentiels pour l'utilisation des isotopes cosmogéniques. C'est dans ce cadre que j'ai effectué ma thèse avec pour objectif de calibrer les taux de production du ^{36}Cl par spallation du Ca et du K, de faciliter l'application de ce nucléide à la quantification des processus superficiels et d'effectuer une inter-calibration des taux de production du ^{36}Cl avec ceux de l'^{3}He et du ^{21}Ne cosmogèniques le long d'une transect altitudinal.

Entre autres, nous avons cherché à répondre aux questions suivantes :

Pourquoi les taux de production pour le ^{36}Cl montrent une telle divergence ? Quelles sont les valeurs les plus proches de la réalité pour les taux de production par spallation du Ca et du K ? Quelle est l'influence des facteurs d'échelle et de leurs incertitudes sur la calibration des taux de production ?

Par ailleurs, la production du ^{36}Cl à partir du ^{35}Cl est difficile à paramétrer dû à la distribution complexe des neutrons de faible énergie à la limite entre l'atmosphère et la roche. Les calculs de production du ^{36}Cl pour un échantillon riche en élément cible ^{35}Cl (e.g. $> \sim 20$ ppm dans un basalte) sont donc rendus complexes du fait des incertitudes liées à la valeur du flux de neutrons de faible énergie et des paramètres qui influent sur ce flux tels qu'une fine couche d'eau ou de neige.

Quel est l'impact des incertitudes inhérentes à cette source de production sur la calibration des taux de production par spallation ?

Jusqu'à présent, l'utilisation du ^{36}Cl pour quantifier les processus superficiels était souvent affectée d'incertitudes liées aux différents taux de production publiés et semblait plus compliquée que d'autres cosmonucléides comme le ^{10}Be ou le ^{26}Al à cause des sources de production nombreuses et spécifiques à ce nucléide. Il apparaît donc nécéssaire de clarifier et de décrire de façon détaillée les différentes sources de production, leurs incertitudes et leurs domaines d'application. De plus, une feuille de calcul simple permettant la détermination des âges d'exposition et des taux d'érosion et intégrant de façon exacte et précise toutes les réactions de production du ^{36}Cl et applicable à tout type de roche paraît aujourd'hui indispensable.

Cette thèse vise donc à combler ces lacunes pour, d'une part, améliorer la justesse des taux de production du ^{36}Cl par spallation, et d'autre part faciliter l'application du ^{36}Cl à la quantification des processus superficiels en proposant une stratégie pour réduire les incertitudes et en fournissant une feuille de calcul simple pour l'application de cette méthode.

Les trois premiers chapitres présentent 1- les principes de la production des nucléides

cosmogénique in situ et leur variabilité dans l'espace et dans le temps, 2- les méthodes utilisées pour l'échantillonage, pour la préparation des échantillons, y compris un nouveau protocole chimique applicable à tout type d'échantillon silicaté, et pour les mesures analytiques, et 3- la description de la nouvelle feuille de calcul pour déterminer des âges d'exposition et des taux d'érosion à partir du ^{36}Cl.

Les résultats principaux qui font l'objet d'articles soit publié soit en cours de publication dans des revues de rang A sont présentés dans les chapitres 4, 5 et 6, et sont résumés ci dessous.

Détermination des sources du ^{36}Cl dans des roches basaltiques : Implications pour la calibration des taux de production.

Pour expliquer les divergences dans les taux de production du ^{36}Cl proposés actuellement dans la littérature plusieurs sources d'erreur peuvent être évoquées à savoir (1) l'âge du site de calibration indépendamment déterminé, (2) les facteurs d'échelle, (3) la composition des roches utilisées, (4) le protocole chimique adopté et (5) des mécanismes de production non considérés. Alors que Phillips et al. (2001) et Zreda et al. (1991) dérivent leur taux de production de différents types de roches totales, Stone et al. (1996) et Evans et al. (1997) ont travaillé sur des minéraux séparés. A partir de cette observation, nous avons entrepris de tester si ces différences pouvaient expliquer les divergences dans les taux de production. Dans le but d'identifier toutes les sources du ^{36}Cl dans la roche, nous avons mené des expériences de lixiviation et de dissolution successive sur des échantillons prélevés sur des coulées basaltiques de l'Etna. Les caractéristiques pahoehoe de ces coulées indiquent que l'érosion est négligeable, et les concentrations en ^{3}He cosmogénique et les âges K-Ar sont connus (Blard et al., 2005). Nous avons travaillé sur des fractions comprises entre 140 et 1000 μm, sur roche totale et sur des plagioclases. Après un premier lessivage dans l'HNO_3 dilué, les échantillons ont été progressivement dissous en 6 à 8 étapes avec des quantités limitées d'un mélange de HF et d'HNO_3. Pour chaque étape, les concentrations en ^{36}Cl et en Cl ont été déterminées par spectrométrie de masse par accélérateur au LLNL (Figs. 4.3 and 4.3), alors que les concentrations des éléments cibles Ca, K, Fe et Ti ont été déterminées au SARM (Fig. 4.5).

Les résultats de ces expériences montrent que (1) les concentrations très élevées en chlore des roches totales (5000 - 300 ppm) entraînent une surestimation de l'âge d'exposition d'environ 30% par rapport à l'âge attendu (Fig. 4.6), et (2) au contraire, la procédure de lixiviation et de décontamination est efficace sur les plagioclases après 20% de dissolution avec des concentrations en chlore faibles. Les âges d'exposition obtenus sont en accord avec ceux attendus.

Nous avons pu écarter une possible contamination par du ^{36}Cl atmosphérique ou magmatique qui pourraient être en partie responsable de ces différences.

Il est donc probable que les divergences dans les taux de production du ^{36}Cl publiés soient liées à la forte teneur en Cl dans certaines des roches utilisées pour les calibrations. En effet, nous pouvons constater que par exemple le taux de production par spallation du Ca publié par Phillips et al. (2001) calibré avec des roches silicatées riches en Cl est presque 30% plus élevé que celui publié par Stone et al. (1996) qui ont utilisé des minéraux avec de faibles teneurs en Cl. La production du ^{36}Cl à partir du ^{35}Cl est en effet sensible à des facteurs externes tels qu'une fine couche d'eau qui peuvent maximiser cette production, ces effets sont difficilement quantifiables et encore peu connus (Phillips et al., 2001; Masarik et al., 2007).

Ces résultats sont présentés dans le chapitre 4 et publiés dans *Quaternary Geochronology* (Schimmelpfennig et al., 2009).

Par ailleurs, nous avons conçu une feuille de calcul Excel®, publiée dans l'article Schimmelpfennig et al. (2009), qui permet de déterminer des âges d'exposition et des taux d'érosion à partir des mesures en ^{36}Cl pour tout type de roche, située à la surface ou en profondeur. Cette feuille permet également de calculer précisément les différentes contributions dans la production de ^{36}Cl, c'est-à-dire connaître de façon précise tous les termes qui sont dans l'équation 2 et contraindre les incertitudes sur les différents paramètres. Toutes les réactions qui engendrent la production du ^{36}Cl y sont intégrées. Cette feuille, facile d'utilisation, permet une visibilité de tous les paramètres rentrant dans le calcul ainsi que des incertitudes associées. Son utilisation et sa fonctionnalité sont détaillées dans le chapitre 3.

Calibration des taux de production du ^{36}Cl à partir de la spallation du Ca et du K

Une des difficultés majeures de la calibration des taux de production du ^{36}Cl est de contraindre les proportions relatives des différentes sources de production qui dépendent de la composition chimique de l'échantillon et particulièrement de sa concentration en chlore. Pour surmonter cette difficulté, il convient de travailler sur des minéraux séparés qui nous permettrons d'isoler la source de production à calibrer, c'est ce que nous avons montré dans le chapitre 4 (Schimmelpfennig et al., 2009). Nous avons donc travaillé sur des minéraux riches en Ca et K, contenant très peu de chlore pour calibrer les taux de production du ^{36}Cl par spallation du Ca et du K.

Des plagioclases riches en Ca ont été séparés à partir de roches basaltiques de 4 coulées provenant du Mt Etna (38°N, Italie), et des sanidines riches en K ont été séparés à partir d'une trachyte d'une coulée prélevée sur le volcan Payun-Matru (36°S, Argentine). Au total, 13 échantillons ont été prélevés sur les 5 coulées dont leur âge a été déterminées de façon indépendante entre 0.4 and 32 ka. Les altitudes des sites d'échantillonnage au Mt. Etna sont entre 500 et 2000 m et de ceux au Payun Matru entre 2300 et 2500 m. Les facteurs d'échelle correspondant ont été calculés en utilisant 5 différents modèles proposés dans la littérature parmi lesquels quatre incluent les variations du champ magnétique. Ces facteurs d'échelle montrent des différences significatives entre les 5 modèles avec des écarts entre modèles allant jusqu'à 23% pour les échantillons du Mt. Etna et jusqu'à 7% pour les échantillons du Payun Matru.

En combinant et modifiant les Eqs. 1 et 2, la relation entre la concentration en ^{36}Cl (N_{36}) et les taux de production (SLHL) à partir du Ca (PR_{Ca}) et du K (PR_K) que nous cherchons à déterminer a donc pu être écrite sous la forme:

$$N_{36} = A \times PR_{Ca} + B \times PR_K + C \tag{4}$$

avec A, B et C, des variables qui dépendent de la composition chimique, de l'âge d'exposition, des autres sources de production et des facteurs d'échelle. Ces variables ont été calculées à l'aide de la feuille de calcul précédemment mentionnée. Pour chaque mesure

du jeu d'échantillons, l'équation 4 a été adoptée et l'ensemble des mesures a été analysé statistiquement avec une approche Bayesienne. Cette approche permet de tenir compte d'une façon consistante des incertitudes inhérentes aux données utilisées notamment sur les âges indépendants.

Les taux de production dérivés sont les plus bas calibrés jusqu'à présent. En appliquant les facteurs d'échelle calculés selon Stone (2000), les taux de production obtenus sont pour PR_{Ca} de 42.2 ± 4.8 atomes ^{36}Cl (g Ca)$^{-1}$ an^{-1} et pour PR_K de 124.9 ± 8.1 atomes ^{36}Cl (g K)$^{-1}$ an^{-1}. Ces nouvelles valeurs sont en accord avec les taux de production précédemment calibrés avec des échantillons faibles en Cl, notamment avec 48.8 ± 1.7 atomes ^{36}Cl (g Ca)$^{-1}$ an^{-1}, publié par Stone et al. (1996), et avec 137 ± 9 atomes ^{36}Cl (g K)$^{-1}$ an^{-1}, publié par Phillips et al. (2001).

Les valeurs obtenus avec les 4 autres modèles de facteurs d'échelle sont très proches et comprises dans les barres d'erreur des valeurs ci-dessus. Elles sont présentées dans le tableau 5.7 du chapitre 5. Alors que nos données se répartissent sur une période de temps importante et des altitudes très différentes, les âges recalculés avec ces nouveaux taux de production sont en accord avec les âges indépendants quelque soit le modèle de facteur d'échelle choisi. Bien qu'il y ait des différences importantes dans les modèles de facteurs d'échelle, celles ci n'engendrent pas de différences significatives dans les taux de production finaux, parce que: 1- les incertitudes sur nos taux de production sont assez importantes (6 - 10%) et elles résultent principalement des incertitudes sur les âges indépendants, et 2- les divergences entre les différents modèles de facteurs d'échelle ont été moyennées sur les gammes d'âge et d'altitude de l'ensemble de nos données.

Ce travail est présenté dans le chapitre 5 et fait l'objet d'une publication que nous pensons soumettre à Geochimica Cosmochimica Acta.

Inter-calibration des taux de production du ^{36}Cl et des gaz rares cosmogéniques ^{3}He et ^{21}Ne

Pour déterminer l'âge d'exposition d'une surface géologique, les taux de production utilisés doivent être ajustés à l'altitude et à la latitude du site d'échantillonnage et intégrés sur le temps d'exposition. Ceci est dû à la variabilité des taux de production avec l'altitude,

la latitude et le temps. Comme discuté précédemment, cette variabilité est quantifiée à partir de facteurs d'échelle eux-mêmes calculés à partir de modèles, encore en discussion. Il est possible que l'inexactitude de ces modèles soit en partie responsable des divergences observées dans les taux de production publiés et par conséquent entraînent des incertitudes sur les âges d'exposition (Chapter 5, Balco et al., 2008, 2009).

Ces modèles sont généralement basés sur l'hypothèse que les réactions produisant le nucléide, par exemple la spallation, sont soumises à la même variabilité spatiale et temporelle, indépendamment de l'élément cible et/ou du nucléide cosmogénique produit. Cependant, nous savons que les réactions qui engendrent la production des cosmonucléides ont des seuils énergétiques différents suivant l'élément cible, c'est-à-dire que la production des divers nucléides cosmogéniques dépend du spectre énergétique des particules cosmiques (Michel et al., 1995; Lal, 1987, Fig. 6.1). Etant donné que l'énergie d'incidence des particules constituant le rayonnement cosmique augmente avec l'altitude et la latitude il est nécessaire d'évaluer si les taux de production des divers cosmonucléides ont des variabilités spatiales et temporelles différentes. Si c'était le cas nous aurions besoin de facteurs d'échelle individuels associés à chaque nucléide ou même à chaque réaction spécifique à partir d'un élément cible. Gayer et al. (2004) et Amidon et al. (2008) ont suggéré une variabilité altitudinale différente pour la production du ^{3}He et du ^{10}Be.

Dans le cadre d'une collaboration avec le CRPG, nous avons entrepris de comparer la production du radionucléide ^{36}Cl avec celles des nucléides stables ^{3}He et ^{21}Ne dans des pyroxènes, riches en Ca, prélevés dans des coulées basaltiques le long d'un profil altitudinal (1000 - 4300 m) au Kilimandjaro (Tanzania, 3°S). Ce travail n'est pas encore totalement abouti puisqu'il sera complété prochainement par des mesures de ces trois mêmes isotopes sur des échantillons de l'Etna qui suite à des problèmes techniques n'ont pas pu être mesurés à temps pour figurer dans cette thèse.

Après avoir validé un nouveau protocole d'extraction du ^{36}Cl à partir des pyroxènes, en mesurant le ^{36}Cl dans des plagioclases co-existant dans un même échantillon, les concentrations en ^{36}Cl, ^{3}He et ^{21}Ne ont été déterminées dans les pyroxènes.

En comparant les rapports ^{36}Cl/^{3}He, ^{21}Ne/^{3}He et ^{36}Cl/^{21}Ne (Fig. 6.9) nous ne con-

statons aucune dépendance significative en fonction de l'altitude. Le rapport $^{21}Ne/^{3}He$, déterminé dans notre étude, est en accord avec ceux d'autres études (Poreda and Cerling, 1992; Niedermann et al., 2007; Fenton et al., 2009).

Les trois nucléides sont également comparés en fonction de leurs âges d'exposition calculés à partir de leurs concentrations. Cette approche à pour but de s'affranchir des particularités liées au nucléide ^{36}Cl par rapport aux deux autres nucléides, notamment sa décroissance radioactive, sa production par capture des muon négatifs lents sur le Ca et sa forte dépendance avec la composition chimique. Là encore, il n'est pas observé de dépendance significative avec l'altitude. Cependant il conviendra de tester à l'avenir une eventuelle dépendance entre des nucléides qui ont des spectres énergétiques plus différents tels que le Ca et le K pour la production par spallation du ^{36}Cl.

Ce travail est présenté dans le chapitre 6 de cette thèse.

Conclusion

Les résultats de cette thèse contribuent considérablement à l'amélioration des aspects méthodologiques et analytiques du nucléide cosmogénique ^{36}Cl. La mise en évidence d'une surestimation des taux de production précédemment publiés avec des échantillons à fortes teneurs en chlore montrent que toutes les différentes sources de production du ^{36}Cl doivent être toutes intégrées et considérées de façon rigoureuse et détaillée pour obtenir des âges d'exposition cohérents et valables.

Les nouveaux taux de production par spallation du Ca et du K proposés dans cette étude sont en accord avec les taux précédement obtenus avec des échantillons faibles en Cl. Ceci permet, d'une part, de reconcilier les précédentes calibrations faites et ouvre ainsi la porte à des déterminations d'âges d'exposition mieux contraintes et, d'autre part, de mettre en évidence les difficultés et les incertitudes inhérentes à l'utilisation d'échantillon riche en Cl du fait du flux de neutrons thermiques peu contraint et sensible à divers paramètres encore difficilement quantifiables.

Contents

General introduction

The use of terrestrial cosmogenic nuclides (TCN) has revolutionized Earth surface sciences over the last decade by their capacity to quantify geological surface processes. The uniqueness of these nuclides lies in their property of being produced in the top few meters of the lithosphere during exposure to cosmic radiation. Secondary cosmic ray particles that bombard the Earth's surface interact with certain target elements in the rock producing long-lived radionuclide (^{10}Be, ^{26}Al, ^{14}C and ^{36}Cl) and stable noble gas isotopes (^{3}He and ^{21}Ne) that usually do not exist in the rock or only in very small quantities.

A rock that is suddenly exposed at the surface accumulates an inventory of such cosmogenic nuclides as time passes by. Hence, the nuclide concentration is a measure of how long the rock has been exposed to cosmic rays, which allows dating the event that led to the exposure of the rock. With the knowledge of the nuclide concentration and of the rate, at which nuclide is produced at the sample site, the exposure duration can be calculated, ignoring for the moment radioactive decay, by the general relationship:

$$\text{Exposure time} = \text{TCN concentration} / \text{Local production rate}$$

The challenge of measuring the extreme low level concentrations of TCN with high precision was overcome in the early 1980's by the groundbreaking improvements in Accelerator Mass Spectrometry (AMS) and in high sensitivity Noble Gas Spectrometry. Since that time the application of the surface exposure dating method has been steadily increasing. However, the accuracy of exposure ages does not only depend on the analytical measurability of the nuclides but also on the accurate knowledge of the mentioned TCN production rates.

For the determination of a TCN production rate at a particular sample site, two funda-

mental questions are: how many atoms of the nuclide are produced per g of target material per year? and how does this production rate vary in space and time?

Production rates are experimentally calibrated with geological samples from surfaces that have simple exposure histories and that have been dated accurately and precisely by independent methods. Since such surfaces are rare, globally valid reference production rates are calculated by normalizing calibration sites to a virtual reference position at sea level and high latitude ($> 60°$), hereafter SLHL, by accounting for the spatial and temporal variability of the production rates. This variability is primarily due to the varying shielding effect of the geomagnetic field and of the atmosphere on the cosmic radiation and is as such mainly a function of the altitude and the latitude of the sample site. The quantification of this variability is made possible by scaling models that provide methods to calculate scaling factors (e.g. Lal, 1991; Dunai, 2001; Lifton et al., 2005). These scaling factors allow extrapolating SLHL production rates to any geographic position and vice versa.

However, SLHL production rates of most of the TCN, calibrated at different locations by different investigators can differ considerably from each other, in the case of ^{36}Cl by up to 50% (e.g. Stone et al., 1996; Swanson and Caffee, 2001). Moreover, numerous existing scaling models yield scaling factors that diverge significantly at some geographic positions. The TCN surface exposure dating method can therefore not yet guarantee a satisfactory accuracy as other geochronometers such as radiocarbon or argon-argon dating.

The European project *CRONUS-EU*, a Marie Curie Research Training Network, had the objective to better constrain TCN production rates and their variability in space and time as well as other parameters related to the systematics of TCN. In addition to the experimental determination of production rates with geological samples, artificial targets and theoretical modeling were used as approaches. This PhD study, funded by *CRONUS-EU*, focuses mainly on the experimental calibration of ^{36}Cl production rates and the use of this radionuclide for surface exposure dating.

Four production pathways are responsible for the in situ production of ^{36}Cl (Fig. 1):

1. At the surface, ^{36}Cl is mostly produced by high-energy neutron-induced spallation

reactions on the target elements Ca and K, and to a lesser degree on Ti and Fe.

2. A minor production pathway at the surface is the capture of slow negative muons by ^{40}Ca and ^{39}K. It becomes important at greater depths.

3. The capture of low-energy (thermal and epithermal) neutrons by ^{35}Cl leads to the production of ^{36}Cl, mainly dependent on the Cl content in the sample.

4. A non-cosmogenic production of ^{36}Cl is due to slowed down radiogenic neutrons that form during the spontaneous fission of ^{238}U and (α,n)-reactions on light elements, where the α-particles are produced during U and Th decay.

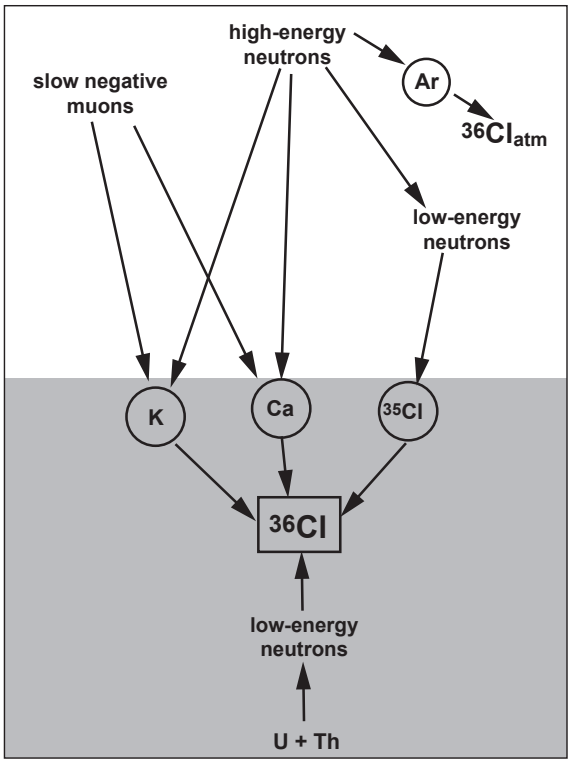

Figure 1: *Schema of production reactions for ^{36}Cl in rock (shaded part) and in the atmosphere (white part). Not illustrated are Ti and Fe, which are also target elements for ^{36}Cl production by interaction with high-energy neutrons (spallation). In addition to in situ production reactions, mentioned in the text, ^{36}Cl is also produced in the atmosphere by spallation of Ar.*

^{36}Cl is often used for surface exposure dating of limestone, since it is currently the only TCN that can be measured in this rock type and its target element Ca is abundant

in limestone. For cristalline rocks or quartz-containing sediments other nuclides are often preferred due to their simpler and better constrained production systematics. However, in situ ^{36}Cl has the advantage that its chemical extraction is apparently possible from any rock and mineral type that contain at least one of its target elements (Ca, K, Ti, Fe), in contrast to the other TCNs, which are restricted e.g. to quartz in the case of ^{10}Be and ^{14}C or to mafic minerals (olivine and pyroxene) in the case of ^{3}He due to certain chemical behaviors of these nuclides. In addition to limestone, ^{36}Cl is routinely extracted from silicate whole rock and feldspars. Other minerals, such as Ca-rich mafic minerals (e.g. pyroxene) and K-rich felsic minerals (e.g. muscovite) have still to be validated to be suitable for reliable ^{36}Cl extraction.

Also, ^{36}Cl is potentially very well suited to study complex exposure histories such as those involving erosion during exposure or the sudden burial of a surface that was exposed before. For this kind of problem, the approach usually consists in measuring two nuclides in the same sample. The principle is based on the different production and decay rates of the two nuclides, which lead to unique TCN concentration ratios that can be assigned to certain exposure histories. ^{36}Cl has a high potential for this approach due its production systematics that differ essentially from those of the other nuclides.

However, as a matter of fact, none of the ^{36}Cl production rates from its divers target elements is well constrained. The so far published SLHL spallation production rates from Ca differ by up to 46% (Stone et al., 1996; Swanson and Caffee, 2001), and those from K by up to 53% (Zreda et al., 1991; Swanson and Caffee, 2001).

Why have the production rates from spallation of Ca and K such high discrepancies? and what are the valid production rate values? What is the influence of the scaling factors and their inaccuracies in production rate calibrations?

Also, the production pathway due to capture of low-energy neutrons is difficult to parameterize due to the complex distribution of the low-energy neutrons at the rock/air boundary and due to its dependency on many environmental factors (e.g. Phillips et al., 2001). This makes the calculations difficult, if the target element ^{35}Cl is abundantly present

in the sample.

What is the impact of this difficulty, when having high Cl contents in the samples, on the calibration of spallation production rates and how can we avoid propagating the related uncertainties into the spallation production rates?

A simple and comprehensible calculator to routinely compute ^{36}Cl production from the various reactions and ^{36}Cl exposure ages from rocks with any composition has been lacking up to now. Quantifying surface processes with ^{36}Cl can therefore be a great challenge, if the investigator is not familiar with these issues. As a consequence, the use of ^{36}Cl is generally avoided and other nuclides are preferred.

How can we facilitate the use of ^{36}Cl for exposure age and erosion rate determinations? Which types of rock are most appropriate for the use of ^{36}Cl in quantifying surface processes? How can we guarantee that also non-experts account correctly for all ^{36}Cl production pathways?

In summary, improvements in the accuracy of the ^{36}Cl production rates, strategies for reducing uncertainties in exposure ages and erosion rates and the supply of an easily usable means to calculate ^{36}Cl exposure ages will facilitate the use of this promising cosmogenic nuclide and thus significantly broaden the possibilities in surface exposure dating.

This PhD study aims at advancing in these issues.

The first three chapters present

1) the principle of TCN production and its variation in space and time,

2) the methods used for sampling, physical and chemical sample preparation, measurements and all analytical uncertainties, including a new chemical protocol for ^{36}Cl extraction from silicate rock types, and

3) the description of a new ^{36}Cl calculator for the determination of exposure ages and erosion rates from any rock type in which ^{36}Cl has been measured.

Chapter 4 deals with the understanding of why the existing calibrated production rates diverge so much. The objective is to pave the way for a higher accuracy in a next calibration attempt. Since in previous calibration studies either different kinds of whole

rock or separated minerals were used, we assumed that the discrepancies in the resulting production rates could be related to the chemical differences of these two kinds of target materials. Therefore, ^{36}Cl exposure ages determined from basaltic whole rock and from Ca-feldspars separated from the same rock are compared with the exposure age of the lava determined independently by K-Ar dating to investigate which type of target material yields the more reliable result. This chapter is accompanied by a detailed review of the theoretical bases for the calculation of ^{36}Cl in any rock type with any composition. It is published in the journal *Quaternary Geochronology* together with the new Excel® spreadsheet for ^{36}Cl calculations.

Chapter 5 presents a new calibration of ^{36}Cl production rates from spallation of the target elements Ca and K, taking into account the results of the first part of this PhD study. For this purpose, Ca- and K-feldspars low in Cl were separated from five basaltic lava surfaces, whose exposure ages are independently known. The samples were taken at the volcanoes Mt. Etna (Sicily) and Payun Matru (Argentina). The SLHL production rates are determined from the sample set consisting of 20 ^{36}Cl measurements by using a Bayesian statistical method accounting for all major uncertainties in the data set.

Chapter 6 of this PhD deals with the comparison of the concentrations of the three cosmogenic nuclides ^{36}Cl, ^{3}He and ^{21}Ne in pyroxene phenocrysts from lava samples taken over an altitude transect between 1000 and 4300 m at Kilimanjaro (Tanzania). The objective of this cross-calibration is to investigate if these three nuclides feature different altitude dependences in their production rates, which could help understanding why the existing scaling methods still fail to describe accurately the spatial variability of TCN production rates.

In addition, this last study aims at confirming the use of Ca-rich pyroxene for the successful extraction of ^{36}Cl, which has, to our knowledge, never been attempted before. This method is validated by measuring ^{36}Cl in cogenetic Ca-feldspar minerals separated from the same sample as the pyroxene.

Chapter 1

The principles of surface exposure dating with terrestrial cosmogenic nuclides (TCN)

1.1 The application of terrestrial cosmogenic nuclides and their limitations

Development of the TCN dating method. In-situ terrestrial cosmogenic nuclides (TCN) are widely used for surface exposure dating in the earth sciences thanks to the rapid improvements in analytical techniques and in the understanding of the TCN systematics (Gosse and Phillips, 2001). This development, however, is quite recent. The first attempt to date a glacially formed surface in a mafic rock with the in-situ cosmogenic nuclide ^{36}Cl was performed in 1955 by Davis and Schaeffer (1955). The lack of an appropriate analytical technique that allowed measuring the extreme low-level concentrations of cosmogenic radionuclides impeded further studies in this field for three decades. The development and refinement of accelerator mass spectrometry (AMS) in the early 1980s (Elmore and Phillips, 1987; Finkel and Suter, 1993) marked the beginning of the subsequently fast progressing research field of cosmogenic isotopes in the earth sciences. The long-lived cosmogenic radionuclides now routinely measured by AMS (see Chapter 2.3.2) are ^{10}Be, ^{14}C, ^{26}Al and ^{36}Cl. Simultaneously to the refinements in AMS, it became possible for the measurement of the stable cosmogenic nuclide ^{3}He (Kurz, 1986a,b) and later ^{21}Ne (Graf et al., 1991) with conventional mass spectrometry to be applied for surface exposure dating.

The first empirical calibrations of TCN production rates were performed for ^{10}Be and ^{26}Al by Nishiizumi et al. (1986), for ^{3}He by Kurz (1986b), for ^{21}Ne by Poreda and Cerling (1992) and for ^{36}Cl by Zreda et al. (1991). Also, the development of a standard means to calculate the relative local production rates for any geographic position on earth (Lal, 1991) (Chapter 1.4) facilitated the routine application of TCN for the quantification of landforming processes.

Geologic applications. Surface exposure dating with TCN has become essential in earth science disciplines such as geomorphology, paleoclimatology and active tectonics. Chronological constraints on the timing and rates of environmental changes (glacial history, erosion) and hazard recurrence frequency (landslides, volcanic and seismic activity) have been quantified using TCN (see reviews in e.g. Gosse and Phillips, 2001; Siame et al., 2006; Muzikar et al., 2003).

Time periods datable with TCN. The TCN method is mainly used to date surfaces generated during the quaternary period. Older surfaces have been dated with the stable cosmogenic noble gases ^{3}He and ^{21}Ne, e.g. sediments with pre-Pliocene ages ($>$ 10 Ma) in Antarctica (Schaefer et al., 1999) or in the Atacama Desert (Dunai et al., 2005). The maximum time range that can be covered with TCN dating is, however, mostly limited to the Quaternary by two factors: the half-life, when using a radioactive nuclide, and the preservation of the surface. In contrast to the two stable nuclides ^{3}He and ^{21}Ne, the buildup of the radioactive nuclides ^{10}Be, ^{14}C, ^{26}Al and ^{36}Cl (half-lives in Table 1.1) increases until steady state is reached, which is when the TCN production is in equilibrium with the radioactive decay (3 - 4 half-lives). For example, ^{36}Cl has a half-life of 301 ka, so that after 1 Ma exposure a surface is very close to saturation, whereas the half-life of 10Be is 1.39 Ma (Chmeleff et al., 2009; Korschinek et al., 2009, it has for a long time considered to be about 1.5 Ma), meaning that the saturation limit is reached much later (Fig. 1.1). This generalization is, however, only true for non-erosion conditions.

As the rock surface is exposed to cosmic radiation, it is usually also subject to erosion. Erosion affects the TCN concentration in a surface sample, mostly lowering the concentration compared to the non-erosion condition (see Fig. 1.1). The older the surface the

higher this effect. There are then two unknowns, the exposure time and the erosion rate (Lal, 1991).

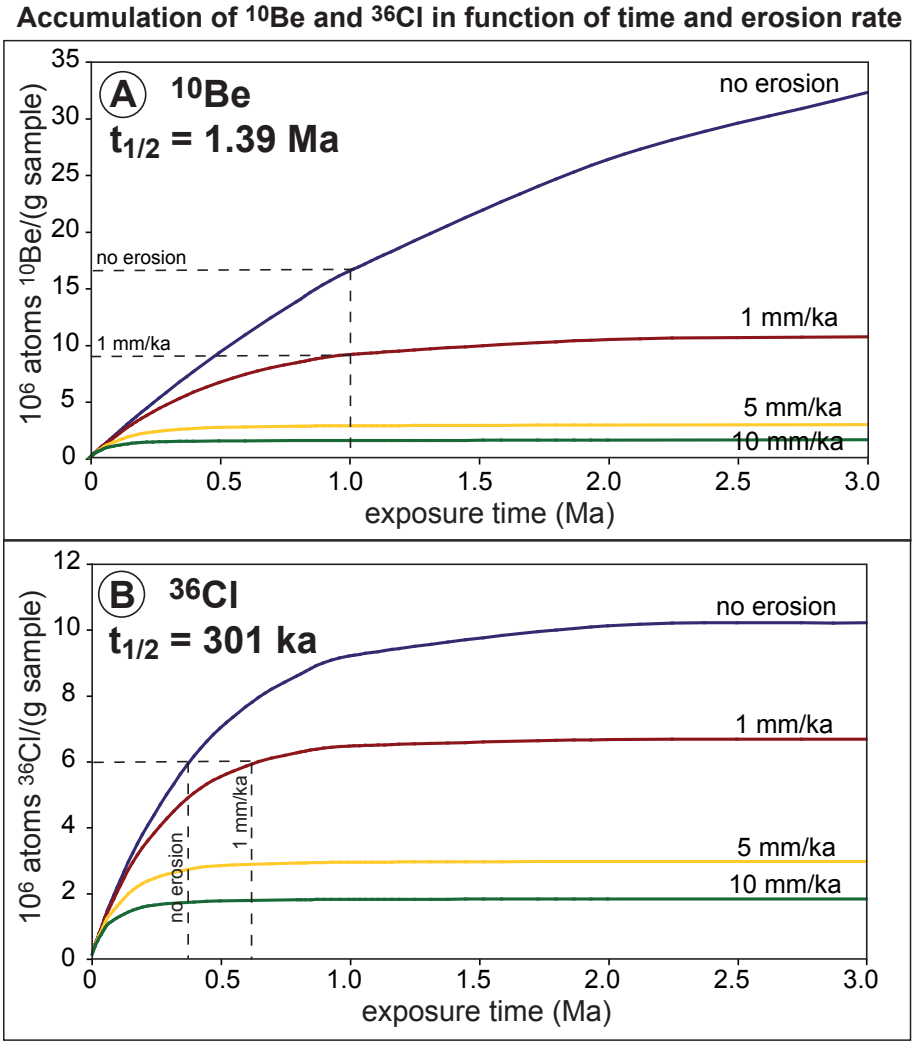

Figure 1.1: *Accumulation of the radionuclides ^{10}Be (A) and ^{36}Cl (B) in a hypothetical surface sample in function of time (0 to 3 Ma) and steady erosion rates. ^{10}Be concentrations are calculated for a quartz sample, and ^{36}Cl concentrations for a Ca-rich Cl-free plagioclase sample (i.e. production from spallation is dominant). In both cases, the sample site is at mid latitude and 2000 m altitude. Due to its shorter half-life, ^{36}Cl reaches earlier its equilibrium concentration. The dashed lines in (A) demonstrate that the nuclide concentration is lower the higher the erosion rate for the same exposure duration. The dashed lines in (B) illustrate that underestimating or ignoring erosion for a given measured nuclide concentration leads to an apparently younger exposure age.*

Exposure age and erosion rate of a surface can be determined simultaneously by combining two TCN with different half-lifes. Up to now, this approach has mainly been used

with the nuclides ^{10}Be and ^{26}Al, since their production mechanisms are fairly well known and simple and both nuclides can be measured in quartz (e.g. Nishiizumi et al., 1991). However, also ^{36}Cl is potentially very useful for this method due to its relatively short half-life and the variety of its production mechanisms (e.g. Liu et al., 1994; Gillespie and Bierman, 1995).

Another method to constrain the exposure age and erosion rate of a surface is by measuring nuclide concentrations over a certain depth range and using the characteristic depth profile, its shape also depending on the erosion rate and the exposure history (e.g. Siame et al., 2004; Braucher et al., 2009, and see Fig. 1.2). ^{36}Cl is particularly suited for this approach due to its unique vertical distribution if production due to low-energy neutrons is dominant (see Fig. 1.12 and Chapter 3.3 for details).

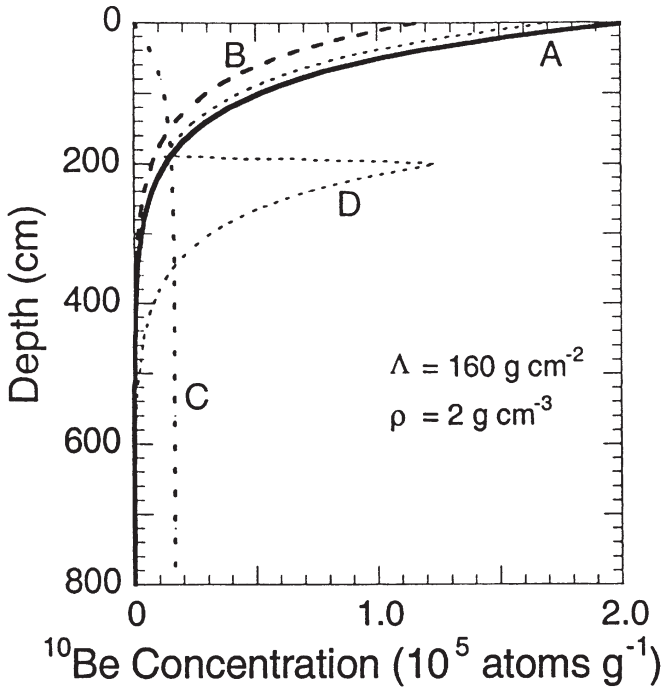

Figure 1.2: *Vertical distribution of ^{10}Be in a depth profile for various exposure histories (from Gosse and Phillips, 2001): A - One simple and continuous exposure event. B - Gradual erosion at a constant rate. C - The surface is continously aggrading by sedimentation at a constant rate. D - After a continuous period of exposure a former surface (now at ∼200 cm) was suddenly burried; the new surface is now constantly exposed.*

Although the time range that can be dated with the stable nuclides ^{3}He and ^{21}Ne is not

restricted to Quaternary surfaces, a drawback of the isotopic stability is that the nuclide clock is never set to zero by decay, so that a more frequent problem is *inheritance*, initially present amounts of the nuclide inherited from exposure periods prior to that of interest (Bierman, 1994).

The minimum time period that can be dated is mainly controlled by the analytical sensitivity and the non-cosmogenic background concentrations of the respective nuclide. The nuclide quantity in a sample can be too low to be accurately detected by the measurement technique (Chapter 2.3.2). In this context the value of the production rate has to be considered because the accumulation of a nuclide in a sample is govered by its production rate: the higher the production rate the faster the accumulation. Of the nuclides mentioned above, ^{10}Be has the lowest reference production rate (about 5 atoms (g quartz)$^{-1}$ a^{-1}) and ^{3}He has the highest production rate in olivine and pyroxene (about 120 atoms/ (g mineral)$^{-1}$ a^{-1}). However, the low-level concentrations in a sample might be compensated by extracting the respective nuclide from a larger sample (see Chapter 2.1 for ^{36}Cl). Due to improvements of the sensitivity of the AMS technique, ^{10}Be exposure ages as young as 200 years with 1 σ analytical uncertainties of less than 10% have been recently determined at LLNL-CAMS (Schaefer et al., 2009; Licciardi et al., 2009). In Chapter 5 of this dissertation the ^{36}Cl measurement of a 400 year young lava flow is part of the data set for the ^{36}Cl production rate calibration. Its ^{36}Cl concentration has been determined with a 1 σ analytical uncertainty of less than 4% at LLNL-CAMS. Non-cosmogenic background concentrations due to radiogenic, nucleogenic and/or magmatic origin of the nuclide can limit the identification of the cosmogenic component in the case of very young samples. This concerns ^{3}He, ^{21}Ne and ^{36}Cl (Chapters 1.3.6, 1.3.7 and 1.3.8).

Choice of nuclide. When applying the TCN method, the choice of the nuclide depends mainly on the lithology of the rock surface of interest, because TCN production varies in different minerals as a function of their composition. Since cosmogenic nuclides are produced by interaction of secondary cosmic ray particles with certain target elements (Chapter 1.3), they can only accumulate in a sample if at least one of the respective target elements is present. The nuclides ^{10}Be, ^{26}Al and ^{14}C are almost always studied in quartz,

Table 1.1: *Half-lives of the cosmogenic radionuclides and the mineral phases each TCN is routinely extracted from with the corresponding lithologies.*

Nuclide	Half-life	Mineral phases	Type of lithology
^{3}He	-	pyroxene, olivine	mafic volcanic rocks
^{10}Be	1.39 Ma	quartz	magnetic rocks, sandstone, conglomaterates
^{14}C	5.73 ka	quartz	magnetic rocks, sandstone, conglomaterates
^{21}Ne	-	quartz, pyroxene, olivine	magnetic rocks, sandstone, conglomaterates
^{26}Al	720 ka	quartz	magnetic rocks, sandstone, conglomaterates
^{36}Cl	301 ka	calcite, Ca/K-rich feldspar, whole rock	magnetic rocks, limestone, Mg-carbonate

because Si and O are their most important target elements (for ^{26}Al only Si) and because certain characteristics of the nuclides can make it difficult to measure them in other mineral phases.

For example, atmospheric ^{10}Be, produced in the atmosphere by spallation of O and N, is highly reactive with mineral surfaces, which therefore require a rigorous decontamination. This atmospheric component is often much larger than the in situ cosmogenic ^{10}Be component. Kohl and Nishiizumi (1992) measured ^{10}Be concentrations in the first leaches of quartz that are two orders of magnitude larger than those measured from completely purified quartz. While quartz can be relatively easily decontaminated from this atmospheric ^{10}Be by acid-leaching (Kohl and Nishiizumi, 1992), other minerals that are less resistant to alteration such as olivine and pyroxene seem to be more problematic (Seidl et al., 1997). Though, ^{10}Be has been successfully measured in mafic minerals (Braucher et al., 2006; Blard et al., 2008). Also, in situ ^{10}Be extraction from carbonates has been unsuccessful until now due to absorption of atmospheric ^{10}Be on clay mineral surfaces (Merchel et al., 2008b). Although the use of ^{10}Be for surface exposure dating is often preferred, because its production systematics are relatively well constrained, its wide use has so far been restricted to lithologies containing quartz.

Also ^{21}Ne can be measured in quartz in contrast to ^{3}He, which diffuses too rapidly from this mineral and other mineral phases (Brook et al., 1993). ^{3}He is most often measured in

olivine and pyroxene, which bear several of its target elements for spallation reactions in varying stoichiometric ratios (O, Mg, Si, Ca, Fe, Al).

^{36}Cl is, besides ^{10}Be and ^{26}Al, the most used TCN. It is produced by various production reactions on target elements commonly abundant in many lithologies, most notably Ca, K and Cl. Like ^{10}Be it is also produced in the atmosphere, by spallation of Ar. Cosmic rays produce 3 - 6 $\times$ 10^4 atoms ^{36}Cl cm^{-2} a^{-1} in traversing the atmosphere, resulting in atmospheric ^{36}Cl/Cl ratios in the range of 10^{-15} (near costs) and 10^{-12} (inland) (Stone et al., 1996, and references herein). In situ cosmogenic ^{36}Cl/Cl ratios are on the order of 10^{-13} to 10^{-11}. In contrast to ^{10}Be, the chemical decontamination from atmospheric ^{36}Cl does not pose a problem due to the hydrophilic behavior of Cl (e.g. Merchel et al., 2008a, see also Fig. 2.11). Also, ^{36}Cl does not diffuse from certain minerals, since it is not a gas. It can therefore be measured in any rock material containing at least one of its target elements such as carbonates, Ca- and K-feldspars and mafic and felsic whole rocks. Even minerals without target elements in the crystal lattice, such as quartz, can be used for the extraction of ^{36}Cl, produced from Cl in fluid inclusions (e.g. Bierman et al., 1995). The multiplicity of the ^{36}Cl production reactions, however, is partly responsible for the discrepancies between the calibrated production rates and sometimes renders the interpretation of ^{36}Cl measurements difficult due to high uncertainties in the involved parameters (Chapter 4).

1.2 Cosmic radiation

In situ cosmogenic nuclides are produced by nuclear reactions between particles coming from the cosmos and certain target elements in the rock material. However, before this cosmic radiation reaches the earth's surface its flux and energy spectrum change as it is "filtered" through the geomagnetic field and as it passes through the atmosphere. A detailed synthesis of the underlying theory is given in Lal and Peters (1967) and in the review paper Gosse and Phillips (2001).

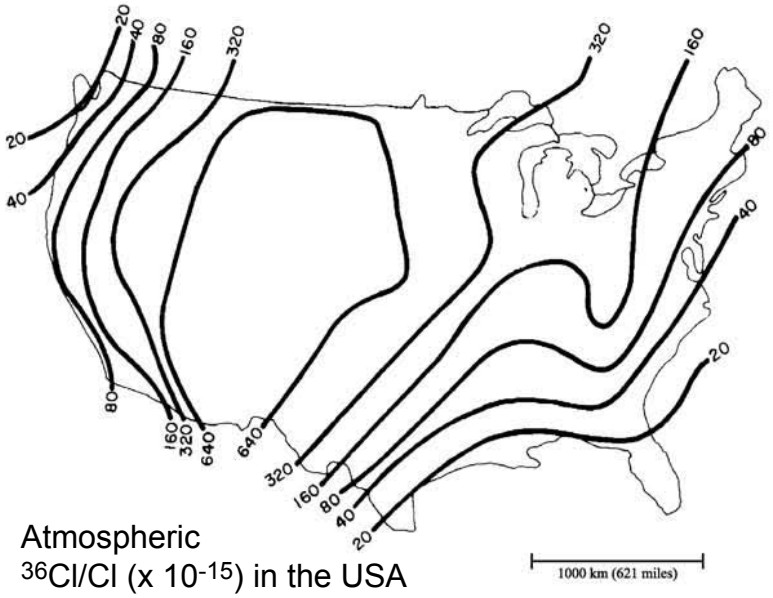

Figure 1.3: *Distribution of $^{36}Cl/Cl$ ratios in meteoric deposition in the United States after Bentley et al. (1986) (taken from Moysey et al., 2003).*

1.2.1 Primary and secondary radiation

The primary cosmic radiation consists of energetic charged particles, primarily protons (∼85%) and α-particles (∼14%), but also including heavier nuclei and electrons. These particles originate mainly from very energetic processes such as supernova explosions within our galaxy and to a small component outside our galaxy, and are called *galactic cosmic radiation*. Cosmic ray particles produced during sporadic solar flare events in the sun are referred to as *solar cosmic radiation*, which is less energetic than the galactic cosmic radiation. Most primary cosmic particles have energies too low to penetrate the earth's atmosphere and the radii of their spiral trajectories in the earth's magnetic field tends to channel them to the poles. The influence of the magnetic field on the primary radiation is described in the next section. However, if the particles are sufficiently energetic (1 GeV $< E < 10^{10}$ GeV), they can penetrate into the upper atmosphere, where they produce nuclear desintegrations. The secondary radiation is a product of these interactions between primary radiation and atoms in the atmosphere, resulting in a cascade of particles and reactions (Fig. 1.4). The cosmic ray flux at depth in the atmosphere is composed of primary and

secondary particles.

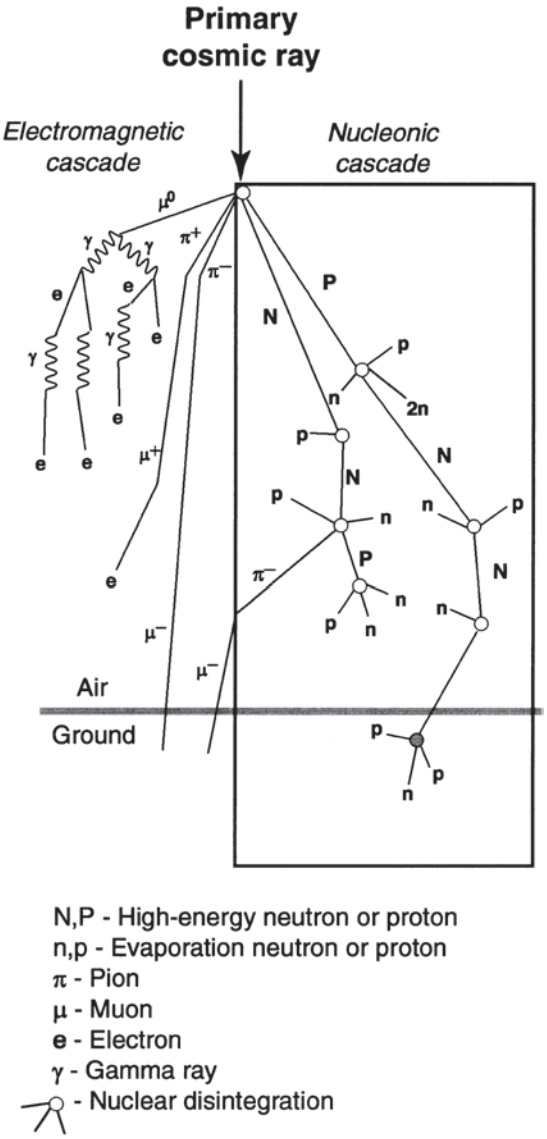

Figure 1.4: *Cascade of secondary cosmic ray particle production in the atmosphere starting with a primary particle penetrating in the upper atmosphere and ending with TCN production in the rock, from Desilets and Zreda (2001). The left part shows the electromagnetic component, dominated by electrons (e) and gamma rays or photons (γ) (low-mass particles that do not contribute to TCN production). The right part shows the hadronic component, dominated by protons (P) and neutrons (N), mostly responsible for TCN production. The middle part shows the mesonic component, here pions (π) are illustrated that decay into muons (μ). Muons have a longer attenuation length than the neutrons and protons (see text).*

1.2.2 Effect of the geomagnetic field

The effect of the geomagnetic field on the cosmic radiation, described in this section, is based on *Stormer's theory* that considers the Earth as a dipole (Stormer, 1935), meaning that the geomagnetic field intensity (or strength) is constant along a single latitude. In reality, the field strength varies longitudinally, indicating that the geomagnetic field is more complicated than a simple dipole field model (see Chapter 1.4 for more details), which, however does not make invalid the general principle of the here described effects.

Approaching the Earth's atmosphere, a charged primary's trajectory is deflected by the terrestrial geomagnetic field. Near the magnetic equator, low-energy primaries are inhibited from penetrating the atmosphere and are deflected away from the Earth. This is because, near the equator, particles must cross the magnetic field lines, while near the poles they can enter the atmosphere parallel to the field lines, which greatly reduces the magnetic shielding effect. Charged primaries with a certain energy, however, can pass through the magnetic field even at low latitudes. In other words, the geomagnetic field imposes a lower limit on the energy of primary cosmic ray particles to enter the upper atmosphere. This shielding effect is usually described by the concept of **cutoff rigidity ($\mathbf{R}_c$)** of the geomagnetic field, which is **a measure for the minimum energy a particle of a given charge must have not to be deflected by the geomagnetic field** . The geomagnetic cutoff rigidity depends on the magnetic field strength and is therefore strongly latitude-dependent. Toward higher latitudes, the dipole field lines become steeper, so that the field strength and the threshold rigidity decreases. Near the magnetic poles, at latitudes higher than 60°, the cutoff rigidity drops below the minimum energy of the primaries required to produce the particle shower in the atmosphere that is responsible for TCN production at the surface of the Earth (next section). The net effect is that a harder (higher average energy) flux penetrates the upper atmosphere at the magnetic equator, and that higher latitudes receive a wider spectrum of energies. TCN production therefore increases with increasing latitude (Fig. 1.5).

Temporal variations in the magnetic field strength only affect the cosmic ray flux below 60° latitude. Analogously, the TCN production is affected by the temporal variations

depending on the latitude (see Chapter 1.4 for more details).

1.2.3 Cosmic ray particle cascade in the atmosphere

Once the primary cosmic ray particle has penetrated the upper atmosphere, it interacts with the nuclei of the atmospheric atoms (O, N and Ar), mostly causing spallation reactions. Spallation is a nuclear reaction at energies above ∼10 MeV, where a large number of nucleons (protons or neutrons) are emitted from a heavy nucleus due to the collision with a high-energy particle. The primary incident particle may escape but loses energy. The remaining atomic weight of the hit nucleus is reduced, resulting in the formation of atmospheric cosmogenic isotopes (e.g. atmospheric ^{10}Be from spallation of O and atmospheric ^{36}Cl from spallation of Ar).

The escaped incident particle and some of the nucleons ejected by spallation are still energetic enough to cause another spallation reaction and so on. The particles produced during this reaction cascade represent the so-called secondary cosmic radiation (Fig. 1.4). Beside nucleons other particles such as mesons (e.g. kaons and muons) and electrons are produced and form part of the cascade. The further the cascade propagates down in the atmosphere the more the particles lose energy, which is mostly due to the above mentioned nuclear interactions. Particles might lose so much energy that they cannot induce nuclear reactions anymore. With increasing atmospheric depth the particle flux is therefore attenuated as it is consumed in interactions with atmospheric nuclei.

The attenuation of the cosmic ray flux is quantitively defined by the *attenuation length* or *absorption mean free path* Λ, which is the "thickness" of air (or rock or other matter) required to attenuate the intensity of the energetic cosmic ray flux by a factor e^{-1} mainly due to nuclear interactions. In reality it depends on the density of the matter, therefore to quantify Λ independently of the type of matter, the numerical value of the length is normalized to density, resulting in the unit g cm^{-2}. The attenuation length is particle-dependent, high-energy neutrons have a shorter attenuation length than muons (because muons are less reactive). It also depends on the energy spectrum of the particle flux (discussed in Desilets and Zreda, 2001, 2003; Desilets et al., 2006b, and subject of Chapter 6), which changes with latitude and atmospheric depth.

The attenuation of the cosmic ray flux in the atmosphere implies that the TCN production is strongly altitude-dependent, since the flux that reaches the surface of the earth determines the rate at which cosmogenic nuclides are produced in exposed rocks. The TCN production rates increase with higher altitudes because the flux becomes stronger (Fig. 1.5 and details in Chapter 1.4). This rise is exponential by 1% with every 10 m of elevation (Stone, 2000, see also Chapter 1.4.2).

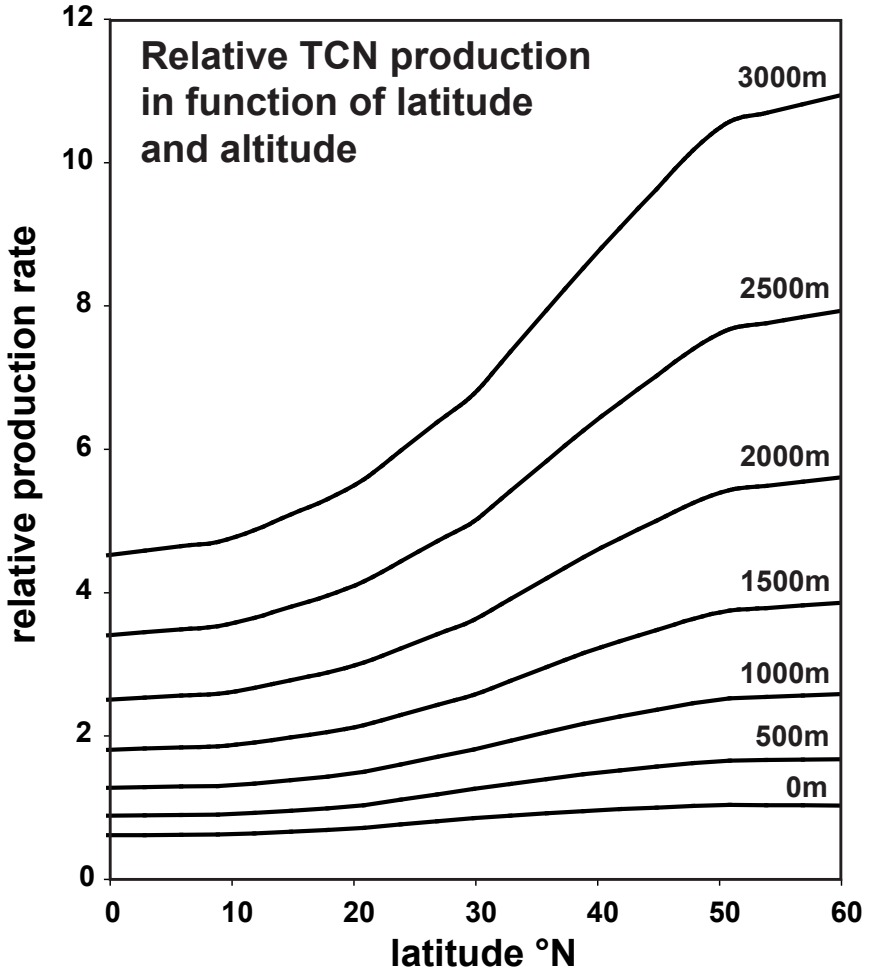

Figure 1.5: *Variation of in situ TCN production rates due to spallation reactions in function of latitude and altitude. The reference position is at sea level and latitudes* $> 60°$*. Values are calculated with the scaling method of Stone (2000).*

1.3 In-situ nuclear reactions and TCN production

The atmospheric cosmic ray flux near the Earth's surface is dominated by secondary *fast neutrons* (fast refers to high-energy with E >10 MeV, see also side note below) and has a minor mesonic component, from which short-lived muons result (Fig. 1.4). The secondary fast neutrons continue to cause spallation reactions in the atmosphere (see Chapter 1.2), hydrosphere and lithosphere keeping on losing energy. At an energy range lower than about 10 MeV they can no longer cause spallation reactions but they continue losing energy during repeated collision with atoms in the air or rock until they pass through the epithermal energy range (E ∼0.1 MeV - 0.5 eV) and finally reach the thermal energy range (E ∼0.025 eV). The *thermal neutrons* are finally absorbed by nuclei of atoms with which they collide, resulting in the formation of "thermal-neutron-produced cosmogenic nuclides" such as ^{14}C through thermal neutron absorption by ^{14}N in the atmosphere, used for radiocarbon dating, and ^{36}Cl through absorption of thermal neutrons by ^{35}Cl in rock material. *Epithermal neutrons* can be absorbed by a nucleus in the same way to produce cosmogenic nuclides, but to a lesser extent, because before they react they might be slowed down from the epithermal to the thermal energy range.

Fast neutrons, epithermal and thermal neutrons and muons are responsible for the production of cosmogenic nuclides in the lithosphere. The nuclear reactions between these secondary cosmic ray particles and the atoms in the rock material will be discussed in the following sections. The corresponding calculations that are given are for the most part taken and adapted from Gosse and Phillips (2001) and are generally valid for all cosmogenic nuclides.

Note that TCN production rates in surface rocks are commonly several orders of magnitude less than average TCN production rates in the atmosphere.

Side note: Here, the term *fast neutrons* is synonymously used for *high-energy neutrons* as it is generally done in the TCN literature. In the strict sens of nuclear physics, however, this is wrong. Fast neutrons occupy the energy range between that of the high-energy neutrons and the epithermal neutrons, approximately from 10 MeV to 100 keV, and therefore they do not initiate spallation reactions (Desilets and Zreda,

2001).

1.3.1 TCN production by fast neutrons (spallation)

In the high-energy range of secondary neutrons, cosmogenic isotopes are produced by spallation reactions: A target nucleus, e.g. a silicon atom, is hit by a fast neutron in this energy range, which spalls several lighter particles (protons and neutrons) from the target nucleus. Consequently, the remaining nucleus has a reduced atomic weight, which is the cosmogenic nuclide. If the initial target nucleus was ^{28}Si, the resulting cosmogenic nuclide can be ^{26}Al, ^{21}Ne, ^{14}C, ^{10}Be or ^{3}He. The notation for such a spallation reaction is e.g. ^{28}Si(n,p2n)^{26}Al, which means that ^{28}Si is the target nucleus, the first "n" in the bracket is the reacting neutron, "p" for one proton and "2n" for two neutrons are the emitted particles and ^{26}Al is the produced cosmogenic nuclide.

The *reference production rate (PR)* of a cosmogenic nuclide is a measure for the probability of the number of nuclides produced by spallation per g of target element and per year at a reference point (rock surface, sea level and high latitude). The production of a nuclide with an atomic mass slightly less than that of the target nucleus is more probable than the production of a lighter nuclide. Therefore, the production rate of ^{10}Be from spallation of ^{28}Si is much lower than that of ^{26}Al from spallation of ^{28}Si. PR also depends on the probability of the target element to interact with the incident particles of the flux. This probability is also called the "cross section" of the target element and depends on the energy of the incident particle.

Variations of spallation production rates in space and time are proportional to variations of the fast neutron flux. Analogous to the attenuation of the secondary cosmic ray particles in the atmosphere (Chapter 1.2), the neutron flux penetrating the rock decreases by the factor e^{-1} after one attenuation length Λ. Therefore, the spallogenic TCN production rate and concentration in the upper few meters of the lithosphere is characterized by an exponential curve (Fig. 1.12). Hence, TCN production by spallation is greatest at the surface and becomes negligible at a few meters depth.

In summary, the rock-specific production rate of a TCN depends on the rock composition and on the depth beneath the rock surface. As already mentioned in Chapter 1.2, the

geographical location (altitude and latitude) also plays a crucial role. This aspect will be adopted in Chapters 1.3.5 and 1.3.4 and discussed in detail in Chapter 1.4.1. Hence, the rock-specific production rate of a TCN by spallation at a given mass depth z [g cm^{-2}] is given by

$$P_s(z) = PR_k\ [k]\ exp(-z/\Lambda_f) \tag{1.1}$$

where PR_k is the spallation production rate by target element k per g of target element per year at the rock surface and at sea level and high latitude, $[k]$ is the mass concentration of element k. Λ_f is the apparent fast neutron attenuation length ("apparent" refers to a horizontal, unshielded surface). Its value is approximately 160 g cm^{-2} according to Gosse and Phillips (2001). This value is estimated as a "mean" from a series a experimentally determined values with cosmogenic nuclide measurements in geological samples in a depth profile. Λ_f is normalized to the density of the material, because the density influences the attenuation of cosmic particle flux. Therefore, the rock density is taken into account in the "mass depth" z, which is the depth in cm multiplied by the density in g cm^{-3}. This means that in a rock with a density of 3 g cm^{-3}, the fast neutron flux is attenuated by the factor e^{-1} at a depth of about 55 cm. At this depth the TCN production is 2.718 (=e) times lower than at the rock surface.

1.3.2 TCN production by muons

Muons are tertiary products of the high-energy component of the secondary cosmic radiation (Fig. 1.4), resulting from the decay of mesons. They are less reactive and have therefore an attenuation length one magnitude longer than the fast neutrons, with Λ_μ about 1500 g cm^{-2}, so that they penetrate deeper into the lithosphere. At a few meters depth their interactions become therefore more important than those by fast neutrons (Fig. 1.13). Muons can be slow or fast and negatively or positively charged. Consequently, they can produce TCN directly and indirectly by various mechanisms (Stone et al., 1998).

The most important TCN production reaction by muons is the *direct capture (or absorption) of slow negative muons* by target nuclei. This reaction implies the loss of energy

and particles from the excited nucleus, which results in a reduced atomic mass. Slow negative muon capture by various target nuclei can produce ^{36}Cl, ^{26}Al, ^{10}Be and ^{14}C.

Muonic TCN production is less well understood and quantified than the TCN production by spallation due to the complexity of the muon reactions. These reactions do not occur proportionally to the abundance of the target elements like the spallation reactions, but they depend also on other chemical properties of the rock. The rock-specific TCN production rate by muons can therefore not be calculated with a reference production rate normalized to the abundance of the target element. Instead, the stopping rate for slow negative muons Ψ_μ is used, for which the value at the rock surface and at sea level is 190 μ g^{-1}a^{-1} according to Heisinger et al. (2002). The slow negative muon stopping rate is always much larger than the production rate of the cosmogenic nuclide by this reaction because most of the muon captures do not result in nuclide production.

The rock-specific production rate of a TCN by capture of slow negative muons at a given mass depth z in a rock is then given by

$$P_\mu(z) = \Psi_\mu \; Y_{\Sigma k} \; exp(-z/\Lambda_\mu) \tag{1.2}$$

where $Y_{\Sigma k}$ is the TCN yield per muon stopped by target element k. If there are several target elements for the production of a TCN by this reaction, like e.g. for ^{36}Cl (Chapter 1.3.6), the yields are added up. $Y_{\Sigma k}$ is calculated with a series of target-element-specific and rock-composition-specific factors:

$$Y_{\Sigma k} = \sum_k f_{c,k} \; f_{i,k} \; f_{n,k} \; f_{d,k} \tag{1.3}$$

where $f_{c,k}$ is the probability that the muons stopped in the rock material are captured by target element k (chemical compound factor); $f_{i,k}$ is the abundance of the isotope of element k that produces the TCN subsequent to slow muon capture; $f_{n,k}$ is the fraction of slow muon captures by element k that produce the TCN ("branching ratio"); and $f_{d,k}$ is the fraction of muons absorbed by the nucleus of element k before decay of the muon.

The chemical compound factor $f_{c,k}$ takes into account the composition of the rock, but it is difficult to estimate. It can be approximated by the "Fermi-Teller Z-law" (Charalambus,

1971):

$$f_{c,k} = \frac{M_k \ Z_k}{\sum_j M_j \ Z_j} \tag{1.4}$$

where M_k and M_j are the molar concentrations of elements k and j, respectively, k refers to the single element whose factor $f_{c,k}$ is to be calculated, and j refers to all elements in the rock. Z_k and Z_j are the respective atomic numbers.

Beside cosmogenic nuclide production due to the direct capture of slow negative muons, muons can also indirectly contribute to TCN production through two processes that generate neutrons, which are then thermalized and can produce certain TCN by epithermal and thermal neutron absorption reactions (next section). One process is the emission of neutrons during the above presented capture of slow negative muons. And the second process is the slowing down of (negative and positive) fast muons, during which bremsstrahlung (gamma rays) is produced. The absorption of the energetic bremsstrahlung by nuclei can cause photo-disintegration reactions that result in the release of neutrons.

According to Gosse and Phillips (2001), the muon-induced neutron production at a given mass depth z [g cm^{-2}] in the upper ~10 m of the lithosphere is approximately

$$P_{n\mu}(z) = (Y_s \ \Psi_\mu + 5.8 * 10^{-6} \ \phi_{\mu f0}) \ exp(-z/\Lambda_\mu) \tag{1.5}$$

where $\phi_{\mu f0}$ is the fast muon flux at land surface with a value of 7.9×10^5 μ cm^{-2}a^{-1}; and Y_s is the average neutron yield per stopped slow negative muon, according to Fabryka-Martin (1988) given by

$$Y_s = \sum_k f_{c,k} f_{d,k} Y_{n,k} \tag{1.6}$$

with $Y_{n,k}$ the average neutron yield per captured muon for element k.

Due to the diffusion of thermal and epithermal neutrons from the rock into air close to the land/atmosphere boundary (*neutron leakage*, explained in the next section), the muon-induced neutron production cannot be proportional to the related TCN production. Therefore, Gosse and Phillips (2001) make the assumption that the muon-induced neutrons follow the same distribution as the spallation-induced epithermal and thermal neutrons near the land/atmosphere boundary, which is discussed in the next section. In

this approach, the TCN production due to capture of epithermal and thermal neutrons is calculated considering all cosmogenic sources of epithermal and thermal neutrons production at once. This approach is presented in the next section.

1.3.3 TCN production by thermal and epithermal neutrons

Cosmogenic epithermal and thermal neutrons (hereafter *low-energy neutrons*) are generated by three processes: mostly by the "slowing down" of secondary fast neutrons due to spallation reactions and collisions with nuclei, described in the first paragraph of this Chapter; during the capture of slow negative muons and during photo-disintegration reactions subsequent to the slowing down of fast muons, both described in the previous section. When these low-energy neutrons collide with atoms they are absorbed resulting in cosmogenic nuclides, which are heavier than the atom before absorption. Since most of the neutrons in the low-energy range are derived from slowed-down fast neutrons and these low-energy neutrons pass first through the epithermal range, the related TCN production rate is proportional to the production rate of epithermal neutrons from fast neutrons in air just above the land/atmosphere boundary. This is the reference parameter $P_f(0)$ with the unit [neutrons (g air)$^{-1}$ a^{-1}].

The most important low-energy neutron produced TCN are ^{36}Cl, ^{3}He and ^{41}Ca due to neutron capture by ^{35}Cl, ^{6}Li and ^{40}Ca, respectively. The corresponding notations for these reactions are ^{35}Cl(n,γ)^{36}Cl, ^{6}Li(n,α)^{3}H(β)^{3}He and ^{40}Ca(n,γ)^{41}Ca.

In general, the production rate of low-energy neutrons and the resulting low-energy neutron flux are in equilibrium, so that the intensity of the flux and the related TCN production follow an exponential distribution with depth, similar to that of the fast neutron flux and TCN production by spallation. However, the low-energy neutrons diffuse from the rock back into air close to the land/atmosphere boundary resulting in a characteristic vertical distribution of the flux intensity, which is increasing just below the rock surface until a peak at about 50 g cm^{-2} (=$\sim$ 20 cm) and exponentially decreases below that peak (Fig. 1.6). This phenomenon is called *neutron leakage* and is due to the abrupt discontinuity in material properties, more precisely in the macroscopic thermal and epithermal neutron

absorption cross sections of the atmosphere and the rock. These parameters describe the tendency of a bulk material of a certain composition to absorb the neutrons. Since the atmosphere has a macroscopic thermal neutron absorption cross section that is about one order of magnitude higher than that of rock, due to the large thermal neutron cross section of nitrogen, the thermal neutron flux intensity is much lower in the atmosphere than in rock. Having gas-like properties, the thermal neutrons therefore diffuse upward to balance this great difference, resulting in a gradual change between the fluxes in the atmosphere and in the rock (O'Brien et al., 1978).

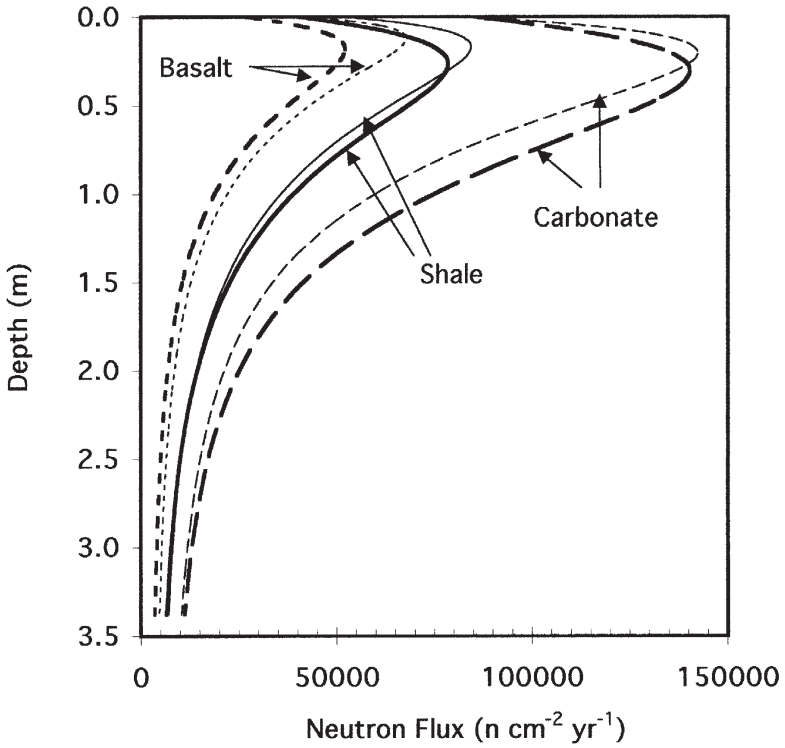

Figure 1.6: *Calculated thermal and epithermal neutron flux distributions (thick and thin lines, respectively) in three different rock types versus depth (from Phillips et al., 2001). The magnitudes of the fluxes and the shapes of the profiles depend on the elemental composition of the rocks. All three rocks are assumed to be dry. The sensitivity to the water content in the rock is explained in the next section and illustrated in Fig. 1.11.*

The TCN production by low-energy neutrons is proportional to the "fluxes" of thermal neutrons ϕ_{th} and of epithermal neutrons ϕ_{eth} [neutrons cm^{-2} a$-$1]. Since these fluxes are independent of the direction of the low-energy neutron transport, they should rather be considered as low-energy neutron "concentrations". Analogous to the attenuation of

the fast neutron flux, ϕ_{th} and ϕ_{eth} decrease with depth according to their attenuation lengths Λ_{th} and Λ_{eth} [g cm^{-2}]. In contrast to the fast neutron attenuation length, Λ_{th} and Λ_{eth} are composition-dependent and are a measure for the tendency of the matter to absorb thermal and epithermal neutrons, respectively: the higher this tendency the shorter the attenuation lengths of the neutrons. The composition dependence of the low-energy flux is illustrated in Fig. 1.6. According to this composition dependence of the flux and similar to the muonic TCN production, the TCN production due to low-energy neutrons does not only depend on the abundance of the target element in the rock (for ^{36}Cl the target element is Cl, more precisely the most abundant stable Cl-isotope ^{35}Cl) but also on other chemical properties of the rock: the bulk-composition-dependent macroscopic thermal neutron absorption cross section Σ_{th} and the macroscopic epithermal neutron absorption cross section I_{eff} (see above). (I_{eff} is also referred to as the effective resonance integral for absorption of epithermal neutrons.) This can be imagined as if the nucleus of the target element (here ^{35}Cl) competes with the nuclei of the rest of the elements to absorb the neutrons. The fractions of the total incident epithermal and thermal neutrons, that are absorbed by ^{35}Cl (with subsequent ^{36}Cl production) instead of by the other elements, f_{th} and f_{eth}, are given by the ratios of the elemental cross section to the macroscopic cross section:

$$f_{th} = \frac{N_k \ \sigma_{th,k}}{\Sigma_{th}} \tag{1.7}$$

and

$$f_{eth} = \frac{N_k \ I_{a,k}}{I_{eff}} \tag{1.8}$$

where N_k is the atomic concentration of the target element in the material (e.g. Cl), $\sigma_{th,k}$ is the thermal neutron absorption cross section and $I_{a,k}$ the epithermal neutron absorption cross section (or dilute resonance integral) of the target element. The macroscopic absorption cross sections Σ_{th} and I_{eff} are calculated by the sum of the respective cross sections of all elements j multiplied by their atomic concentrations:

$$\Sigma_{th} = \sum_j N_j \ \sigma_{th,j} \tag{1.9}$$

and

$$I_{eff} = \sum_j N_j \ I_{a,j} \tag{1.10}$$

As mentioned in the first section of this chapter, only a part of the neutrons in the epithermal energy range can be absorbed to produce TCN, the other part loses energy during collisions and "escapes" to the thermal energy range. The likelihood that a neutron will escape from the epithermal to the thermal range before it can be absorbed is quantified by the resonance escape probability $p(E_{th})$, which also depends on the material composition.

Hence, the rock-specific TCN production rate by capture of thermal and epithermal neutrons, respectively, at a given mass depth z in a rock is given by

$$P_{th}(z) = \frac{f_{th}}{\Lambda_{th}} \phi_{th}(z) \tag{1.11}$$

and

$$P_{eth}(z) = \frac{f_{eth}}{\Lambda_{eth}} \phi_{eth}(z)(1 - p(E_{th})) \tag{1.12}$$

The calculation of the fluxes ϕ_{th} and ϕ_{eth}, the attenuation lengths Λ_{th} and Λ_{eth} and the resonance escape probability $p(E_{th})$ as well as the elemental constant parameters necessary for these calculations are given in Appendix A.2. These calculations take into account the various sources of low-energy neutron production described above and in which all the different secondary cosmic particle fluxes (fast neutrons, muons, epithermal neutrons and thermal neutrons) are involved. Hence, all corresponding attenuation lengths (Λ_f, Λ_μ, Λ_{eth} and Λ_{th}) appear in the calculations. Additionally, the effect of the neutron leakage is accounted for, based on the composition-dependent thermal and epithermal *neutron diffusion lengths* L_{th} and L_{eth}. They quantify the diffusion of the low-energy neutrons back into air close to the land/atmosphere boundary, resulting in the characteristic shape of the vertical flux distribution.

The parts of the calculations of ϕ_{th} and ϕ_{eth} that quantify the fluxes derived from the slowed-down fast neutrons comprise the above mentioned reference parameter $P_f(0)$,

the production rate of epithermal neutrons from fast neutrons in air above the land/ atmosphere boundary.

1.3.4 Total site-specific TCN production and controlling factors

The total production of a cosmogenic nuclide in a geological sample cannot just be the sum of the previously discussed production rates from the different nuclear reactions because these production rates do not only depend on target-element-specific and TCN-specific parameters and on the rock composition, but they also depend on several site-specific factors. These site-specific factors are not the same for all production reactions, so that each production reaction needs individual corrections.

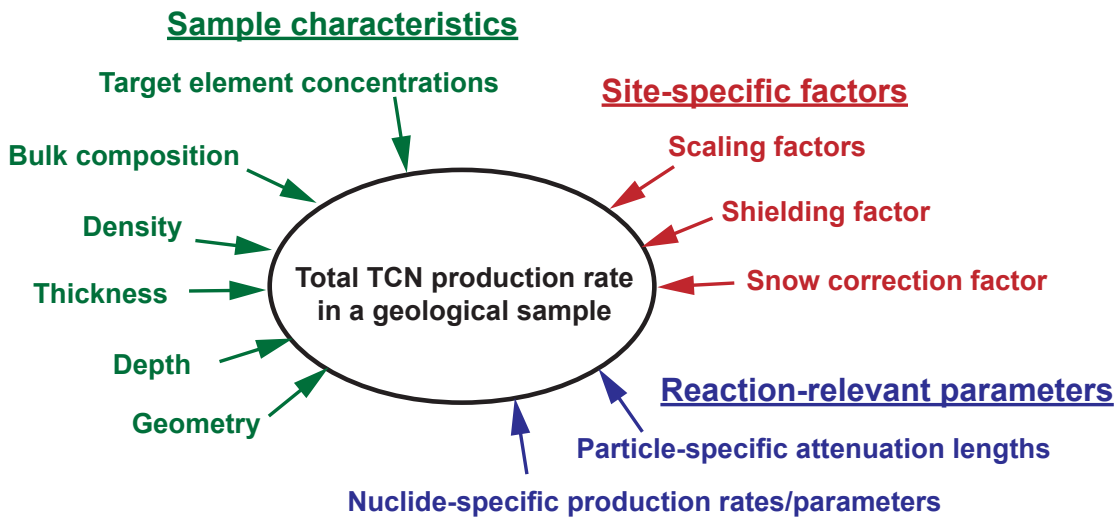

Figure 1.7: *Variables that control the total production rate of a cosmogenic nuclide in a sample.*

As mentioned in Chapter 1.2, TCN production rates depend strongly on the geographic location, especially on the **altitude** and on the **latitude** of the site. This will further be discussed in Chapter 1.4. These geographic effects are quantified with *scaling factors*, which serve to extrapolate known TCN production rates from a reference position (sea level and high latitude, i.e. $> 60°$, hereafter *SLHL*) to the geographic site of interest by multiplication. These scaling factors are not the same for the divers production mechanisms, because the underlying different cosmic ray particle fluxes vary differently with altitude and latitude (Chapter 1.2). For example, the fast neutron flux does not have the

same altitude-dependency as the muon flux. How to scale the TCN production due to low-energy neutrons is controversial. According to the assumption that the low-energy neutrons responsible for TCN production are mostly derived from the fast neutron flux just above the rock surface (see previous section), the same scaling as for the spallation reaction should be appropriate. Gosse and Phillips (2001) therefore use the same scaling factor for the TCN production due to spallation and due to low-energy neutrons. However, Desilets et al. (2006b) show that the scaling factor for the low-energy neutron reaction should be lower than that for the spallation above an altitude of 1500 m (Fig. 1.8). But they do not provide a scaling method to take account of this. Therefore, here the approach of Gosse and Phillips (2001) is followed and the low-energy neutron reaction is scaled with the spallation scaling factor. Hence, two scaling factors are involved in the calculation of the in situ cosmogenic nuclides: $S_{el,s}$, the scaling factor for spallation reactions (and for low-energy neutron reactions) and $S_{el,\mu}$, the scaling factor for the muonic reactions.

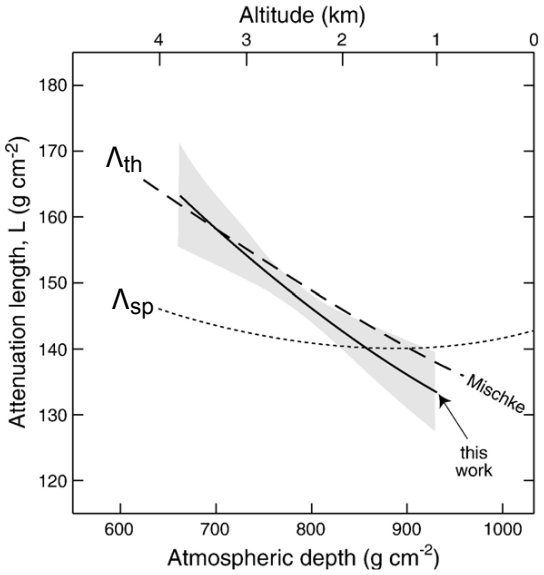

Figure 1.8: *Altitude dependence of the attenuation lengths Λ_{sp} for spallation reactions and Λ_{th} for low-energy neutron fluxes (from Desilets et al., 2006b) based on neutron monitor measurements. The data on low-energy neutrons show that above 1500 m altitude Λ_{th} is higher and below 1500 m it is lower than Λ_{sp}. Scaling factors for low-energy neutron reactions should therefore be lower than those for spallation reaction above 1500 m, and higher below 1500 m.*

Another important site-specific factor that affects the TCN production in a sample is the **topographic shielding**. Generally, it is assumed that the cosmic-ray flux is integrated

over the entire sky and that it bombards a horizontal surface surrounded by a horizontal horizon. If, however, the surface of interest is not fully exposed, because the cosmic-ray flux is "screened" or "shielded" by topographic obstacles like moutains, cliffs, slopes or buildings, the TCN production will be lower than in an unshielded surface (Fig. 1.9). This is taken into acount in the production rate calculations with the *shielding factor* S_T, which is equally applied to all production reactions. It can be calculated according to Dunne et al. (1999).

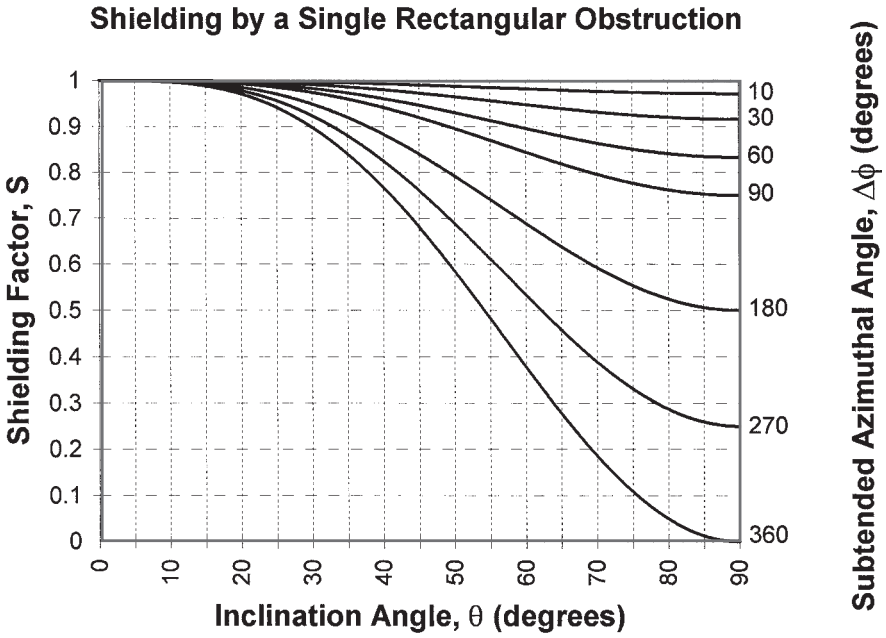

Figure 1.9: *Shielding factor that results from a rectangular obstruction screening a surface from cosmic rays, depending on the inclination angle (angle in vertical direction between horizontal and top of the obstruction, measured from the sample site) and the azimuthal angle (angle between the two endpoints of the obstruction in the horizontal plane) (from Dunne et al., 1999). A factor of 1 means no shielding, while a factor of 0 means complete shielding.*

Other factors such as the **irregular geometry** of the rock surface and **snow cover** or **soil** affect the TCN production in the rock, particularly that by fast and low-energy neutrons, so that corrections should ideally be taken into account. This is however rarely done, because firstly, it is often difficult to correctly quantify e.g. an irregular surface shape or the duration and thickness of snow cover over a long exposure time, and secondly, their effects on the TCN production are not well understood and constrained. It is known that

the effects, both of irregular geometry and of snow cover, are not the same on the reactions due to fast neutrons and due to low-energy neutrons. The flux of low-energy neutrons is affected by the geometry of the rock surface due to *neutron leakage* at the land/atmosphere boundary (see previous section), because a non-flat surface shape increases the diffusion of low-energy neutrons out of the solid rock into air. This is however difficult to quantify. According to Zreda et al. (1993) and references herein it might lower the low-energy flux below the rock surface by up to 30%. Whether irregular shapes also affect the diffusion of fast neutrons in rock is controversial. According to Masarik and Wieler (2003), who modeled the diffusion of fast neutrons in boulders of different shapes, production rates at boulder surfaces can be up to 12% lower than at infinite flat surfaces, depending on the shape and the size of the boulder and on the distance of the sample from the edges (e.g. Fig. 1.10). However, measurements of ^{10}Be, which is mainly produced by spallation, in natural samples from different parts of a boulder yield the same cosmogenic nuclide concentrations (personal communication M. Kurz, J. Schaefer CRONUS-Earth and CRONUS-EU meeting, Davos, 2009). This shows that spallation reactions seem not to be affected by the shape of the sampled surface.

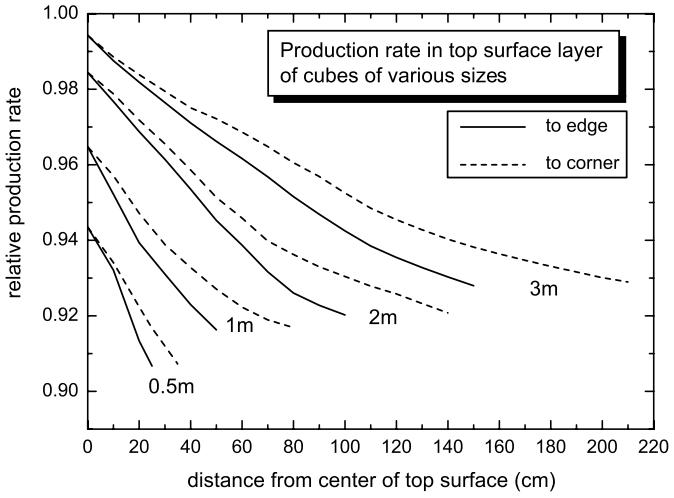

Figure 1.10: *Relative production rates in cubic boulders of four different diameters depending on the distance from the center of the top surface towards the center of an edge (solid lines) or towards the corner (dashed lines). Production rates are averaged for a 5 cm surface layer and normalized to production rates in an infinite flat surface.*

While snow cover has a shielding effect on fast neutrons and therefore lowers the TCN

production due to spallation (e.g. Schildgen et al., 2005; Benson et al., 2004), it can be responsible for the increase of TCN production due to low-energy neutrons below the rock surface based on the following process. Hydrogen has a big neutron scattering cross section and therefore enhances the thermalization of epithermal neutrons, i.e. neutrons pass more frequently from the epithermal to the thermal energy range (Fig. 1.11a). Consequently, more thermal neutrons can be absorbed by the target element to produce the TCN (Phillips et al., 2001). On the other hand, hydrogen also absorbs thermal neutrons competing with the target element of the TCN and therefore reduces the TCN production. Masarik et al. (2007) calculated numerically that snow equivalent to a water cover thickness of up to 20 cm results in a more efficient neutron thermalization just below the rock surface, while a thicker water cover leads to a decrease of the thermal neutron flux due to a decreasing neutron production above the Earth surface (Fig. 1.11b).

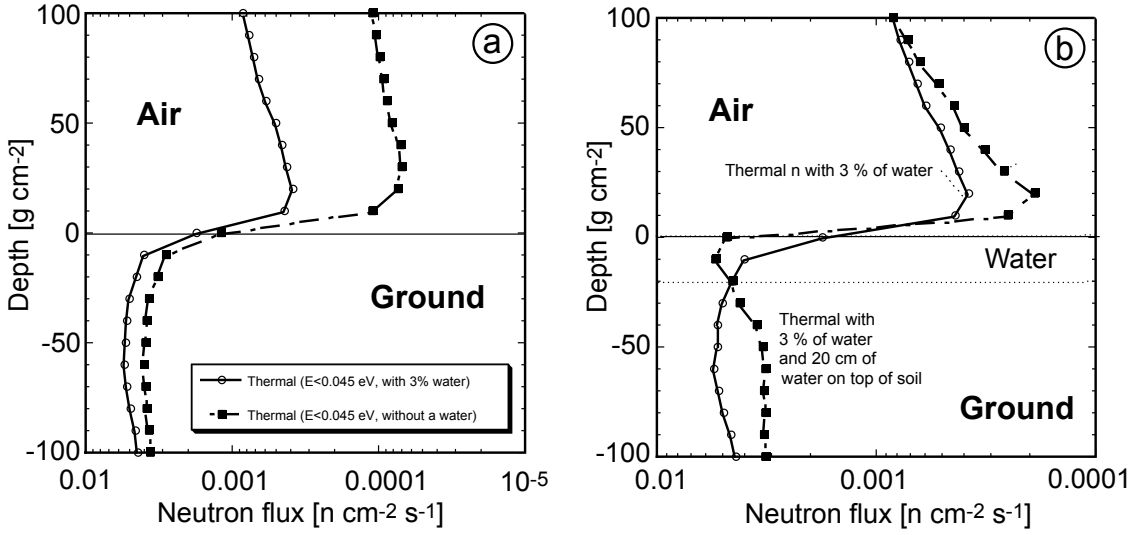

Figure 1.11: *Calculated thermal neutron fluxes at the air/ground boundary (modified from Masarik et al., 2007). (a) Comparison between flux for dry ground (black dots) and ground with a water content of 3% (white dots). This water content leads to an increase of the thermal neutron flux (note that the abscissa is in reverse sense). As the water content increases above 5%, the resulting increase in density and the thermal neutron absorption cross-section reduces the thermal neutron flux (Phillips et al., 2001). (b) Comparison between the flux for a ground with a water content of 3% without (white dots) and with a water layer of 20 cm on the surface (black dots). See text for explication.*

Finally, to calculate the TCN production rate for a geological sample with a certain thickness, the depth dependency of the cosmic ray flux in the rock (due to the attenuation

of the particle fluxes with depth) has to be taken into account. Therefore the production rate has to be averaged by integration over the thickness. This is typically done by a correction factor that quantifies the production rate in the whole sample relative to the production rate at a reference depth, which can be the top or the center of the sample. Since the various cosmic ray fluxes are attenuated differently, each production reaction needs an individual thickness integration factor (Q). Such Q-factors are given in Gosse and Phillips (2001), which are, however, only valid for surface samples that are not subject to erosion. Schlagenhauf et al. (2009) developed Q-factors that are also valid for deeper samples and eroding surfaces. Their calculations are also given in Appendix A.5.

In summary, the rock- and site-specific total TCN production rate [atoms g^{-1} a^{-1}] in a sample of finite thickness at mass depth z is given by

$$P_{total}(z) = S_{el,s}\ F_s\ Q_s\ P_s(z) + S_{el,s}\ F_n\ (Q_{eth}\ P_{eth}(z) + Q_{th}\ P_{th}(z)) + S_{el,\mu}\ F_\mu\ Q_\mu\ P_\mu(z) \tag{1.13}$$

where the reaction types are indicated by the subscripts: s stands for spallation, eth for epithermal neutron capture, th for thermal neutron capture, n for reactions involving fast or low-energy neutrons and μ for slow negative muon capture. F_x include all correction factors other than the scaling factor and the thickness integration factor, such as shielding, snow or geometry correction.

This equation is only valid for uneroded samples. The calculation in case of erosion is discussed in the next section.

1.3.5 Total TCN concentrations in samples with simple and complex exposure history

The total TCN production rate is the number of atoms of a TCN accumulating in a gram of sample during one year [atoms g^{-1} a^{-1}]. Hence, for the simple case of an uneroded surface and a stable TCN, the total TCN concentration [atoms g^{-1}] in a sample that has been exposed to cosmic radiation can be calculated by multiplying the total production rate by the exposure time t_{expo}:

$$N_{total}(z,t) = P_{total}(z)t_{expo}(t) \tag{1.14}$$

For radioactive cosmogenic nuclides, the decay of the radionuclide during the exposure time has additionally to be taken into account. Then the "time factor" becomes:

$$t_{cosm}(t) = (1 - exp^{-t_{expo}\lambda})/\lambda \tag{1.15}$$

where λ is the decay constant of the radionuclide; and the TCN concentration becomes:

$$N_{total}(z,t) = P_{total}(z)t_{cosm}(t) \tag{1.16}$$

If the sample had been exposed to cosmic radiation prior to the exposure event of interest (*inheritance*) the sample might already have had a significant TCN concentration at time $t_{expo} = 0$. This inherited TCN concentration $N_{inher}(0)$ is, in the case of a radioactive TCN, also subject to radioactive decay during the duration of recent exposure. In this case the total number of atoms TCN is given by

$$N_{total}(z,t) = N_{inher}(0)exp^{-t_{expo}\lambda} + P_{total}(z)t_{cosm}(t) \tag{1.17}$$

In the case of a surface eroding with a constant erosion rate, the whole calculation needs to be rearranged. This is because during erosion, layers of rock are gradually removed from the surface, revealing parts of the rock, which were previously at depth (see also Fig. 3.6), and this implies that the different depth-dependencies of the various TCN production reactions, due to the different attenuation lengths of the particle fluxes, become of importance. This effect is accounted for in the time factor t_{cosm}, which has to be calculated individually for each production reaction.

For production reactions due to spallation :

$$t_{cosm,s}(t,\varepsilon) = \Big(1 - exp\Big(-t_{expo}\Big(\lambda + \frac{\rho\ \varepsilon}{\Lambda_f}\Big)\Big)\Big)/\Big(\lambda + \frac{\rho\ \varepsilon}{\Lambda_f}\Big) \tag{1.18}$$

For production reactions due to epithermal neutron capture:

$$t_{cosm,eth}(t,\varepsilon) = \Big(1 - exp\Big(-t\Big(\lambda_{36} + \frac{\rho\ \varepsilon}{L_{eth}}\Big)\Big)\Big) / \Big(\lambda_{36} + \frac{\rho\ \varepsilon}{L_{eth}}\Big) \tag{1.19}$$

For production reactions due to thermal neutron capture:

$$t_{cosm,th}(t,\varepsilon) = \Big(1 - exp\Big(-t\Big(\lambda_{36} + \frac{\rho\ \varepsilon}{L_{th}}\Big)\Big)\Big) / \Big(\lambda_{36} + \frac{\rho\ \varepsilon}{L_{th}}\Big) \tag{1.20}$$

For production reactions due to slow negative muon capture:

$$t_{cosm,\mu}(t,\varepsilon) = \Big(1 - exp\Big(-t\Big(\lambda_{36} + \frac{\rho\ \varepsilon}{\Lambda_{\mu}}\Big)\Big)\Big) / \Big(\lambda_{36} + \frac{\rho\ \varepsilon}{\Lambda_{\mu}}\Big) \tag{1.21}$$

where ε is the constant erosion rate [cm a^{-1}] and ρ the density of the sample [g cm^{-3}].

For an eroding surface, the total TCN concentration [atoms g^{-1}] in a sample of finite thickness at mass depth z is given by

$$\begin{aligned} N_{total}(z,t,\varepsilon) = S_{el,s}\ S_T\ \Big(& J_{Q,s}\ exp(-\frac{z}{\Lambda_f})\ t_{cosm,s}(t,\varepsilon) \\ & + J_{Q,eth}\ exp(-\frac{z}{L_{eth}})\ t_{cosm,eth}(t,\varepsilon) \\ & + J_{Q,th}\ exp(-\frac{z}{L_{th}})\ t_{cosm,th}(t,\varepsilon) \\ & + J_{Q,\mu}\ exp(-\frac{z}{\Lambda_{\mu}})\ t_{cosm,\mu}(t,\varepsilon)\Big) \end{aligned} \tag{1.22}$$

where $J_{Q,x}$ are the production rate coefficients including the sample thickness integration factors for the respective reaction types and correction factors for snow cover and irregular geometry. Their calculations are given in detail in Appendix A.6. Here, it is important to mention that these production rate coefficients are not assigned to the final nuclear reaction that produces the TCN like in the previous section for the case of no erosion, but they are arranged according to the initial secondary particle flux, which finally leads to different TCN producing reactions. These initial particle fluxes are attenuated according to their attenuation lengths (independently of the nuclear reactions for which they are responsible), which also explains why each production rate coefficients $J_{Q,x}$ is assigned to the corresponding attenuation lengths. The two most important initial secondary particle fluxes are those of the fast neutrons and the muons. Beside direct TCN

production they also generate low-energy neutron fluxes (Chapter 1.3.3), subsequently resulting in TCN production by low-energy neutrons, which is accounted for in $J_{Q,s}$ and $J_{Q,\mu}$. Therefore , $J_{Q,eth}$ and $J_{Q,th}$ rather quantify the neutron leakage effect, the diffusion of the low-energy neutrons back into air near the land/atmosphere boundary (see Chapter 1.3.3), which is why the epithermal and thermal neutron diffusion lengths L_{eth} and L_{th} appear in the calculation (Eq. 1.22) and why $J_{Q,th}$ results in negative values.

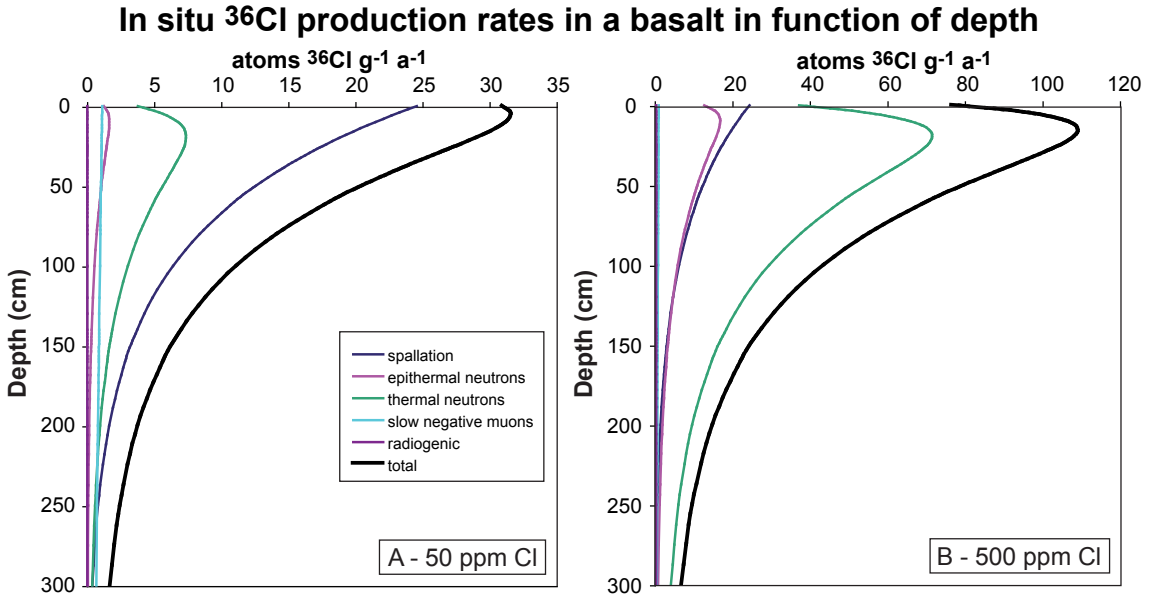

Figure 1.12: *Vertical distribution of the ^{36}Cl production rates from all production reactions in the first 3 m of a basaltic whole rock. The target element concentrations are 6% Ca, 1% K, 1% Ti, 7% Fe and 50 ppm Cl in panel A and 500 ppm Cl in panel B; U and Th concentrations are 4 ppm and 15 ppm, respectively. The difference in the Cl concentration changes considerably the total ^{36}Cl production rate and the shape of the distribution. In panel A, production by spallation is dominant, while in panel B production by low-energy capture on ^{35}Cl prevails.*

1.3.6 Production of ^{36}Cl

^{36}Cl is a radioactive TCN, which is produced by all production mechanisms introduced in Chapter 1.3. The target elements are Ca, K, Ti and Fe for spallation, ^{40}Ca and ^{39}K for slow negative muon capture and ^{35}Cl for low-energy neutron capture. The in situ production rates and production parameters of these reactions are discussed below. Fig. 1.12 shows

the vertical distribution of the ^{36}Cl production rates from all reactions in the first 3 m of a basaltic rock. And Fig. 1.13 illustrates the corresponding relative ^{36}Cl contributions from these reactions in percent.

From the chemical point of view, ^{36}Cl can be extracted from any rock type that bears at least one of these target elements. This can be magmatic whole rocks, carbonates or minerals such as feldspar or pyroxene separated from any rock type. Drawbacks and advantages of the use of the different sample types in terms of their target element concentrations are the topic of Chapter 4.

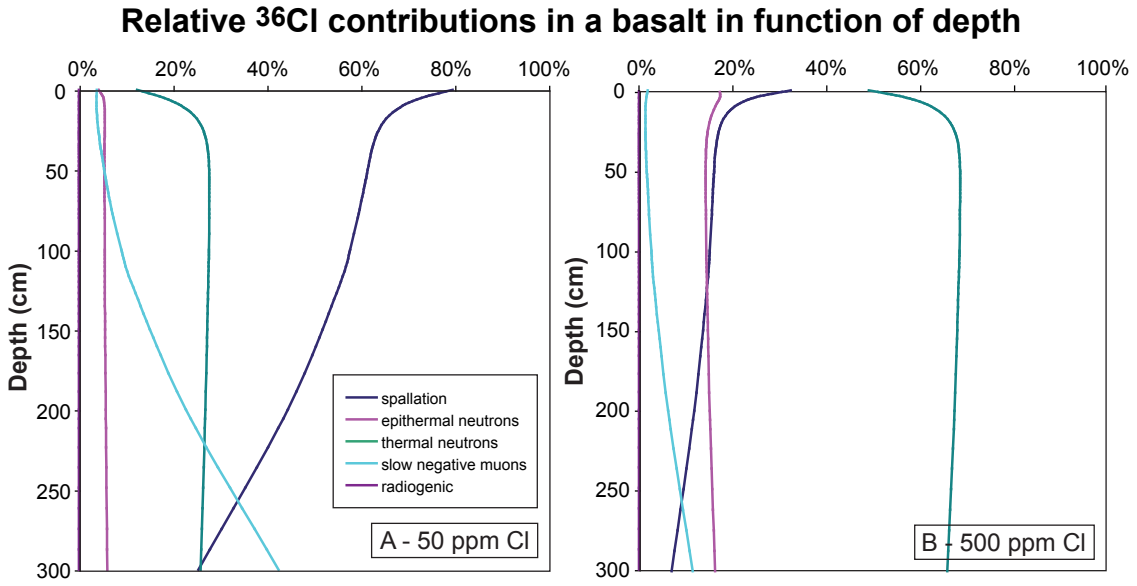

Figure 1.13: *Relative ^{36}Cl contributions from all production reactions in the first 3 m of a basaltic whole rock. The compositions are the same as in Fig. 1.12. In panel A, production by spallation is dominant until 2.5 m. Below that depth, production by slow negative muons becomes dominant, because the muons are less attenuated in the rock than neutrons. In panel B, production by low-energy capture on ^{35}Cl prevails due to the high Cl concentration.*

Beside the above mentioned cosmogenic production reactions, in situ ^{36}Cl is also produced "radiogenically" , independently of cosmic radiation and therefore independently of depth and surface exposure duration. (Note that sometimes "nucleogenic" is used instead of "radiogenic".) Its production starts with the formation of the rock, which might be different from the onset of exposure. Spontaneous fission of ^{238}U and (α,n) reactions on nuclei

of light elements, where the α-particles are produced during U and Th decay, generate a flux of neutrons. If slowed down to the low-energy range, the neutrons can be captured by ^{35}Cl to produce ^{36}Cl (Fabryka-Martin, 1988). The radiogenic neutron production and hence the related ^{36}Cl production rate P_r depend therefore on the U and Th content in the bulk rock. Usually, its contribution in a surface sample is insignificant relative to production by other mechanisms. It should nevertheless be accounted for to avoid overestimating the cosmogenic ^{36}Cl production.

Hence, according to Eq. 1.13 , the total ^{36}Cl production rate [atoms ^{36}Cl g^{-1} a^{-1}] in a uneroded sample of finite thickness at mass depth z is given by

$$P_{total}(z) = S_{el,s}\ F_s\ Q_s\ P_s(z) + S_{el,s}\ F_n\ (Q_{eth}\ P_{eth}(z) + Q_{th}\ P_{th}(z)) + S_{el,\mu}\ F_\mu\ Q_\mu\ P_\mu(z) + P_r \tag{1.23}$$

The calculation of P_r is given in Appendix A.4.

Accordingly, for an eroding surface, the total ^{36}Cl concentration [atoms ^{36}Cl g^{-1}] in a sample of finite thickness at mass depth z is given by

$$\begin{aligned} N_{total}(z,t,\varepsilon) = S_{el,s}\ S_T\ \Big(& J_{Q,s}\ exp(-\frac{z}{\Lambda_f})\ t_{cosm,s}(t,\varepsilon) \\ & + J_{Q,eth}\ exp(-\frac{z}{L_{eth}})\ t_{cosm,eth}(t,\varepsilon) \\ & + J_{Q,th}\ exp(-\frac{z}{L_{th}})\ t_{cosm,th}(t,\varepsilon) \\ & + J_{Q,\mu}\ exp(-\frac{z}{\Lambda_\mu})\ t_{cosm,\mu}(t,\varepsilon)\Big) + P_r\ t_r \end{aligned} \tag{1.24}$$

where t_r is the time factor for the radiogenic ^{36}Cl production during the formation time t_{form} of the rock including the radioactive decay of ^{36}Cl:

$$t_r = \frac{1 - exp(-t_{form}\lambda_{36})}{\lambda_{36}} \tag{1.25}$$

The decay constant of ^{36}Cl λ_{36} has a value of 2.303×10^{-6} a^{-1}.

Since the ^{36}Cl contribution due to this radiogenic reaction depends on the Cl concentration (because ^{35}Cl is the target element) and on the U and Th concentration in the sample, its calculation is especially of importance for magmatic whole rock samples, which often

have higher Cl and U and Th concentrations than other samples. To calculate correctly the radiogenic ^{36}Cl, the formation age of the rock should be known. As this is rarely the case, the formation age is usually assumed to be infinite, equal to several half-lives of ^{36}Cl, (e.g. in CHLOE, Phillips and Plummer, 1996), which results in the saturation concentration of radiogenic ^{36}Cl, meaning that the radiogenic ^{36}Cl production is in equilibrium with the radioactive decay. However, this approach might considerably overestimate the radiogenic ^{36}Cl contribution, especially in young samples for which the formation age is equal to the exposure age. Therefore, another approach is followed in the Excel® spreadsheet for ^{36}Cl calculations, developed in this PhD study, published in Schimmelpfennig et al. (2009) and presented in Chapter 3, allowing a control on the radiogenic ^{36}Cl contribution and a more accurate estimation. The known or estimated formation age of the rock has to be input individually, which makes possible to account for a more realistic radiogenic ^{36}Cl contribution if the formation age is not very long. If it can be assumed that the formation age is equal to the exposure age, the best procedure is to first calculate the exposure age without correction for radiogenic ^{36}Cl and then to input the approximate exposure age for the formation age in a second calculation run.

So far, published ^{36}Cl production calculations and available ^{36}Cl calculators do not differentiate between bulk rock and target fraction composition. This is another development integrated in the new ^{36}Cl calculation spreadsheet and will be discussed in the following. As explained in Chapter 1.3, TCN production by muons and low-energy neutrons does not only depend on the abundance of the target elements in the rock or part of the rock dissolved for TCN extraction, but it also depends on the abundance of many other elements in the bulk rock. This is because certain chemical properties of the rock influence the muon and low-energy neutron flux behaviour and therefore indirectly affect the TCN production. This is also the case for the production of ^{36}Cl due to muons and low-energy neutrons and has therefore to be taken into account in the calculations. For the calculation of the particle flux behaviour, the composition of the bulk rock is relevant, independently of from which part of the rock ^{36}Cl is extracted. For this, it is assumed that the bulk composition is homogeneous. On the other hand, ^{36}Cl is often extracted from parts of the

rock (hereafter *target fraction*) such as separated minerals or pretreated whole rock with a composition different to that of the untreated bulk rock. ^{36}Cl does not diffuse in the rock and therefore it can be assumed that the ^{36}Cl concentration extracted from the target fraction is proportional to the target element concentration in the target fraction. Hence, for the ^{36}Cl production calculations, the composition of the target fraction is relevant. This is not yet accounted for in the calculations presented in the previous sections but is specified in the following.

In the case of the low-energy neutron reactions, the relevant terms are those of the fluxes ϕ_{th} and ϕ_{eth} and those of the factors f_{th} and f_{eth}, appearing in Eqs. 1.11 and 1.12. The calculations of ϕ_{th} and ϕ_{eth} are done with the composition of the bulk rock (Appendix A.2). f_{th} and f_{eth}, given in Eqs. 1.7 and 1.8, respectively, estimate the fraction of the total incident low-energy neutrons that are absorbed by ^{35}Cl relative to those that are absorbed by the other elements in the bulk. The absorption of ^{35}Cl results in production of ^{36}Cl, hence, the ^{35}Cl (or Cl) concentration in the target fraction is used for the numerator, while the absorption by the elements in the bulk governs the total flux, so that the composition of the bulk is used for the denominator. Eqs. 1.7 and 1.8 become therefore

$$f_{th} = \frac{N_{Cl,target}\sigma_{th,Cl}}{\Sigma_{th}} \tag{1.26}$$

and

$$f_{eth} = \frac{N_{Cl,target}I_{a,Cl}}{I_{eff}} \tag{1.27}$$

where $N_{Cl,target}$ is the atomic concentration of Cl in the target fraction, $\sigma_{th,Cl}$ is the thermal neutron absorption cross section, and $I_{a,Cl}$ the epithermal neutron absorption cross section (or dilute resonance integral) of Cl. Σ_{th} and I_{eff} are calculated according to Eqs. 1.9 and 1.10 using the atomic concentrations of the elements in the bulk rock.

Analogously, for the slow negative muon capture, the difference between the target element concentration in the target fraction, relevant for the ^{36}Cl production, and the bulk composition, relevant for the muon flux, are taken into account in the chemical compound factor $f_{c,k}$, which is the probability that the muons stopped in the rock material are cap-

tured by target element k. It can be approximated by the "Fermi-Teller Z-law" (Eq. 1.4), which then becomes

$$f_{c,k,target} = \frac{M_{k,target} Z_k}{\sum_j M_{j,bulk} Z_j} \tag{1.28}$$

where $M_{k,target}$ are the molar concentrations of the target elements ^{40}Ca and ^{39}K in the target fraction and $M_{j,bulk}$ are the molar concentrations of elements j in the bulk.

Published ^{36}Cl production rates and production parameters

The relative contribution of each production reaction in the total ^{36}Cl production in a sample mainly depends on three important factors. The first is the abundance of the respective target element, the second is the production rate from this target element, and the third is the depth under consideration. Since the various production mechanisms underlie different nuclear reactions with different attenuation lengths, all three factors have to be taken into account when comparing the relative contributions. Therefore, reference production rates and parameters (Table 1.2) cannot be compared directly, except for the four spallation target elements.

All four SLHL production rates PR_k (k = Ca, K, Ti or Fe) are poorly constrained. Several values, primarily for PR_{Ca} and PR_K, have been proposed, which however vary by up to 50%. This is discussed in detail in Chapters 4 and 5. The spallation target element with the highest production rate is K. Experimentally calibrated values for PR_K range between about 110 and 230 atoms ^{36}Cl (g K)$^{-1}$ a^{-1} (Table 1.2), being two to three times higher than PR_{Ca}, which has published values between about 50 and 90 atoms ^{36}Cl (g Ca)$^{-1}$ a^{-1} (Table 1.2). The reference production rate from Ti PR_{Ti} has not been calibrated with geological samples but was determined by numerical simulation to a value of about 13 atoms ^{36}Cl (g Ti)$^{-1}$ a^{-1} (Masarik, 2002; Fink et al., 2000). The reference production rate from Fe PR_{Fe} was calibrated experimentally with iron oxide minerals to a value of about 2 atoms ^{36}Cl (g Fe)$^{-1}$ a^{-1} (Stone, 2005) and by numerical simulation to a value of about 7 atoms ^{36}Cl (g Fe)$^{-1}$ a^{-1} (Masarik, 2002).

For the ^{36}Cl production due to slow negative muon capture and low-energy neutron

Table 1.2: *Published values of ^{36}Cl SLHL production rates and parameters, determined experimentally unless they are indicated as calculated in the comment.*

Spallation			
Target element	Production rate [at ^{36}Cl (g)$^{-1}$ a^{-1}]	Reference	Comment
	76 ± 5	Zreda et al. (1991)	includes muonic ^{36}Cl production
	73 ± 5	Phillips et al. (1996)	includes muonic ^{36}Cl production
	48.8 ± 1.7	Stone et al. (1996)	
Ca	65	Masarik and Reedy (1996)	calculated
	66.8 ± 4.4	Phillips et al. (2001)	
	91 ± 5	Swanson and Caffee (2001)	includes muonic ^{36}Cl production
	68	Masarik (2002)	calculated
	52 ± 5	Licciardi et al. (2008)	corrected for abnormal atmospheric pressure in Iceland
	106 ± 8	Zreda et al. (1991)	includes muonic ^{36}Cl production
	154 ± 10	Phillips et al. (1996)	includes muonic ^{36}Cl production
	129	Masarik and Reedy (1996)	calculated
K	170 ± 25	Evans et al. (1997)	includes muonic ^{36}Cl production
	137 ± 9	Phillips et al. (2001)	
	228 ±18	Swanson and Caffee (2001)	includes muonic ^{36}Cl production
	122	Masarik (2002)	calculated
	16	Masarik and Reedy (1996)	calculated
Ti	13 ± 3	Fink et al. (2000)	
	13.5	Masarik (2002)	calculated
	0.9	Masarik and Reedy (1996)	calculated
Fe	6.75	Masarik (2002)	calculated
	1.9	Stone (2005)	
Low-energy neutron capture			
	Production rate [neutr (g air)$^{-1}$ a^{-1}]	Reference	Comment
	307 ± 24	Zreda et al. (1991)	neutron production rate in rock [neutrons (g rock)$^{-1}$ a^{-1}]
	586 ± 40	Phillips et al. (1996)	
	626 ± 46	Phillips et al. (2001)	
	762 ± 28	Swanson and Caffee (2001)	
Slow negative muon capture			
	Slow negative stopping rate [μ (g rock)$^{-1}$ a^{-1}]	Reference	
	175	Stone et al. (1998)	
	190	Heisinger et al. (2002)	

capture, it is generally not possible to calibrate global reference production rates per target element as for the spallation reaction because of the influence of the bulk rock composition on the ^{36}Cl production presented above. In the case of slow negative muon capture, the "reference production parameters" can be considered in the *slow negative stopping rate* at the rock surface and in the branching ratios $f_{n,^{40}Ca}$ and $f_{n,^{39}K}$, introduced in Chapter 1.3.2 and specified in Chapter 4.3. Since Ca and K are both target elements for spallation and for slow negative muon capture, the production rates from both reactions can be compared, but only regarding the same geographic site, the same depth and if the rock composition does not change. This has been done by Stone et al. (1998), who calibrated a SLHL production rate for slow negative muon capture by Ca in limestone to a value of 5.3 atoms ^{36}Cl (g Ca)$^{-1}$ a^{-1}. In a surface sample, this results in a ^{36}Cl contribution due to muon capture of about 10% of the total production from Ca, assuming a total SLHL production rate of 54 atoms ^{36}Cl (g Ca)$^{-1}$ a^{-1} (Stone et al., 1998). It has to be noted again that this has been determined for limestone and is only valid for the reference point sea level and high latitude. For other rocks, the relationship between the contributions from spallation of Ca and from muon capture by Ca is often assumed to be the same, which is strictly speaken not correct. Similarly, the ^{36}Cl contribution due to muon capture by K is estimated to be about 5% of the total ^{36}Cl production from K at the surface according to Evans et al. (1997).

Analogously, the "reference production parameters" for ^{36}Cl production due to low-energy neutron capture by ^{35}Cl can be seen in $P_f(0)$, the production rate of epithermal neutrons from fast neutrons in air and in the cross sections of Cl for the absorption of epithermal and thermal neutrons (with subsequent ^{36}Cl production) $I_{a,Cl}$ and $\sigma_{th,Cl}$. For $P_f(0)$, however, different values have been proposed (Table 1.2), of which that by Phillips et al. (2001) with 626 epithermal neutrons (g air)$^{-1}$ a^{-1} is the most accepted and used. ^{36}Cl contributions due to low-energy neutron capture are not proportionally related to the other production reactions, because target elements and production parameters are completely different.

1.3.7 Production of ^{3}He

A comprehensive review of the production of cosmogenic noble gases can be found in Niedermann (2002). ^{3}He is a stable TCN produced in crystal lattices, by spallation of the target elements O, Si, Mg, Fe, Ca and Al and by low-energy capture on ^{6}Li. Production of cosmogenic ^{3}He from low-energy capture by ^{6}Li is generally considered insignificant although in a recent study, Dunai et al. (2007) demonstrate it may be important in Li-rich minerals.

In addition to cosmogenic ^{3}He, other terrestrial He components include magmatic He (composed of primordial ^{3}He and radiogenic ^{4}He from decay of U and Th), atmospheric He, and nucleogenic ^{3}He. Atmospheric He is dominated by ^{4}He and has a He isotopic ratio ($R_A = {}^3\mathrm{He}/{}^4\mathrm{He}$) of 1.384×10^{-6}. When adsorbed onto the surfaces of crystals, it is easily degassed by heating at temperatures of around 100°C.

The magmatic He components are derived from the mantle and retained in melt and fluid inclusions in crystals. Magmatic He is easily extracted from crystals by crushing them under vacuum, thereby rupturing any inclusions and allowing determination of the ^{3}He/^{4}He ratio.

Nucleogenic ^{3}He is produced in the crystal lattice. Production of the nucleogenic component is analogous to the radiogenic ^{36}Cl production (Chapter 1.3.6), from capture of radiogenic low-energy neutrons by ^{6}Li. The notation for this reaction is ^{6}Li(n,α)^{3}H(β^{-1})^{3}He. Note that for ^{3}He the term *nucleogenic* is used, because the nuclide is not a direct product of radioactive disintegration of U and Th, in contrast to *radiogenic* ^{4}He, but indirectly produced by radiogenic low-energy neutrons. In the ^{36}Cl terminology, however, *radiogenic* is usually used for the same type of reaction.

Radiogenic ^{4}He is a direct product of the decay of U and Th. As well as characterizing atmospheric and magmatic components, ^{4}He can also be found in the crystal lattice. Here, it is either produced in situ from U and Th decay following crystallization, or implanted by alpha-injection from adjacent minerals or the rock matrix. In rocks with young crystallization ages (<100 ka), the radiogenic ^{4}He component is generally assumed to be negligible, and all ^{4}He present in extractions is assumed to have a magmatic origin. This allows for

Table 1.3: *Origins of ^{3}He and ^{4}He in mafic phenocrysts.*

^{3}He	^{4}He
Cosmogenic - spallation of O, Si, Mg, Fe, Ca, Al - low-energy neutron capture on ^{6}Li	
Primordial (magmatic)	Primordial (magmatic)
Nucleogenic - radiogenic low-energy neutron capture on ^{6}Li	Radiogenic - during decay of U and Th

easy discrimination of cosmogenic ^{3}He from magmatic ^{3}He, using magmatic ^{3}He/^{4}He ratios determined from crush experiments. However, in older lithologies, in U- and Th-rich mineral phases and lithologies, or even in samples with very young exposure ages, the radiogenic ^{4}He component may be important and should be corrected for (e.g. Blard and Farley, 2008).

Cosmogenic ^{3}He is produced in the crystal lattice and most commonly measured in olivine and pyroxene phenocrysts. In contrast to other common rock-forming minerals, such as quartz, plagioclase or K-feldspar (Brook et al., 1993), ^{3}He does not diffuse out of olivines and pyroxenes due to their low diffusion coefficients (Trull et al., 1991). In addition, the low concentrations of U, Th and Li in olivines and pyroxenes and their host-rocks, and as a result the low contributions from radiogenic/nucleogenic components, make these two minerals particularly suitable for cosmogenic ^{3}He applications. Other minerals from which cosmogenic ^{3}He has been successfully extracted include apatite, titanite, zircon (Farley et al., 2006), garnet (Gayer et al., 2004) and Fe-Ti-oxides (Kober et al., 2005).

Published ^{3}He production rates

Because cosmogenic ^{3}He is produced from numerous target elements, reference ^{3}He production rates are generally calibrated for mineral phases and not per target element as is the case with ^{36}Cl. The majority of experimental ^{3}He production rate calibration studies have been performed using olivine and/or pyroxene phenocrysts in lava-flows. Production rates are either globally determined for both phenocryst phases (e.g. Cerling and Craig,

1994) or determined for a single phase (e.g. Licciardi et al., 1999; Schaefer et al., 1999; Dunai, 2001; Ackert et al., 2003; Blard et al., 2006). Experimentally calibrated reference production rates range between 105 and 130 atoms ^{3}He (g mineral)$^{-1}$ a^{-1}.

Olivine and pyroxene compositions may vary, depending on the incorporated ions in the crystal latice (see side note below).

Masarik and Reedy (1996) and Masarik (2002) calculated elemental ^{3}He production rates for the target elements O, Si, Mg, Fe, Ca and Al, allowing calculation of ^{3}He production rates as a function of mineral composition. By this methodology, similar production rates for both mineral phases are usually obtained (e.g. Ackert et al., 2003). Furthermore, cosmogenic ^{3}He concentrations measured in coexisting olivines and pyroxenes are often indistinguishable (e.g. Ackert et al., 2003; Blard et al., 2005, 2006). As such, the nuclide is often considered to be produced at the same rate in olivine and pyroxene. Calibrations of ^{3}He production rates in other mineral phases, however, have yielded significantly different values, most likely reflecting their compositional dependence, e.g. in titanite 97 $\pm$ 10 atoms ^{3}He g^{-1} a^{-1}, in zircon 87 $\pm$ 9 atoms ^{3}He g^{-1} a^{-1} Farley et al. (2006).

Side note: Olivine has the formula (Mg,Fe)$_2$[SiO$_4$] with varying Mg:Fe ratios between Mg$_2$[SiO$_4$] (forsterite) and Fe$_2$[SiO$_4$] (fayalite). The general formula for pyroxene is $XY[Z_2O_6]$. The X-position can be occupied by Na^{+}, Ca^{2+}, Fe^{2+}, Mg^{2+}, Mn^{2+}, the Y-position by Fe^{2+}, Mg^{2+}, Mn^{2+}, Zn^{2+}, Fe^{3+}, Al^{3+}, and others (Matthes, 1996).

1.3.8 Production of ^{21}Ne

^{21}Ne is the other commonly used stable TCN. Also a noble gas, it is produced by spallation of the target elements Mg, Na, Al, Fe and Si. Like ^{3}He, the non-cosmogenic ^{21}Ne components include magmatic ^{21}Ne trapped in the inclusions and nucleogenic ^{21}Ne. The magmatic Ne component usually has a ^{21}Ne/^{20}Ne composition close to that of air (0.002959; Niedermann, 2002) but may also have a MORB-type composition, or, rarely, a solar neon composition. Nucleogenic ^{21}Ne is derived from the reactions ^{18}O(α,n)^{21}Ne and ^{24,25}Mg(n,α)^{21,22}Ne.

The other neon isotopes, ^{20}Ne and ^{22}Ne, allow measured ^{21}Ne to be corrected for the presence of the non-cosmogenic components. Measured neon isotope data can be plotted on a three-isotope Ne diagram (^{21}Ne/^{20}Ne against ^{22}Ne/^{20}Ne), which clearly distinguishes the diverse origins of the isotopes (Niedermann, 2002). If the analytical data plot within error of the air-spallation mixing-line, it is reasonable to assume that the trapped component has an atmospheric ^{21}Ne/^{20}Ne composition and no nucleogenic ^{21}Ne is present. The measured ^{20}Ne is then used to calculate the concentration of trapped ^{21}Ne, which is then subtracted from the total ^{21}Ne to give the cosmogenic ^{21}Ne concentration. If the trapped component is demonstrated to have a more MORB-type composition, crushing experiments can be used to determine the Ne isotopic composition of the trapped component more accurately.

In contrast to ^{3}He, ^{21}Ne is well retained in quartz and sanidine, which allows it to be measured in these mineral in addition to pyroxene and olivine.

Published ^{21}Ne production rates

As for ^{3}He production rates, reference ^{21}Ne production rates are either experimentally calibrated per mineral phase or calculated per target element. Calibrated reference production rates in quartz are about 20 atoms ^{21}Ne (g SiO_2)$^{-1}$ a^{-1} (Niedermann et al., 1994; Niedermann, 2000; Balco and Shuster, 2009), about 45 atoms ^{21}Ne (g mineral)$^{-1}$ a^{-1} in olivine (Fo_{81}) (Poreda and Cerling, 1992), and about 30 atoms ^{21}Ne (g mineral)$^{-1}$ a^{-1} in sanidine (Kober et al., 2005). Modelled production rates per target element have been published by Masarik and Reedy (1996), Masarik (2002), Schaefer et al. (1999) and Kober et al. (2005).

1.4 TCN production rates in space and time

As displayed in Chapter 1.2, the cosmic ray particle fluxes above the surface of the earth and hence TCN production rates increase with altitude and latitude. Additionally, the latitude, and to a minor degree the altitude dependence are subject to temporal variations mainly in the strength of the geomagnetic field. Therefore, surface exposure dating with TCN requires a reliable means to determine the production rate at any given latitude,

altitude, and for any exposure period. The concept of determining production rates at any position on the earth consists in using a constrained *reference production rate* for a "virtual" reference point, which is traditionally at sea level (with a standard atmospheric pressure of 1013.25 hPa) and at high latitudes (>60°) (hereafter SLHL), and calculating a *scaling factor* with the help of a scaling model that quantifies the spatial and temporal variations. The scaling factor then serves to extrapolate the SLHL production rate to the location of interest by multiplication. It has to be noted that the scaling factor for neutron induced ractions ($S_{el,s}$) is different from the scaling factor of muon induced reactions ($S_{el,\mu}$).

Unfortunately, these scaling factors are difficult to derive due to the complexities in the shielding effects of the geomagnetic field and of the atmosphere. This is e.g. because the rate of change in cosmic-ray flux with depth in the atmosphere is not constant with latitude, the atmosphere does not comprise a homogeneous or simple layered shell, and the earth's magnetic field cannot always be considered a geocentric dipole (Gosse and Phillips, 2001).

Nevertheless, several models have been developed for the calculation of scaling factors. Lal (1991) published a method to scale ^{10}Be and ^{26}Al production rates as a function of latitude and elevation with a third degree polynomial. It is based on neutron monitor count rates and "stars" (multi-pronged tracks) produced in photographic emulsions by cosmic ray spallation events. It is the so far most used and accepted model, although it considerably simplifies reality because it does not provide for integration of temporal variations. It considers the earth's geomagnetic field as a simple dipole and assumes for every position on earth standard atmosphere conditions. Stone (2000) refined this first method by expressing the elevation dependency in terms of atmospheric pressure, which makes possible taking account of regional differences in mean atmospheric pressure, encountered e.g. near the poles. Later authors (Dunai, 2000, 2001; Desilets and Zreda, 2003; Desilets et al., 2006b; Lifton et al., 2005, 2008) developed more sophisticated methods that account for the elevation effect in function of atmospheric depth, for the latitude effect derived from cutoff-rigidity, and for the temporal fluctuations quantified with the help of published records of secular geomagnetic variations. Despite intensive investigation since almost 20

years and considerable recent improvements in the understanding of this issue the different existing models are still controversial and at present time, none of the models seems to describe perfectly the local and time-dependent production rates.

1.4.1 Five different scaling methods

For the ^{36}Cl production rate calibration study of this PhD (Chapter 5), five of the above mentioned methods were used to derive scaling factors for the spallation and the muon induced reactions: Stone (2000), Dunai (2001), Desilets et al. (2006b), Lifton et al. (2005) and Lifton et al. (2008). Their models and calculations will be discussed in the following. For the ^{36}Cl calibration, the scaling factors according to Stone (2000) were calculated with CosmoCalc (Vermeesch, 2007); concerning the methods of Dunai (2001) and Desilets et al. (2006b), the calculations of the scaling factors follow strictly the instructions in the respective source paper; and in the case of Lifton et al. (2005), scaling factors were calculated in the spreadsheet published as supplementary data in Lifton et al. (2005), integrating the time-dependent scaling factors over the samples exposure durations for $S_{el,s}$ and $S_{el,\mu}$. The same procedure was done for the method of Lifton et al. (2008) with an extended version of the Lifton et al. (2005) spreadsheet (personal communication by N. Lifton), which reintegrates the improvements published in Lifton et al. (2008).

In contrast to Stone (2000), the methods of Dunai (2001), Desilets et al. (2006b), Lifton et al. (2005) and Lifton et al. (2008) account for temporal variations in the geomagnetic field by calculating the cutoff rigidity R_c of the geomagnetic field as a function of the time-dependent field intensity, based on dipole moment data by Ohno and Hamano (1993), Yang et al. (2000) and Guyodo and Valet (1999) (Fig. 1.14). The cutoff rigidity quantifies the minimum energy a particle needs not to be deflected but to pass through the geomagnetic field. R_c is highest at low latitudes (where it is most sensitive to temporal variations in the field intensity) and decreases towards high latitudes. It is therefore a function of time and of the geomagnetic latitude of the site. For the last 10 ka, the latitude in the calculation of R_c is expressed as the geomagnetic latitude (varying due to polar wander) calculated with the equation of Merrill et al. (1996) and paleopole position data from Ohno and Hamano (1993), Merrill and McElhinny (1983), Jackson et al. (2000) and/or Korte and Constable

(2005). The four scaling methods Dunai (2001), Desilets et al. (2006b), Lifton et al. (2005) and Lifton et al. (2008) quantify R_c with different approaches, which will be detailed in the next paragraphs.

Scaling method of Stone (2000)

The scaling method by Stone (2000) is based on the fitted third polynomial function of Lal (1991), expressing the altitude dependency in function of mean annual pressure. Additionally, Stone (2000) provides calculations for scaling factors for spallation and muon induced reactions instead of local production rates for certain TCN as done by Lal (1991). This allows applying the scaling factors for any TCN and for individual production reactions.

The spallation scaling factor is calculated

$$S_{el,s} = a + b\ exp\Big(\frac{-p}{150}\Big) + c\ p + d\ p^2 + e\ p^3 \tag{1.29}$$

where a, b, c, d and e are the latitude dependent scaling coefficients given in Table 1 of Stone (2000), and p is the atmospheric pressure at the site of interest in hPa, valid for altitudes between -20 m and 6000 m.

TCN production by muon reactions are less sensitive to altitude and latitude changes than the production due to spallation.

The muon scaling factor is calculated

$$S_{el,\mu} = M_{\lambda,1013.25}\ exp\Big(\frac{1013.25 - p}{242}\Big) \tag{1.30}$$

where $M_{\lambda,1013.25}$ is the latitude dependent scaling coefficient given in Table 1 of Stone (2000).

The atmospheric pressure p at the site of interest can be calculated:

$$p = p_0\Big(1 - \frac{\beta_0\ h}{T_0}\Big)^{g_0/R_d\beta_0} \tag{1.31}$$

with p_0 the standard pressure at sea level (1013.25 hPa), β_0 the temperature decrease with elevation (0.0065 K/m), h the altitude in [m], T_0 the standard temperature at sea level (288.15 K), g_0 the standard sea level value of the acceleration due to gravity (9.80665

m/s^2), and R_d the gas constant (287.05 J/kg/K).

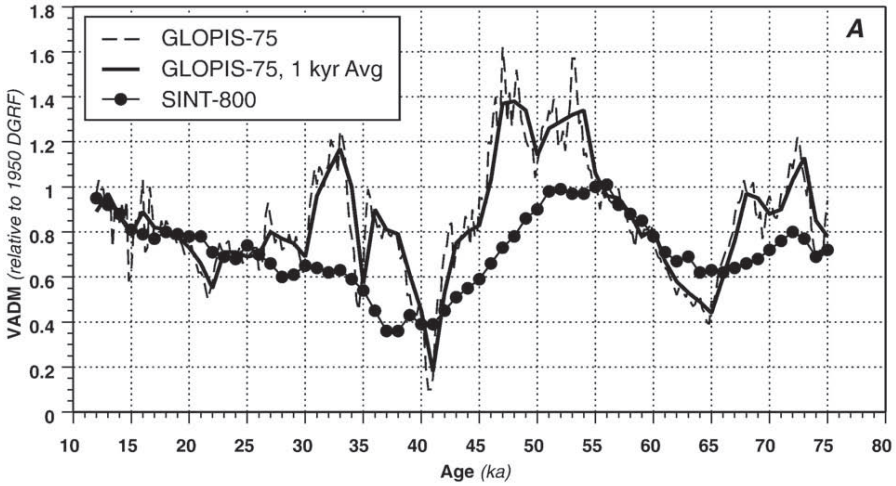

Figure 1.14: *Comparison of Virtual Axial Dipole Moment (VADM) records SINT-800 (Guyodo and Valet, 1999) and GLOPIS-75 (Laj et al., 2004), normalized to 1950 Definitive Geomagnetic Reference Field (DGRF) for the period 12-75 ka (from Lifton et al., 2008) From 12 to 20 ka, differences between both records are minimal. Before 20 ka trends are similar but GLOPIS-75 shows significantly larger fluctuations due to its higher resolution. SINT-800 has a lower resolution but covers the last 800 ka, a much longer time than GLOPIS-75 (75 ka).*

Scaling method of Dunai (2001)

Dunai (2000) had derived a new set of scaling factors by incorporing the effect of non-dipole field components on the original neutron monitor data used by Lal (1991). Dunai (2001) then expanded his first paper including the time-dependency of the scaling factors.

To quantify R_c for the last 10 ka, Dunai (2001) uses the formulation of Rothwell (1958)

$$R_c(t) = \frac{R}{4} \frac{H(t)\ c}{(1 + 0.25\ tan^2\ I(t))^{3/2}} \tag{1.32}$$

where R is the radius of the Earth (6370 km), H is the time-dependent horizontal field intensity, c is the velocity of light (2.979×10^8 m/s) and I is the time-dependent inclination of the geomagnetic field. The inclination allows accounting for the local non-dipolar field, and should therefore ideally be calculated with paleoinclination data acquired as near as possible to the site for which the scaling factor is to be determined.

$$I(t) = I(t)_{calib.meas} - I_{calib.exp} + I_{site.exp} \tag{1.33}$$

where $I(t)_{calib.meas}$ is the measured time-dependent inclination at the location of the paleomagnetic record; $I_{calib.exp}$ and $I_{site.exp}$ are the expected inclinations at the paleomagnetic record site and at the sampling site, respectively, if the Earth were a pure axial dipole. $I_{calib.exp}$ and $I_{site.exp}$ can be calculated with their respective latitudes λ according to

$$I = arctan\ (2\ tan\ \lambda) \tag{1.34}$$

The horizontal geomagnetic field strength H is given by

$$H(t) = \frac{M(t)\ \mu_0\ sin\ \theta(t)}{4\ \pi\ R^2} \tag{1.35}$$

where M is the time-dependent dipole moment [VDM], for which Dunai (2001) recommends the dipole moment data of Ohno and Hamano (1993) for the last 10 ka years; μ_0 is the permeability of the free space (1.25667×10^{-6} Wb A^{-1} m^{-6}); and θ is the time-dependent colatitude, which is calculated:

$$\theta(t) = acos\ (sin\lambda_{site}\ sin\ \lambda(t)_p + cos\ \lambda_{site}\ cos\ \lambda(t)_p\ cos\ (\phi(t)_p - \phi_{site})) \tag{1.36}$$

where λ_{site} is the geographic latitude of the sampling site, $\lambda(t)_p$ is the time-dependent geographic latitude of the pole position, ϕ_{site} is the longitude of the sampling site and $\phi(t)_p$ is the time-dependent longitude of the pole position.

Dunai (2001) expects that the fluctuations due to non-dipole component and polar-wander average out to a geocentric axial dipole field (GAD) for periods longer than 50 ka. However, due to the lack of local inclination and paleopole position records for the time before 10 ka, the approximation of a GAD is already made for periods longer than only 10 ka. In this case, R_c is calculated according to Elsasser et al. (1956):

$$R_c(t) = \frac{M(t)\ \mu_0\ c}{16\ \pi\ R^2}\ cos^4\ \lambda_{site} \tag{1.37}$$

Dunai (2001) recommends the dipole moment databases of Yang et al. (2000) and Guyodo and Valet (1999).

With the time-dependent values of R_c, calculated with Eq. 1.32 or 1.37, the time-dependent neutron flux at sea level is determined with the fitted equation:

$$N_{1030}(P,t) = 0.4952 + \frac{0.5221}{\left[1 + exp(-\frac{R_c(t)-4.2822}{-1.7211})\right]^{0.3345}} \tag{1.38}$$

The time-dependent attenuation length of the fast neutron flux in the atmosphere $\Lambda_{f,atm}$ between 7000 m and sea level is calculated:

$$\Lambda_{f,atm}(P,t) = 130.11 + \frac{17.183}{\left[1 + exp(-\frac{R_c(t)-2.2964}{2.060})\right]^{5.9164}} \tag{1.39}$$

The time-dependent scaling factor for spallation reactions $S_{el,s}$ at a given point on the surface is then calculated:

$$S_{el,s}(t) = N_{1030}(P,t)\ exp\Big(\frac{z(h)}{\Lambda_{f,atm}(P,t)}\Big) \tag{1.40}$$

where $z(h)$ is the difference in atmospheric depth $(x_0 - x)$ at height h compared to sea level. According to Dunai (2000), the atmospheric depth at sea level x_0 and the atmospheric depth at the sample site x are calculated:

$$x_0 = 10\frac{p_0}{g_0} \tag{1.41}$$

$$x = 10\frac{p}{g_0} \tag{1.42}$$

where p_0 is the atmospheric pressure at sea level (1013.25 hPa), p the atmospheric pressure at the sampling site and g_0 the standard sea level value of acceleration due to gravity.

The time-integrated scaling factor for spallation reactions $S_{el,s}$ is then obtained by averaging the time-independent values over the exposure duration.

There is no formulation for the muon scaling factor $S_{el,\mu}$ in Dunai (2001), since he considers its sensitivity to temporal variations as insignificant (personal communication).

Instead, $S_{el,\mu}$ can be calculated according to Dunai (2000) time-independently in function of the elevation and the latitude-dependent inclination I, assuming a GAD:

$$S_{el,\mu} = N_{1030}(I)\ exp\Big(\frac{z(h)}{\Lambda_{\mu,atm}}\Big) \tag{1.43}$$

where $\Lambda_{\mu,atm}$ has a value of 247 g cm^{-2} and $N_{1030}(I)$ is calculated:

$$N_{1030}(I) = 0.5555 + \frac{0.4450}{\Big[1 + exp(-\frac{I-62.698}{4.1703})\Big]^{0.3350}} \tag{1.44}$$

and I is calculated with the present-day geographic latitude according to Eq. 1.34.

Scaling method of Desilets et al. (2006b)

The scaling method of Desilets et al. (2006b) is an improved version of the method by Desilets and Zreda (2003), their model being based on a trajectory tracing code of Shea et al. (1965) and Dorman et al. (2000), with its coefficients fitted from cosmic ray fluxes measured with neutron monitors by different investigators since the 1950's.

Desilets and Zreda (2003) include non-GAD components in their model but acknowledge that for the calculation of R_c a GAD must generally be assumed due to the lack of accurate local non-dipole component records. The geomagnetic field intensity $M(t)$ is taken into account by normalizing it to the DGRF value M_0 (e.g. Smart and Shea, 2003). The time-dependent R_c is then given by

$$R_c(t) = \sum_{i=0}^{i=6}\Big(e_i + f_i\Big(\frac{M(t)}{M_0}\Big)\Big)\ {\lambda_{site}}^i \tag{1.45}$$

with the coefficients e_i and f_i given in Table 8 of Desilets and Zreda (2003).

Although not explicitly mentioned in the papers, polarwander is considered for the period < 10 ka to derive the scaling factors for the calibration study (Chapter 5), using Eq. 1.36 and the paleopole position data of Ohno and Hamano (1993) and Merrill and McElhinny (1983) to calculate the time-dependent colatitude.

The time-dependent latitude component of the scaling factor at sea level $f(R_c)$ is given by the Dorman function:

$$f(R_c, t) = 1 - exp(-\alpha\ R_c(t)^{-k}) \tag{1.46}$$

with $\alpha = 10.275$ and $k = 0.9615$ for spallation reactions and $\alpha = 38.51$ and $k = 1.03$ for muonic reactions (Dorman et al., 2000; Desilets and Zreda, 2003)

The improvement of Desilets et al. (2006b) compared to Desilets and Zreda (2003) concerns the elevation component of the spallation scaling factor: new coefficients for the polynomial calculation of the effective attenuation based on additional neutron flux measurements are provided.

The time-dependent elevation component of the scaling factor for spallation reactions $f(x, t)$ for the atmospheric depth x at the site of interest is given by:

$$f(x,t) = exp[n(1+exp(-\alpha\ R_c(t)^{-k})^{-1}(1033-x)+1/2(a_0+a_1\ R_c(t)+a_2 R_c(t)^2)(1033-x)^2$$

$$+1/3(a_3+a_4\ R_c(t)+a_5\ R_c(t)^2)(1033-x)^3+1/4(a_6+a_7\ R_c(t)+a_8\ R_c(t)^2)(1033-x)^4] \tag{1.47}$$

with the coefficients n, α, k and a_i given in Table 2 of Desilets et al. (2006b).

The time-dependent elevation component of the scaling factor for muon reactions is given by

$$f(x, t) = exp\Big(\frac{1033 - x}{\Lambda_{eff,\mu^-}(R_c)}\Big) \tag{1.48}$$

with the effective attenuation length for slow negative muons in the atmosphere

$$\Lambda_{eff,\mu^-} = 233 + 3.68\ R_c \tag{1.49}$$

The spallation scaling factor $S_{el,s}$ and the muon scaling factor $S_{el,\mu}$ are then calculated

$$S_{el,x}(t) = f(x, t)\ f(R_c, t) \tag{1.50}$$

The time-integrated scaling factors are obtained by averaging the time-independent values over the exposure duration.

According to Desilets and Zreda (2003), neutron monitor data suggest that thermal neutrons have significantly higher effective atmospheric attenuation lengths than high-energy neutrons. Although neutron monitor data for thermal neutrons are sparse and likely to be associated with higher uncertainties, Desilets and Zreda (2003) provide a fitted function to calculate the atmospheric attenuation length for thermal neutrons:

$$\Lambda_{th,atm}(t) = \frac{1033 - x}{(c_0 + c_1\ R_c(t) + c_2\ R_c(t)^2)\ (1033 - x) + 1/2(c_3 + c_4\ R_c)\ (1033 - x)^2} \\ +1/3(c_5 + c_6\ R_c(t))\ (1033 - x)^3 + 1/4(c_7 + c_8\ R_c(t))(1033 - x)^4 \qquad (1.51)$$

with the coefficients c_i given in Table 6 of Desilets and Zreda (2003).

Although Desilets and Zreda (2003) point out the need to consider the sensitivity of the primary cosmic ray flux to changes in the solar activity (solar modulation), they disregard its effects in their model due to the lack of well-constrained solar modulation records.

Scaling method of Lifton et al. (2005)

Lifton et al. (2005) primary modifications compared to Desilets and Zreda (2003) consist in two points, firstly in a new formulation for R_c based on the fit of a trajectory-derived R_c data from a world grid (Shea et al., 1968) to a cosine function, and secondly in the incorporation of temporal solar modulation variation in their method, which is based on a sunspot number reconstruction (Solanki et al., 2004).

Assuming that effects of eccentric dipole and non-dipole fields can be averaged, the formulation for the time-dependent R_c is:

$$R_c(t) = d_1\Big(\frac{M(t)}{M_0}\Big) cos^{d_2}\ \lambda_{site} \qquad (1.52)$$

with the coefficients $d_1 = 15.765$ and $d_2 = 3.800$.

The time-dependent spallation scaling factor $S_{el,s}$ is given by

$$S_{el,s}(t) = exp\Big[c_1\ ln(x\ S(t)) - S(t)\ exp\Big(\frac{c_2\ S(t)}{(R_c(t) + 5\ S)^{2S(t)}}\Big) + c_3\ x^{c_4} + c_5\ [(R_c(t) + 4\ S(t))\ x]^{c_6} \\ +c_7\ (R_c(t) + 4\ S(t))^{c_8}\Big] \qquad (1.53)$$

where x is the atmospheric depth and S a time-dependent correction factor quantifying the solar modulation based on the variation in monthly mean relative intensity. The fitted coefficients c_i are given in Table 1 of Lifton et al. (2005).

The time-dependent scaling factor for slow negative muon reactions $S_{el,\mu}$ is given by

$$S_{el,\mu}(t) = exp\Big[a_1 + a_2\ x + a_3\ x^2 + a_4\ x\ R_c(t) + a_5\ R_c(t) + a_6\ R_c(t)^2\Big] \tag{1.54}$$

The fitted coefficients a_i are given in Table 1 of Lifton et al. (2005).

Scaling method of Lifton et al. (2008)

Lifton et al. (2008) extend the Lifton et al. (2005) method by extrapolating R_c values directly from the continuous non-dipole geomagnetic field model CALS7K.2 (Korte and Constable, 2005) with a grid resolution of 5° latitude by 15° in 500 year steps for the last 7 ka years. This approach allows accounting for non-dipole field effects and longitudinal variability. For time periods after 7 ka, a function for the time-dependent R_c was fit based on the CALS7K.2 data:

$$R_c(t) = \frac{M(t)}{M_0} \sum_{i=1}^{i=6} a_{2i-1}\ cos^i\Big(\lambda_{site} + \frac{a_{2i}}{M(t)/M_0}\Big) \tag{1.55}$$

with the fitted coefficients a_{2i} given in Table 1 of Lifton et al. (2008).

Furthermore, the above mentioned Lifton et al. (2008) spreadsheet provides the possibility to take into account the variability in the atmospheric depth based on sea level temperature and pressure data from NCEP/NCAR reanalysis. For the calibration study presented in Chapter 5, this possibility was utilized in the calculation of the scaling factors according to Lifton et al. (2008) .

1.4.2 Quantitative differences between scaling methods

In this section, an overview of the quantitative effects of variations in altitude, latitude and time on local production rates is given by plotting the scaling factor $S_{el,s}$ for spallation reactions as a function of these three variables, comparing various hypothetical geographic positions (low-, mid- and high-altitude and low-, mid- and high-latitude). In each plot,

the $S_{el,s}$-curves predicted from each of the five scaling methods, which are presented in the previous section, are shown. It will be demonstrated that the differences between predicted local production rates calculated with the different methods vary with altitude, latitude and exposure duration. This means that none of the scaling methods systematically yields higher or lower scaling factors than the others. When comparing the numerical values of $S_{el,s}$ from the five methods for a given geographic position it has to be kept in mind that a higher value of $S_{el,s}$ would correspond to a lower exposure age.

Fig. 1.15 shows $S_{el,s}$ as a function of the altitude for low-, mid- and high-latitude on the Northern hemisphere. The present geomagnetic field strength is assumed, which means that $S_{el,s}$ is not integrated over a certain time span but calculated for t = 0 years.

The altitude is representative for the atmospheric depth, which controls the effect of the atmosphere on the attenuation of the cosmic ray flux and hence the TCN production on the Earth's surface. As such, the altitude is the variable that has the largest effect on variations of TCN production rates. The increase of the production rate with altitude is exponential. The higher the latitude the greater this increase. Fig. 1.15 shows that at low latitude the scaling methods of Desilets et al. (2006b) (De) and Dunai (2001) (Du) predict a higher while that of Lifton et al. (2005) (Li05) and Lifton et al. (2008) (Li08) predict a lower altitude-effect than that of Stone (2000) (St). At mid latitude, values of $S_{el,s}$ calculated according to Li05 increase faster with altitude than those calculated according to Du, St and Li08, and at high latitude they increase fastest of all. $S_{el,s}$ calculated according to Li08 are lowest at mid latitude but second highest at high latitude. At high latitude, the method according to St predicts the lowest production rate increase with altitude.

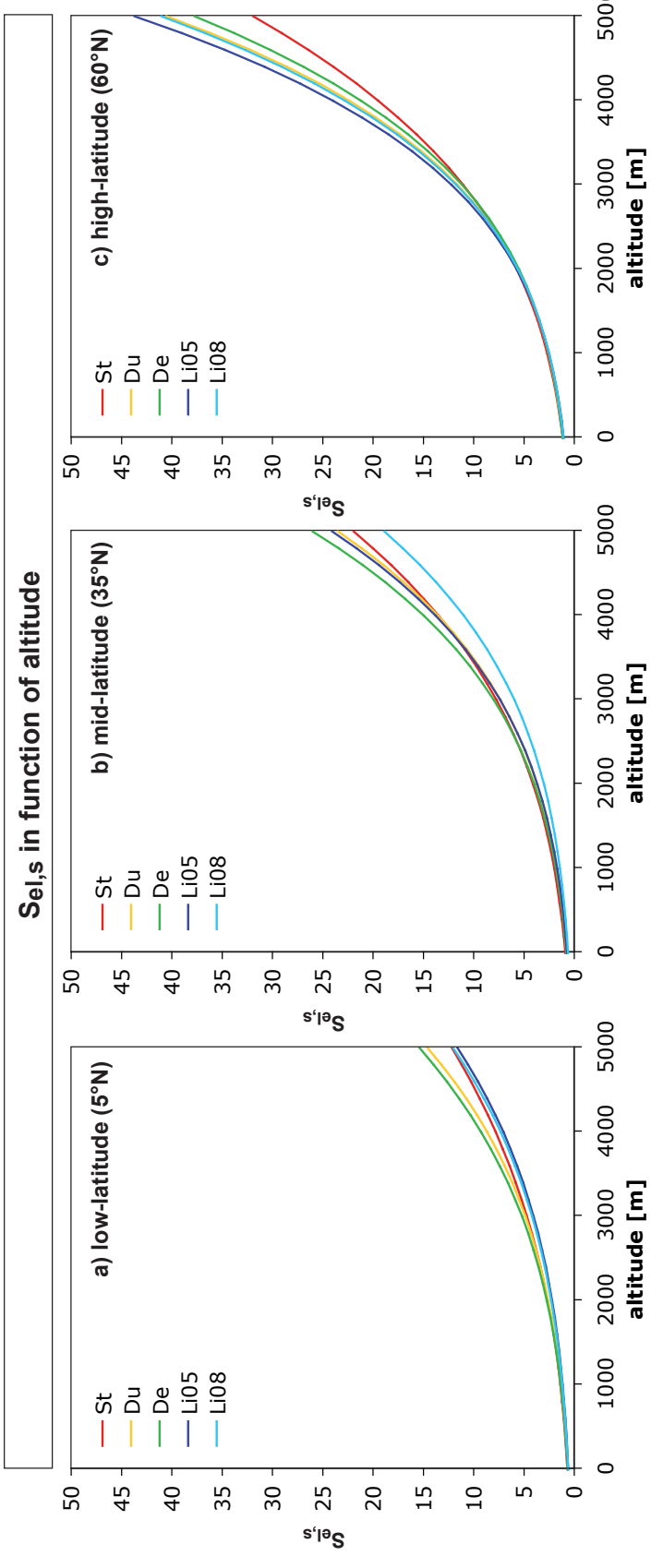

Figure 1.15: *The scaling factor $S_{el,s}$ for spallation reactions in function of altitude for (a) low-latitude (5°N), (b) mid-latitude (35°N) and (c) high-latitude (60°N), assuming the present geomagnetic field strength. The longitude for all graphs is 15°E. The abbreviations in the legend represent the following scaling methods: St = Stone (2000), Du = Dunai (2001), De = Desilets et al. (2006b), Li05 = Lifton et al. (2005), Li08 = Lifton et al. (2008). In the case of Du the GAD assumed and R_c is calculated with the dipole moment of Yang et al. (2000).*

Fig. 1.16 shows $S_{el,s}$ as a function of the latitude on the Northern hemisphere for low-, mid- and high-altitude. Here again, the present geomagnetic field strength is assumed.

The latitude represents the cutoff rigidity of the geomagnetic field, which controls the cosmic ray flux intensity and its energy spectrum penetrating in the atmposphere (Chapter 1.2.2). Due to the higher cutoff rigidity at low latitudes, the secondary cosmic ray flux has higher energies but lower intensity than at high latitudes. Therefore, the TCN production increases with latitude. From low to high latitudes, the local production rates increase by about a factor 2 at low altitude and a factor of 4 at high altitude. In addition, the rate increase is highest at mid-latitudes, between about 25° and 45°.

Fig. 1.16 shows that at low altitude, the differences between the values of $S_{el,s}$ calculated according to the five methods are almost continuously systematic in function of the latitude: St > Du ≈ De > Li05 > Li08. At mid and high altitude, the differences are not systematic but vary strongly with latitude. It can be noted that at mid altitude values of $S_{el,s}$ calculated according to Li08 are for the most part of the latitude range lower than those calculated according to the other methods.

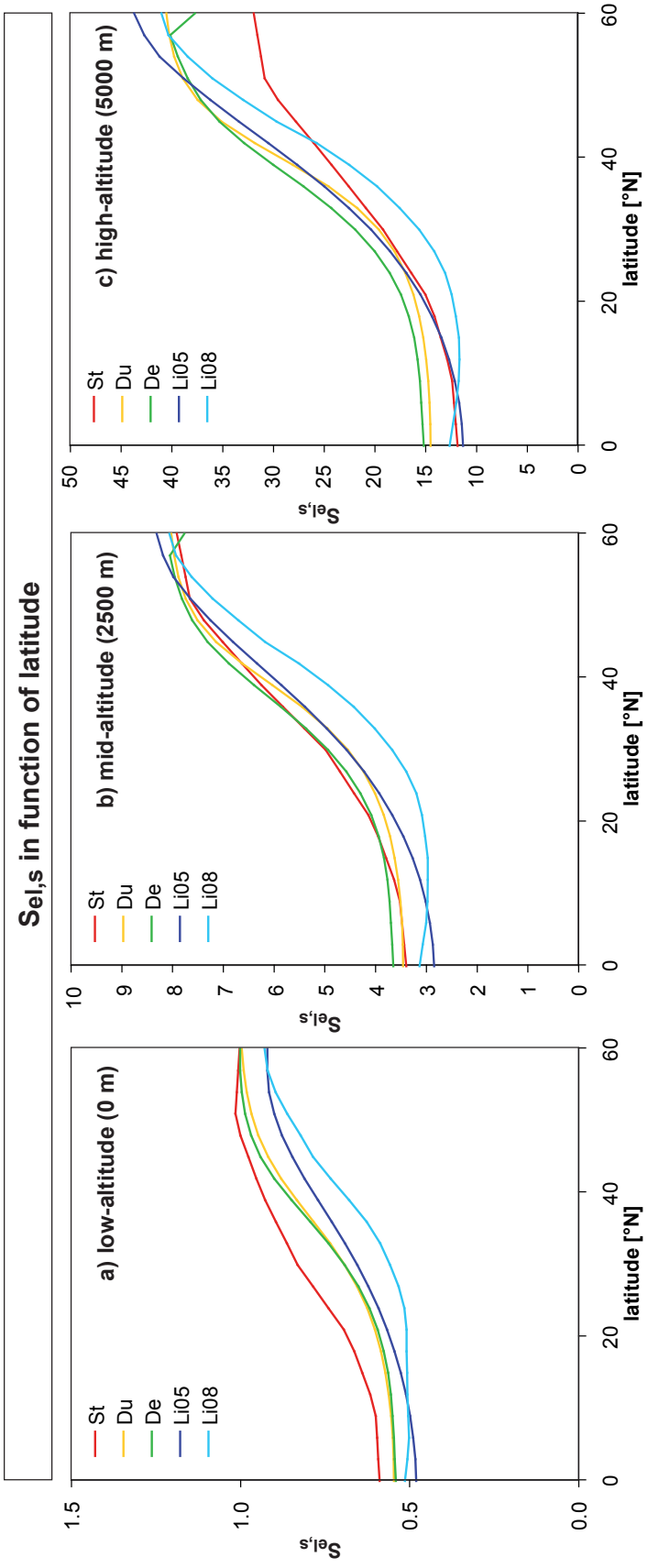

Figure 1.16: *The scaling factor $S_{el,s}$ for spallation reactions in function of latitude for (a) low-altitude (0 m), (b) mid-altitude (2500 m) and (c) high-altitude (5000 m), assuming the present geomagnetic field strength. The longitude for all graphs is 15°E. Note that the scales of the axes of ordinates are different for each panel. The abbreviations in the legend represent the following scaling methods: St = Stone (2000), Du = Dunai (2001), De = Desilets et al. (2006b), Li05 = Lifton et al. (2005), Li08 = Lifton et al. (2008). In the case of Du the GAD assumed and R_c is calculated with the dipole moment of Yang et al. (2000).*

Figs. 1.17, 1.18 and 1.19 show $S_{el,s}$ as a function of time for all possible combinations between low-, mid- and high-altitude and low-, mid- and high-latitude. St is the only scaling method of those presented here that does not consider temporal variations but calculates present production rates.

The temporal variability of the TCN production rates is mainly controlled by the fluctuations in the geomagnetic field strength, which is expressed in the cutoff rigidity. Therefore, the temporal variations are most notable when comparing different latitudes. At low latitudes, the sensitivity of the production rates to fluctuations in the geomagnetic field strength is highest (Fig. 1.17), while at high latitudes the TCN production is almost invariable with time (Fig. 1.19). When comparing the three panels of each figure, it becomes evident that the temporal variations increase with increasing altitude. Over the last 20 ka, the time-dependent scaling factors generally decrease, which is due to an increase of the geomagnetic field strength (Balco et al., 2008).

For the quantification of the effect of the temporal fluctuations on theTCN concentration accumulated in a sample, the time-depending production rates are integrated over the exposure duration of the surface. This effect does not only depend on the latitude and on the altitude, as described above, but also on the exposure duration. For example, when comparing $S_{el,s}$ calculated according to Li05 (dark blue curve) and calculated to St (red curve) in Fig. 1.17, it is clear that for an exposure duration of the last 4 ka the time-integrated production rate from Li05 would be lower than that of St, whereas for an exposure duration of 20 ka it would be about the same.

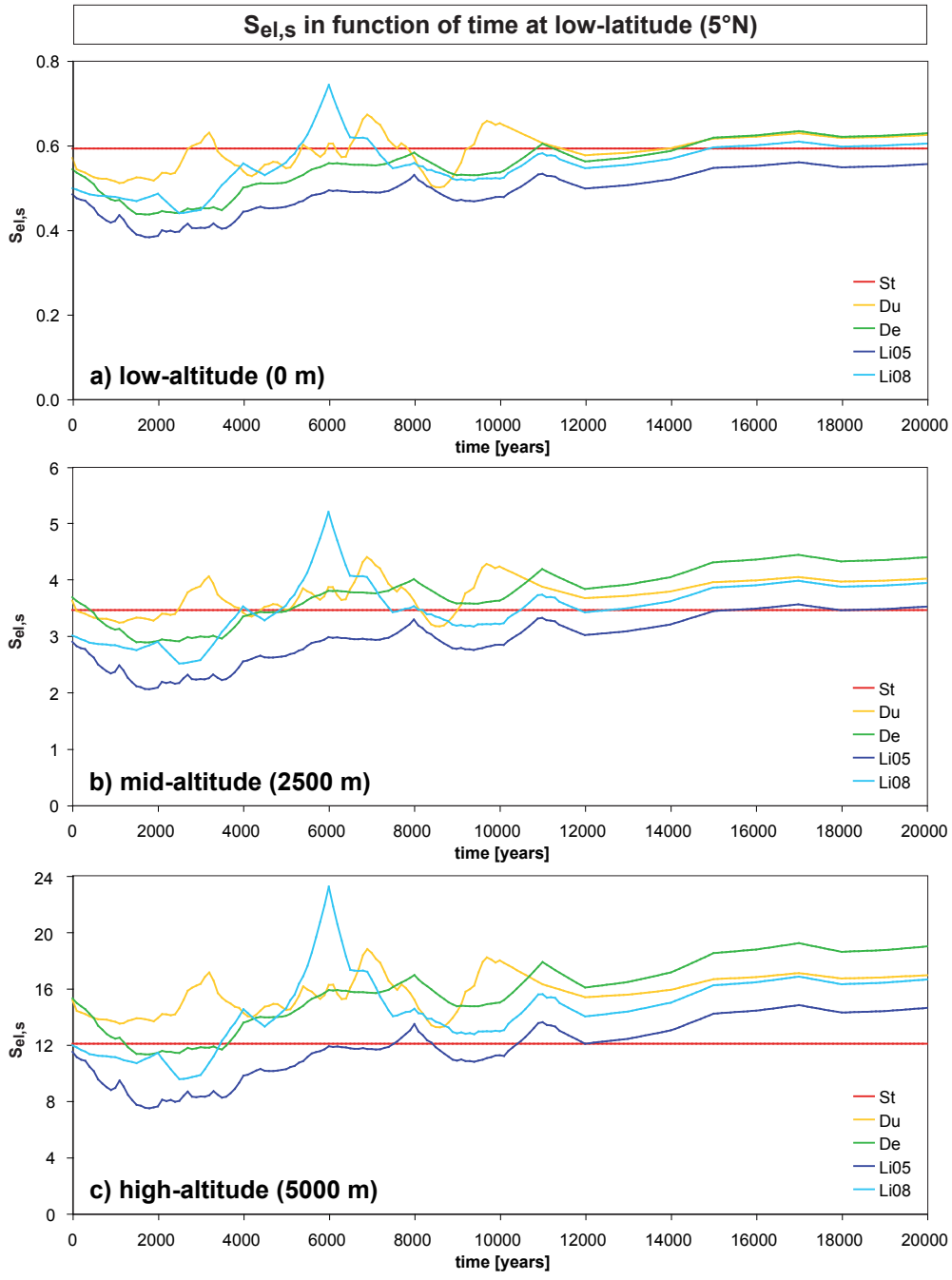

Figure 1.17: *The scaling factor $S_{el,s}$ for spallation reactions in function of time (0 - 20 ka) at low-latitude (5° N) for (a) low-altitude (0 m), (b) mid-altitude (2500 m) and (c) high-altitude (5000 m). Note that the scales of the axes of ordinates are different for each panel. The abbreviations in the legend represent the following scaling methods: St = Stone (2000), Du = Dunai (2001), De = Desilets et al. (2006b), Li05 = Lifton et al. (2005), Li08 = Lifton et al. (2008). In the case of Du, for the first 10 ka, non-dipole components are considered based on the paleoinclination record of Brandt et al. (1999) from 42.5° N (Italy).*

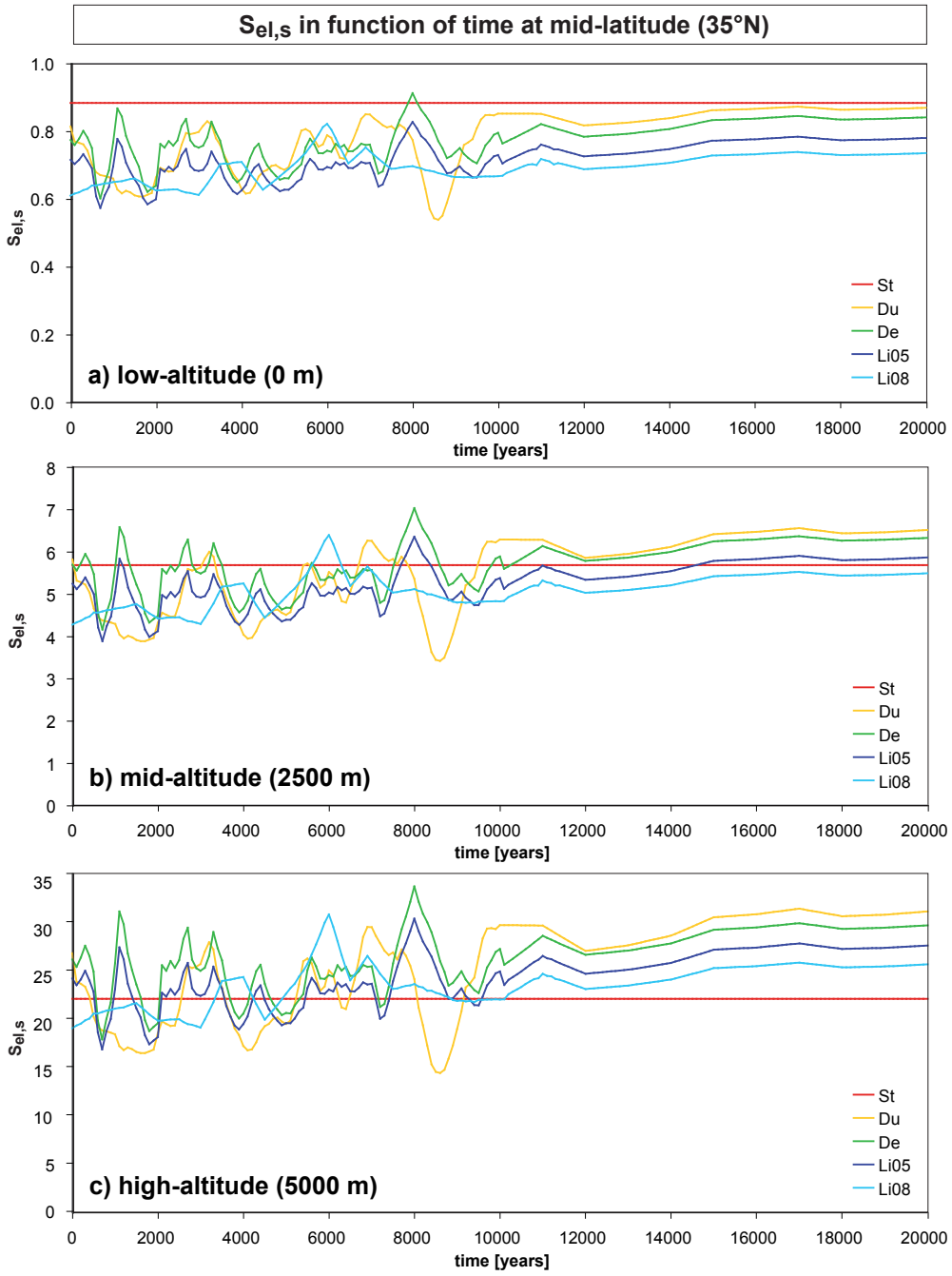

Figure 1.18: *The scaling factor $S_{el,s}$ for spallation reactions in function of time (0 - 20 ka) at mid-latitude (35°N) for (a) low-altitude (0 m), (b) mid-altitude (2500 m) and (c) high-altitude (5000 m). Note that the scales of the axes of ordinates are different for each panel. The abbreviations in the legend represent the following scaling methods: St = Stone (2000), Du = Dunai (2001), De = Desilets et al. (2006b), Li05 = Lifton et al. (2005), Li08 = Lifton et al. (2008). In the case of Du, for the first 10 ka, non-dipole components are considered based on the paleoinclination record of Brandt et al. (1999) from 42.5°N (Italy).*

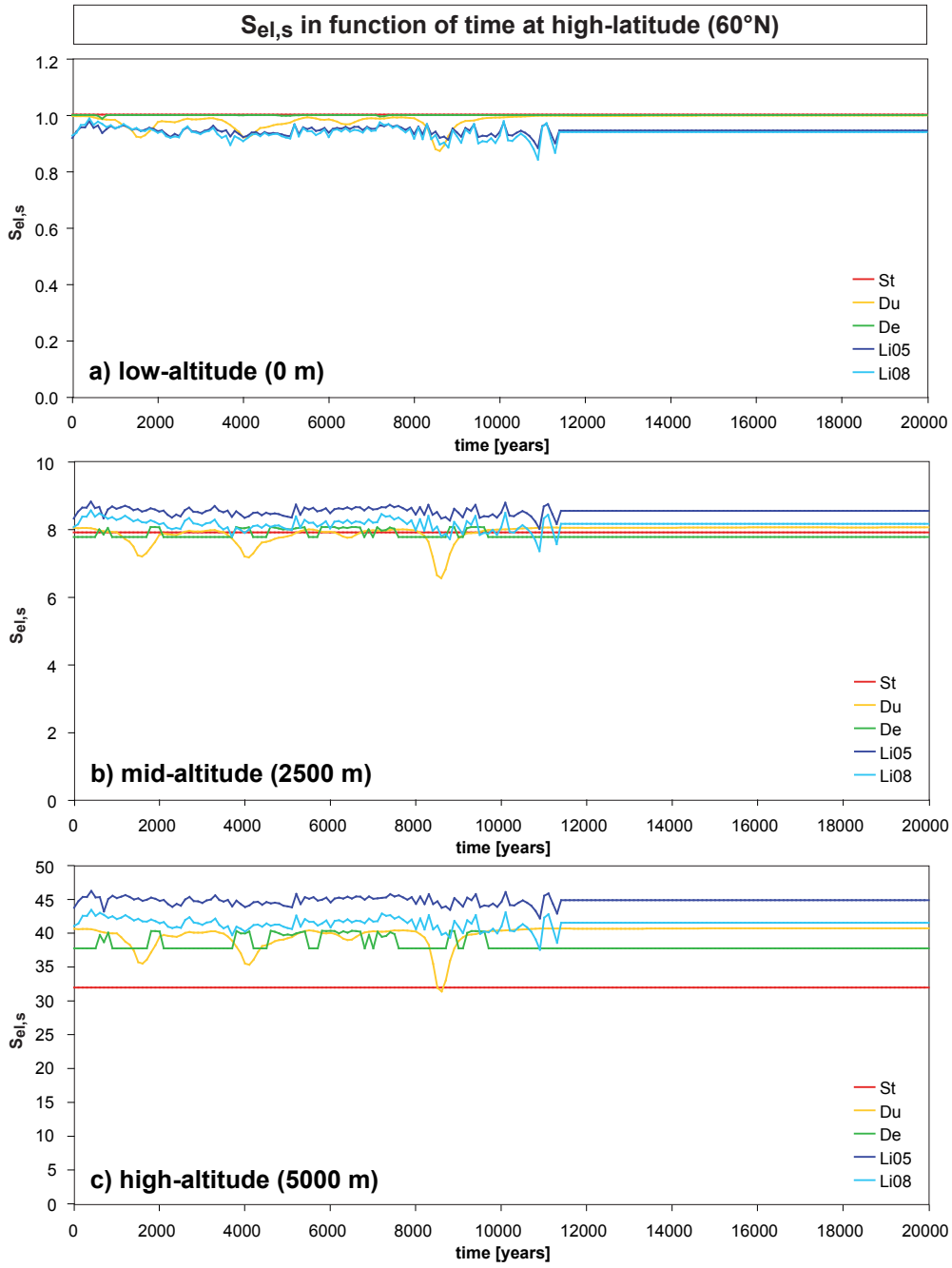

Figure 1.19: *The scaling factor $S_{el,s}$ for spallation reactions in function of time (0 - 20 ka) at high-latitude (60° N) for (a) low-altitude (0 m), (b) mid-altitude (2500 m) and (c) high-altitude (5000 m). Note that the scales of the axes of ordinates are different for each panel. The abbreviations in the legend represent the following scaling methods: St = Stone (2000), Du = Dunai (2001), De = Desilets et al. (2006b), Li05 = Lifton et al. (2005), Li08 = Lifton et al. (2008). In the case of Du, for the first 10 ka, non-dipole components are considered based on the paleoinclination record of Brandt et al. (1999) from 42.5° N (Italy).*

Balco et al. (2008) do a similar comparison, regarding exposure ages calculated with scaling factors according to five different scaling methods, which are those of Stone (2000) (St), Dunai (2001) (Du), Lifton et al. (2005) (Li), Desilets et al. (2006b) (De) and Lal (1991) with integration of geomagnetic field variations according to the formulation in Nishiizumi et al. (1989) (Lm). The 3D plots in Fig. 1.20 illustrate the differences between exposure ages calculated with St and with De and between those calculated with Lm and with De in function of altitude, latitude and exposure time. General conclusions from their comparison are that 1- the scaling method ignoring the temporal effect (St) will yield older or younger exposure ages, depending on whether the sample site's exposure age is older or younger, respectively, than the calibration site to which the SLHL production rate used refers (because production rates generally decrease from older to more recent times and reference production rates are integrated over a certain exposure duration) (Fig. 1.20a); 2- the altitude dependence in the scaling methods Du, Li and De is stronger than in St and Lm (Fig. 1.20b), resulting in older exposure ages from Du, Li and De than St and Lm at low altitudes and younger exposure ages at high latitudes as it can be seen in Fig. 1.16.

Pigati and Lifton (2004) discuss the difference between modern production rates of the two nuclides ^{14}C and ^{10}Be and those integrated over the exposure time, based on the scaling method of Desilets and Zreda (2003) (Fig. 1.21). The differentiation between the two radionuclides is due to the fact that they have extremely different half-lives. ^{14}C is short-lived ($t_{1/2}$ = 5.73 ka) and decays more rapidly than the long-lived ^{10}Be ($t_{1/2}$ = 1.36 Ma). For a relatively short exposure duration, say 25 ka, most of the ^{14}C initially produced will have decayed at the moment of measurement (only about 6% of the originally produced nuclide has remained), while less than 1% of the ^{10}Be will have decayed. The recent temporal fluctuations have therefore a much higher influence on the accumulated ^{14}C concentration, while for ^{10}Be, the influence is constant over the whole exposure duration.

Pigati and Lifton (2004) highlight in their discussion that when intensity variations of the geomagnetic field and polar wander are accounted for in the production rate calculations, values can be up to 27% higher and 24% lower (in the case of ^{14}C) and 48% higher and 26% lower (in the case of ^{10}Be) than modern production rates (Fig. 1.21), depending

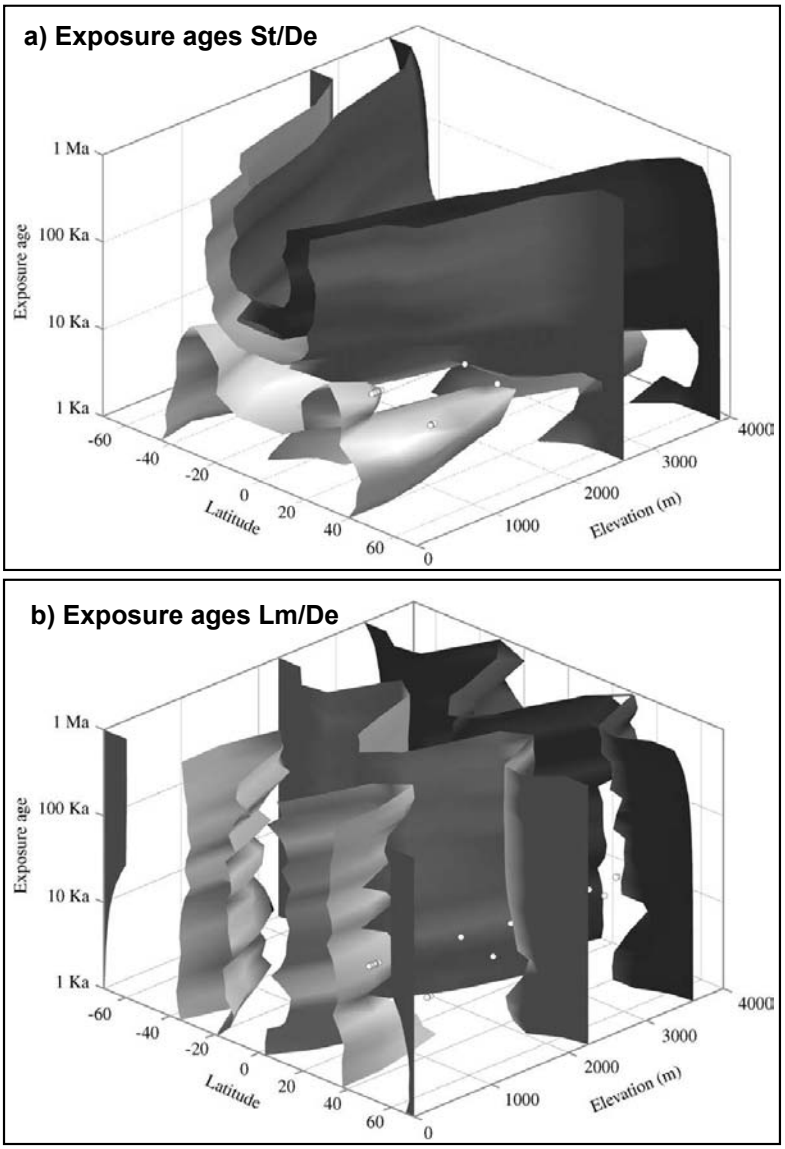

Figure 1.20: *Differences in exposure ages calculated with scaling factors from Stone (2000) (St), Desilets et al. (2006b) (De) and Lal (1991), integrating variations of the geomagnetic field intensity according to Nishiizumi et al. (1989) (Lm), in function of altitude, latitude and exposure duration (from Balco et al., 2008). Longitude is 100° W. The intermediate surfaces in panel a and panel b represent exposure age ratios of 1, the dark surfaces ratios of 1.1 and the light surfaces ratios of 0.9. Conclusions from exposure age ratios St/De (a) are that exposure ages calculated with St increase compared to those calculated with De the higher the altitude and the longer the exposure duration (because St does not take temporal effects into account). Conclusions from exposure age ratios Lm/De (b) are that exposure ages calculated with Lm increase compared to those calculated with De with increasing altitude. Differences do not depend strongly on age, because both methods take temporal effects into account.*

on the latitude and on the exposure duration. Differences between integrated and modern production rates increase significantly at higher altitudes (19% greater at 4000 m than at sea level). The impact of polar wander is secondary compared to that of the field intensity variations except at mid-latitudes (30-40°) along a longitudinal plane defined by the 105° and 285° meridians, which is the plane of motion of the geomegnetic pole. Production rates generally increase near the longitude 105° in the Northern hemisphere and near 285° in the Southern hemisphere and decrease near 285° in the Northern hemisphere and near 105° in the Southern hemisphere (Fig. 1.21).

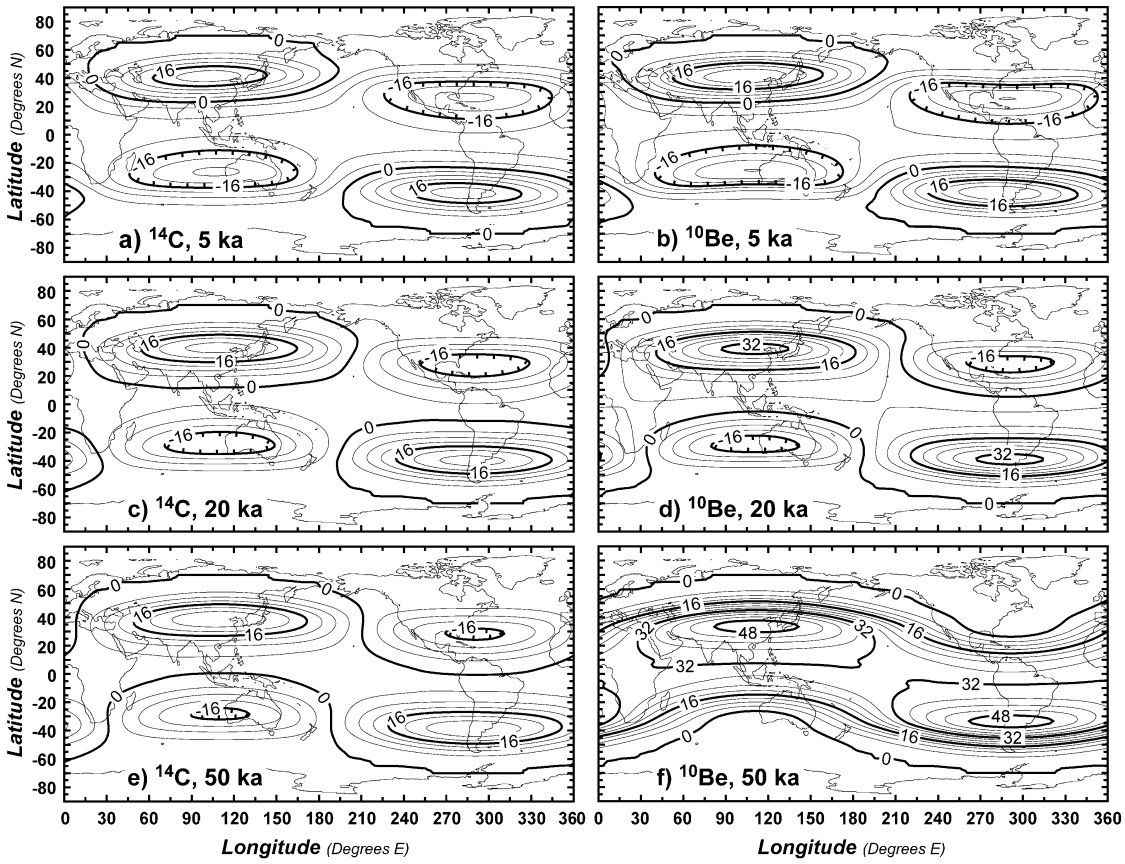

Figure 1.21: *Global maps of time-integrated production rates at sea level normalized to modern production rates, both calculated according to Desilets and Zreda (2003), for the two radionuclides ^{14}C and ^{10}Be for three different exposure durations (5 ka, 20 ka and 50 ka) (from Pigati and Lifton, 2004). Time-integrated prodution rates account for variations in the intensity of the geomagnetic field and for polar wander. Counter intervals are 4%. See text for explication.*

Chapter 2

From sampling to TCN concentrations: Material and methods

2.1 Sampling strategies for calibration of production rates

For the measurement of cosmogenic nuclides in natural samples the sample strategies depend on the kind of application and its objective. The strategies are not the same if e.g. erosion rates, incision rates, deglaciation histories, seismic activity or paleoaltimetry are studied.

Here, the sample strategies for the *calibration of production rates* as applied for this PhD study are illustrated. The sample site has to fulfil certain conditions related to the exposure duration, the exposure history, the rock type and the rock surface to be an appropriate calibration site. This will be discussed in the following paragraphs.

Exposure history

To calibrate cosmogenic nuclide production rates with natural samples the exposure history has to be clear and the exposure duration must be accurately known. The types of surfaces most often used for ^{36}Cl calibration studies, due to their simply traceable exposure history, are lava flows (e.g. Stone et al., 1996; Phillips et al., 1996, 2001) and deglaciation surface features such as moarine boulders and glacially abraded bedrock (e.g. Zreda et al., 1991; Swanson and Caffee, 2001).

The exposure duration of deglaciation surface features is determined with radiocarbon (^{14}C) dating of organic material in till (unsorted glacial sediment) or in postglacial lakes.

The resulting ages are, however, rather minimum ages and do not necessarily represent the exposure time of the rock material used for the TCN calibration. Another drawback when using deglaciation features is that *inheritance*, cosmogenic nuclide concentrations accumulated during exposure periods prior to the presently ongoing one, cannot be completely excluded, because the formation age of the rock is much longer than its exposure duration.

Lava flows afford better characteristics allowing the control of the exposure history. The exposure to cosmic radiation of a lava flow begins at the time of eruption. This means for the topmost lava flows that the formation age of the flow is equal to the exposure duration of its surface. Inheritance can be excluded in lava flows. Lava flow surfaces can be buried by superposing flows like the surface studied in Chapter 4. In this case, however, the exposure history is easily reconstructed because the formation age of the underlying flow minus the formation age of the superposed flow results in the exposure duration of the buried lava surface.

There exist several dating methods to determine the formation age of a lava flow. The most common ones are K/Ar, Ar/Ar and radiocarbon (^{14}C) dating. However, whether the rocks can be dated with one of these methods depends on certain conditions. The three methods are described e.g. in Bradley (1999).

For ^{40}K/^{40}Ar and ^{40}Ar/^{39}Ar dating a K-bearing rock material is needed. This can be minerals such as sanidine or whole rock. The rock sample to be dated must be chosen very carefully. Any alteration or fracturing means that the potassium or the argon or both have been disturbed. This is the most difficult limitation of the methods. Additionally, young rocks have low levels of ^{40}Ar, which delimits these methods to rocks that are at least 10 ka old. Older rocks yield more accurate and more precise results.

^{14}C dating depends on the existence of remnants of organic material such as charcoal or shells preserved within or on the lava, which makes the application of this method rare for direct age dating of lava flows. Dating shells with ^{14}C for lava flow chronologies as done in Branca (2003) provides only minimum eruption ages because the marine fauna must have colonized the lava after its emplacement. The charred material in tephra layers (=pyroclastic fallout deposits) between lava flows can easily be dated with ^{14}C as in Coltelli

et al. (2000), which can then be used as time markers for the reconstruction of lava flow chronologies (Branca, 2003) and provide minimum and maximum ages for emplacements. This approach was used for the exposure age constraint of "Solicchiata Flow" in Chapter 5. Also historical records can be used as exposure age constraint for very young lava flows as done for the "Historical Flow" in Chapter 5.

Rock type and mineralogy

It has to be ensured that the rock type is appropriate for extraction of the cosmogenic nuclide. In theory, ^{36}Cl can be extracted from any rock that bears at least one of its target elements (Chapters 1.1 and 1.3.6). If the nuclide is to be extracted from certain mineral phases with the purpose to maximize the concentration of particular target elements such as Ca and K in feldspars or Ca in pyroxenes (Chapter 5), the rock type has to be chosen in function of the presence of these mineral phases. ^{3}He and ^{21}Ne are typically extracted from olivines and pyroxenes, ^{21}Ne also from quartz (Chapters 1.3.7 and 1.3.8). During the inspection of the rock in the field it has to be assessed if the amount of the minerals present in the rocks is high enough for the nuclide extraction.

Surface preservation

Erosion changes the accumulation of cosmogenic nuclides at the rock surface (Chapters 1.3.5 and 3.3). The effect of erosion is difficult to quantify except with means of cosmogenic nuclide measurements. The safest way to avoid this problem is to sample surfaces that are well preserved so that erosion is negligible. In contrast to other rock types such as limestones, lava surfaces allow easily checking the erosion conditions due to their characteristic surface features. There are two types of lava morphologies, *pahoehoe* and *aa* lava (Fig. 2.1). Pahoehoe lava has an undulating, or often ropy surface. These surface features are due to the movement of very fluid lava under a congealing surface crust. Aa lava is characterized by a rough or rubbly surface composed of broken blocks. Both types of surfaces reveal notedly if they have been subject to erosion because their typical relief would be altered by weathering and smoothed (Fig. 2.2) or even polished by erosion.

The older a lava flow the higher the risk that surface has undergone substantial erosion. However, the degree of erosion is not only a function of time but also depends on the

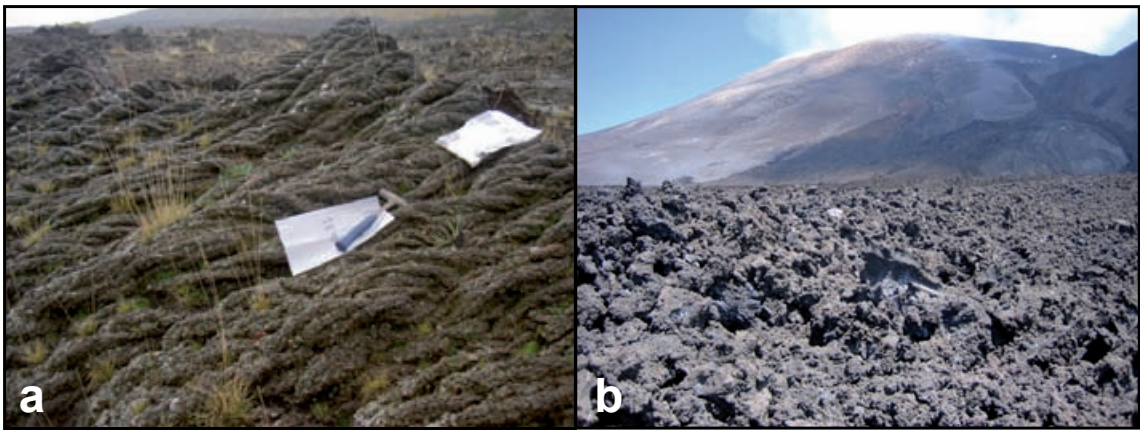

Figure 2.1: *Examples for pahoehoe (a) and aa (b) lava types. Both pictures are taken at Mt. Etna.*

Figure 2.2: *Examples for a smoothed pahoehoe surface (Mt. Etna).*

climate. The wetter the climate the stronger weathering and erosion. At Mt. Etna there is a notable difference between the erosion degrees on the south-east flank, the more humid side orientated to the sea, and the north-west flank, the drier side orientated to the inland. This is also reflected by the vegetation density on both sides. It is therefore easier to find well preserved lava surfaces of a certain age on the northern or western flank than on the southern or eastern flank.

Technical considerations for the field work

During sampling for cosmogenic nuclide measurements certain tools are needed to choose the most appropriate sample site and to record all information necessary for the correct analysis of the results (Chapters 1.3.4 and 3).

For the recognition of minerals in the rock, the use of a loupe is helpful. Carbonatic rocks can be identified with a drop of hydrochloric acid (HCl).

The determination of the exact geographic location with a GPS (*Global Positioning System*), including the altitude, the latitude and the longitude at the site, is required to calculate the *scaling factors* to obtain the local production rate at the site (Chapter 1.3.4 and 1.4).

The topography surrounding the sample site has to be quantified with an inclinometer in order to determining the *shielding correction* for the production rate calculation. This is because the exposure of a surface to cosmic radiation is "screened" or "shielded" by topographic obstacles like moutains, cliffs, slopes or buildings. The inclination and orientation of the surface itself has to be measured in order to calculate the *self-shielding* of the surface. Also, irregular geometry of the surface, e.g. in the case of boulders or *hornitos* (small lava cones, Fig. 2.3), should be recorded and measured due to the diffusion of low-energy neutrons out of the rock into air near the land/atmosphere boundary (neutron leakage, Chapter 1.3.3).

Figure 2.3: *Hornitos at Mt. Etna.*

In addition to recording the surrounding topography and the shape of the surface other elements potentially influencing the cosmic ray flux or the diffusion of particles in the rock

Table 2.1: *List of tools needed during sampling and their functions.*

Tool	Function
Loupe	Identification of minerals
Dilute HCl	Identification of carbonatic rocks
GPS	Documentation of altitude, latitude, longitude (scaling)
Inclinometer	Documentation of topography and geometry of the surface (shielding)
Camera	Pictures of sample, sample site and landscape
Hammer	Sampling
Chisel	Sampling
Sledge hammer	Sampling
Measuring tape	Determination of sample thickness

have to be noted down, such as vegetation, soil cover or air spaces in the rock. Vegetation and soil cover have shielding effects. Air spaces in the rock influence the density and thus the attenuation of the cosmic ray flux. In the case of big air spaces, the diffusion of low-energy neutrons out of the rock might occur.

For all these reasons it is important to take photographs of the sample site (before and after sampling), of the surrounding landscape and of the sample itself.

Samples are taken with a hammer and a chisel. The hardness of basaltic lava requires in most of the cases the use of a sledge hammer. Before sampling it should be estimated how much sample material is needed to extract a sufficient amount of the cosmogenic nuclide from the sample. The calculation of this estimation is given in the next paragraph.

Finally, the thickness of the sample taken has to be measured with a measuring tape. This is necessary because the flux of the cosmic ray particles is attenuated in the rock material and decreases exponentially with depth (Chapter 1.3.4). To account for this effect *thickness integration factors* are calculated and used to integrate the nuclide production over the thickness of the sample.

Each measurement in the field is associated with a certain uncertainty due to the imprecission of the tools (GPS, inclinometer, measuring tape) and to the inaccuracy related to the perception of the person who is measuring. The effect of these uncertainties on calculated exposure ages is illustrated in Fig. 2.4, taking the example of the altitude and the sample thickness. Errors in the measurements of the altitude of $\pm$ 10 m and of the sample thickness of $\pm$ 1 cm result in less than 1% error in the calculated exposure age.

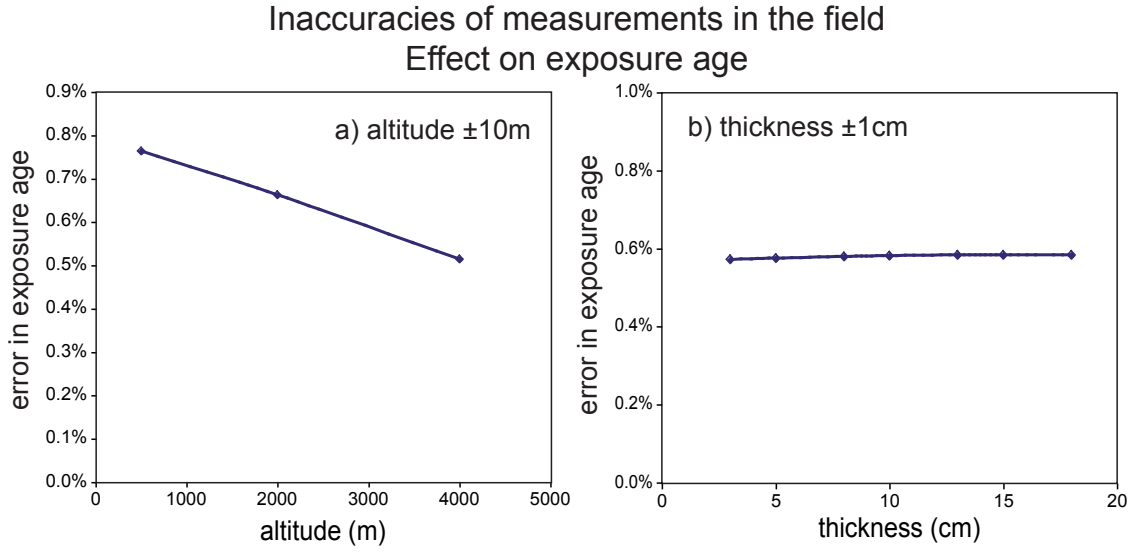

Figure 2.4: *Effect of inaccurate measurements of (a) the altitude and (b) the sample thickness on the exposure age of a sample. For the altitude an inaccuracy of 10 m is assumed. The resulting error in the exposure age is less than 1%, decreasing with increasing altitude. For the thickness an accuracy of 1 cm is assumed resulting in an error in the exposure age of 0.6% no matter which real thickness the sample has.*

How much sample must be taken?

If the quantity of a cosmogenic nuclide in a sample is too small it is difficult to get accurate and precise mesaurements. In general, for AMS measurements the nuclide level that can be measured by AMS or noble gas mass spectrometry depends on the sensitivity of the machine and on the blank level (Chapters 2.3.2 and 2.4.1).

The size of the sample determines the absolute amount of the nuclide that can be extracted from the material. The nuclide concentration in the sample depends on several factors, most notably on the exposure duration of the surface, the composition of the material and the altitude of the site. With the knowledge or an idea of these factors it can therefore be estimated how much material is needed to be able to extract a sufficient amount of the nuclide in order to obtain results above the blank level. The estimate should especially be done for very young samples and if ^{36}Cl is extracted from mineral separates since target element concentrations relative to the bulk rock can be very small.

The sample mass required for ^{36}Cl measurements at LLNL-CAMS (Chapter 2.3.2) using a spike enriched in ^{35}Cl (99.9%) (see Chapter 2.3.3) is:

$$m_{requ} = R_{ideal}^{36/35}\ N_{sp}^{35}\ [^{36}Cl]_{estim} \tag{2.1}$$

where m_{requ} is the required sample mass; $R_{ideal}^{36/35}$ is the ideal ^{36}Cl/^{35}Cl ratio to be measured, which should be assumed as 10 times higher than the procedure blank, e.g. 1 $\times$ 10^{-13} if the procedure blank is in the order of 1 $\times$ 10^{-14}; N_{sp}^{35} is the number of atoms ^{35}Cl from the spike, which can be calculated according to the amount of spike-Cl added to the sample multiplied by the 0.999, the fraction of ^{35}Cl in the spike-Cl; $[^{36}Cl]_{estim}$ is the estimated ^{36}Cl concentration in the sample.

The ^{36}Cl concentration in the sample can be estimated as follows. If ^{36}Cl is to be measured in the whole rock its target element concentrations (typically Ca and K) have to be known or estimated ($[Ca]_{bulk}$ and $[K]_{bulk}$). Then the scaled production rate for each target element (P_{Ca}^{sc}, P_{K}^{sc}) has to be calculated by multiplication of the spallation scaling factor for the site with the SLHL production rate for the target element. With the knowledge (or estimate) of the exposure duration t_{expo} the ^{36}Cl concentration produced in the whole rock can be gauged by the calculation

$$[^{36}Cl]_{estim} = P_{Ca}^{sc}\ [Ca]_{bulk}\ t_{expo} + P_{K}^{sc}\ [K]_{bulk}\ t_{expo} \tag{2.2}$$

If ^{36}Cl is to be measured in separated minerals Eq. 2.2 becomes

$$[^{36}Cl]_{estim} = P_{Ca}^{sc}\ [Ca]_{min}\ \frac{\%_{min}}{100}\ t_{expo} + P_{K}^{sc}\ [K]_{min}\ \frac{\%_{min}}{100}\ t_{expo} \tag{2.3}$$

where $[Ca]_{min}$ and $[K]_{min}$ are the target element concentrations in the minerals and $\%_{min}$ is the estimated percentage of minerals that can be separated from the bulk rock for ^{36}Cl extraction.

In this estimation the presence of Cl as a target element and the production from slow negative muons are ignored but both production reactions still augment the ^{36}Cl concentration.

2.2 Physical sample preparation

Before the cosmogenic nuclide can be extracted from the material several physical preparation steps need to be done. The rock material taken in the field is **cleaned** from soil and moss and **dried** if it is still wet. Each sample is **described** according to its alteration, mineral content and porosity, and **photographs** are taken to record their physical aspect (Fig. 2.5). If possible each sample is **chiseled** in order to obtain a homogeneous **thickness**, which is then measured and documented for later calculations. Per sample at least 2 **pieces of rock** of about 3 cm diameter are kept for density determination, chemical analysis of the bulk rock and thin section fabrication.

The density of the bulk rock needs to be known in order to calculate the attenuation of cosmic ray particles in the rock material (Chapter 1.3.4).

- *Determination of the bulk rock density by the Archimedes principle.* The Archimedes principle is based on the fact that an object, immersed in a fluid, is buoyed up by a force equal to the weight of the fluid that is displaced by the object. The weight of the displaced fluid is proportional to the volume of the displaced fluid. Since water has a density of 1 g cm^{-3}, the weight and the volume of the displaced water have the same value. If a beaker full of water is tared on a balance and then a piece of rock of known weight is completely submerged into the water without touching the bottom or the beaker wall the difference in weight gives the volume of the water displaced by the rock, which is equal to the volume of the rock. Hence, the density of the piece of rock is given by:

$$\text{density of rock} = \frac{\text{mass of dry rock}}{\text{difference in mass of filled beaker without and with submerged rock}}$$

Ideally the density is determined on several rock pieces, at least two, since then a mean value can be calculated.

The **chemical analysis of the bulk rock** is necessary, in the case of ^{36}Cl, for the modelling of the low-energy neutron distribution, which is strongly composition depending

Table 2.2: *Examples for bulk rock densities determined with the Archimedes principle. Samples are basaltic rock from Mt. Etna.*

Sample	m (dry) [g]	m (in water) [g]	ρ [g cm−2]
SO1	20.13	8.20	2.45
	13.34	6.01	2.22
	23.73	10.74	2.21
	7.48	3.18	2.35
	7.89	3.47	2.27
			mean 2.30
SO2	15.83	6.53	2.42
	11.53	4.64	2.48
	13.37	5.44	2.46
			mean 2.45
SO3	20.78	8.66	2.40
	32.26	13.75	2.35
			mean 2.38
IS9	34.46	12.47	2.76
	23.44	8.50	2.76
			mean 2.76

(Chapter 1.3.6), and in the case of ^{3}He, for the calculation of the radiogenic ^{4}He and the nucleogenic ^{3}He background (Chapter 1.3.7). For some of the samples of this dissertation (Chapter 4) the whole rock grains after crushing and sieving (see below) were used for the chemical analysis of the bulk. However, since the divers mineralogical phases in the rock might fractionize differently during crushing, a preliminary sorting of those mineralogical phases could occur by sieving to different grain size fractions. A piece of rock of some cm diameter, which will be homogenized before analysis, is therefore considered to be more representative for the samples bulk composition. All chemical analysis were performed at the Service d'Analyse des Roches et Minéraux du CNRS (SARM) at the Centre de Recherches Pétrographiques et Géochimiques (CRPG), Nancy. Major elements were measured by ICP-OES and trace elements by ICP-MS, except Li (atomic absorption), B (colorimetry), H_2O (Karl Fischer titration) and Cl (spectrophotometry).

Thin sections might be useful to identify mineral assemblages. For the study presented in Chapter 4 a thin section was used to locate semi-quantitatively the mineralogical site of high Cl concentrations in the basaltic rock by electron microprobe analysis.

The sample pieces destined for TCN extraction are then **crushed** in a jaw crusher and **sieved** to grain size fractions between 100 and 1000 μm, e.g. 100 - 400 μm, 250 - 500 μm or 500 - 1000 μm. The respective finer and coarser material is kept. ^{36}Cl extractions from different grains sizes resulted in the same ^{36}Cl concentrations (e.g. sample SI29 in the study presented in Chapter 5), which shows that in terms of cosmonuclide yield the grain size is not important. However, separation of phenocrysts (see below) is more efficient the finer the grain size, because most of the minerals break to smaller sizes than their original size in the rock matrix. The grain size range 100 - 400 μm was found to be the most rewarding.

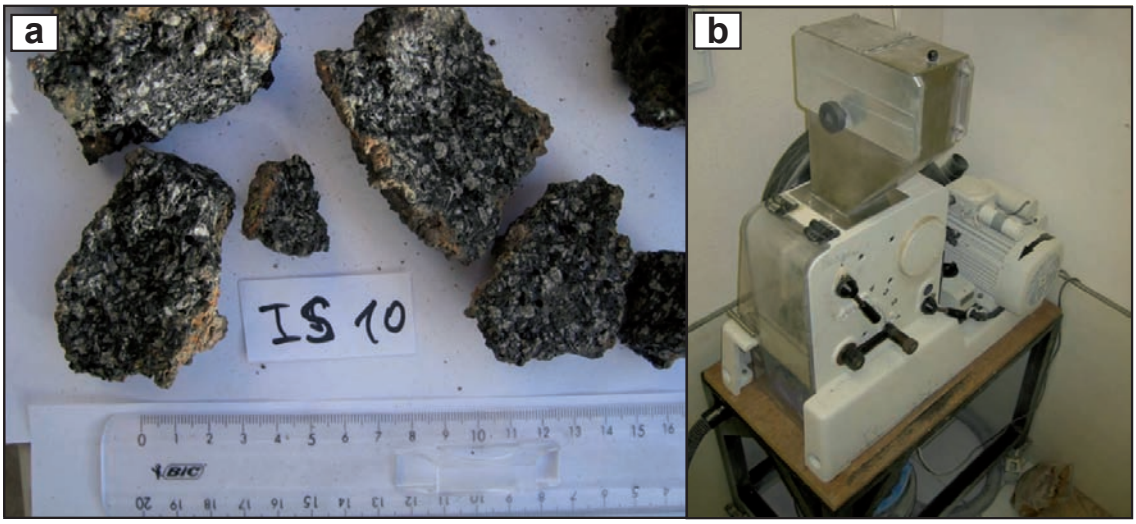

Figure 2.5: *(a) Photographic documentation of basaltic sample from Mt. Etna before crushing. White spots are plagioclase phenocrysts. (b) Jaw crusher at CEREGE.*

Mineral separation

Magnetic mineral separation: If the minerals designated for ^{36}Cl extraction are feldspars they are often the only non-ferromagnetic mineral phase in the lavas and can therefore be separated completely by magnetic methods. First, the most magnetic grains are removed with a handmagnet. This is beneficial since it reduces the sample material and makes the handling with the Frantz magnetic separator easier in the next step. The magnetic separator consists of a large electromagnet through which the grains can be passed on a

Table 2.3: *Things to do during the physical sample preparation before ^{36}Cl and ^{3}He extraction.*

Action	Purpose
Cleaning and drying	
Sample description	Documentation of sample aspect and non-measurable charactersitics
Pictures	Documentation of sample aspect
Chiseling	Homogeneous thickness
Thickness	Needed for calculations
Keep 2-3 pieces of rock	Determination of density, bulk rock composition, thinsections
Density	Needed for calculations
Bulk rock analysis	Needed for calculations
Thin sections	Identification of minerals
Crushing	
Sieving	Obtain certain grain size fraction
Mineral Separation	Isolate target mineral from the remaining rock

metal trough which is divided near its exit end. Varying the strength of the magnetic field and/or slope of the separation trough is used to separate minerals. It is preferential to start with a low current at the Frantz magnetic separator, e.g. 0.3 A, to run the grains through a first separation, recover the less magnetic part, increase the current and run the grains through another separation and so on. This might be repeated several times until the less magnetic parts consists of pure feldspar grains.

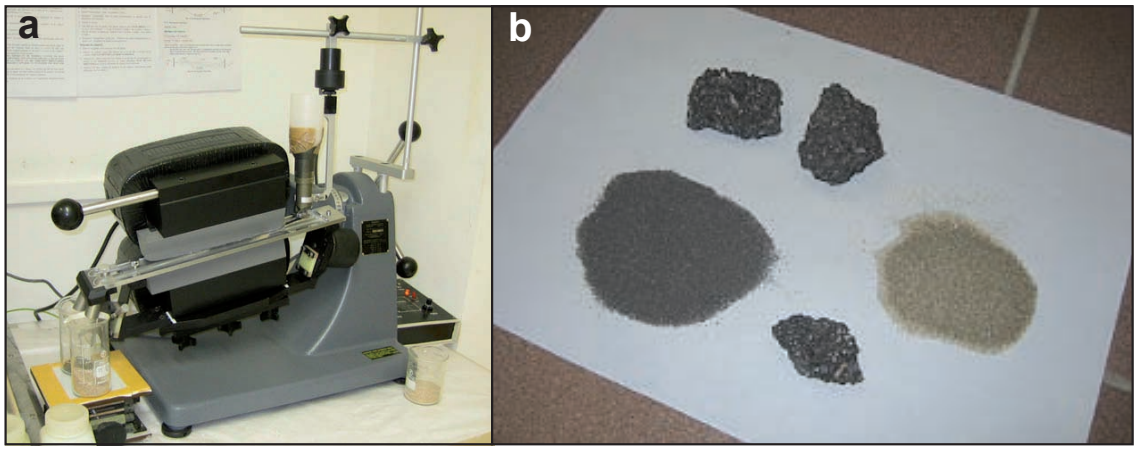

Figure 2.6: *(a) The Frantz magnetic separator at CEREGE. (b) Magnetically separated plagioclases (right) from basaltic whole rock (left).*

Heavy liquids: The principle of mineral separation by heavy liquids is based on the differences of densities between the phases. The sample grains are poured into a separatory

funnel filled with a liquid of known density. The mineral phases having a higher density than the liquid sink to the bottom, while the others stay at the surface. In order to separate the mafic minerals olivine and pyroxene (ρ 3.4 - 3.5 g cm^{-3}) from the basaltic groundmass, bromoform ($CHBr_3$, ρ ~2.9 g cm^{-3}) and/or methylene iodide (CH_2I_2, ρ ~3.3 g cm^{-3}) are used, the latter being more efficient for the separation.

Figure 2.7: *Set-up for mineral separation with heavy liquids. The heavy liquid used here is methylene iodide.*

Hand picking: For noble gas measurements, it is necessary to analyze pure olivine and pyroxene grains without fluid or melt inclusions and without groundmass traces. In addition, the two mineral phases olivine and pyroxene cannot be separated from each other by heavy liquids, since their densities are too similar. Therefore, the grains destined for analysis have to be hand-picked under a binocular microscope with a pair of tweezers (Fig. 2.8).

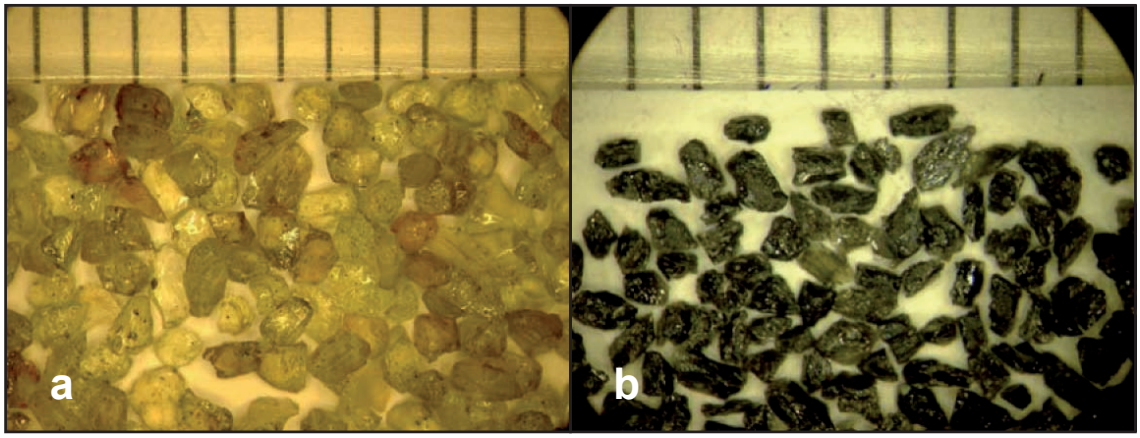

Figure 2.8: *Handpicked olivine (a) and pyroxene (b) from a basalt at Mauna Kea (Hawaii) (pictures from Blard, 2006). Units on the scale in the upper parts of the pictures correspond to 1 mm.*

2.3 Measuring ^{36}Cl

2.3.1 From sample material to AgCl targets: Chemical ^{36}Cl extraction from silicate rocks

The chemical extraction of ^{36}Cl from rocks can be performed in different ways depending on the capacities of the laboratory and the habits and preferences of the user. There is not only *one* correct procedure. The so far most cited protocol for the ^{36}Cl extraction from silicate rocks is that set up at the University of Washington (Stone et al., 1996). Its detailed description is given on the website http://depts.washington.edu/cosmolab/chem.html. From this protocol differing procedures can be found in Zreda et al. (1991) and Desilets et al. (2006a). In these two papers, the procedures are, however, rather roughly explained.

The here described procedure was initially inspired by Stone et al. (1996) but finally differs considerably in some steps. It results from divers experiments, and according to experience it is found to be the most convenient and easiest performance in the ^{36}Cl laboratory at *CEREGE*. It is schematically illustrated in Fig. 2.10. Alternatives to the preferred procedure and differences to the protocol of Stone et al. (1996) are discussed in this section.

Table 2.4: *Silicate rock and mineral types, processed for ^{36}Cl extraction at CEREGE* according to the new chemical protocol described in this chapter, and their principle target element concentrations. "n.d." means not yet determined. The listed samples are either part of this PhD work or were processed in the scope of other studies, for which I trained students and postdoc-researchers to the new ^{36}Cl extraction procedure.

Rock type	Sample site	Ca [wt%]	K [wt%]	Cl [ppm]
Basaltic whole rock	Mt. Etna	6-7	1.3	800-1000
	Fogo	10	1	280-340
	Stromboli	8	2.5	120-1270
	Tibet	n.d.	n.d.	n.d.
Ca-Plagioclase	Mt. Etna (lava)	8	0.5	2-6
	Ascension Island (lava)	8-11	<0.2	n.d.
	Kilimanjaro (lava)	7	0.5	5
	Iran (cristallin bedrock)	7	1	50-70
	Tibet (lava)	15	-	20
	Bolivia (moraines)	3-5	1-2	n.d.
K-Feldspar	Tibet (lava)	1	8	13-120
	Payun Matru, Argentina (lava)	0.5	5	6-14
Ca-Pyroxene	Kilimanjaro (lava)	15	-	3-10

The presented ^{36}Cl extraction is applicable to separated silicate minerals and whole silicate rock. The types of rocks and minerals so far processed at *CEREGE* according to this protocol are listed in Table 2.4.

The procedure will be described for one sample with one blank even though several samples can be processed in one batch with a common blank. The grouping of samples should be chosen in function of their estimated exposure ages (or better beforehand estimated ^{36}Cl concentration, see Chapter 2.1) not to risk cross-contamination between the samples.

In general, during the whole procedure, bottles should be kept covered by their lids as much as possible to avoid contamination from outside or cross-contamination between the samples.

Preparation

For the whole extraction procedure, HDPE bottles (*high density polyethylene*) are used. The use of PTFE bottles (*polytetrafluroethylene*, also known under the brand name *Teflon*)

Figure 2.9: *Parts of the equipment for chemical ^{36}Cl extraction at CEREGE.*

(Stone et al., 1996) was found to be of disadvantage, since they are highly electrostatic after drying and sample grains are often lost when opening the bottles. HDPE bottles do not have this characteristic and were found to be sufficiently acid resistant. However, they are not re-used but thrown away after use. The bottle size depends on the sample amount that will be processed. The right bottle size has to be chosen before starting the procedure by estimating how much acid will be needed to totally dissolve the sample material (see below "Total dissolution").

Two bottles, one for the sample and one for the blank are rinsed with MQ water and dried in the oven for several hours or overnight in order to remove any moisture. When they have cooled down the bottle for the sample is tared and the weight is written down. Then the sample grains are poured into this bottle and weighed.

Chemical pretreatment

Before the sample material is dissolved for ^{36}Cl extraction is has to be pretreated for several reasons.

Firstly, it has to be ensured that the ^{36}Cl and Cl extracted from the rock are not coming from other sources than from the rock itself. Cl is abundantly present in the air, in rain- and sea-water, on the human skin etc., and ^{36}Cl is produced in the atmosphere by spallation of ^{40}Ar. To the best of our knowledge, the only study in which the presence of atmospheric ^{36}Cl in limestone was demonstrated is Merchel et al. (2008a) (Fig. 2.11a). Their experiment showed that a repeated water-leaching is sufficient to decontaminate

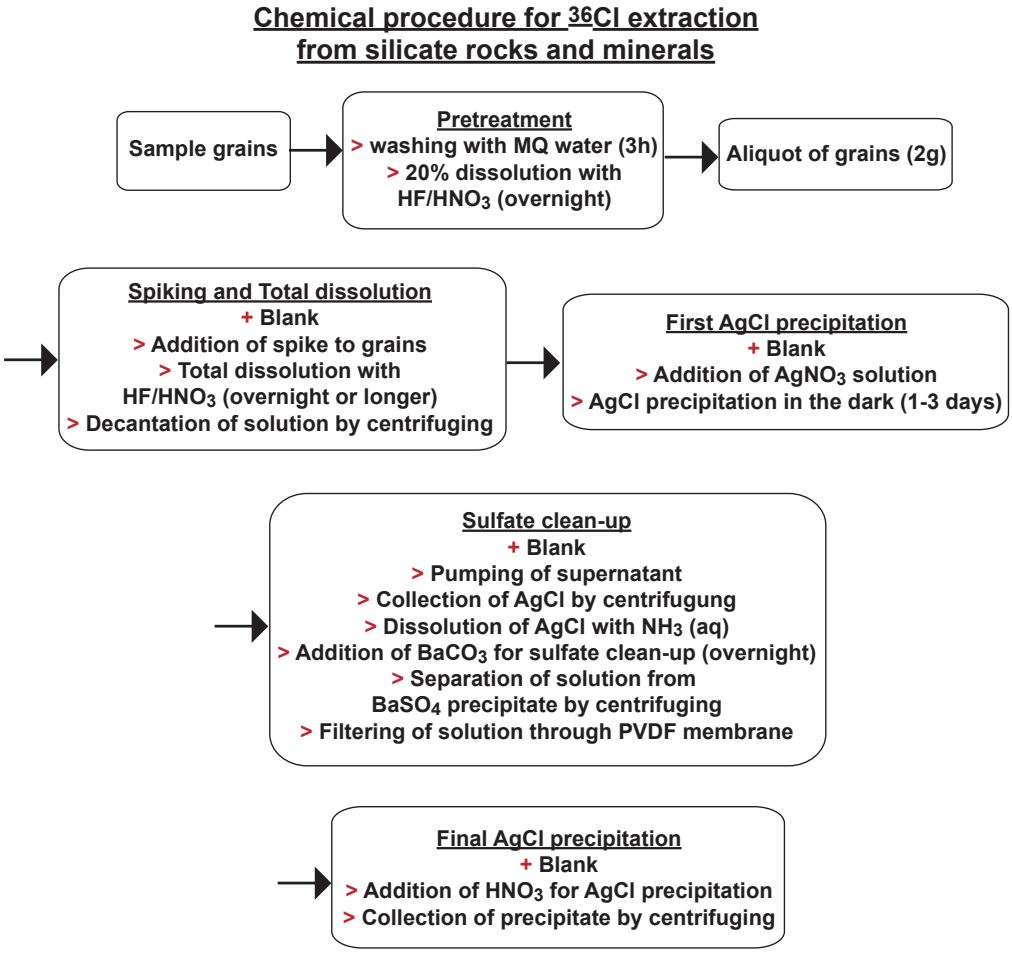

Figure 2.10: *Schema of chemical protocol for ^{36}Cl extraction from silicate rocks and minerals.*

limestone from atmospheric ^{36}Cl, which is due to the hydrophilic nature of Cl. In former studies, atmospheric ^{36}Cl could not be detected (Zreda et al., 1991; Stone et al., 1996; Evans et al., 1997, see Fig. 2.11). Nevertheless, a decontamination step through water and/or dilute HNO_3 leaching is generally performed as a precaution. The issue of atmospheric ^{36}Cl and Cl contamination is further discussed in Chapter 4.5.

The second reason for a chemical pretreatment of the sample material is, in the case of separated minerals, that the purity of the minerals can be increased by a pre-dissolution step. Cl rich parts of the rock such as groundmass or glass can be removed. This is shown in Schimmelpfennig et al. (2009) (Chapter 4), where the Cl concentrations in dissolution steps of the plagioclase grains could be reduced from 450 ppm to less than 3 ppm after 16%

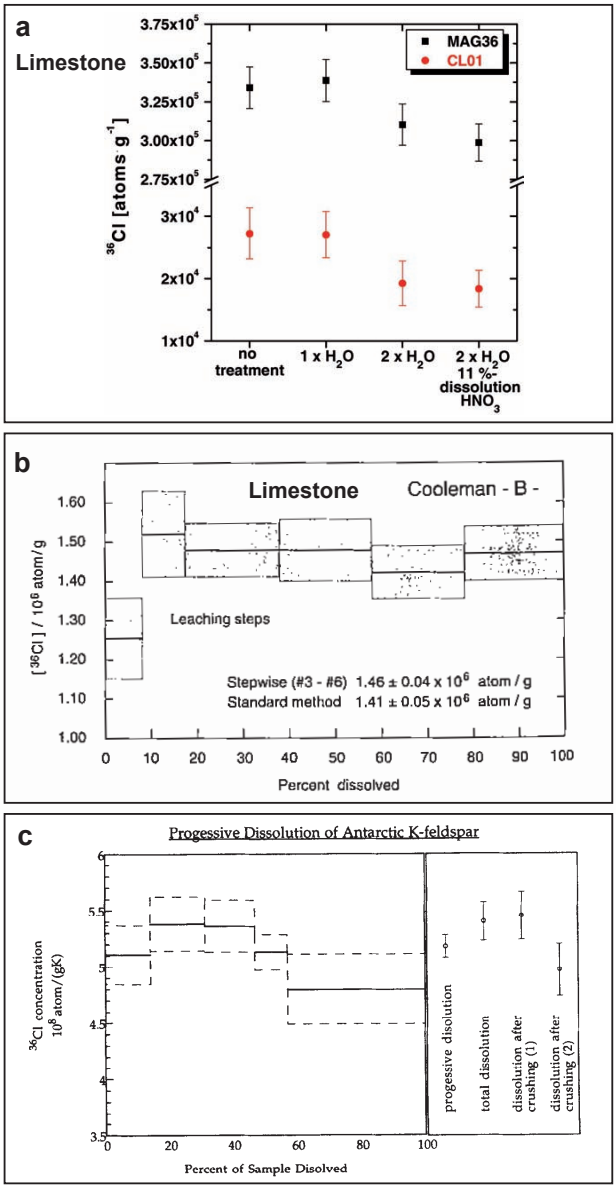

Figure 2.11: *Dissolution experiments with limestone in Merchel et al. (2008a) (a) and Stone et al. (1996) (b) and with K-feldspar (Evans et al., 1997) (c). Merchel et al. (2008a) showed that slightly higher ^{36}Cl concentrations, assigned to an atmospheric component, are extracted from the sample if it is not pretreated or only pretreated with one water leaching. In neither of the other two studies, atmospheric contamination could be observed, which would have been evident from higher ^{36}Cl concentrations in the first dissolution step compared to the following dissolution steps. The low ^{36}Cl concentration in the first step of (b) could be due to a slight lost of in situ ^{36}Cl by natural dissolution of the grain surfaces (Stone et al., 1996).*

dissolution. In the case of whole rock, which is usually much richer in Cl than separated minerals, a strong pre-dissolution can diminish the Cl concentration. The Cl concentra-

tions in the sequential dissolution steps of the whole rock in Chapter 4 decrease gradually.

Based on these findings, the pretreatment of the sample material consists of two steps, a washing with MQ water and a 20% pre-dissolution with a HF/HNO_3 mixture. For the water-washing, MQ water is filled on the top of the sample grains to about 3/4 of the bottle. The closed bottle is put on the shaker table and shaken for about 3 hours. Then, the water is discarded and the powder fraction is flushed out, if necessary by several times rinsing with MQ water. The sample grains in the bottle are dried overnight in the oven at 80°C and weighed when cooled down. The sample weight lost during the water-washing can be determined (usually 2-5%).

For the 20% pre-dissolution, the sample grains are wetted with some water, then 0.72 ml diluted HNO_3 (10%) per g sample is added. HNO_3 dissolves carbonates, e.g. potential calcite precipitations in cracks and hole of the rock, and oxidizes organic material and metal. It has also a security function: If HNO_3 gets on the skin it causes a pain, so that a contact with the acid is noticed immediately. The contact with HF, on the other hand, is not perceived until it reacts with the bone. This characteristic renders it extremely dangerous.

In the next step, HF is added to the sample grains. It must have a very high purity grade (e.g. MERCK "suprapur®" brand HF), because less pure acids could have significant amounts of Cl and ^{36}Cl and thus contaminate the sample as shown in Fig. 2.12.

HF can react violently, especially if the sample is a whole rock. Apart from danger for the user, the problem is that if heat and fume develops during the heavy reaction Cl might be volatilized in form of neutral HCl (Desilets et al., 2006a). At this stage this would be less problematic but is an issue for the total dissolution step. To slow down the reaction the bottle is put in an ice bath while adding the HF. 0.36 ml concentrated HF (40%) per g of sample is very slowly added. This amount of HF dissolves approximately 20% of the sample material. It was initially calculated stoichiometrically for a *anorthite* (Ca-plagioclase) according to the equation

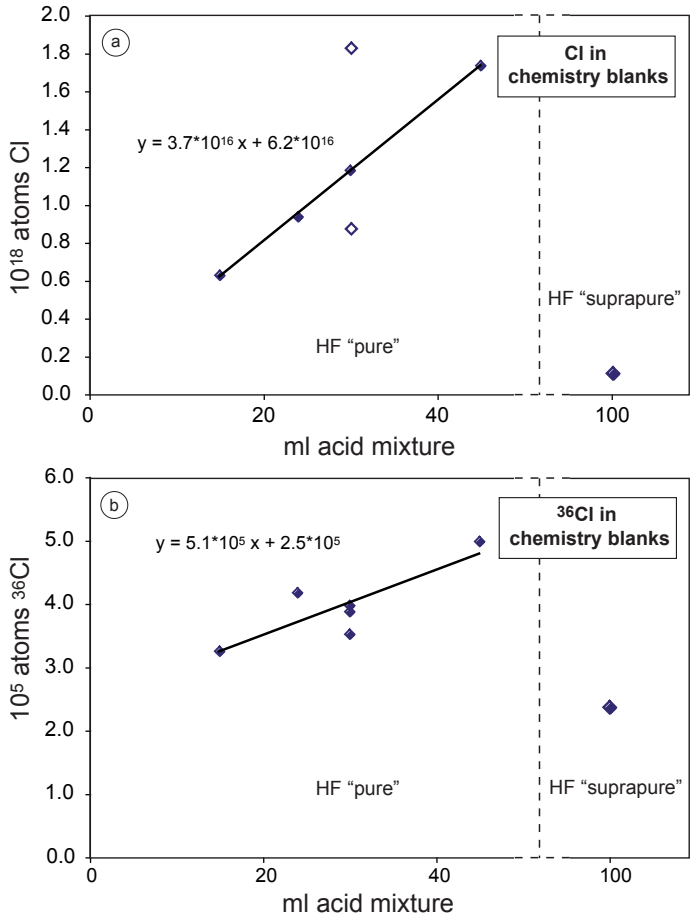

Figure 2.12: *Absolute numbers of (a) atoms Cl and (b) atoms ^{36}Cl in chemistry blanks versus ml of acid mixture (one part HF, conc., two parts HNO_3, 10%). On the left side of both plots, HF brand Chimie-Plus Laboratoires reagent grade "pure" was used, on the right side, HF brand MERCK "suprapur®" was used. The linear relationship on the left side indicates that HF "pure" contains significant amounts of Cl and ^{36}Cl. Open symbols are considered as outliers. In this case, the blank correction of the sample has to be done in function of the amount of acid used to dissolve the sample.*

$$6HF + CaAl_2Si_2O_8 \rightarrow 2H^{2+} + SiF_6^{2-} + SiO_2 + 4O^{2-} + Ca^{2+} + 2Al^{3+} + 2H_2O \quad (2.4)$$

Finally an average value was adjusted from experiments with different silicate materials. Therefore, adding 0.36 ml concentrated HF (40%) per g of sample does not always dissolve exactly 20% of the material, but can dissolve more or less. This depends on the sample composition, its reactivity and the time of dissolution. The closed bottle is then put in a plastic zip bag and shaken overnight on the shaker table at 190 rpm. The plastic bag

serves as a protection if acid leaks out of the bottle. The bottle should be put upright on the shaker table to avoid that acid that stayed in the lid drops out when the bottle will be opened.

During the dissolution steps the solution is not heated as it is done in Stone et al. (1996). This is mainly because it was found that dissolution works well without heating and the handling with the cold HF solution is much more confortable and less dangerous. Additionally, HDPE bottles can not stand temperatures higher than 110°C and might melt on the hotplate if they get too hot. If heating was necessary PTFE bottles should be used.

The next day, the acid mixture is decanted and discarded into the acid waste, and the grains are rinsed several times (at least three times) with a lot of MQ water (at least the volume of the grains). This water is also discarded into the acid waste. Then the grains are dried overnight in the oven at 80°C and weighed when cooled down. The sample weight lost during the pre-dissolution step can be determined.

Spiking and total dissolution

An aliquot of about 2 g has to be taken with a spatula from the pretreated grains for the determination of the target element concentrations that correspond to the part of rock from which the ^{36}Cl is extracted. The remaining sample grains are weighed again and the weight has to be written down.

From now on, the procedure blank is prepared simultaneously to the processing of the sample by treating the bottle, which was prepared for the blank in the beginning, as if it had sample grains.

Spike solution enriched in ^{35}Cl or ^{37}Cl is added to the sample bottle and to the blank bottle. It has two functions. Firstly, it allows determining the concentrations of both ^{36}Cl and Cl in the sample simultaneously from one AMS measurement by the principle of *isotope dilution*, which is explained in Chapter 2.3.3. Secondly, it acts like a *carrier*, which means that a known amount of Cl is added providing that the final AgCl target (see below) is big enough to be measured by AMS (Chapter 2.3.2). Typically, 1.5 mg Cl is sufficient to yield enough AgCl (4 - 5 mg). If the Cl concentration of the spike solution is 3 mg/g, then a mass of 0.5 g spike solution has to be weighed per sample to add 1.5 mg Cl. The

solution is weighed very carefully in small vials and the exact weight is written down.

The spike can be added before or after the addition of the acid mixture to dissolve the sample grains. It is, however, crucial that neither spike-Cl is lost before complete dissolution of the sample nor sample solution is lost before adding the spike (Desilets et al., 2006a). Only if the ratio of spike-Cl to sample-Cl is maintained throughout the whole extraction, accurate ^{36}Cl and Cl concentrations in the sample material can be determined. When the isotope ratios are measured later (Chapter 2.3.2) it is assumed that spike and sample solution were completely homogenized without any loss. Adding the spike before the acids might result from a lost of spike-Cl if the acids react heavily with the sample grains and heat and fume develops resulting in volatilization of Cl in form of neutral HCl molecules (Desilets et al., 2006a). These authors could show, though, that closed-vessel and open-vessel methods for ^{36}Cl extraction from carbonate rock yield the same exposure ages, when adding the spike before dissolution, i.e. spike-Cl is not lost by volatilization. Adding the spike before the total dissolution is therefore more advisable than after the dissolution when the sample solution has been centrifuged and recovered (see below). Losing some of the sample solution during the handling before spiking is more likely than volatilization of spike-Cl. Another advantage of adding the spike before the acids is that the handling is easier, because the weighed spike solution can be poured immediately into the bottles (sample and blank) next to the balance. If the acids are already in the bottles, they should not be opened outside of the fume hood and the weighed spike solutions have to be carried to the fume hood.

For the total dissolution of the sample grains, the procedure is very similar to the 20% pre-dissolution: First the sample grains are wetted with some water, then 9 ml diluted HNO_3 (10%) per g sample are added. When the sample bottle is in the ice bath, 4.5 ml concentrated HF (40%) per g sample are added very slowly. This amount of acid is about 2.5 times more than would be stoichiometrically needed to dissolve the sample grains. This is to have better chances that the material dissolves completely. The amounts of acids used should be written down, especially when using the acids for the first time, in case that a contamination of the acids is identified (see Chapter 4.2.2). Since here much more acid is

used compared to the pretreatment, almost always heat develops while adding the acids to the sample. This is especially the case if the sample is a whole rock, because certain parts of the rock such as groundmass and glass react rapidly with HF. It is therefore very important to add the HF slowly in small quantities checking from time to time at the outside of the bottle if the sample heats up and if so to let it cool down for a moment. The lid should be put on the bottle (does not have to be screwed) to avoid any contamination. At the same time while adding the HF, the bottle should be carefully swirled from time to time to allow all grains to get in contact with the acid and to avoid that fluoride gel forms, coats the grains and clumps together. The fluoride gel consists of insoluble compounds, mainly CaF_2. When the addition of HF is complete, the lid is put on the bottle but not screwed, and the bottle is swirled from time to time, leaving it in the ice bath and waiting that it has cooled down. As soon as no heat develops anymore, the bottled is closed, put in a plastic zip bag and shaken on the shaker table at 190 rpm at least overnight. Here again the solution is not heated for reasons of easier handling and security.

The procedure blank is prepared before or after the sample. Ideally about the same amount of acid should be used for the blank as for the sample. However, if in a batch with several samples different amounts of acid are used because the sample weights vary or if a lot of acid is needed for the sample then the blank can be prepared with less amount of acid. Since there is no reaction in the blank bottle it does not have to be put in the ice bath and the acids can be poured at once.

The next day, it should be checked if the sample grains dissolved completely. In the case of felspars, it is probable that the grains have already completely dissolved. Pyroxene and quartz need more time. And also whole rock samples might have some minerals that dissolve more slowly than others. In that case, the dissolution should be continued. If for example the day after no dissolution progress can be observed the solution can be decanted (see next paragraph) and more acid can be added to the remaining grains to try to dissolve them.

50 ml centrifuge tubes for the sample and for the blank are labeled and rinsed with MQ water. If there are doubts that they are clean they can also be rinsed with a few ml

very dilute HNO_3 and MQ water. If the sample is very big and a lot of solution has to be decanted several centrifuge tubes can be prepared for one sample. The bottles are taken from the shaker table and the solutions are carefully poured into the tubes. It has to be payed attention that the right solution is always poured in the corresponding tube. Then the filled tubes are centrifuged for 5 minutes at 3000 rpm. If sample solution remains in the bottle it should be put on the shaker table again and shaken while waiting for the centrifuge to finish. This is again to avoid that the fluoride gel clumps. In the meanwhile new HDPE bottles are prepared for the sample and for the blank by rinsing them with MQ water (or dilute HNO_3 and MQ water) and labeling them. When the centrifuge has finished the solutions are decanted from the tubes to the corresponding new HDPE bottles, which will be stored in the fume hood with the lid closed while the remaining solutions are centrifuged.

The procedure is continued until no solution remains in the first bottles. Each time, the same tubes can be used for centrifuge. However, the fluoride gel from the total dissolution will accumulate more and more on the bottom of the tube and possibly fill up the tube so that each time less solution can be poured in the tube. In this case a new tube can be used for the sample solution. If undissolved grains remain on the bottom of the bottle it should be tried not to pour them into the tubes but to recover them. This can be done by rinsing them rigorously when the solution transfer is complete, drying them in the oven and weighing them. Often most of the particles left after drying come from the fluoride gel. It has to be decided, in function of how much material is left and if the particles are really sample grains, if the sample weight dissolved for the ^{36}Cl extraction has to be corrected for the remaining grains. If the weight of the material is insignificant compared to the initial sample weight a correction is not necessary. If enough undissolved grains remain they should be analysed for their composition to determine correctly the target element concentrations that correspond to the ^{36}Cl concentration of the part of sample dissolved.

If the sample has not been spiked until now the spike solution should at this stage be added to the centrifuged sample solution. Before that, the fluoride gel in the tubes should be washed to ensure that all the chlorine extracted from the sample is recovered.

The gel, especially if centrifuged several times will be very compact and stiff. It can be carefully broken up with a plastic spatula before adding the MQ water to wash it using the vortex. If the sample was spiked before the dissolution the gel does not necessarily have to be rinsed. If some of the Cl is not recovered this does not have any effect on the later measured isotope ratios which is fixed since the spike and the sample solution have been mixed. However, if there are doubts that enough AgCl can be yielded from the solution (see next step) the gel might be rinsed in either case.

First AgCl precipitation

To precipitate AgCl, 2 ml of a $AgNO_3$ solution (10% in 2N HNO_3) are added to the sample and to the blank solutions. The amount of silver added should be in excess to ensure that all the Cl will be precipitated. Here again, adding the $AgNO_3$ solution is performed without heating in contrast to the protocol of Stone et al. (1996) because the AgCl yield is high enough without heating, and handling of the dangerous HF solution is easier. Usually, a white cloud starts to form when the $AgNO_3$ solution has been added. The closed bottle is swirled and stood in a dark place for at least one day, better two or three. Standing the bottles in a dark place is necessary because the white AgCl is sensitive to light. If it is exposure to light for a long time it dissociates to Ag (metal) and Cl. The first indication of this dissociation can be seen after a short time when the AgCl precipitate starts to turn violet. Silver metal is black.

Sulfate clean-up

After one to three days in a dark place all the silver should have reacted with the chlorine in the solution to precipitate AgCl, which has settled on the bottom of the bottle. However, the silver does not only react with Cl but also with S and other elements. Since ^{36}S causes isobaric interferences during the ^{36}Cl AMS measurement (Chapter 2.3.2) the precipitate has to be cleaned from sulfur.

50 ml centrifuge tubes are labeled and rinsed for the sample and for the blank. The supernatant in the HDPE bottles is now pumped away under the fume hood using a peristaltic pump. It has to be payed attention that the precipitation at the bottom of the bottle is not disturbed or partly pumped away. A bit of the solution can stay at the

bottom, about 1 cm height. The precipitate is resuspended in this remaining solution and transferred into the centrifuge tube. If necessary the bottle is rinsed with a few ml of water until no AgCl remains. 1-2 ml of NH_3(aq) solution (NH_3 : H_2O = 1 : 1) can be added to the bottle to dissolve remaining AgCl.

The tubes of the sample and the blank are centrifuged and the supernatant is discarded into the acid waste. The precipitate is rinsed by adding about 3 ml MQ water to the tube, washing it using the vortex, centrifuging and discarding the solution. 1-2 ml NH_3(aq) solution and the solution in the HDPE bottle are added to the precipitate to dissolve it, using the vortex. Then 1 ml saturated $Ba(NO_3)_2$ solution is added to the solution, mixed and stood in the fume hood overnight with the cap left loose on the tube. Hereby, $BaSO_4$, $BaCO_3$ and other compounds precipitate from the solution. Leaving the tubes unscrewed allows an exchange with the air, which makes easier the precipitation of $BaSO_4$ together with $BaCO_3$ due to the supply of CO_2 from the atmosphere.

The next day, 15 ml centrifuge tubes are rinsed and labeled. The 50 ml tubes with the solutions are centrifuged. To separated the cleaned solution from the precipitate, the supernatant is filtered through an "acrodisc" filter with 0.45μm PVDF membrane into the 15 ml tube using a sterile syringe. The $BaSO_4$/$BaCO_3$ precipitate can be rinsed with 2 ml of water and 2 drops of NH_3(aq) using the vortex, centrifuging and filtering it again through the syringe into the tube. This step might be necessary if only little AgCl precipitates in the next step, which is usually not the case.

Final AgCl precipitation

To the solution in the 15 ml tubes 2-3 ml dilute HNO_3 (conc. HNO_3 : H_2O = 1 : 1) are added. The amount of acid depends on the reaction. As soon as adding the acid results in forming a white cloud in the tube, another ml should be added. Swirling the solution in the tube by using the vortex results in the formation of white AgCl flocs.

If the AgCl does not precipitate, NH_3(aq) should be added again to the 50 ml tube in which the $BaSO_4$/$BaCO_3$ was precipitated. It is possible that the AgCl has not completely dissolved in the last step or precipitated again during the sulfate clean-up. The tube is then centrifuged and the solution filtered through the syringe with the "acrodisc" filter

into the 15 ml tube. Dilute HNO_3 is added and AgCl should now precipitate.

The precipitate settles completely down in the dark for one night. The next day the tubes are centrifuged, the supernatants are discarded and the precipitates are rinsed twice with MQ water by adding about 3 ml MQ water to the tubes, washing them using the vortex, centrifuging and discarding the solutions.

Small black sample vials are labeled and weighed and the weights are written down. The wet AgCl precipitates are carefully transferred into the sample vials with the help of long plastic spatulas. The precipitates are dried at 80°C overnight and weighed the next day when they have cooled down. The weight is usually between 4 and 5 mg. It should have at least 0.5 mg to be measured by at the LLNL-CAMS facilities.

2.3.2 From AgCl targets to isotope ratios: ^{36}Cl measurement by Accelerator Mass Spectrometry

The ^{36}Cl measurements presented in this PhD study were performed with the 10 MV FN Tandem Van de Graaff Accelerator at Lawrence-Livermore National Laboratory - Center for Accelerator Mass Spectrometry (LLNL-CAMS). In this chapter the AMS technique is described with emphasize on ^{36}Cl measurement.

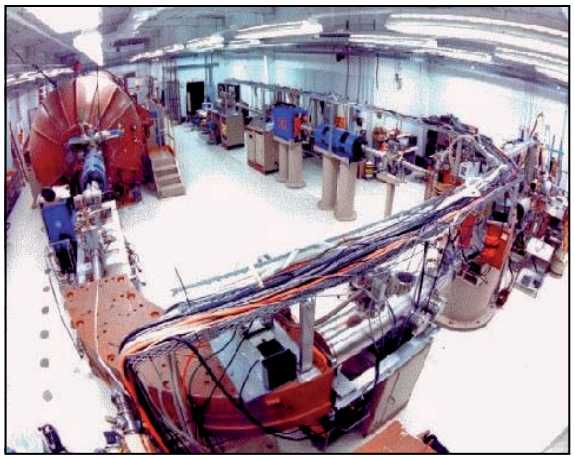

Figure 2.13: *Measurement facilities at LLNL-CAMS.*

The principle of AMS is similar to that of conventional mass spectrometry. In both techniques isotope ratios are measured, after ionization of the sample, acceleration of the ion beam and separation of the ions in function of their mass and charge in a magnetic

field. The difference is that AMS can measure very small quantities of isotopes with high sensitivity because it accelerates ions to extraordinarily high kinetic energies (tens of MeV) by using a tandem accelerator (Elmore and Phillips, 1987; Finkel and Suter, 1993). This allows measuring long-lived radionuclides such as the cosmogenic nuclides ^{10}Be, ^{14}C, ^{26}Al, ^{36}Cl, ^{41}Ca and ^{129}I, whose half-lives are too long to be measured by decay counting and too short to be abundant enough for the conventional mass spectrometry technique (Muzikar et al., 2003).

The target material used for the measurement is a compound containing the nuclide of interest, which was extracted chemically from the rock sample. In the case of ^{36}Cl this is AgCl (Chapter 2.3.1). Since only fractions of the target material can be analyzed, it is not possible to determined absolute abundances of the nuclide in a sample. Instead, isotope ratios are measured, which is the number of ions of the rare (radioactive) isotope to the number of ions of an abundant (stable) isotope of the same element. For ^{36}Cl this means ^{36}Cl/^{35}Cl and ^{36}Cl/^{37}Cl. These ratios range usually between 10^{-14} and 10^{-12}.

At the high energy produced by the accelerator, various steps during the measurement process allow effectively eliminating unwanted nuclides such as molecules and isobars that cause interferences with the nuclide of interest. These steps and the principle of AMS will now be illustrated on the basis of Fig. 2.14, the numeration below corresponding to the numbers in the figure.

1) Ion sputter source. The target material being loaded in the ion sputter source is bombarded with cesium ions (Cs^+) to produce a negative ion beam. Electric fields in the ion source provide that only negative ions are transported in the ion beam, i.e. atoms not forming negative ions are seperated out such as ^{36}Ar, which otherwise would be an isobar for ^{36}Cl (Muzikar et al., 2003).

2) First magnetic mass analyzer. The negative ion beam is accelerated to 40-100 keV by an electric field and passes through a first magnetic mass spectrometer. Here, the ions are deflected in function of their mass and charge. Only ions having a certain value

of ME/q^2 (M: mass, E: kinetic energy, q: charge) are selected and continue the track. The intensity of ions with masses similar to that of the isotope of interest can thus be considerably reduced.

3) Electron stripper in tandem accelerator. In the first half of the accelerator ("tandem van de Graaff accelerator") the ions are accelerated to the high voltage terminal where the electron stripper is situated. The stripper is a low density gas or a thin carbon foil, which removes electrons from the ions passing through. Hereby, negative ions are turned to positive ions and molecular isobars are destroyed, which allows the removal of their fragments in the next step. In the case of ^{36}Cl measurements, energies on the order of 7 MeV are needed to produce Cl^{+7} ions (Muzikar et al., 2003).

4) a) Second magnetic mass analyzer. After being accelerated again in the second half of the accelerator the positive ions pass through a second magnetic mass spectrometer. Again certain ions are selected according to their ME/q^2 value. **b) Electrostatic deflector.** Since molecules were broken up in the accelerator and charges changed during previous processes, a small continuous background of species with various energy and charge state combinations is present, so that unwanted ions may have the same ME/q^2 value as the isotope of interest. Therefore, an electrostatic deflector is often additionally included, rejecting ions with unwanted E/q values.

5) Detector. Finally, the ions are identified in a detector system, the rare isotopes are counted in a gas counter or in a solid state detector and the electrical currents of the stable isotopes in faraday cups. In this last step, ^{36}S, a so far not rejected isobar of ^{36}Cl, can be reduced if it is not too abundant: The gas detector measures the energy loss of the ion per unit distance of its passage through the gas, which depends on the atomic number Z of the element. ^{36}S ($Z = 16$) loses its kinetic energy at a slower rate than ^{36}Cl ($Z = 17$) allowing to distinguish their energy-loss spectra (Muzikar et al., 2003). Energies of 40-80 MeV are required for the separation of ^{36}S and ^{36}Cl which are obtained with tandem accelerators

operating at 6-10 MV (Finkel and Suter, 1993).

Simultaneously to the $^{36}Cl/^{35}Cl$ or $^{36}Cl/^{37}Cl$ ratio, the "stable ratio" is determined, which is the isotope ratio of the two stable Cl isotopes $^{35}Cl/^{37}Cl$. This is possible because the currents of both stable isotopes are individually measured in two different faraday cups in the detector region.

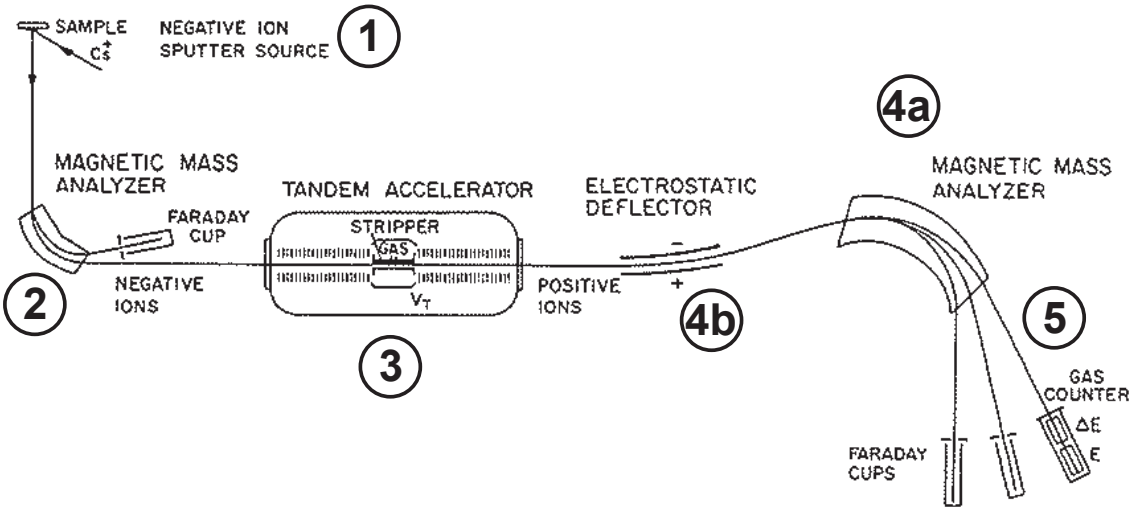

Figure 2.14: *Schematic configuration of a facility for Accelerator Mass Spectrometry after Finkel and Suter (1993). The sample is bombarded with Cs ions in the ion sputter source to produce a beam of negative ions of the nuclide of interest (1). Accelerated to 40-100 keV, the negative ion beam passes through the magnetic mass analyzer (2). In the first half of the tandem accelerator, the ions are accelerated to a high energy (several MeV). In the central part of the accelerator (terminal) the beam passes through a gas or foil stripper that turns the negative ions into positive ions by removing several electrons from the ions (3). In the second part of the accelerator the beam is again accelerated to a high energy. It passes through another magnetic (4a) and usually through an electrostatic mass analyzer (4b). The stable isotopes are measured in form of an electrical current in the faraday cups, while the rare isotope is counted one atom at a time, usually by a gas-ionization detector (5).*

Corrections for drifts and background

During the time of the measurement, drifts due to machine environment changes can occur, and the two isotopes of the measured ratio, e.g. $^{36}Cl/^{35}Cl$, might be subject to different ionization and transmission conditions. These irregularities are reflected in the isotope ratio of a known standard material measured along with the samples (Fig. 2.15). The deviations determined from the measurement of the standard are used for the correction of the measured ratio of the sample in order to obtain the true isotope ratio (Finkel and Suter, 1993).

The mimimum isotope ratio that can be measured and the minimum number of atoms that can be detected is limited by the *background*. The background has two origins: One is a contamination with the isotope of interest and its stable isotope(s) coming from sources other than the sample itself, e.g. from the chemicals used during the extraction procedure (Chapter 2.3.1) or from the machine. Therefore, a procedure blank is processed during the chemical preparation of the sample whose measured ratio is used for the correction of the sample (Chapter 2.3.3). Also, cross-contamination can occur in the ion source, e.g. for ^{36}Cl measurements when the sputter region is not well pumped (Finkel and Suter, 1993). The other origin of the background is due to particles reaching the detector, because they have not been eliminated on their track through the machine, and being wrongly detected as the nuclide of interest. To reduced this background risk as much as possible for the measurement of ^{36}Cl, where ^{36}S is the most problematic isobar, a special sulfur cleaning step is performed during the chemical preparation of the sample (Chapter 2.3.1).

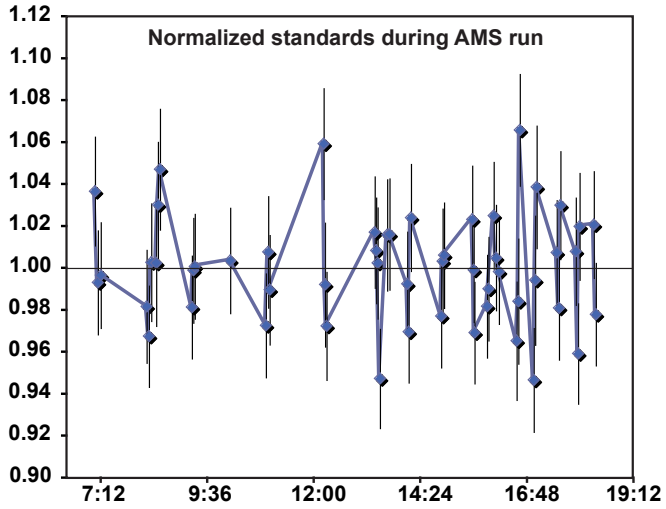

Figure 2.15: *Standards measured during the ^{36}Cl run on 26 January 2008 between 7 am and 7 pm at LLNL-CAMS. The standard material was prepared by K. Nishiizumi (Sharma et al., 1990). Individual values are normalized to the theoretical value of the standard material. Error bars correspond to σ. No outliers can be identified and no drift is observed during the time of measurement.*

Precision and accuracy

To increase the accuracy of the measurement, systematic errors due to machine drifts and contamination are reduced by the measurement of standards and blanks (previous

paragraph). Additionally, high counting rates are needed for the measurement of the $^{36}Cl/^{35}Cl$ and $^{36}Cl/^{37}Cl$ ratios to reach low statistical errors and high accuracy. Therefore, it has to be ensured that enough ^{36}Cl is extracted from the rock material (Chapter 2.1) and that enough AgCl is loaded in the target holder. At least a few mg of AgCl are needed to have sufficient target material to get high enough counting rates. If sufficient target material is loaded but the isotope level is low, the counting statistic can be improved by longer measurement time. The statistical uncertainty (standard deviation σ) of the number of counts N is determined by $\sqrt{N}$, implying that the higher N the lower σ. The statistical uncertainty of the stable ratio $^{35}Cl/^{37}Cl$ is determined from the standard deviation of the mean value of usually three repeated measurements.

2.3.3 From isotope ratios to ^{36}Cl and Cl concentrations: ^{36}Cl Data analysis

Both ^{36}Cl and Cl concentrations of a sample can be determined simultaneously from one AMS measurement due to the performance of *isotope dilution* AMS (Chapter 2.3.2). For this, a *spike* with a $^{35}Cl/^{37}Cl$ ratio different to the natural one (=3.1271) and with a known Cl concentration is added to the sample during the dissolution procedure (Chapter 2.3.1). The $^{35}Cl/^{37}Cl$ ratio of the spike is guaranteed by the laboratory where it is produced (Fig. 2.16) The principle of isotope dilution is explained in Fig. 2.17. In literature Ivy-Ochs et al. (2004) and Desilets et al. (2006a) address this subject for ^{36}Cl measurements.

In the following, it will be explained how ^{36}Cl and Cl concentrations are derived from isotope ratios measured by AMS. The isotope ratios resulting from the AMS measurements are in the form of $^{35}Cl/^{37}Cl$ and $^{36}Cl/^{35}Cl$ or $^{36}Cl/^{35}Cl$, depending on if the spike used is enriched in ^{35}Cl or in ^{37}Cl. In order to convert the measured isotope ratios into ^{36}Cl and Cl concentrations the following information is necessary: the relative abundance of atoms ^{35}Cl and ^{37}Cl in the spike [%], the Cl concentration of the spike solution [mg/g], the amount of spike solution weighed for the sample [g] and the rock sample weight dissolved for the extraction [g]. For the procedure blank correction, the measured isotope ratios of the blank and the amount of spike solution used for it have to be known.

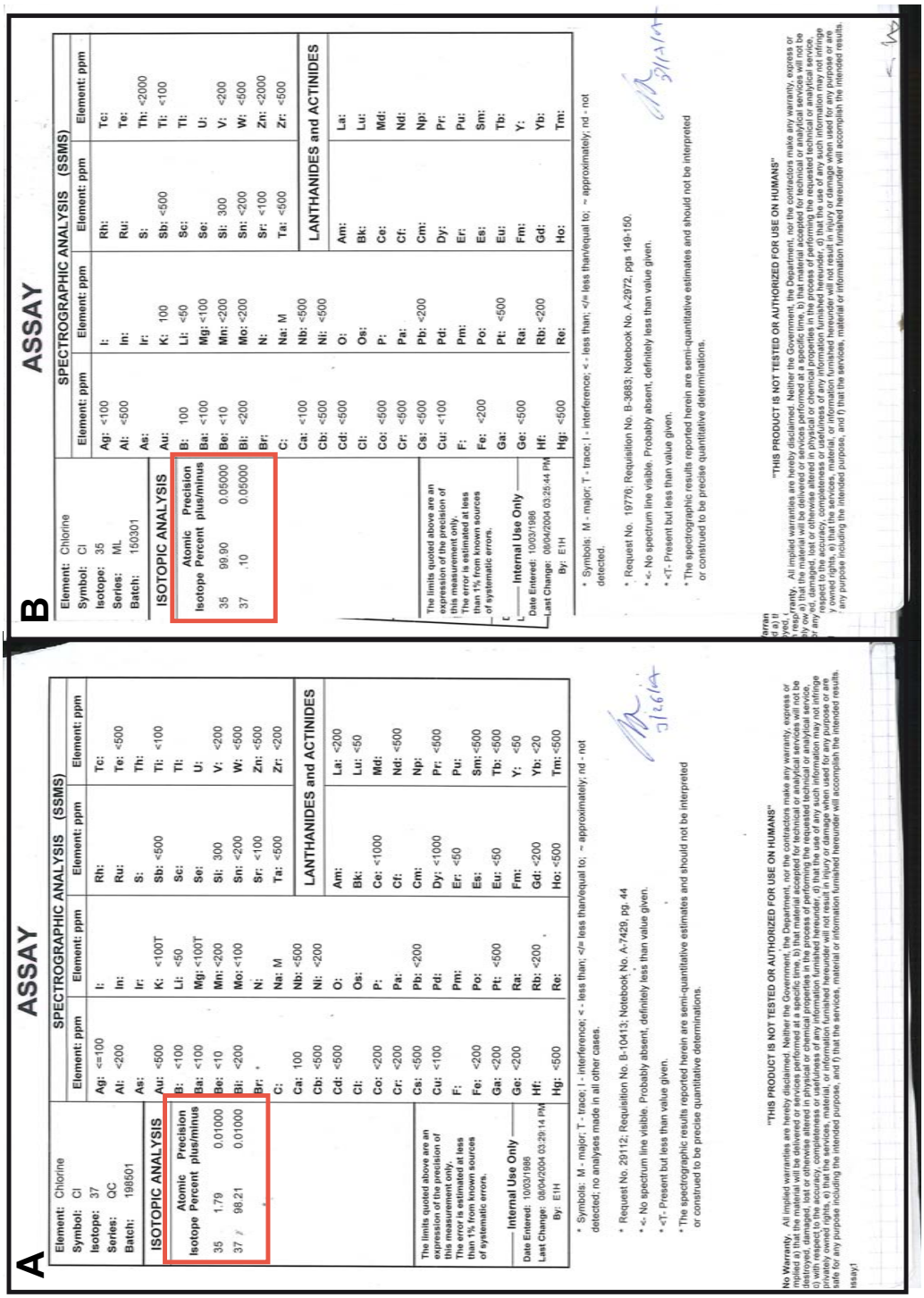

Figure 2.16: *Certificates provided by OakRidge National Laboratory for delivered spikes enriched in ^{37}Cl (A) and ^{35}Cl (B). Guaranteed relative concentrations of each isotope with the corresponding precisions are highlighted by the red-framed fields.*

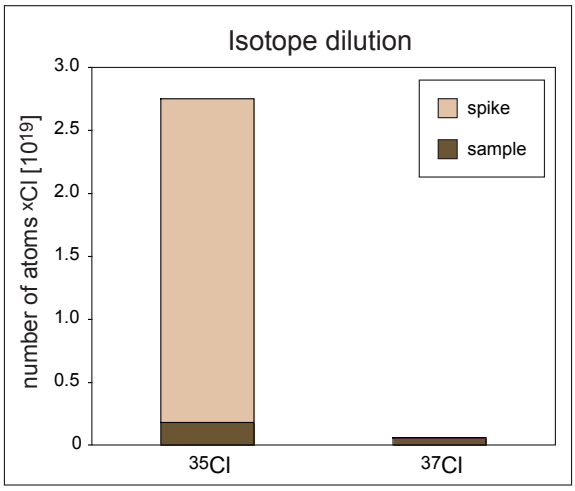

Figure 2.17: *Principle of isotope dilution. The spike, having a known Cl content and a $^{35}Cl/^{37}Cl$ ratio different to the natural one, allows determining the natural Cl content in the sample. The natural $^{35}Cl/^{37}Cl$ ratio is always 3.1271 (= 75.77% ^{35}Cl + 24.23% ^{37}Cl). Here, the spike $^{35}Cl/^{37}Cl$ ratio is 999 (= 99.9% ^{35}Cl + 0.1% ^{37}Cl). The measured ratio, which is a mixture of natural and spike ratio, lies between the two values; in this example, it is 45.9. The exact value of the measured ratio depends on the natural Cl content in the sample: the more natural Cl is in the sample (i.e. the heights of both dark brown columns would increase keeping their proportions) the closer the measured ratio gets to the natural ratio 3.1. This dependence allows calculating the natural Cl content in the sample (see Eqs. 2.8 to 2.12).*

Below, the following notation will be used:

m_{sp}^{Cl}: mass of Cl in spike solution [mg]

m_{sp}: mass of spike solution [g]

m_{nat}^{Cl}: mass of Cl in the sample [mg]

m_{diss}: mass of sample dissolved for ^{36}Cl extraction [g]

$[Cl]_{sp}$: Cl concentration in spike solution [mg/g]

$[Cl]_{nat}$: Cl concentration in the sample [ppm]

$[^{36}Cl]_{nat}$: ^{36}Cl concentration in the sample [atoms ^{36}Cl/(g sample)]

N_{sp}^{Cl}: number of atoms Cl in the spike solution

N_{nat}^{Cl}: number of atoms Cl in the sample

N_{sp}^{35}: number of atoms ^{35}Cl in the spike solution

N_{sp}^{37}: number of atoms ^{37}Cl in the spike solution

N_{nat}^{35}: number of atoms ^{35}Cl in the sample

N_{nat}^{37}: number of atoms ^{37}Cl in the sample

N_{nat}^{36}: number of atoms ^{36}Cl in the sample MM_{sp}: molar mass of Cl in spike [g]

MM_{nat}: molar mass of Cl in nature (35.4572 g)

MM_{35}: molar mass of ^{35}Cl (34.96885 g)

MM_{37}: molar mass of ^{37}Cl (36.9659 g)

Av: number of Avogadro (6.022×10^{23})

$\%_{sp}^{35}$: relative abundance of ^{35}Cl in the spike

$\%_{sp}^{37}$: relative abundance of ^{37}Cl in the spike

$\%_{nat}^{35}$: relative abundance of ^{35}Cl in nature (75.77%)

$\%_{nat}^{37}$: relative abundance of ^{37}Cl in nature (24.23%)

$R_m^{35/37}$: measured ^{35}Cl/^{37}Cl ratio

$R_{sp}^{35/37}$: ^{35}Cl/^{37}Cl ratio in the spike

$R_{nat}^{35/37}$: ^{35}Cl/^{37}Cl ratio in nature (3.1271)

$R_m^{36/35}$: measured ^{36}Cl/^{35}Cl ratio

The determination of the Cl concentration in the sample is possible due to the spike added, since the spike has a ^{35}Cl/^{37}Cl ratio different to the natural one (=3.1271) and its Cl content N_{sp}^{Cl} can be calculated:

$$m_{sp}^{Cl} = m_{sp}\ [Cl]_{sp} \tag{2.5}$$

$$N_{sp}^{Cl} = \frac{m_{sp}^{Cl}\ 10^{-3}}{MM_{sp}} Av \tag{2.6}$$

The molar mass of Cl in the spike MM_{sp} is calculated:

$$MM_{sp} = \%_{sp}^{35}\ MM_{35} + \%_{sp}^{37}\ MM_{37} \tag{2.7}$$

The measured ^{35}Cl/^{37}Cl ratio of the spiked sample $R_m^{35/37}$ is a mixture of the unknown natural Cl content N_{nat}^{Cl} in the sample with the known natural ^{35}Cl/^{37}Cl ratio $R_{nat}^{35/37}$ and the known Cl content in the spike N_{sp}^{Cl} with the known ^{35}Cl/^{37}Cl ratio in the spike $R_{sp}^{35/37}$ (Fig. 2.17). This can be expressed as:

$$R_m^{35/37} = \frac{N_{nat}^{35} + N_{sp}^{35}}{N_{nat}^{37} + N_{sp}^{37}} \tag{2.8}$$

N_{nat}^{35} and N_{nat}^{37} are both unknown but their known relationship to N_{nat}^{Cl} ($N_{nat}^{35} = N_{nat}^{Cl}\ \%_{nat}^{35}$ and $N_{nat}^{37} = N_{nat}^{Cl}\ \%_{nat}^{37}$) can be used to calculate the Cl concentration in the sample:

$$R_m^{35/37}\ N_{nat}^{37} + R_m^{35/37}\ N_{sp}^{37} = N_{nat}^{35} + N_{sp}^{35} \tag{2.9}$$

$$R_m^{35/37}\ N_{nat}^{Cl}\ \%_{nat}^{37} + R_m^{35/37}\ N_{sp}^{Cl}\ \%_{sp}^{37} = N_{nat}^{Cl}\ \%_{nat}^{35} + N_{sp}^{Cl}\ \%_{sp}^{35} \tag{2.10}$$

$$N_{nat}^{Cl}\ \%_{nat}^{35} - R_m^{35/37}\ N_{nat}^{Cl}\ \%_{nat}^{37} = R_m^{35/37}\ N_{sp}^{Cl}\ \%_{sp}^{37} - N_{sp}^{Cl}\ \%_{sp}^{35} \tag{2.11}$$

$$N_{nat}^{Cl} = N_{sp}^{Cl}\ \frac{R_m^{35/37}\ \%_{sp}^{37} - \%_{sp}^{35}}{\%_{nat}^{35} - R_m^{35/37}\ \%_{nat}^{37}} \tag{2.12}$$

Eqs. 2.8 to 2.11 are the intermediate steps to derive the calculation of N_{nat}^{Cl} with the help of *isotope dilution* (Eq. 2.12).

At this stage, the *procedure blank correction* is done: The number of atoms Cl in the blank is calculated in the same way as the number of atoms Cl in the sample and is subtracted from N_{nat}^{Cl}.

The number of atoms Cl in the sample N_{nat}^{Cl} is then converted into the mass of Cl m_{nat}^{Cl} and into the Cl concentration $[Cl]_{nat}$ in the sample in *ppm*:

$$m_{nat}^{Cl} = \frac{N_{nat}^{Cl}\ 10^3}{Av}\ MM_{nat} \tag{2.13}$$

$$[Cl]_{nat} = \frac{m_{nat}^{Cl}\ 10^3}{m_{diss}} \tag{2.14}$$

Now, based on the knowledge of the Cl content in the sample, the ^{36}Cl concentration $[^{36}Cl]_{nat}$ can be calculated. Here, it is assumed that a spike enriched in ^{35}Cl is used, the measured ^{36}Cl/(stable Cl) is then ^{36}Cl/^{35}Cl. (If a spike enriched in ^{37}Cl was used, the measured ^{36}Cl/(stable Cl) would be ^{36}Cl/^{37}Cl.) The number of atoms ^{36}Cl in the sample is then:

$$N_{nat}^{36} = R_m^{36/35} \ (N_{sp}^{Cl} \ \%_{sp}^{35} + N_{nat}^{Cl} \ \%_{nat}^{35}) \tag{2.15}$$

The number of atoms ^{36}Cl in the procedure blank is calculated in the same way and subtracted from the result in Eq. 2.15 for the *procedure blank correction*. This includes also a potential correction for a ^{36}Cl contamination in the spike since the blank is spiked with the same amount of spike as the sample (Chapter 2.3.1).

The ^{36}Cl concentration is calculated as *number of atoms* ^{36}*Cl/(g sample)*:

$$[^{36}Cl]_{nat} = \frac{N_{nat}^{36}}{m_{diss}} \tag{2.16}$$

The ^{36}Cl concentration serves to calculate surface exposure ages and erosion rates (Chapter 3).

More about procedure blank correction:

When ^{36}Cl and Cl are extracted from a rock sample, different chemicals are used (Chapter 2.3.1), which might themselves have certain amounts of ^{36}Cl and Cl and thus "contaminate" the AgCl target and falsify the results of the extraction procedure. The idea of performing a procedure blank is to determine how much Cl and ^{36}Cl comes from the chemicals, so that the sample measurement can be corrected for this contamination. As described in this section, the procedure blank correction for both Cl and ^{36}Cl is done in terms of number of atoms, which means that the number of atoms Cl and ^{36}Cl, relatively, in the blank is subtracted from that in the sample.

Subtracting the measured ratio of the blank $R_{blank}^{36/(stableCl)}$ from the measured ratio of the sample $R_m^{36/(stableCl)}$ is not correct, which will now be shown by means of the ^{36}Cl/^{37}Cl ratios of sample and blank (i.e. both spiked with a ^{37}Cl enriched spiked).

When measuring a sample AgCl target, the ^{36}Cl isotopes counted and the ^{37}Cl isotopes detected in the faraday cups of the AMS (Chapter 2.3.2) come from various sources, from the rock material (index *rock*), from the spike (index *sp*) and from the chemicals (index *chem*). This can be expressed as

$$R_m^{36/37} = \frac{N_{rock}^{36} + N_{chem}^{36}}{N_{rock}^{37} + N_{chem}^{37} + N_{sp}^{37}} \tag{2.17}$$

It has to be mentioned that the spike itself can be contaminated with ^{36}Cl or natural Cl. This contamination is accounted for in N_{chem}^{36} and N_{chem}^{37}, the number of atoms ^{36}Cl and ^{37}Cl, respectively, in the chemicals. This is because in terms of contamination the spike is considered as a chemical. The number of atoms ^{37}Cl coming from the spike N_{sp}^{37} is calculated theoretically by means of its certified ^{35}Cl/^{37}Cl ratio and of its calculated Cl concentration based on the assumption that the spike is not contaminated.

When measuring the AgCl target of the procedure blank the ^{36}Cl and ^{37}Cl isotopes come only from the chemicals and from the spike:

$$R_{blank}^{36/37} = \frac{N_{chem}^{36}}{N_{chem}^{37} + N_{sp}^{37}} \tag{2.18}$$

Comparing the two equations 2.17 and 2.18 it becomes clear that the two ratios $R_m^{36/37}$ and $R_{blank}^{36/37}$ do not have the same denominator; in the case of the sample, the total number of atoms ^{37}Cl is a sum of ^{37}Cl in the rock, in the chemicals and in the spike, whereas in the blank ^{37}Cl only comes from the chemicals and from the spike. This means that the number of atoms ^{36}Cl in sample and blank are not normalized to the same value and can therefore not be subtracted from each other. This would only be possible if the sample had no natural Cl, which is rarely the case.

2.4 Measuring ^{3}He

2.4.1 ^{3}He by Noble Gas Mass Spectrometry

The ^{3}He measurements presented in this PhD study were undertaken by Alice Williams and Samuel Niedermann at the noble gas laboratories at the Centre de Recherches Pétrographiques et Géochimiques (CRPG), Nancy, and Geoforschungszentrum (GFZ), Potsdam. Measurements were made using the GV instruments Helix Split Flight Tube and Helix Multicollector mass spectrometers at CRPG, and using a VG5400 mass spectrometer at GFZ.

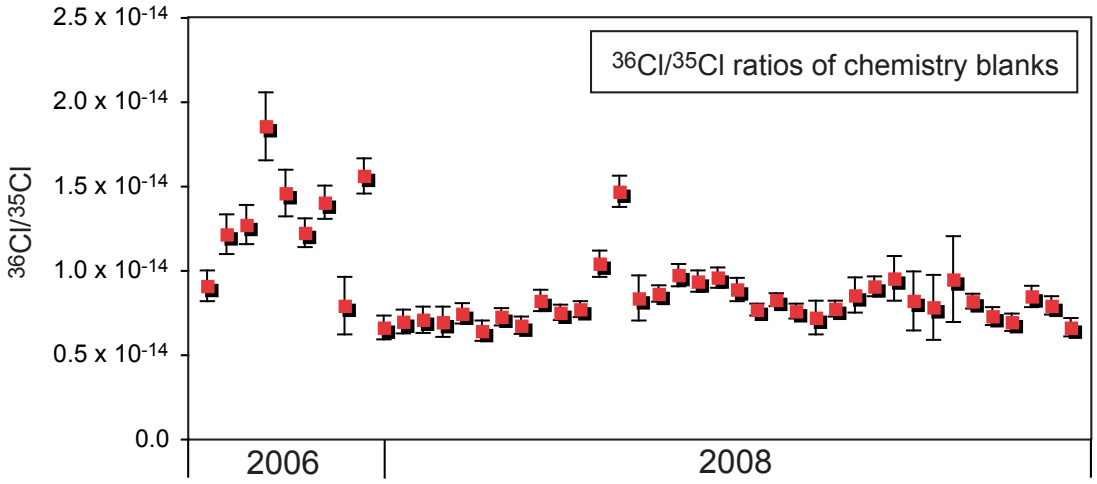

Figure 2.18: *$^{36}Cl/^{35}Cl$ ratios of chemistry blanks processed at CEREGE and measured at LLNL-CAMS in 2006 and 2008. These blanks were propared by 5 different lab users. High ratios in 2006 are mainly due to contaminated chemicals (see Fig. 2.12). In 2008, ratios are constant with a mean value of 0.84 × 10^{-14}.*

The measurement of one sample consists of two extraction steps. In the first step, ^{3}He and ^{4}He in fluid and melt inclusions are measured by in vacuo crushing, allowing the magmatic ^{3}He/^{4}He ratio of the samples to be determined, necessary for the correction of the magmatic ^{3}He component (Chapter 1.3.7).

Approximately 1 g of pure, hand-picked phenocryst separates are loaded into steel tubes and an iron-slug inserted into the tube above the sample. The loaded crushing tubes and gas purification line are then baked at 100°C overnight. The following day, once the equipment has cooled to room temperature, the iron-slug is activated by solenoids and the sample crushed over a 2 minute period, at a rate of approximately 100 strokes/min. After crushing, the gas was expanded into the purification line. Firstly, it was cleaned over 20 minutes using a charcoal-finger, cooled with liquid nitrogen to -180°C. By adsorption, the charcoal traps most of the H_2O, CO_2 and the heavy hydrocarbons as well as O_2, N_2 Cl_2, and the heavy noble gases Xe, Kr and Ar. Secondly, a chemical getter traps by chemisorption H_2, the residual CO, CO_2 and the hydrocarbons.

After purification, the gas is expanded into the mass spectrometer where ^{3}He and ^{4}He isotope concentrations are measured simultaneously and the magmatic ^{3}He/^{4}He deter-

mined. Procedural blanks are performed in an identical manner but using empty crushing tubes.

In the second step, the total ^{3}He and ^{4}He present in the crystal lattice is measured by high-temperature crystal fusion ($^3He_{fusion}$ and $^4He_{fusion}$).

100 - 250 mg of pure phenocryst separates, lightly hand-crushed to 0.5 mm to avoid loss of cosmogenic ^{3}He (Blard et al., 2006), are cleaned in acetone then wrapped in either Cu-foil (CRPG) or Al-foil (GFZ) and loaded into a sample carrousel positioned above a high-temperature resistance furnace. The sample carrousel and purification line are then brought to vacuum using a turbo molecular pump and baked over several days at approximately 110°C to remove adsorbed gases and H20. Next, the extraction furnace is degassed by gradual increase of the furnace temperature to 1700°C. Cold and hot (800°C and 1700°C) furnace blanks are then performed to ensure adequate furnace degassing and low ^{4}He and ^{3}He blanks. For sample analysis, different extraction methods are used at the two laboratories. At CRPG, the furnace temperature is increased to 800°C and the sample drops into the furnace. Over 20 minutes, the furnace temperature is increased to 1600°C. Samples are fused at 1600°C over a 15 minute period, then the furnace temperature reduced back to 800°C. Gases are then expanded into the purification line and cleaned and analysed in the same manner described for crush extractions. A second extraction, and if necessary a third extraction at 1600°C, ensure total extraction of He from the sample. At GFZ, samples are first heated to 900°C and measured, and then a second extraction is performed at 1750°C.

The sensitivity of the mass spectrometers to different gas pressures is determined by analyzing aliquots of a standard gas with known He isotopic composition.

After each extraction step, the purified gas is conducted into the mass spectrometer, where the electric field of the magnetic mass analyzer separates the ions of the isotopes ^{3}He and ^{4}He. The ^{3}He peak is separated from HD at mass 3 and the ^{3}He ions are measured in an electron multiplier detector (in counts per second). ^{4}He ions are detected in a Faraday cup and the amplitude of the ^{4}He peak is measured in Volts. The electronic background in both detectors is measured and subtracted from the ^{3}He and ^{4}He signals.

To convert the measured signals into atomic abundances of ^{3}He and ^{4}He, the mass spectrometer sensitivity, the dilution coefficient and the mass spectrometer blanks are taken into account.

To inter-calibrate laboratories, measurements of the CRONUS pyroxene He standard, "P", were undertaken at CRPG and GFZ . The resulting $^3He_{cos}$ concentrations were (4.95 $\pm$ 0.10) $\times$ 10^9 at g^{-1} at CRPG (mean of 6 analyses), and 4.97 $\pm$ 0.21 $\times$ 10^9 at g^{-1} on the VG5400 at GFZ (mean of three analyses).

2.4.2 ^{3}He Data analysis

Assuming that the initial magmatic ^{3}He/^{4}He is homogeneous within crystal lattice and fluid inclusions, i.e. $(^3\text{He}/^4\text{He})_{crush} = (^3\text{He}/^4\text{He})_{magmatic}$, and that there is no contribution from radiogenic ^{4}He, the cosmogenic ^{3}He component [atoms g^{-1}] can be computed

$$^3He_{cosm} =^3 He_{fusion} -^4 He_{fusion} \, (^3He/^4He)_{crush} \tag{2.19}$$

The radiogenic ^{4}He can be neglected for U/Th-poor minerals in young volcanic rocks. In older rocks and in U/Th-rich minerals, a contribution from radiogenic ^{4}He in the crystal lattice must be expected.

For the ^{3}He data in Chapter 6, a correction for the radiogenic ^{4}He component was made according to Blard and Pik (2008).

Chapter 3

From ^{36}Cl concentrations to surface exposure ages and erosion rates: A new Excel calculation spreadsheet

If the cosmogenic ^{36}Cl concentration N_{meas} and the rock- and site-specific total production rate P_{total} of a sample are known (Chapter 1.3.4), its exposure age t_{expo}, if no erosion and inheritance is considered, is given by

$$t_{expo} = \frac{-ln(1 - N_{meas}\ \lambda_{36}/P_{total})}{\lambda_{36}} \tag{3.1}$$

with λ_{36} the decay constant of ^{36}Cl equal to $2.303 \times 10^{-6}\mathrm{a}^{-1}$.

Unlike the other cosmogenic nuclides most frequently used to quantify surface processes (^{10}Be, ^{26}Al, ^{3}He, ^{21}Ne), ^{36}Cl is produced by numerous and relatively complicated production mechanisms, their contributions strongly depending on the composition of the rock (Chapter 1.3.6). When determining ^{36}Cl exposure ages, consideration of all these production mechanisms is necessary to obtain accurate results. The complex production mechanism due to capture of low-energy-neutrons by ^{35}Cl in particular requires extensive calculations (Chapters 1.3.3 and 1.3.6). So far, the only complete calculator for such calculations was CHLOE (CHLOrine-36 Exposure program) (Phillips and Plummer, 1996), available on request from the authors. It is a large Excel file which includes computation for shielding and scaling factors, geometry and snow correction, banana plots and conver-

sion of measured ratios to ^{36}Cl concentrations. It has however several drawbacks including (1) that it is not user-friendly for someone who is not fully versed in the intricacies of ^{36}Cl and cosmogenic nuclide methodology, and (2) it can only calculate the ^{36}Cl production in a bulk whole rock, i.e. it does not differentiate between the composition of the bulk rock to calculate the low-energy neutron flux and the composition of the target fraction to calculate the ^{36}Cl production (Chapter 1.3.6).

The lack of a comprehensible and straightforward calculator for ^{36}Cl exposure ages and erosion rates was therefore the motivation for the creation and publication of a new calculator that can easily be used by non-experts. The use of ^{36}Cl for geomorphologic problems is thereby facilitated to a broad community of scientists studying surface processes.

The here presented ^{36}Cl calculator integrates the complete ^{36}Cl computations given in Appendix A and is published as supplementary data in Schimmelpfennig et al. (2009) (see Appendix B for the link to the online version).

3.1 Particularities of the new ^{36}Cl calculator

The particularities of this calculator are:

- It differentiates between bulk rock composition and target fraction composition, which is necessary for correct computation of low-energy neutron flux in the bulk rock and ^{36}Cl production in the part of rock dissolved for ^{36}Cl extraction (Chapter 1.3.6).

- Calculations for shielding, scaling and correction factors are not integrated, what keeps the spreadsheet clear and handy. These factors will be input as numbers calculated by other means. Various possibities exist to do these calculations in external sources (e.g. via the CRONUS-Earth online calculators http://hess.ess.washington.edu/).

- The conversion of isotope ratios measured by AMS into ^{36}Cl concentrations (Chapter 2.3.3) is not integrated, since these calculations depend in some cases on the AMS facility used (e.g. at PRIME lab Purdue ratios are given as ^{36}Cl/Cl, whereas at

LLNL-CAMS and ETH Zuerich are given as $^{36}Cl/^{35}Cl$ or $^{36}Cl/^{37}Cl$). Also, the procedure blank correction might need special attention in some cases (Chapter 2.3.3).

- The transparency of the calculations is kept in the spreadsheet, since no macros are used and no links to others files are inserted. This allows that the calculations can be understood and changed by the user if necessary. Also individual parameters such as reference production rates can be easily changed.

- The integration of newly developed calculations for sample thickness correction factors (Schlagenhauf et al., 2009) provides that the computations are possible for deeper samples and eroding surfaces. The corresponding calculations in Gosse and Phillips (2001) are only valid for surface samples without erosion.

3.2 What can we do with it?

Based on the input of a number of sample relevant information, the new ^{36}Cl calculation spreadsheet allows calculating the ^{36}Cl exposure age of a sample from an uneroded or an eroding surface or the erosion rate for an eroding surface. It also affords the prediction of the relative contributions from the various ^{36}Cl production mechanisms. This provides the opportunity to assess precisely how relevant one or another production mechanisms is in a sample as done in Chapters 4, 5 and 6. Finally, depth profiles showing the vertical distributions of the total calculated ^{36}Cl concentration and the sample-specific production rates are generated automatically. The calculated ^{36}Cl concentration curve can be fitted to measured ^{36}Cl concentrations in a depth profile by adjusting free parameters such as the exposure age and/or the erosion rate to reconstruct the exposure history of the surface.

The spreadsheet works for any rock type and any composition and for whole rocks and separated minerals.

3.3 How to use it?

The Excel file consists of three worksheets.

The first worksheet comprises detailed instructions on how to use the spreadsheet, references and a legend, which explains the meaning of colors used for certain cells on the second and third worksheets. The second worksheet contains the part where the sample relevant information will be input, the output for a surface sample and the complete calculations for a surface sample. The third worksheet displays the depth profiles generated automatically according to the sample specific input on the second worksheet and it contains the part where the measured ^{36}Cl concentrations in a depth profile will be input.

1- Input	symbol	units	calculations	Uncertainties	Ca
(and output for eroding surfaces)					bu
element concentration in bulk rock: major element as oxides [wt-%] and trace elements [wt-ppm]					
					tar
element concentration in target fraction: major element as oxides [wt-%] and Cl in [wt-ppm]					
uncertainty target element concentration in target fraction (oxides in [wt-%] and Cl in [wt-ppm])					
depth reference: top of sample		cm	0		
sample thickness		cm	15		
bulk rock density	rho	g cm^{-3}	2,37		
mass depth reference: center of sample	z	g cm^{-2}	17,775		
mass thickness	z_s	g cm^{-2}	35,55		
scaling factor for nucleonic production as a function of elevation, latitude (and temporal variations)	$S_{el,s}$, $S_{el,n}$	-	4,553	0,228	
scaling factor for muonic production as a function of elevation, latitude (and temporal variations)	$S_{el,\mu}$	-	2,308	0,115	
correction factor for shielding of a sample of arbitrary orientation by surrounding topography	S_T	-	1	0,01	
correction factor for geometry effects on spallogenic production	S_{shape}	-	1	0,03	
correction factor for snow shielding for spallogenic production	S_{snow}	-	1	0,01	
effective fast neutron attenuation coefficient	Λ_{sp}	g cm^{-2}	177		
estimated ^{36}Cl concentration from inheritance at t_{expo}=0	$N_{inher}(0)$	atoms ^{36}Cl g^{-1}			
measured ^{36}Cl concentration in sample	N_{meas}	atoms ^{36}Cl g^{-1}	2,47E+05	11325	
exposure duration (independently determined or estimated)	t_{expo}	a	10000	3000	
formation age of rock (independently determined or estimated) for radiogenic correction	t_{form}	a	20000	1000	
erosion rate	ε	mm ka^{-1}	0	0	

Figure 3.1: *Detail of box 1 "Input" on the second worksheet in the Excel calculation spreadsheet. The yellow cells are input cells. This cutout shows the input in vertical direction, which is related to the non-compositional sample relevant information.*

Input

All yellow cells in the files are input cells. The sample relevant information has to be input at the top of the second worksheet, in box 1 "Input". The input cells arranged in vertical direction concern all the information, which is not related to the composition of the sample (Fig. 3.1): depth of sample, sample thickness, bulk rock density, scaling and correction factors, the effective fast neutron attenuation length, the estimated inherited ^{36}Cl concentration, the measured ^{36}Cl concentration and its uncertainty, the estimated or

independently determined exposure duration and formation age of the rock and the erosion rate of the surface. Input cells in horizontal direction are composition related (Fig. 3.2). Major and trace elements of the bulk rock have to be input in the upper line and the concentrations of the target elements in the target fraction and their uncertainties have to be input in the lower lines (major elements as oxides in wt-% and trace elements in wt-ppm).

More input cells are in box 6, where the sample specific ^{36}Cl production due to spallation is calculated (Fig. 3.3). Here, the different values for the SLHL production rates of the various target elements and their uncertainties can be chosen or changed. Suggestions from literature are made in comment fields.

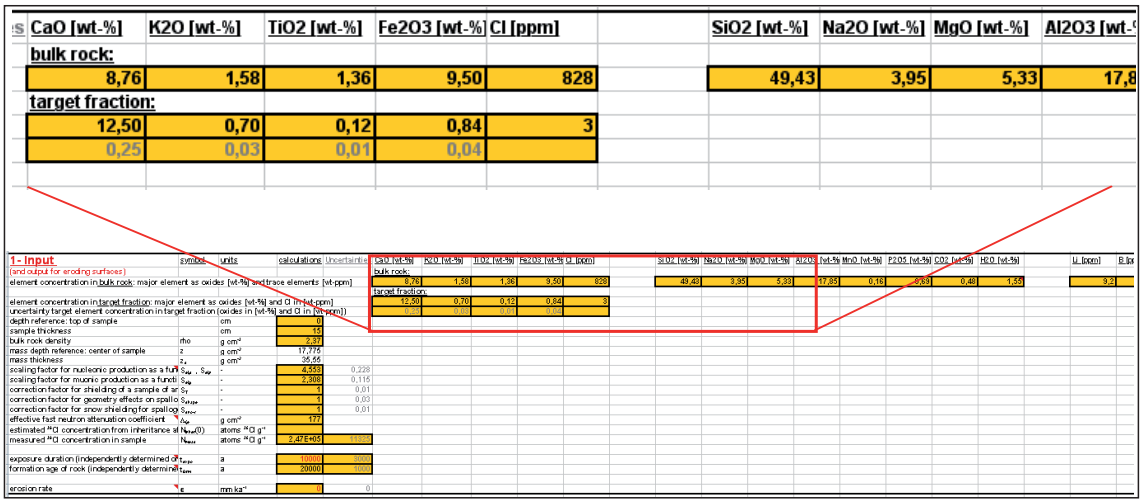

Figure 3.2: *Details of box 1 "Input" on the second worksheet in the Excel calculation spreadsheet. The yellow cells are input cells. The upper panel shows a part of the input in horizontal direction, the compositional sample relevant information. The upper line contains the bulk rock composition and the two lower lines are for the input of concentrations of the target elements Ca, K, Ti, Fe and Cl. Major element input as oxides in wt-% and trace element input in wt-ppm.*

Output

All blue cells are output cells. Box 2 is the "Output A" (Fig. 3.4), which displays the resulting exposure age for an uneroded surface, also called the *apparent age*, meaning that all potential complexities of the exposure history such as erosion, inheritance or burial are ignored. The uncertainty of this exposure age results from propagation of the uncertainties

6- unscaled sample specific ^{36}Cl production rate by spallation of target elements				
spallation production rate for Ca, SLHL	PR$_{Ca}$		can be chosen from literature, e.g. 48.8±3.4 Stone et al. (1996) 66.8±6.8 Phillips et al. (2001)	3,4
mass concentration of Ca in **target fraction**	C$_{Ca}$			0,002
result unscaled ^{36}Cl production by spallation of ^{40}Ca	**P$_{s,Ca}$**			0,286
spallation production rate for K, SLHL	PR$_{K}$	atoms ^{36}Cl (g K)$^{-1}$	162	25
mass concentration of K in **target fraction**	C$_{K}$	g K (g rock)$^{-1}$	0,006	0,000
result unscaled ^{36}Cl production by spallation of ^{39}K	**P$_{s,K}$**	atoms ^{36}Cl (g K)$^{-1}$	**0,847**	0,131
spallation production rate for Ti, SLHL	PR$_{Ti}$	atoms ^{36}Cl (g Ti)$^{-1}$	13	3
mass concentration of Ti in **target fraction**	C$_{Ti}$	g Ti (g rock)$^{-1}$	0,001	0,000
result unscaled ^{36}Cl production by spallation of Ti	**P$_{s,Ti}$**	atoms ^{36}Cl (g Ti)$^{-1}$	**0,009**	0,002
spallation production rate for Fe, SLHL	PR$_{Fe}$	atoms ^{36}Cl (g Fe)$^{-1}$	1,9	0,200
mass concentration of Fe in **target fraction**	C$_{Fe}$	g Fe (g rock)$^{-1}$	0,006	0,000
result unscaled ^{36}Cl production by spallation of Fe	**P$_{s,Fe}$**	atoms ^{36}Cl (g Fe)	**0,010**	0,001
result unscaled sample specific ^{36}Cl production rate by spallation of target elements	**P$_{s}$**	atoms ^{36}Cl (g)$^{-1}$ a	**4,811**	0,314

Figure 3.3: *Box 6 "unscaled sample specific ^{36}Cl production rate by spallation of target elements" on the second worksheet in the Excel calculation spreadsheet. The reference SLHL production rates and their uncertainties can be changed in the yellow input cells. Suggestions from literature are given in the comment fields.*

in the target element concentrations (except Cl), the measured ^{36}Cl concentration, the SLHL production rates, all correction and scaling factors, and of 10% uncertainty in the ^{36}Cl production from low-energy neutrons and 25% uncertainty in the ^{36}Cl production from slow negative muons.

2- Output A: exposure age of sample (only for uneroded surface)				
decay constant for ^{36}Cl	λ_{36}	a^{-1}	2,30E-06	1,52E-08
scaled total sample specific ^{36}Cl production rate without radiogenic	P$_{total}$	atoms ^{36}Cl g^{-1} a^{-1}	23,9	2,0
time factor radiogenic	t$_{f}$		19546	955,0
calculated concentration of radiogenically produced ^{36}Cl atoms for estimated age	N$_{r}$	atoms ^{36}Cl g^{-1}	66,5	4,6
estimated ^{36}Cl concentration from inheritance at time of sampling	N$_{inher}$(t)	atoms ^{36}Cl g^{-1}	0,0	
measured ^{36}Cl concentration in sample corrected from radiogenic component and inheritance	N$_{meas-inher}$	atoms ^{36}Cl g^{-1}	2,47E+05	11324,7
exposure age of sample	**t**	**a**	**10442**	1026,0

Figure 3.4: *Box 2 "Output A: exposure age of sample (only for uneroded surfaces)" on the second worksheet in the Excel calculation spreadsheet. The blue cells are output cells for the apparent age of the sample and its uncertainty.*

Box 3 is the "Output B" (Fig. 3.5), which does not contain any blue cell but allows finding either the erosion rate for an eroding surface if the exposure age is known/estimated or the exposure age if the erosion rate is known/estimated. This is because the ^{36}Cl concentration calculated according to the sample specific input in box 1 is compared to the measured ^{36}Cl concentration (input in box 1). The difference between both is given in the black-framed cell and can be minimized by adjusting iteratively the exposure duration or the erosion rate in box 1. In this case, the input cells for the exposure duration and the erosion rate have also the function of output cells, which is marked by the red colour of the numbers.

3- Output B: eroding surface				
calculated ^{36}Cl concentration for an eroding sample	$N_{calc,total}$	atoms ^{36}Cl g^{-1}	**2,36E+05**	
difference measured/calculated ^{36}Cl concentration in eroding sample	$\Delta N_{meas-calc}$		**4,19%**	
erosion rate	ε	cm a^{-1}	0	0
time factor with erosion for spallation reaction	$t_{cosm,s}$		9886	2932
time factor with erosion for capture of epithermal neutrons	$t_{cosm,eth}$		9886	2932
time factor with erosion for capture of thermal neutrons	$t_{cosm,th}$		9886	2932
time factor with erosion for capture of slow negative muons	$t_{cosm,\mu}$		9886	2932
depth reference factor for spallogenic reaction	d_s		0,904	
depth reference factor for capture of epithermal neutrons	d		0,259	

Figure 3.5: *Box 3 "Output B: eroding surface" on the second worksheet in the Excel calculation spreadsheet. The black-frames cell shows the difference between calculated and measured ^{36}Cl concentrations, which can be minimized by iteratively adjusting free parameters in box 1 such as the exposure age or the erosion rate.*

In the case of a surface sample of unknown exposure duration and unknown erosion rate, the *minimum exposure age* and the *maximum erosion rate* can be determined as follows.

If inheritance or burial can be excluded the *minimum exposure age* is generally given by the apparent age (Output A) where potential erosion is not taken into account. The apparent age is equal to the minimum exposure age because ignoring erosion results in a lower exposure age compared to if erosion is accounted for, what is illustrated in Figs. 3.6 A and 3.7 A. However, while this is always true for the cosmogenic nuclides, which are mainly produced by spallation (^{10}Be, ^{26}Al, ^{3}He, ^{21}Ne), ^{36}Cl apparent exposure ages have to be interpreted with caution if Cl contents are high in the sample. The vertical ^{36}Cl production curve due to low-energy neutrons near the land/atmosphere boundary has a characteristic distribution describing a peak of maximum production around 15 cm. The phenomen responsible for this distribution is called *neutron leakage*, because the low-energy neutrons escape back into air in the top centimeters under the rock surface (Chapter 1.3.3). Therefore, for samples high in Cl the apparent exposure age is not always the minimum exposure age. Therefore, only if Cl contents are low the apparent ^{36}Cl age can for sure be considered as the minimum exposure age, i.e. the real exposure age of the sample cannot be lower.

Measured and calculated ^{36}Cl concentration of an eroding surface sample will match if an assumed higher exposure duration is compensated by a higher erosion rate. The

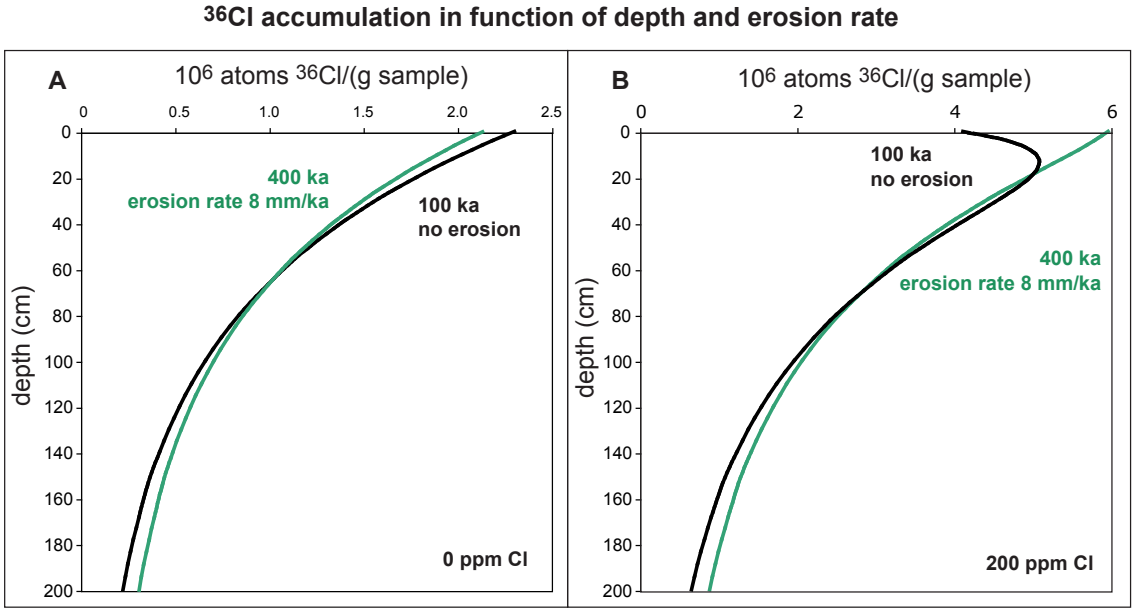

Figure 3.6: *Vertical distributions of theoretical ^{36}Cl concentrations in a basalt sample at 2000 m altitude: In panel A it is assumed that the sample has 0 ppm Cl, 8.9% Ca and 0.6% K. ^{36}Cl production is therefore dominated by spallation reactions (by 93%), responsible for the exponential shape of the curve. In panel B it is assumed that the same sample has 200 ppm Cl, which results in a ^{36}Cl contribution from capture of low-energy neutrons of 57%. This explains the characteristic shape of the black curve with a peak of maximum ^{36}Cl production at a about 15 cm depth, which is due to neutron leakage back into air near the land/atmosphere boundary. When a depth profile is measured and both exposure age and erosion rate are to be determined (see paragraph "Depth profile" in this section), this characteristic shape can help identifying the values for the two free parameters with less ambiguities than if production is dominated by spallation. In panel A, two very similar theoretic vertical distributions can be explained by very different exposure age/erosion rate combinations. In panel B, on the other hand, the same exposure age/erosion rate combinations result in clearly different shapes of the theoretical profile. The form of the curves changes in panel B, because in the case of erosion, layers of the material are steadily removed from the surface while ^{36}Cl production continues at the same rate. This can be imagined as if deeper parts of the curves were uplifted to the surface, which explains why the peak of maximum production in panel B has moved to the surface.*

maximum erosion rate of a surface can be determined by assuming that the surface has been exposed for a very long time (1 Ma or more, input cell "exposure duration" in box 1) resulting in a ^{36}Cl concentration which is in equilibrium between production and radioactive decay, called *steady state* (explained in Fig. 3.8). The measured ^{36}Cl concentration of the sample cannot be higher than this equilibrium (or saturation) concentration. The erosion rate that minimizes the difference between calculated and measured ^{36}Cl concentrations is the maximum possible erosion rate. Even for very long exposure times the erosion rate cannot be higher and for shorter exposure the erosion rate must be lower.

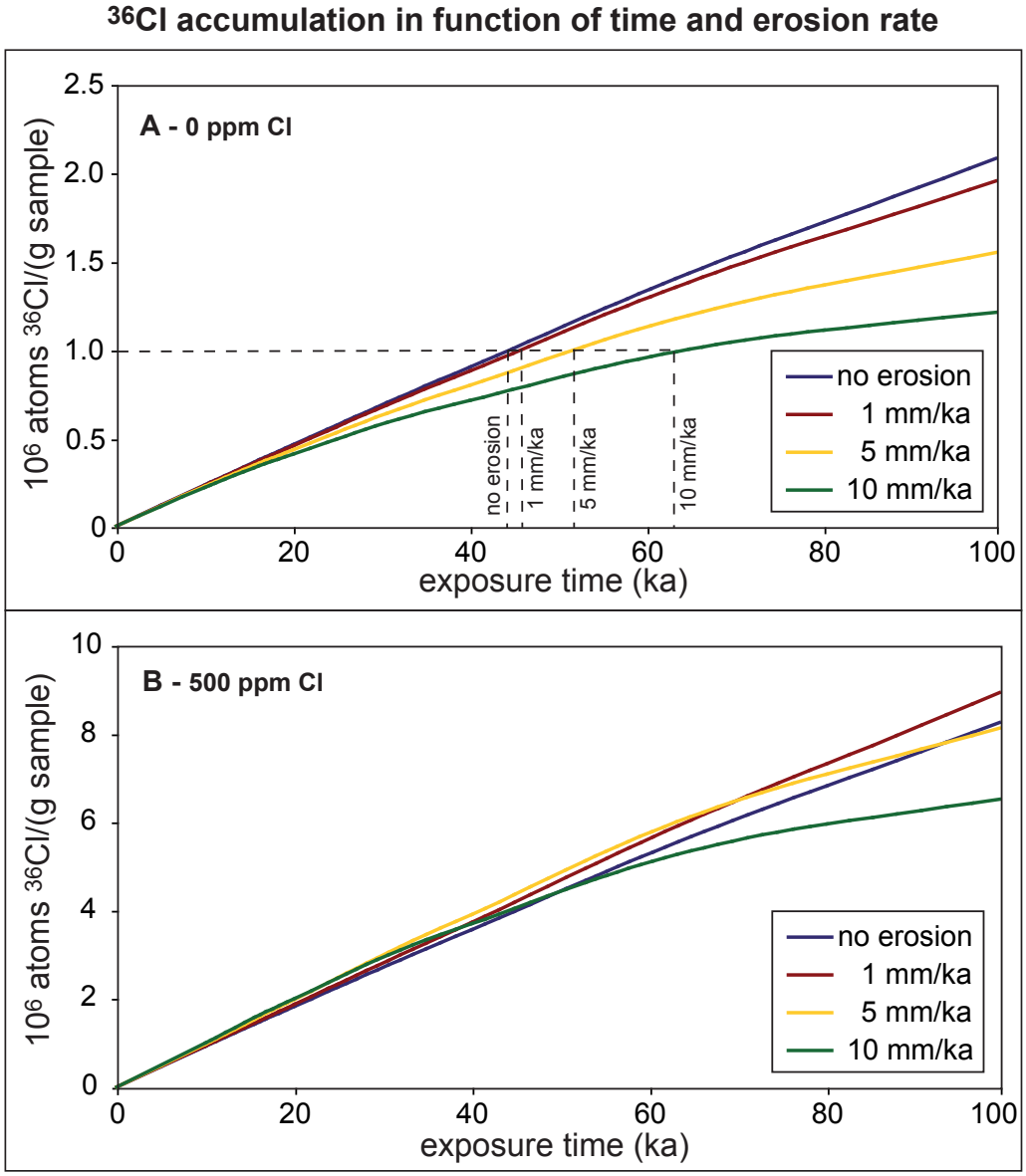

Figure 3.7: *^{36}Cl concentration in a surface sample of 10 cm thickness in function of time (0 to 100 ka) and erosion. Ca and K concentrations and altitude are the same as in Fig. 3.6. In panel A the ^{36}Cl production is dominated by spallation because the sample is free from Cl. In this case, the higher the steady erosion rate the lower the ^{36}Cl concentration. Therefore, not accounting for erosion systematically leads to a lower exposure age, indicated by the dashed line: for a measured ^{36}Cl concentration of $1\times\ 10^{-6}$ atoms g^{-1} the calculated exposure age is lowest if "no erosion" is assumed. In panel B the sample has 500 ppm Cl, so that the ^{36}Cl production is dominated by capture of low-energy neutrons. Depending on the erosion rate and on the exposure time the ^{36}Cl concentration can be higher with erosion than without erosion. In this example, erosion does not result in a significant impact on the calculated exposure age for exposure durations <60 ka.*

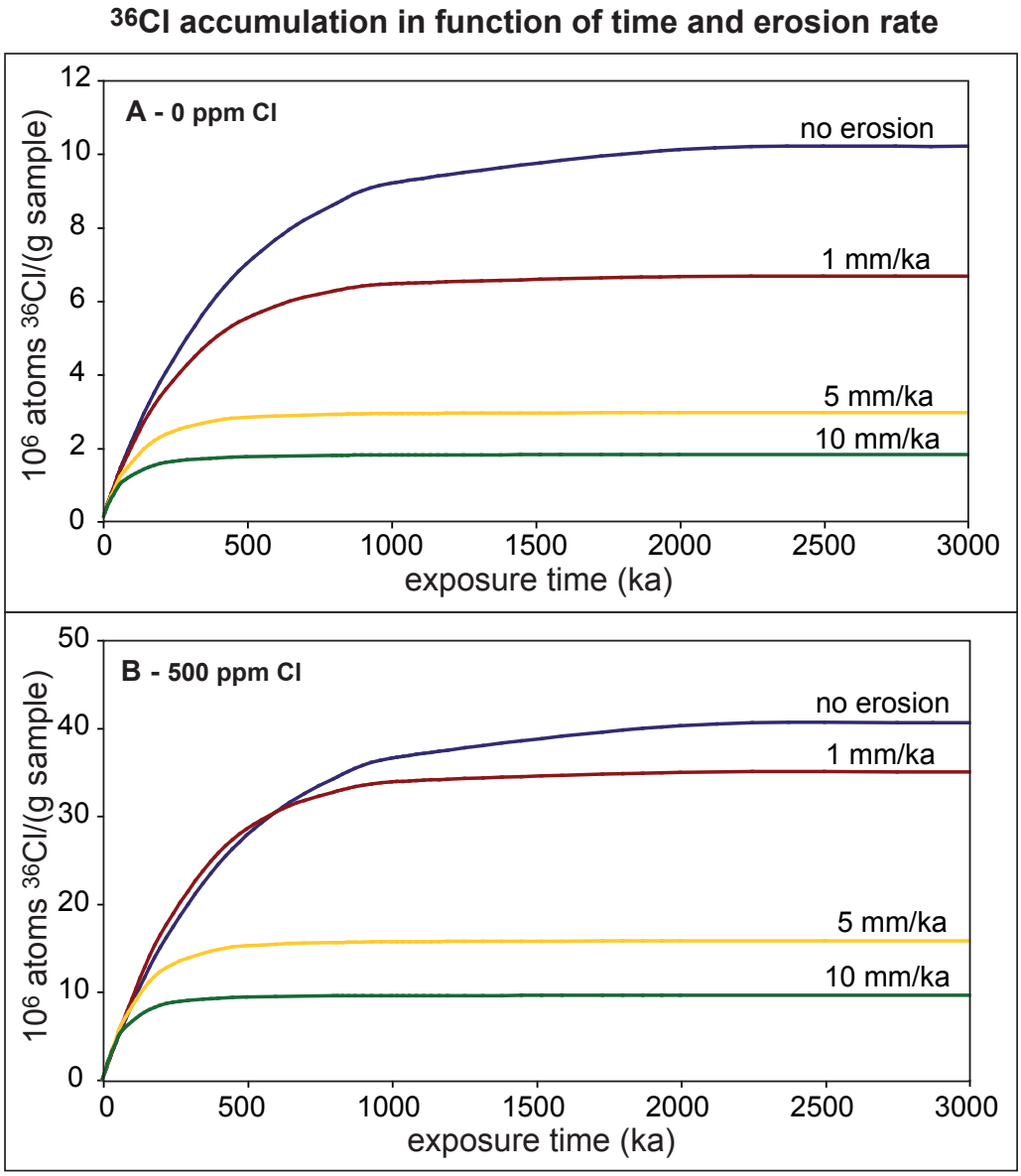

Figure 3.8: *^{36}Cl accumulation in a surface sample of 10 cm thickness in function of time (0 to 3 Ma) and erosion. Compositions and altitude are the same as in Fig. 3.7. In panel A the ^{36}Cl production is dominated by spallation, while in panel B it is dominated by capture of low-energy neutrons. Both panels show that the equilibrium ^{36}Cl concentration (equilibrium between production and decay = steady state) is characteristic for a certain erosion rate. Equilibrium is reached earlier the higher the erosion rate. If assuming that the measured ^{36}Cl concentration in a sample is the equilibrium concentration the maximum erosion rate for the surface can be determined.*

Depth profile

To create a ^{36}Cl depth profile, several samples have to be measured, taken over a certain depth range in e.g. a quarry, an incised cliff or a digged hole. The measured ^{36}Cl concen-

trations can be input on the third worksheet of the file (Fig. 3.9 B). These concentrations are automatically plotted in a graph showing the vertical distribution of the measured and the theoretic ^{36}Cl concentrations. The theoretic ^{36}Cl concentrations correspond to the sample relevant input (Fig. 3.9 A) assuming a homogeneous composition over the whole depth. The shape of the measured depth profile can be used to reconstruct the exposure history in terms of exposure duration, erosion rate and inheritance. By adjusting these free parameters in box 1 of the second worksheet the calculated ^{36}Cl concentration curve can be fitted to the measured ^{36}Cl curve. In this case, the presence of Cl can be helpful, since the characteristic vertical distribution of ^{36}Cl due to the capture of low-energy neutrons results in less ambiguities in the choice of the values for the free parameters (Fig. 3.6).

More output: ^{36}Cl contributions

The contributions in percent from all ^{36}Cl production mechanisms is displayed in box 4 "Output C" (Fig. 3.10). It depends most notably on the compositional input. Since ^{36}Cl is produced by various target elements and production mechanisms, the partitioning of the reactions is always dependent on the content of all target elements. For example, it is not possible to predict that a certain amount of ppm Cl will lead to a typical ^{36}Cl contribution from capture of low-energy neutrons without taking into account the ^{36}Cl contribution due to Ca and K.

The contributions are given for the spallation reactions from each target element (Ca, K, Ti, Fe), for the sum of all spallation reactions, for both the capture of epithermal neutrons and of thermal neutrons, for the sum of both, for the capture of slow negative muons and for the radiogenic ^{36}Cl production.

Also, the vertical distribution of the sample-specific production rates in the right graph on the third worksheet (Fig. 3.9 A) gives information about how relevant each production reaction is for the total ^{36}Cl production in the surface sample. In contrast to the output in box 4, the curves display the depth-dependent production rates continuously over a depth range and do not show production rates integrated over the sample thickness.

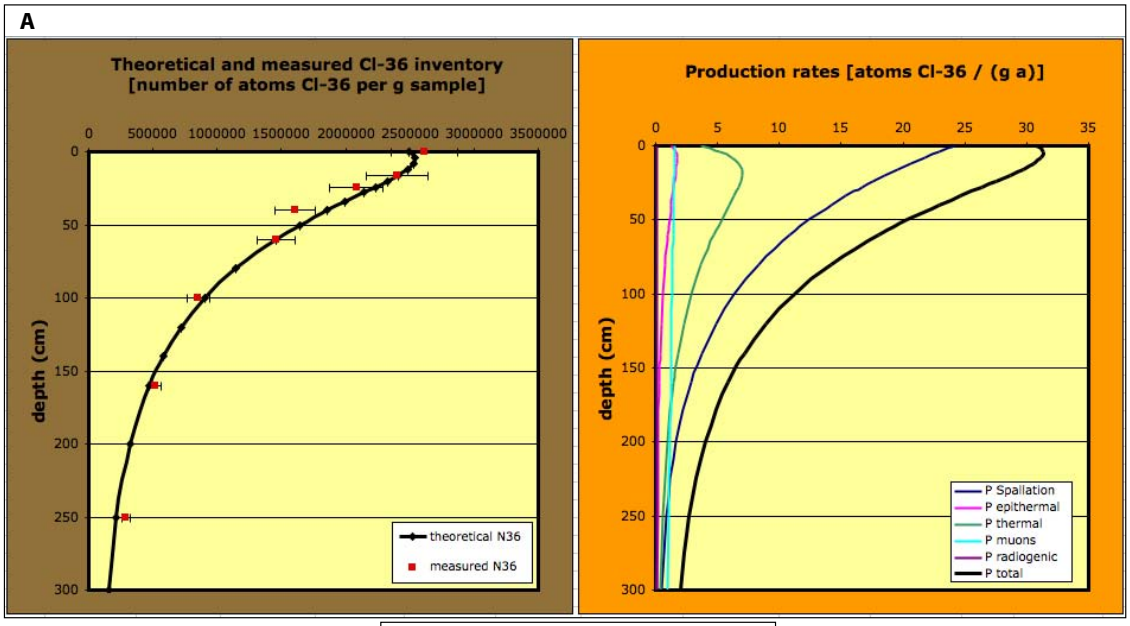

B

Input: Depth profile

sample name	depth [cm]	N_{meas} [at ^{36}Cl g^{-1}]	± [at 36Cl g-1]
A-0	0	2615000	261500
A-12	16	2398000	239800
A-24	24	2083000	208300
A-34	40	1607400	160740
A-60	60	1458900	145890
A-100	100	854100	85410
A-160	160	514000	51400
A-250	250	289900	28990

Figure 3.9: *Panel A shows the vertical distributions of the total calculated ^{36}Cl concentration (black curve in left graph) and the sample-specific production rates (right graph) generated automatically from the sample relevant input on the second worksheet. Panel B shows the input box for measured ^{36}Cl concentrations in a depth profile, which are plotted automatically in the left graph (red spots).*

A

4- Output C: calculated ^{36}Cl contributions from all production mechanism				
time factor cosmogenic without erosion	t_{cosm}		9886	2932
calculated ^{36}Cl concentration for given time + radiogenic	$N_{calc,total}$	atoms ^{36}Cl g^{-1}	2,36E+05	72958
difference measured/calculated ^{36}Cl concentration	$\Delta N_{meas-calc}$		4,19%	
contribution from each production mechanism:				
number of atoms ^{36}Cl per g by spallation of Ca	$N_{s,Ca}$	atoms ^{36}Cl g^{-1}	177852	75,22%
number of atoms ^{36}Cl per g by spallation of K	$N_{s,K}$	atoms ^{36}Cl g^{-1}	38194	16,15%
number of atoms ^{36}Cl per g by spallation of Ti	$N_{s,Ti}$	atoms ^{36}Cl g^{-1}	386	0,16%
number of atoms ^{36}Cl per g by spallation of Fe	$N_{s,Fe}$	atoms ^{36}Cl g^{-1}	455	0,19%
number of atoms ^{36}Cl per g by spallation of target elements	N_s	atoms ^{36}Cl g^{-1}	216887	91,73%
number of atoms ^{36}Cl per g by capture of thermal neutrons	N_{th}	atoms ^{36}Cl g^{-1}	3439	1,45%
number of atoms ^{36}Cl per g by capture of epithermal neutrons	N_{epi}	atoms ^{36}Cl g^{-1}	966	0,41%
number of atoms ^{36}Cl per g by capture of thermal and epithermal neutrons	N_n	atoms ^{36}Cl g^{-1}	4405	1,86%
number of atoms ^{36}Cl per g by capture of slow negative muons	N_μ	atoms ^{36}Cl g^{-1}	15077	6,38%
number of atoms ^{36}Cl per g by radiogenic production	N_r	atoms ^{36}Cl g^{-1}	66	0,03%
				100,00%

B

contribution from each production mechanism:				
number of atoms ^{36}Cl per g by spallation of Ca	$N_{s,Ca}$	atoms ^{36}Cl g^{-1}	177852	12,49%
number of atoms ^{36}Cl per g by spallation of K	$N_{s,K}$	atoms ^{36}Cl g^{-1}	38194	2,68%
number of atoms ^{36}Cl per g by spallation of Ti	$N_{s,Ti}$	atoms ^{36}Cl g^{-1}	386	0,03%
number of atoms ^{36}Cl per g by spallation of Fe	$N_{s,Fe}$	atoms ^{36}Cl g^{-1}	455	0,03%
number of atoms ^{36}Cl per g by spallation of target elements	N_s	atoms ^{36}Cl g^{-1}	216887	15,23%
number of atoms ^{36}Cl per g by capture of thermal neutrons	N_{th}	atoms ^{36}Cl g^{-1}	917135	64,39%
number of atoms ^{36}Cl per g by capture of epithermal neutrons	N_{epi}	atoms ^{36}Cl g^{-1}	257551	18,08%
number of atoms ^{36}Cl per g by capture of thermal and epithermal neutrons	N_n	atoms ^{36}Cl g^{-1}	1174686	82,47%
number of atoms ^{36}Cl per g by capture of slow negative muons	N_μ	atoms ^{36}Cl g^{-1}	15066	1,06%
number of atoms ^{36}Cl per g by radiogenic production	N_r	atoms ^{36}Cl g^{-1}	17733	1,24%
				100,00%

Figure 3.10: *Box 4 "Output C: calculated ^{36}Cl contributions from all production mechanisms" on the second worksheet in the Excel calculation spreadsheet. The blue output cells display the relative contributions in percent from all production mechanisms and target elements. The partitioning depends most notably on the composition of the material dissolved for ^{36}Cl extraction, but also on the reference SLHL production rates of the reactions. Panel A corresponds to a plagioclase (separated from basaltic lava) with 8.9% Ca, 0.6% K, 0.1% Ti, 0.1% Fe and 3 ppm Cl with the production rates: PR_{Ca} (Stone et al., 1996), PR_K (Evans et al., 1997), PR_{Ti} (Fink et al., 2000), PR_{Fe} (Stone, 2000) and $P_f(0)$ (Phillips et al., 2001). In panel B the Cl content has been hypothetically set to 800 ppm for the same mineral in order to demonstrate how the contributions from the production mechanisms change relatively in that case: the contribution due to capture of low-energy neutrons by ^{35}Cl increases from less than 2% to 82%, while the contribution due to spallation of all target elements decreases from 92% to 15%.*

Chapter 4

Sources of in-situ ^{36}Cl in basaltic rocks. Implications for calibration of production rates

Irene Schimmelpfennig[a], Lucilla Benedetti[a], Robert Finkel[a,c], Raphaël Pik[b], Pierre-Henri Blard[b], Didier Bourlès[a], Pete Burnard[b], Alice Williams[b]

[a] *CEREGE, UMR 6635 CNRS, Université Paul Cézanne, Europôle de l'Arbois, 13545 Aix en Provence, France*

[b] *CRPG, UPR 2300 CNRS, 15 rue Notre Dame des Pauvres, 54501 Vandoeuvre-lès-Nancy, France*

[c] *Earth and Planetary Science Department, University of California Berkley, Berkley, CA 94720-4767, USA*

This chapter is published in *Quaternary Geochronology* :

Schimmelpfennig, I., Benedetti, L., Finkel, R., Pik, R., Blard, P.-H., Bourlès, D., Burnard, P., Williams, A., 2009. Sources of in-situ ^{36}Cl in basaltic rocks. Implications for calibration of production rates. Quaternary Geochronology 4, 441-46.

Abstract

In-situ cosmogenic ^{36}Cl production rates from spallation of Ca and K determined in several previously published calibration studies differ by up to 50%. In this study we compare whole rock ^{36}Cl exposure ages with ^{36}Cl exposure ages evaluated in Ca-rich plagioclase in the same 10 ± 3 ka lava sample taken from Mt. Etna (Sicily, 38° N). The exposure age of the sample was determined by K-Ar and corroborated by cosmogenic ^{3}He measurements on cogenetic pyroxene phenocrysts. Sequential dissolution experiments showed that high Cl concentrations in plagioclase grains could be reduced from 450 ppm to less than 3 ppm after 16% dissolution. ^{36}Cl exposure ages calculated from the successive dissolution steps of this leached plagioclase sample are in good agreement with K-Ar and ^{3}He age. Stepwise dissolution of whole rock grains, on the other hand, is not as effective in reducing high Cl concentrations as it is for the plagioclase. 330 ppm Cl still remains after 85% dissolution. The ^{36}Cl exposure ages derived are systematically about 30% higher than the ages calculated from the plagioclase. We could exclude contamination by atmospheric ^{36}Cl as an explanation for this overestimate. Magmatic ^{36}Cl was estimated by measuring a totally shielded sample, but was found to account for only an insignificant amount of ^{36}Cl in the case of the 10 ka whole rock sample. We suspect that the overestimate of the whole rock exposure age is due to the difficulty in accurately assessing all the factors which control production of ^{36}Cl by low-energy neutron capture on ^{35}Cl, particularly variable water content and variable snow cover. We conclude that some of the published ^{36}Cl spallation production rates might be overestimated due to high Cl concentrations in the calibration samples. The use of rigorously pretreated mineral separates reduces Cl concentrations, allowing better estimates of the spallation production rates.

In the Appendix of this paper we document in detail the equations used. These equations are also incorporated into a ^{36}Cl calculation spreadsheet made available in the supplementary data.

Keywords: Cosmogenic-nuclide surface exposure dating, ^{36}Cl, Whole rock, Separated minerals, Low-energy neutron activation, Production rate calibration

4.1 Introduction

In-situ cosmogenic chlorine-36 is widely used to quantify surface processes in geosciences (e.g. Zreda and Phillips, 1994; Benedetti et al., 2003; Shabanian et al., 2009). Clearly, accurate results require that the production rates be well constrained. However, since the first evaluation of ^{36}Cl production rates (Zreda et al., 1991), their determination has been controversial. Different studies have proposed values that vary by up to 50% (Table 4.1). Possible explanations for these discrepancies were discussed in Swanson and Caffee (2001) and Licciardi et al. (2008). These include the effects of inheritance or erosion on the calibration samples, poorly constrained absolute ages, uncertainties in altitude-latitude scaling effects, temporal magnetic field variability, and neglecting to consider minor production mechanisms.

Cosmogenic ^{36}Cl is produced by various reaction mechanisms in rocks: spallation of K, Ca, Ti and Fe; slow negative muon capture by K and Ca; and low-energy (thermal and epithermal) neutron capture by ^{35}Cl. The ^{36}Cl contributions from each production mechanism depend mainly on the target element concentrations in the rock material from which ^{36}Cl is extracted. The most important target elements are Ca, K and ^{35}Cl. Since ^{35}Cl accounts for 75% of total chlorine in nature, low-energy neutron induced ^{36}Cl production is strongly dependent on the Cl content. The complex behavior of the low-energy-neutron flux at the land/atmosphere boundary and its high sensitivity to water content, snow cover, surface geometry, and erosion (e.g. Phillips et al., 2001) serve to make this production mechanism complicated compared to the spallogenic and muonic pathways.

In this paper we explore the role of mineralogy and composition on ^{36}Cl production. In previous ^{36}Cl production rate studies (Table 4.1) many types of rock (Zreda et al., 1991; Phillips et al., 2001; Swanson and Caffee, 2001; Licciardi et al., 2008), and separated minerals (Stone et al., 1996; Evans et al., 1997) were used. How have these variable compositions and especially the variable Cl contents affected the results of the production rate calibrations? Stone et al. (1996) and Evans et al. (1997) pointed out that using separated minerals makes possible the isolation of the target element whose production rate is to be calibrated, by minimizing contributions from other production mechanisms.

Here, we compare the calculated ^{36}Cl ages from whole rock and separated plagioclase phenocrysts of the same sample taken from a well-dated basaltic lava flow from Mt. Etna (Sicily), and we show how high Cl contents can lead to misinterpretation of the spallation production rates.

We also investigate whether chemical pretreatment of the sample to remove atmospheric or other ^{36}Cl contamination has the same effect on whole rock as on separated minerals. In previous studies, atmospheric contamination could never be proved (Zreda et al., 1991; Stone et al., 1996; Evans et al., 1997). Nevertheless, pretreatment to remove atmospheric ^{36}Cl is always performed as a precaution. Because it is assumed that any atmospheric Cl attached to the grains is easily removed due to its hydrophilic nature, this is usually accomplished through water and dilute $HN0_3$ leaching, regardless of the rock type (Table 4.1). Conducting sequential dissolution experiments on whole rock and plagioclase phenocrysts enabled us to track how ^{36}Cl and Cl were released in the course of the chemical treatment. We performed the same experiment on a completely shielded Etna sample from a historic lava flow in order to investigate the possible existence of an unknown source of ^{36}Cl in volcanic rocks such as magmatic ^{36}Cl.

In Appendix A we compile all formulas used to calculate total in-situ ^{36}Cl production and exposure ages. Calculations for any rock type or composition can be done using the Microsoft Excel® spreadsheet provided (Appendix B). The spreadsheet is valid for ^{36}Cl extraction from bulk rock and for partly dissolved samples like mineral separates.

Table 4.1: *^{36}Cl production rate calibration studies. Production rates are scaled to sea level and high geographic latitude (> 60°). The scaling methods used are given in the referenced papers. Total production rates from Ca and K comprise spallation and slow negative muon capture and are, thus, not directly comparable to spallation production rates (in bold) or muon capture production rates.*

Study	Production pathway	SLHL Production rate from Ca[a]	SLHL Production rate from K[a]	SLHL Production rate from Low-energy neutrons	Rock material	Cl content in rock material [ppm] (determined by)	^{36}Cl extraction method	Pretreatment	Comment
Zreda et al. (1991)	Spallation of Ca	**76±5**			Basaltic whole rock	94-111 (ion-selective electrode)	Air stripping method, closed system, no carrier	24hrs leaching in MQ water (+ 2hrs leaching in 10%HNO_3 in the case of basaltic whole rock)	Stone et al. (1996) recalculated total prod. rate from Ca to 54.8±5.0 and spall. prod. rate from K to 190
	Spallation of K		**106±8**		Bulk rock and K-microcline	Bulk rock: 130-160, microcline: 140, Qtz: 100-135 (ion-selective electrode)			
	low-energy-neutron capture on ^{35}Cl			307±24[c]	Bulk rock and quartz				
Stone et al. (1996)	Total production from Ca	53.6±3.6			Ca-feldspar from basalt	2-5 (ion chromatography)	Method "Stone et al. (1996)", with and without carrier	Leaching in deionised water + 2x in 2% HNO_3 (approx. 15% leached)	Sequential dissolution experiment on limestone: no atmospheric ^{36}Cl found
	Spallation of Ca	**48.8±3.4**							
	Muon capture on Ca	4.8±1.2							
Evans et al. (1997)	Total production from K		170±25		K-feldspar	0-315 (ion chromatography)	Method "Stone et al. (1996)", with carrier	Leaching in hot 10% HNO_3 in ultrasonic bath	Sequential dissolution experiment: no atmospheric ^{36}Cl found
Stone et al. (1998)	Muon capture on Ca	5.3±1.0			Calcite from marble	25-190 (ion chromatography)	Method "Stone et al. (1996)"	like "Stone et al. (1996)"	
Phillips et al. (2001)	Spallation of Ca	**66.8±4.4**			Divers whole silicate rocks	6-350 (not specified)	not specified	not specified	Recalibration of production rates of Phillips et al. (1996)
	Spallation of K		**137±9**						
	low-energy-neutron capture on ^{35}Cl			626±46[b]					
Swanson and Caffee (2001)	Total production rate from Ca	91±5			Whole silicate rocks	42-290 (ion-selective electrode)	Modified from Zreda et al. (1991), no carrier	not specified	Discussion of validity of ^{14}C dating used (Easterbrook, 2003; Swanson, 2005)
	Total production rate from K		228±18						
	low-energy-neutron capture on ^{35}Cl			762±28[b]					
Licciardi et al. (2008)	Spallation of Ca	**57±5**			Basaltic whole rock	29-61 (isotope dilution)	Modified from Stone et al. (1996), with carrier	Sonication in distilled water and 2% HNO_3	Higher production rate relative to Stone et al. (1996) interpreted as due to atmospheric pressure anomalies in Iceland

[a] [atoms ^{36}Cl (g target element)$^{-1}$ a^{-1}]
[b] [neutrons (g air)$^{-1}$ a^{-1}]
[c] [neutrons (g rock)$^{-1}$ a^{-1}]

4.2 Methods

4.2.1 Sampling sites and sample description

For this study, we worked on two basaltic lava samples from Mt. Etna (Sicily, 38°N), the largest active stratovolcano in Europe, its summit reaching 3330 m asl. Mt. Etna has not undergone major altitudinal changes since the flows we studied were emplaced (Monaco et al., 1997; Blard et al., 2005), indicating that the ^{36}Cl production rate was constant during exposure time.

Sample SI43 (altitude 2070 m, N 37.7095°, E 15.0258°) was taken on the southern shoulder of the "Valle del Bove" depression, a collapse structure on the south-east of the volcano summit formed at approximately 10 ka (Bonforte and Puglisi, 2006), from a "fossil"-exposed surface (Fig. 4.1a and b). It is overlain by a younger 250 cm thick lava flow, and now outcrops at the top of a 300 m high cliff that slopes at 70°. This steep angle implies a rapid retreat of the outcrop wall. We can therefore assume negligible recent exposure of the cliff wall to cosmic radiation. This assumption is supported by the absence of cosmogenic ^{3}He in a sample of the cliff several meters below the SI43 fossil surface (Blard et al., 2005). The lava is a trachybasalt rich in phenocrysts (around 30%), with dominant plagioclase associated with minor olivine and clinopyroxene. The clearly distinguishable pahoehoe cords of the underlying flowtop appeared only slightly weathered, indicating very little erosion. Paleosol or ash deposits were not observed at the contact between the two flows. Snow cover cannot be excluded and will be discussed later. Both flows, overlying and underlying, were dated by K-Ar at 10 ± 3 ka and 20 ± 1 ka, respectively, resulting in a surface exposure age of 10 ± 3 ka for SI43, before it was completely shielded (Blard et al., 2005). In the following we will call the exposure before burial the "fossil" exposure. The exposure age deduced from the K-Ar dates was corroborated by cosmogenic ^{3}He measurements on cogenetic pyroxene phenocrysts in SI43 (Blard et al., 2008), yielding an exposure age of 9.4 ± 0.9 ka using the ^{3}He production rate 128 ± 5 atoms ^{3}He g^{-1} a^{-1} (Blard et al., 2006).

Sample IS9 was collected in 2005 on the northern flank of Mt. Etna inside the "Grotta dei Lamponi" cave (altitude 1718 m, N 37.8181°, E 15.0097°, Fig. 4.1a and c) from a

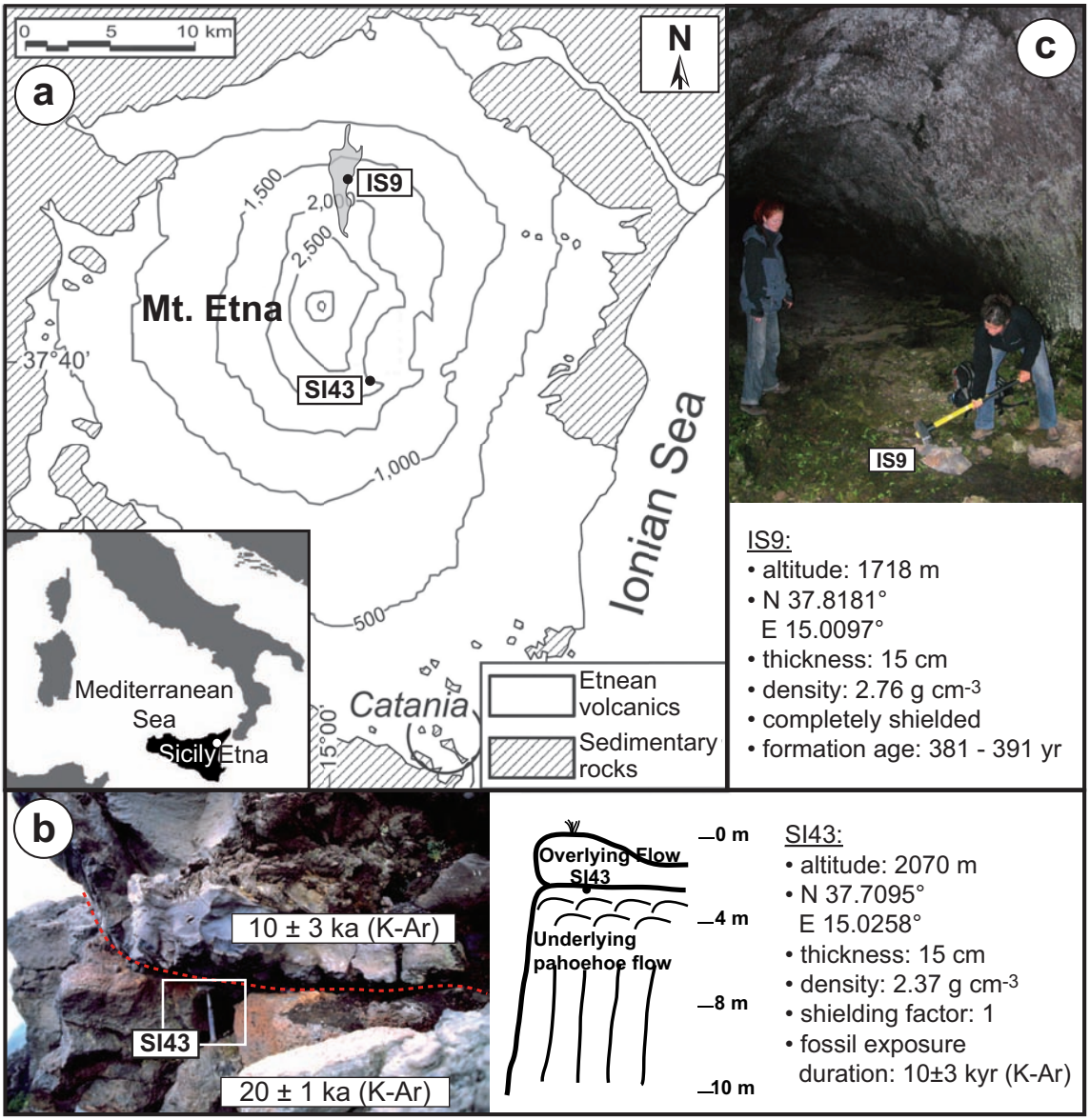

Figure 4.1: *(a) Map of Mount Etna with sample locations. Pictures of sample sites and sample characteristics of (b) SI43 and (c) IS9.*

historic flow erupted between 1614 and 1624 A.D. (Tanguy et al., 2007). Since the flow's emplacement, 381 - 391 years ago, the sample has been shielded by a 2 m thick lava ceiling. Given the very young age and the shielding from cosmic radiation, we expect this sample to contain only negligible amounts of cosmogenic and radiogenic ^{36}Cl. Morphologically and petrographically, this lava is very similar to the SI43 lava. Both are pahoehoe lavas bearing abundant plagioclase and fewer olivine and pyroxene phenocrysts.

4.2.2 Sample preparation and sequential ^{36}Cl extraction

Both samples were crushed in a jaw crusher and sieved to 140 - 400 μm (SI43) and 250 - 500 μm (IS9). Dry rock densities were determined on several rock pieces (around 3 cm diameter) using the Archimedes principle and found to be 2.37 g cm^{-3} for SI43 and 2.76 g cm^{-3} for IS9. An aliquot of a few grams of the sieved whole rock grains was taken from each sample for bulk composition analysis. Mineral separation exclusively relied on magnetic methods since the plagioclase phenocrysts are the only non-ferromagnetic mineral phase in the sample. In a first step, the most magnetic grains were taken off with a strong hand magnet, then the less magnetic fractions were progressively removed with a Frantz magnetic separator.

The initial sample weights for the sequential ^{36}Cl extraction experiments were 400 g of SI43 and IS9 whole rock grains (WR) and 60 g of SI43 plagioclase grains (PLG). After a leaching step in hot HNO_3 (2M), the grains were dissolved in a stepwise fashion by limited amounts of an HF (48%)/ HNO_3 (2M) mixture (volume ratio 1:2). WR was completely dissolved after 7 steps and PLG after 9 steps (Table 4.3, Fig. 4.3), the number of steps only depending on the amount of acid used. Before each extraction step, 2 g aliquots of the solid grains were taken for analysis of the chemical composition. After each step, the remaining sample grains were dried and weighed to calculate the mass of sample lost by dissolution. The solutions obtained from each step were collected for subsequent ^{36}Cl and Cl analysis. First, they were centrifuged to remove the undissolved residue in suspension, which was dried, weighed and collected for chemical analysis. Then a chloride carrier (Oak Ridge National Laboratory) was added to each solution, containing 1.5 mg Cl and enriched in ^{35}Cl (99.9%) in the case of SI43 and in ^{37}Cl (98.2%) in the case of IS9. AgCl was

precipitated by adding $AgNO_3$. This first precipitate was re-dissolved in dilute NH_4OH, and, in order to reduce the isobaric interferences of ^{36}S during the ^{36}Cl AMS measurements, $Ba(NO_3)_2$ was added to precipitate $BaS0_4/BaCO_3$. The AgCl, re-precipitated from the resulting solution by acidification with HNO_3 and collected by centrifuging, was rinsed and dried and ^{36}Cl was measured at LLNL-CAMS. AgCl yields, including carrier and natural Cl, accounted for 6 to 77 mg for the whole rocks and for 1 to 7 mg for the plagioclase.

For the sequential ^{36}Cl extraction from WR SI43 and PLG SI43 we used Chimie-Plus Laboratoires reagent grade "pure" brand HF, with a certified Cl concentration of maximum 50 ppm. For sample IS9 we used MERCK "suprapur®" brand HF, with a certified Cl concentration of maximum 500 ppb. In order to check a possible Cl contamination from the acids, several blanks with different amounts of acid were processed throughout the chemistry. The calculated number of atoms Cl and ^{36}Cl is higher in the case of the acid mixtures with HF "pure" than with HF "suprapur" or using only HNO_3 (Table 4.2). A linear relationship between the amount of HF "pure" used and the number of atoms Cl and ^{36}Cl is evident from Fig. 4.2 a and b. In these plots the intercept represents a constant background from the laboratory facility, carrier and AMS, and the slope corresponds to the number of atoms Cl and ^{36}Cl, respectively, per ml acid. One ml of the acid mixture using "pure" HF contains 3.7×10^{16} atoms Cl and 5.1×10^{3} atoms ^{36}Cl, while using "suprapur" HF we find only 1×10^{15} atoms Cl per ml and ^{36}Cl values that are not distinguishable from the background.

Table 4.2: *Chemistry blanks. The number of atoms Cl and ^{36}Cl are absolute values in the blank solutions (Cl from carrier not included).*

Blank	Acid mixture [ml]	^{35}Cl carrier [mg]	^{35}Cl/^{37}Cl	^{36}Cl/^{35}Cl [10^{-14}]	Cl [10^{17} atoms]	^{36}Cl [10^5 atoms]
Blanks corresponding to sequential dissolution of whole rock SI43						
B-D1	30	1.566	116±21	1.27±0.12	8.6±1.9	3.52±0.32
F-D5	45	1.480	60.31±0.30	1.85±0.20	17.12±0.86	4.98±0.54
Blanks corresponding to sequential dissolution of plagioclase SI43						
BLH-L[a]	100	1.786	269.09±0.31	0.797±0.053	3.45±0.17	2.48±0.17
BLH-D1	15	1.793	171.9±2.6	1.032±0.058	6.19±0.33	3.25±0.18
BLH-D2	24	1.793	122.98±0.17	1.32±0.24	9.24±0.46	4.17±0.75
BLH-D3	30	1.793	100.44±0.45	1.22±0.73	11.67±0.59	3.89±0.23
BLH-D4	30	1.794	68.06±0.02	1.22±0.23	18.11±0.91	3.96±0.76
		^{37}Cl carrier [mg]		^{36}Cl/^{37}Cl [10^{-14}]		
Blanks corresponding to sequential dissolution of whole rock IS9						
BL9[a]	100	1.494	0.025±—	1.21±0.26	2.37±0.12	2.95±0.64
BD9[b]	65	1.494	0.023±—	0.99±0.17	1.656±0.083	2.41±0.42

The acid mixture is composed of one part HF (48%, reagent degree "pure") and two parts HNO_3 (2M), except
[a] only HNO_3 (2M) and
[b] one part HF (40%, reagent degree "suprapur") and two parts HNO_3 (2M).

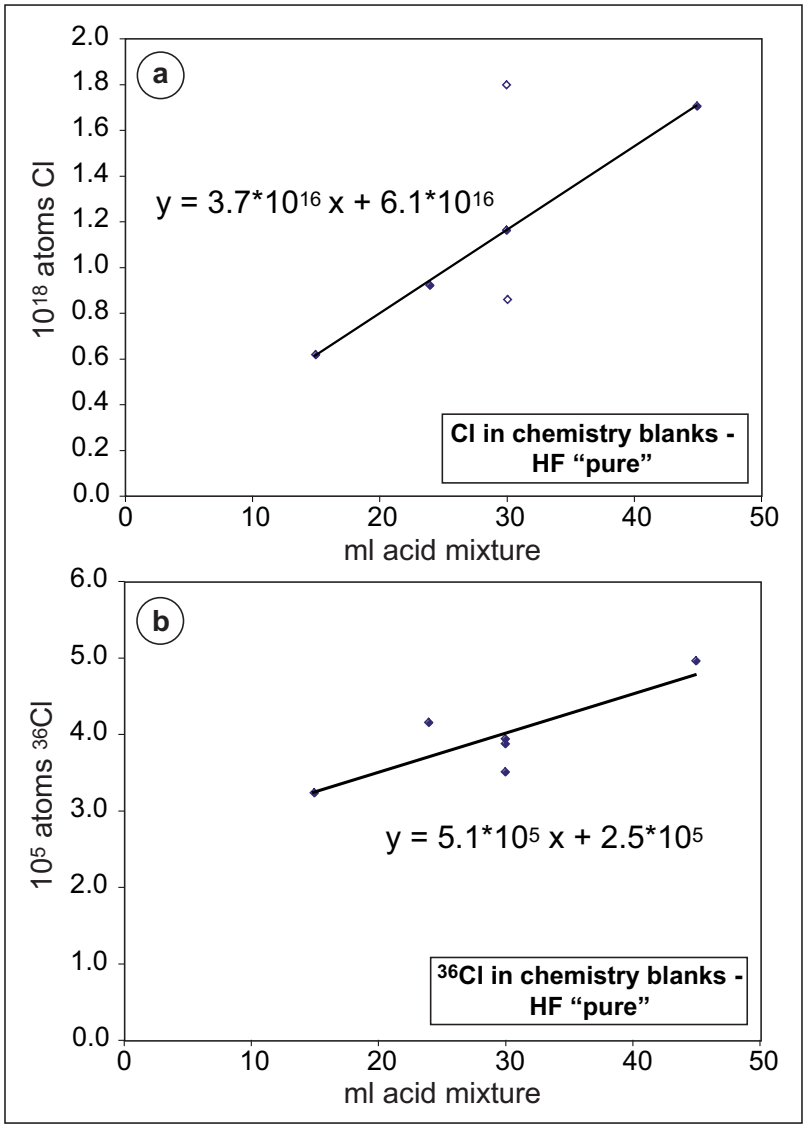

Figure 4.2: *Absolute number of (a) atoms Cl and (b) atoms ^{36}Cl in chemistry blanks versus ml of acid mixture (one part HF, "pure", 48%, two parts HNO_3, 2M). Open symbols are considered as outliers. The linear relationship indicates that HF "pure" contains significant amounts of Cl and ^{36}Cl. See text in section 4.2.2 for details.*

4.2.3 Measurements

^{36}Cl and Cl concentrations in the sequential extracts were determined using the Lawrence Livermore National Laboratory FN accelerator mass spectrometer (LLNL-CAMS) operating at 8.3 MV. Three isotopes of chlorine were measured: ^{35}Cl, ^{36}Cl and ^{37}Cl. ^{36}Cl/^{35}Cl (SI43) and ^{36}Cl/^{37}Cl (IS9), depending on the spike used, were determined by normal-

izing to a ^{36}Cl standard prepared by K. Nishiizumi (Sharma et al., 1990). The stable ratio ^{35}Cl/^{37}Cl was normalized to the same standard assuming the natural ratio of 3.127. Measured ratios as well as the resulting ^{36}Cl and Cl concentrations are listed in Table 4.3. Chemistry blank ratios range between 0.8×10^{-14} and 1.8×10^{-14} (Table 4.2), being 13 times lower than the ^{36}Cl/^{35}Cl of WR SI43, 3-10 times lower than the ^{36}Cl/^{35}Cl of PLG SI43, and very close to the ^{36}Cl/^{37}Cl of WR IS9. The relatively high blank values corresponding to SI43 are due to a non-negligible content of Cl and ^{36}Cl in the HF "pure" used (section 4.2.2). Measurements of WR and PLG SI43 were therefore corrected according to the amount of acid used, whereas IS9 measurements were only corrected for their corresponding blank value. All chemistry blank corrections were done in terms of number of atoms ^{36}Cl and Cl.

Table 4.3: *AMS measurements, Cl, ^{36}Cl and target element concentrations in stepwise dissolution of samples SI43 (whole rock and separated plagioclase) and IS9 (whole rock). Cl and ^{36}Cl were determined from the AMS measurements. The determination of the concentrations of Ca, K, Ti and Fe is described in section 4.2.3.*

Sample material	Dissol. step	Dissol. progress	Weight loss [g]	$^{35}Cl/^{37}Cl$	$^{36}Cl/^{35}Cl$ [10^{-14}]	Cl [ppm]	$^{36}Cl_m$ [10^6 atoms g^{-1}]	Ca [wt%]	K [wt%]	Ti [wt%]	Fe [wt%]
WR SI43	L	4%	10.23	3.246±0.012	15.27±0.36	5890±680	12.0±1.4	9.9±3.5	0.3±1.8	0.1±1.2	14.6±3.6
	D1	9%	7.13	3.443±0.009	15.88±0.38	2750±160	6.16±0.36	4.6±2.9	1.1±1.6	1.1±1.0	18.5±2.8
	D2	16%	21.16	3.304±0.024	15.59±0.46	1830±270	3.87±0.56	4.2±3.9	2.1±2.0	0.9±1.3	10.0±3.4
	D3	23%	23.96	3.338±0.023	15.84±0.71	1190±140	2.59±0.32	7.3±2.8	0.9±1.4	0.91±0.93	12.0±2.3
	D4	32%	31.92	3.332±0.007	17.16±0.34	926±56	2.17±0.13	7.2±1.5	1.34±0.71	0.80±0.47	6.5±1.1
	D5	85%	160.93	3.238±0.003	22.07±0.94	334±20	0.991±0.073	5.52±0.23	0.81±0.11	0.665±0.071	3.85±0.16
	D6	100%	21.94	37.853±0.074	14.91±0.61	9.00±0.50	0.216±0.012	10.24±0.22	0.278±0.042	0.698±0.038	5.31±0.11
PLG SI43	L	2%	0.61	27.14±0.33	2.47±0.14	457±26	1.00±0.11	3±17	0.0±2.7	0.37±0.76	4.8±3.0
	D1	9%	3.27	37±–	8.9±1.5	51±—	(0.81±—)	12.2±5.2	0.91±0.85	0.15±0.23	0.95±0.89
	D2	16%	3.58	95.77±0.88	4.33±0.22	6.5±1.2	0.288±0.022	9.1±3.6	0.58±0.57	0.09±0.15	0.68±0.60
	D3	25%	5.04	96.61±0.51	3.92±0.13	0.72±0.87	0.169±0.012	7.4±2.4	0.49±0.38	0.06±0.10	0.54±0.40
	D4	35%	5.03	80.13±0.51	5.17±0.16	2.8±1.0	0.247±0.013	8.9±1.9	0.58±0.31	0.073±0.080	0.59±0.32
	D5	45%	4.97	78.91±0.41	4.48±0.16	3.1±1.0	0.205±0.013	6.6±1.7	0.44±0.27	0.057±0.071	0.46±0.28
	D6	60%	7.50	56.14±0.57	6.36±0.23	2.48±0.98	0.209±0.013	7.48±0.58	0.464±0.092	0.062±0.024	0.50±0.10
	D7	78%	9.77	46.01±0.59	7.94±0.21	2.02±0.94	0.209±0.011	7.39±0.41	0.477±0.065	0.062±0.017	0.479±0.067
	D8	100%	13.06	32.32±0.36	9.83±0.33	1.2±1.0	0.196±0.012	7.58±0.15	0.484±0.024	0.0624±0.0062	0.502±0.025
					$^{36}Cl/^{37}Cl$ [10^{-14}]		$^{36}Cl_m$ [10^4 atoms g^{-1}]				
WR IS9	L	5%	12.69	3.041±0.007	1.39±0.22	17200±1600	99±18				
	D1	9%	12.19	2.560±0.005	1.69±0.18	2270±120	17.2±2.9				
	D2	20%	32.29	2.376±0.003	1.31±0.25	600±30	3.5±1.1				
	D3	32%	26.69	1.750±0.003	1.40±0.24	290±15	2.0±1.0				
	D4	41%	19.99	1.301±0.003	1.09±0.13	217±11	1.1±1.2				
	D5	72%	95.95	2.057±0.004	1.18±0.22	122.5±6.2	0.64±0.30				
	D6	100%	85.00	0.865±0.002	1.30±0.23	27.1±1.4	0.23±0.30				

The external reproducibility (1σ standard deviation of repeated measurements) of the ^{35}Cl/^{37}Cl ratios of all sample measurements is better than 1.3%. They range between 2% and 5.6% for ^{36}Cl/^{35}Cl ratios of SI43, except in step D1 of the plagioclase for which measurement time was limited by the small amount of AgCl (1.4 mg) present (Table 4.3). Therefore, its value is not reliable, and its precision could not be determined. External reproducibilities on ^{36}Cl/^{37}Cl ratios of IS9 are not better than 12% and 19% (Table 4.3), because the values are very close to the blank. Uncertainties in the ^{36}Cl and Cl concentrations were calculated according to the standard propagation of uncertainties equation (e.g. Taylor, 1997):

$$\delta q = \sqrt{\left(\frac{\partial q}{\partial x}\delta x\right)^2 + \left(\frac{\partial q}{\partial y}\delta y\right)^2 + \left(\frac{\partial q}{\partial z}\delta z\right)^2} \tag{4.1}$$

if q is any function of several variables x,y,z.

Analysis of chemical compositions were performed at the Service d'Analyse des Roches et des Minéraux du CNRS (SARM) at Centre de Recherches Pétrographiques et Géochimiques (CRPG), Nancy. Major elements were measured by ICP-OES and trace elements by ICP-MS, except Li (atomic absorption), B (colorimetry), and H_2O (Karl Fischer titration). The bulk rock composition of samples SI43 and IS9 was analyzed on sieved grain aliquots before any pretreatment (Table 4.4). The target element concentrations released in each dissolution step of WR and PLG SI43 could not be determined directly from the solution due to the presence of HF. Therefore, aliquots of the solid grains taken before and between the extraction steps served for the determination of [Ca], [K], [Ti] and [Fe], calculated by mass balance as follows:

$$[k]_{dissolved} = ([k]_{before} \times m_{before} - [k]_{after} \times m_{after} - [k]_{residue} \times m_{residue})/m_{dissolved} \tag{4.2}$$

where $[k]$ is the concentration of element k and m the mass of the sample material, with $m_{dissolved} = m_{before} - m_{after} - m_{residue}$. The subscripts $before$, $after$ and $residue$ refer to "before dissolution", "after dissolution" and the undissolved residue in suspension, respectively. Error propagation of the analytical uncertainties during these mass balance calculations is partly responsible for the high uncertainties for the dissolved target element

Table 4.4: *Bulk rock composition of samples SI43 and IS9, determined on whole rock before any chemical treatment.*

sample		[wt%]		[wt%]		[ppm]		[ppm]
SI43 bulk	O	45.5±1.2	Mg	3.21±0.06	H	1640±33	U	4.3±0.1
	Si	23.08±0.23	Na	2.93±0.44	Li	9.2±0.5	Th	14.8±0.7
	Al	9.44±0.09	K	1.31±0.07	B	11.0±1.1	Cl	830±37
	Fe	6.64±0.13	Ti	0.82±0.04	Sm	9.6±0.5		
	Ca	6.27±0.13	Mn	0.13±0.01	Gd	7.2±0.4		
IS9 bulk	O	45.2±1.2	Mg	3.18±0.06	H	159±3	U	2.8±0.2
	Si	22.93±0.23	Na	3.06±0.46	Li	9.4±0.5	Th	10.1±0.5
	Al	9.89±0.10	K	1.27±0.08	B	7±0.7	Cl	1093±80
	Fe	6.62±0.13	Ti	0.83±0.07	Sm	8.9±0.4		
	Ca	7.46±0.15	Mn	0.12±0.01	Gd	6.9±0.3		

concentrations (Table 4.3). We checked the accuracy of this procedure by comparing, for each target element, the sum of the calculated amounts at each extraction step with the concentrations analyzed in the bulk rock (Table 4.4). In all cases the sum of the fractional masses accounts for at least 95% of the total, suggesting that the uncertainties in the mass balance calculations are probably overestimated.

The Cl concentrations of the bulk of samples SI43 and IS9, presented in Table 4.4, were calculated by adding the Cl contents of each of the sequentially dissolved fraction of WR SI43 and WR IS9 as determined by isotope dilution during the AMS measurements (Table 4.3). SI43 gave 830 ppm and IS9 gave 1093 ppm.

4.3 In-situ ^{36}Cl production mechanisms and calculations

In-situ ^{36}Cl is produced by several different reactions in a rock. The three main cosmogenic production mechanisms are spallation of the target elements Ca, K, Ti and Fe by high-energy secondary neutrons (E > ∼10 MeV), capture of thermal (E < 0.5 eV) and epithermal (E ≈ 0.1 MeV - 0.5 eV) neutrons (hereafter referred to as low-energy neutrons) by ^{35}Cl, and capture of slow negative muons by ^{40}Ca and ^{39}K. In-situ ^{36}Cl is also produced by a radiogenic reaction, resulting from the capture by ^{35}Cl of low-energy neutrons that are generated during the decay of U and Th (non-cosmogenic). Further theoretical discussion

can be found e.g. in Gosse and Phillips (2001), Stone et al. (1998), Bierman et al. (1995) and Fabryka-Martin (1988). These authors propose partially different approaches to calculating the ^{36}Cl production in a sample. In this study, calculations are for the most part based on Gosse and Phillips (2001). In the following sections we discuss our choices of published parameters and calculation methods. Detailed equations are given in Appendix A, and calculations can be done for any rock type and chemical composition using the calculation spreadsheet provided (Appendix B).

Total in-situ ^{36}Cl production. For an uneroded rock sample of finite thickness, the total sample-specific in-situ ^{36}Cl production rate [atoms ^{36}Cl g^{-1} a^{-1}] at mass depth z [g cm^{-2}] is given by

$$P_{total}(z) = S_{el,s}F_sQ_sP_s(z)+S_{el,n}F_n(Q_{eth}P_{eth}(z)+Q_{th}P_{th}(z))+S_{el,\mu}F_\mu Q_\mu P_\mu(z)+P_r \quad (4.3)$$

with the subscripts: s for spallation, eth for epithermal neutron capture on ^{35}Cl, th for thermal neutron capture on ^{35}Cl, n for low-energy-neutron capture, μ for direct capture of slow negative muons on ^{40}Ca and ^{39}K, and r for radiogenic production. $S_{el,s}$, $S_{el,n}$ and $S_{el,\mu}$ are the scaling factors used to translate production rates from the reference point at sea level and high latitude to the geographic location and elevation of the the sample site. F_s, F_n and F_μ include all correction factors such as topographic shielding, snow shielding and geometry. The Q_q are the sample thickness integration factors for the respective reaction type, given that the sample-specific production rates of each reaction type refer to a mass depth z. The Q_q factors in Gosse and Phillips (2001) refer to the top of the sample, (i.e. in the case of a surface sample z=0 g cm^{-2}) but are only valid for surface samples that are not eroding. We therefore have adopted the recent calculations by Schlagenhauf et al. (2009), which were developed to treat the more general case of a subsurface sample in the presence of erosion. In accord with these calculations z does not refer to the top of the sample but to its center (for details see Appendix A.5 and A.6). $P_q(z)$ are the sample-specific depth dependent ^{36}Cl production rates due to the respective reaction types, referenced to sea level and high latitude.

The total number of atoms ^{36}Cl that accumulate in an uneroded sample of simple

exposure history and finite thickness is obtained by multiplying its total production rate by the time factor which takes into account the radioactive decay of ^{36}Cl:

$$N_{total} = P_{total}(z)(1 - exp^{-t\lambda_{36}})/\lambda_{36} \tag{4.4}$$

where t is the exposure time [a] and λ_{36} the ^{36}Cl decay constant equal to 2.303×10^{-6}a^{-1}.

The exposure age of a sample of the same characteristics is given by

$$t = \Big(-ln(1 - N_{meas}\lambda_{36}/P_{total}(z))\Big)/\lambda_{36} \tag{4.5}$$

where N_{meas} is the measured number of atoms of ^{36}Cl, corrected for all non-cosmogenic components, such as radiogenic.

All production mechanisms are composition dependent. The chemical composition of a sample is therefore crucial for determining which mechanism dominates ^{36}Cl production.

Spallation. For the calculations of the spallogenic ^{36}Cl contribution, we use the following spallation production rates (at sea level and high latitude): PR_{Ca}= 48.8 ± 3.4 atoms ^{36}Cl (g Ca)$^{-1}$ a^{-1} (Stone et al., 1996), PR_K= 162 ± 24 atoms ^{36}Cl (g K)$^{-1}$ a^{-1} (Evans et al., 1997), PR_{Ti}= 13 ± 3 atoms ^{36}Cl (g Ti)$^{-1}$ a^{-1} (Fink et al., 2000), and PR_{Fe}= 1.9 atoms ^{36}Cl (g Fe)$^{-1}$ a^{-1} (Stone, 2005). Note that the ^{36}Cl production rate for K given in Evans et al. (1997) with a value of 170 ± 25 atoms ^{36}Cl (g K)$^{-1}$ a^{-1}, includes 5% due to slow negative muon capture on K. The spallation production rate used has been corrected for this contribution. The apparent fast neutron attenuation coefficient Λ_f has a value of about 160 g cm^{-2} according to Gosse and Phillips (2001). We use the value 177 g cm^{-2} from Farber et al. (2008) since it was experimentally determined from ^{10}Be measurements in geological samples.

Low-energy neutron capture. The ^{36}Cl contribution due to low-energy-neutron capture on ^{35}Cl will be significant if the Cl concentration in the sample is high. Furthermore, the distribution of the low-energy neutrons in the first few meters below a rock surface is influenced by the concentration of elements that absorb and scatter low-energy neutrons. The most important species that need to be considered in this light are the major elements, and the trace elements H, Li, B, Sm, and Gd. The elemental absorption

and scattering cross-sections are listed in Appendix A (Table A.1). High concentrations of the thermal neutron absorbers enhance the macroscopic thermal neutron absorption cross-section, resulting in lower ^{36}Cl production by thermal neutron capture. We calculate the sample-specific production rates due to thermal and epithermal neutron capture on ^{35}Cl according to Gosse and Phillips (2001). Their calculations take into account both the thermal and the epithermal neutron reaction mechanisms and include all reactions that produce low-energy neutrons. Moreover, these calculations are valid for any chemical composition. The corresponding calculations in Stone et al. (1998), on the other hand, do not mention the epithermal neutron production mechanism and are specific for ^{36}Cl production in calcite. We used $P_f(0) = 626 \pm 46$ neutrons g^{-1} a^{-1} from Phillips et al. (2001) for the production rate of epithermal neutrons from fast neutrons in the atmosphere at the land/atmosphere interface (at sea level and high latitude).

Slow negative muon capture. The sample-specific muonic ^{36}Cl production rate is a product of $\Psi_\mu(z)$, the depth dependent slow muon negative stopping rate, and $Y_{\Sigma k}$, the ^{36}Cl production coefficient from absorption of slow negative muons (Eq. A.47 in Appendix A.3). Different authors propose different ways of calculating both parameters (Gosse and Phillips, 2001; Heisinger et al., 2002; Stone et al., 1998). We follow the approach of Gosse and Phillips (2001) and Heisinger et al. (2002) to calculate $\Psi_\mu(z)$ (Eq. A.48 in Appendix A.3), with a slow muon negative stopping rate at the surface $\Psi_\mu(0)$ of 190 μ g^{-1}a^{-1} (Heisinger et al., 2002). Among the parameters that serve to calculate $Y_{\Sigma k}$ (Eq. A.49 in Appendix A.3), the branching ratio $f_{n,k}$ and the compound factor $f_{c,k}$ are badly constrained. Values for $f_{n,k}$ in the literature differ considerably (Dockhorn et al., 1991; Fabryka-Martin, 1988; Heisinger et al., 2002). We have taken the experimentally determined values published by Heisinger et al. (2002) ($f_{n,^{40}Ca} = 4.5\pm0.5\%$ and $f_{n,^{39}K} = 3.5\pm0.5\%$), since they are in good agreement with the mean of previously published values. We calculate the compound factor $f_{c,k}$ with the "Fermi-Teller Z-law" (Charalambus, 1971) (Eq. A.21 in Appendix A.2.1 and Eq. A.50 in Appendix A.3) because it takes into account the bulk rock composition. That this is an approximate calculation is indicated by the 25% uncertainty assigned to $f_{c,k}$ by Gosse and Phillips (2001).

Radiogenic. The radiogenic ^{36}Cl production is calculated according to Fabryka-Martin (1988) and CHLOE (Phillips and Plummer, 1996). It is not related to cosmic radiation and is therefore independent of sample depth and surface exposure duration, but starts with the formation of the rock. Spontaneous fission of ^{238}U and (α,n) reactions on nuclei of light elements, where the α-particles are produced during U and Th decay, generate a flux of neutrons. If slowed down to the low-energy range, the neutrons can be captured by ^{35}Cl to produce ^{36}Cl. The radiogenic ^{36}Cl production depends therefore on the U and Th content in the bulk rock. Usually, its contribution in a surface sample is insignificant relative to production by other mechanisms.

Partly dissolved samples. All published cosmogenic production calculations and calculator applications, e.g. CHLOE (Phillips and Plummer, 1996), consider only the case that ^{36}Cl is extracted from a bulk rock which has not undergone any compositional changes by chemical pretreatment. In the following we call the part of rock dissolved for ^{36}Cl extraction the "target fraction". This can be separated minerals or parts of a whole rock. Compositions of bulk rock and target fractions can be considerably different, even in the case that only a few percent of the bulk rock has been leached. When working with target fractions, we must consider that the flux of low-energy neutrons is controlled by the bulk composition of the rock, while the ^{36}Cl production in the target fraction is governed by the local target element concentration. We take this into account in the calculations as follows: the macroscopic low-energy-neutron distribution is calculated from the bulk rock composition assuming that it is a homogeneous material (e.g. Eqs. A.11 and A.32, and similar for the macroscopic slow negative muon absorption, Eq. A.50 in Appendix), while the production of ^{36}Cl due to all reaction types is calculated with the target element concentrations released in the dissolved target fractions (Eqs. A.5, A.7, A.30 and A.50 in Appendix). The determination of the target element concentrations for the spallogenic and the muonic production mechanisms (Ca, K, Ti and Fe) is described in section 4.2.3. The target element for the low-energy neutron induced ^{36}Cl production is Cl, which was determined from the AMS measurements.

Scaling factors. The altitudinal and latitudinal scaling factors for nucleogenic and

muonic reactions were calculated in CosmoCalc (Vermeesch, 2007) using the scaling method of Stone (2000). We obtain $S_{el,s} = 4.553$ and $S_{el,\mu} = 2.308$ for sample SI43. The time dependence of the magnetic field variations has not been taken into account. It would yield a relatively unimportant correction of the local production rate of sample SI43 and is irrelevant for the comparison between WR SI43 and PLG SI43, since it would be equally applied to both fractions. Methods to integrate temporal variations of the production rates can be found e.g. in Dunai (2001), Lifton et al. (2005) and Desilets et al. (2006b).

Fossil and non-fossil ^{36}Cl components. The ^{36}Cl concentrations that are expected in the sequentially dissolved fractions of sample SI43 were calculated with the independently determined "fossil" exposure duration of 10 ± 3 ka, based on K-Ar (section 4.2.1). We also take into account the ^{36}Cl accumulation at a depth of 250 cm for the time since the overlying flow has covered the surface, 10 ± 3 ka. We call this the "non-fossil" component. The recent cosmogenic ^{36}Cl production on the cliff face is considered to be negligible, as discussed in section 4.2.1. For the overlying lava flow we assume a density of 2.5 g cm^{-3}. This value corresponds to the density we typically determined experimentally for basaltic surface samples. Less porous deeper basalt might in reality be denser. However, we tested the effect of assuming a density of 3 g cm^{-3} for the overlying lava flow and found that it would lead to insignificant differences in the final results. Finally, the theoretical ^{36}Cl concentrations in each extraction step of sample SI43 are obtained by adding the fossil and non-fossil component.

Calculated ^{36}Cl exposure ages. The ^{36}Cl exposure ages of the sequentially dissolved fractions of sample SI43 were calculated according to Eq. 4.5, using the measured ^{36}Cl concentrations of each extraction step, which were corrected for radiogenic and non-fossil ^{36}Cl components.

4.4 Results

Fig. 4.3 shows the ^{36}Cl concentrations measured in each extraction step of the whole rock (WR) and plagioclase (PLG) fractions of sample SI43. Fig. 4.4 and 4.5 show the corresponding Cl and target element (Ca, K, Ti and Fe) concentrations. All concentrations are listed in Table 4.3.

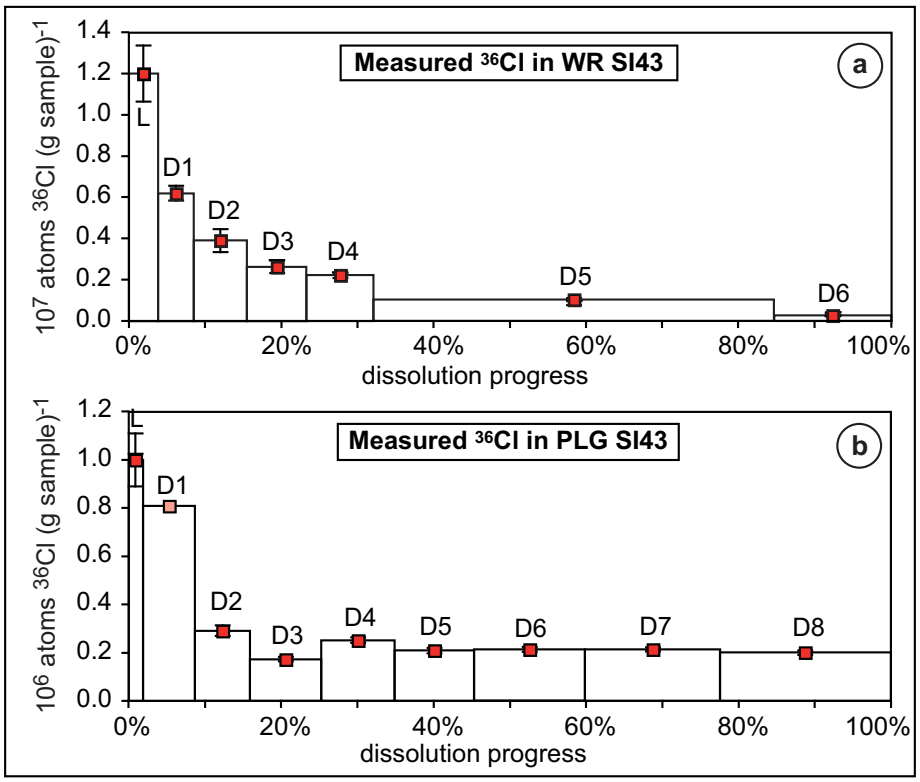

Figure 4.3: *Measured number of atoms ^{36}Cl per g sample in each dissolution step of (a) whole rock and (b) plagioclase of sample SI43. The value of D1 of PLG is not reliable because its AgCl yield was insufficient for the AMS measurement, it can only be seen as indicative of the trend. Uncertainties are shown. In most cases they are smaller than the plotted squares.*

In the case of WR, ^{36}Cl concentrations decrease gradually from 12×10^6 atoms ^{36}Cl (g sample)$^{-1}$ in the first step to 0.2×10^6 atoms ^{36}Cl (g sample)$^{-1}$ in the last (Fig. 4.3a). The same pattern, but more accentuated, is observed for Cl, with concentrations decreasing from 5900 to 9 ppm (Fig. 4.4a). For the target elements Ca, K, Ti and Fe the trends are different (Fig. 4.5a): Ca release is strongest, at around 10%, in the HNO_3-leaching step (L) and in the last dissolution step (D6). At intermediate steps concentrations range between

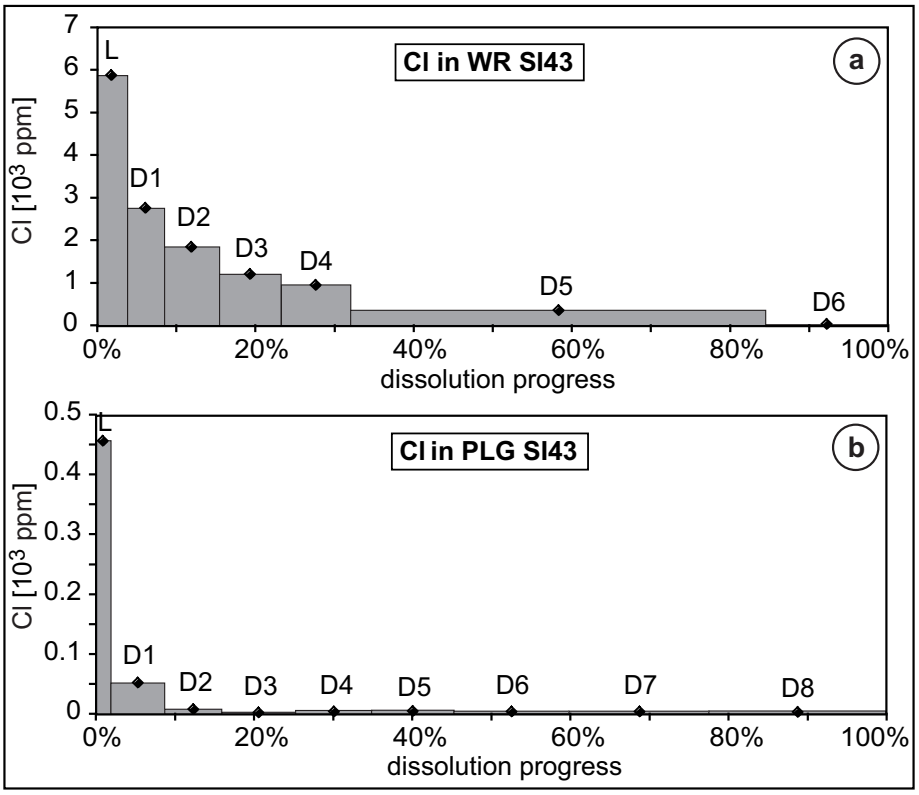

Figure 4.4: *Cl concentration in each extraction step of (a) whole rock and (b) plagioclase of sample SI43.*

4.2% and 7.3%. Little K and Ti is released in step L. After a peak of 2.1% K in step D2 its leached concentration decreases to 0.3%. Ti also shows a slight decrease from 1.1% to 0.7%. Fe release is high in step L (14.6%) and D1 (18.5%), afterwards it decreases to 5.3% in step D6.

In the case of PLG, extraction patterns differ from those for WR for all elements throughout the dissolution series. Measured ^{36}Cl concentrations in step L are 12 times lower than for WR. They start at 1×10^6 atoms ^{36}Cl (g sample)$^{-1}$, decrease and reach a plateau of stable ^{36}Cl concentrations at around 2×10^5 atoms ^{36}Cl (g sample)$^{-1}$ after 16% dissolution (D2) (Fig. 4.3b). The value of step D1 is not reliable since insufficient AgCl was precipitated for the AMS measurement, it can only be seen as indicative of the trend. Cl concentrations are as high as 455 ppm in step L, but drop to 1-3 ppm after step D2 (Fig. 4.4b). Extraction patterns of Ca, K, Ti and Fe are very similar to ^{36}Cl and Cl (Fig. 4.5b), except that Ca and K concentrations are very low in step L and their maximum

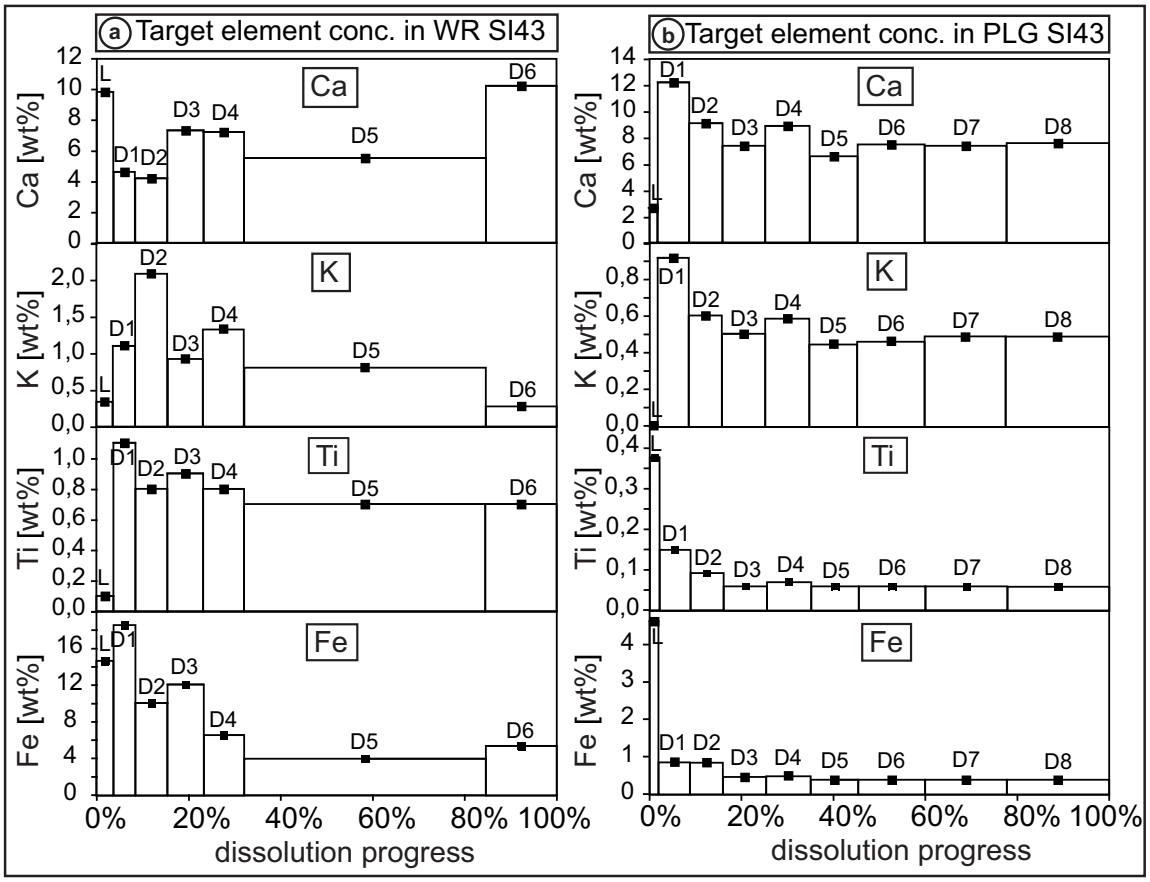

Figure 4.5: *Target element concentrations in each extraction step of (a) whole rock and (b) plagioclase of sample SI43.*

release is in step D1 (12.2% Ca and 0.9% K), while Ti and Fe are most strongly released in step L (0.4% Ti and 4.8% Fe). All four element concentrations remain constant after step D2: around 7.5% Ca, 0.5% K, 0.1% Ti and 0.5% Fe.

Table 4.5: *Calculated ^{36}Cl exposure ages for all extraction steps of sample SI43 (whole rock and plagioclase). The calculated non-fossil ^{36}Cl component ($^{36}Cl_{calc,non-fossil}$) corresponds to the ^{36}Cl production in 250 cm depth after the sample surface was buried. The total calculated ^{36}Cl concentrations (Total $^{36}Cl_{calc}$) comprises the ^{36}Cl production during surface exposure and after burial. The measured ^{36}Cl concentrations (see Table 4.3) are here corrected for the radiogenic and the non-fossil component ($^{36}Cl_{m,corr}$), which served to calculate the exposure ages.*

Sample material	Dissol. step	Dissol. progress	$^{36}Cl_{calc,non-fossil}$ [10^6 atoms g^{-1}]	Total $^{36}Cl_{calc}$ [10^6 atoms g^{-1}]	$^{36}Cl_{m,corr}$ [10^6 atoms g^{-1}]	Calculated exposure ages [ka]
WR SI43	L	4%	0.94±0.25	9.8±2.7	10.87±1.38	12.5±2.0
	D1	9%	0.44±0.12	4.6±1.3	5.63±0.38	13.6±1.7
	D2	16%	0.298±0.081	3.21±0.91	3.51±0.56	12.3±2.4
	D3	23%	0.200±0.054	2.17±0.62	2.35±0.32	12.1±2.1
	D4	32%	0.159±0.043	1.76±0.50	1.98±0.14	12.6±1.5
	D5	85%	0.062±0.017	0.73±0.20	0.916±0.075	14.0±1.7
	D6	100%	0.0171±0.0058	0.275±0.079	0.197±0.013	7.6±0.8
PLG SI43	L	2%	0.076±0.022	0.81±0.41	0.91±0.11	12.7±6.2
	D1	9%	0.0277±0.0090	0.42±0.22	(0.775±—)	
	D2	16%	0.0154±0.0054	0.26±0.14	0.270±0.023	11.1±3.9
	D3	25%	0.0119±0.0043	0.20±0.10	0.155±0.012	8.1±2.4
	D4	35%	0.0147±0.0051	0.25±0.10	0.231±0.014	9.9±2.1
	D5	45%	0.0110±0.0038	0.185±0.081	0.193±0.014	11.1±2.7
	D6	60%	0.0122±0.0042	0.206±0.066	0.195±0.013	10.0±1.3
	D7	78%	0.0121±0.0042	0.205±0.068	0.196±0.011	10.2±1.1
	D8	100%	0.0122±0.0042	0.208±0.065	0.182±0.013	9.3±1.0

In Table 4.5, the calculated non-fossil, i.e. post-burial ^{36}Cl component and the total calculated ^{36}Cl concentrations of each extraction step are listed. The non-fossil component accounts for 5 - 10% of the total calculated ^{36}Cl. Also given in Table 4.5 are the measured ^{36}Cl concentrations, corrected for the radiogenic and the non-fossil components, and the resulting surface exposure ages from the extraction steps of WR and PLG SI43. The calculated ages of Cl-rich steps L - D5 of WR and of the Cl-poor steps D4 - D8 of PLG are shown in Fig. 4.6 together with the corresponding mean values, the independent K-Ar age and the ^{3}He exposure age from cogenetic pyroxene phenocrysts (see section 4.2.1). High uncertainties in the calculated cosmogenic ages result from the error propagation of the analytical uncertainties in the composition of the different fractions, which arises from the mass balance calculations of the target element concentrations in the dissolved fractions. Individual values are very consistent for WR and PLG, respectively, and the mean values of both are significantly different, 12.8 $\pm$ 0.8 ka in the case of WR and 10.1 $\pm$ 0.6 ka in the case of PLG (1 σ standard deviation).

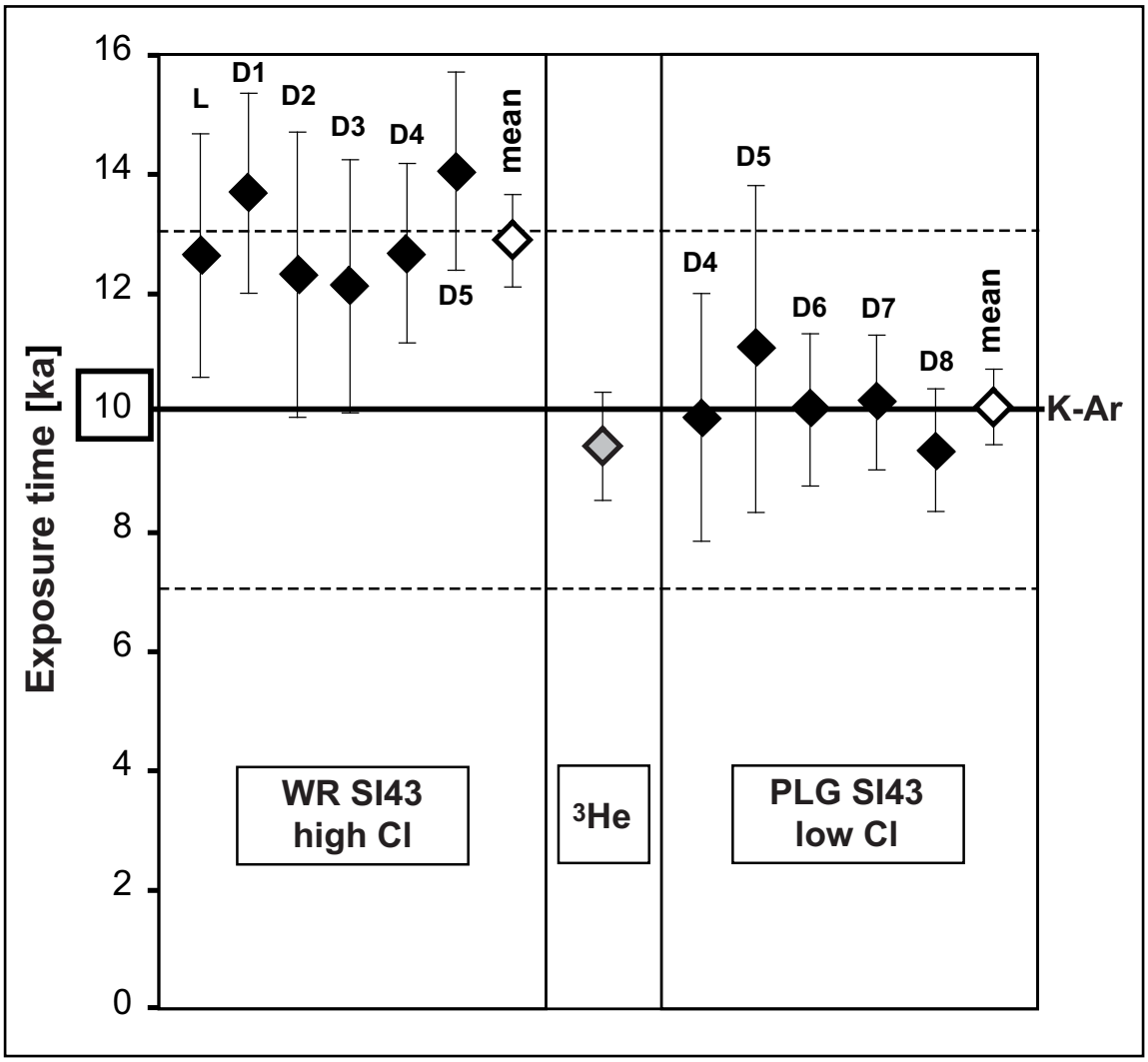

Figure 4.6: *^{36}Cl exposure ages calculated from the Cl-rich extraction steps of WR SI43 and the Cl-low extraction steps of PLG SI43, their respective mean values, independent K-Ar age and ^{3}He exposure age in cogenetic pyroxene phenocrysts of sample SI43 calculated with the production rate of Blard et al. (2006).*

Table 4.6: *^{36}Cl contribution from different production mechanisms in each extraction step of sample SI43 (whole rock and plagioclase). For details on how calculations are done see section 4.3 and the Appendix. Only the fossil component is taken into account.*

Production mechanism	Spall. of Ca	Spall. of K	Spall. of Ti	Spall. of Fe	**Total spall.**	Thermal neutron capture	Epitherm. neutron capture	**Total low-energy-neutron capture**	**Slow negative muon capture**	**Radiogenic**
Production parameter (SLHL)	48.8±3.4[a] (Stone et al., 1996)	162±24[a] (Evans et al., 1997)	13±3[a] (Fink et al., 2000)	1.9[a] (Stone, 2005)				626±46[b] (Phillips et al., 2001)	190[c] (Heisinger et al., 2002)	
WR SI43										
L	2.9%	0.3%	0.01%	0.2%	**3.5%**	80.4%	14.4%	**94.8%**	**0.2%**	**1.5%**
D1	2.8%	2.3%	0.2%	0.5%	**5.8%**	78.5%	14.1%	**92.5%**	**0.3%**	**1.5%**
D2	3.7%	6.2%	0.2%	0.4%	**10.4%**	74.5%	13.3%	**87.8%**	**0.4%**	**1.4%**
D3	9.5%	4.0%	0.3%	0.6%	**14.4%**	70.8%	12.7%	**83.5%**	**0.8%**	**1.3%**
D4	11.3%	7.0%	0.3%	0.4%	**19.0%**	66.8%	12.0%	**78.7%**	**1.0%**	**1.2%**
D5	20.0%	9.8%	0.7%	0.6%	**31.0%**	56.1%	10.0%	**66.1%**	**1.8%**	**1.0%**
D6	79.3%	7.2%	1.4%	1.6%	**89.6%**	3.2%	0.6%	**3.8%**	**6.6%**	**0.1%**
PLG SI43										
L	9.5%	0.0%	0.4%	0.7%	**10.5%**	74.1%	13.3%	**87.3%**	**0.8%**	**1.4%**
D1	63.8%	15.8%	0.2%	0.2%	**80.0%**	12.2%	2.2%	**14.3%**	**5.5%**	**0.2%**
D2	74.4%	15.8%	0.2%	0.3%	**90.7%**	2.5%	0.4%	**2.9%**	**6.3%**	**0.1%**
D3	76.1%	16.7%	0.2%	0.2%	**93.1%**	0.3%	0.1%	**0.4%**	**6.5%**	**0.0%**
D4	75.6%	16.3%	0.2%	0.2%	**92.3%**	1.1%	0.2%	**1.3%**	**6.4%**	**0.0%**
D5	74.8%	16.6%	0.2%	0.2%	**91.7%**	1.6%	0.3%	**1.9%**	**6.4%**	**0.0%**
D6	76.2%	15.6%	0.2%	0.2%	**92.1%**	1.2%	0.2%	**1.4%**	**6.5%**	**0.0%**
D7	75.7%	16.3%	0.2%	0.2%	**92.4%**	1.0%	0.2%	**1.1%**	**6.5%**	**0.0%**
D8	78.1%	16.4%	0.2%	0.2%	**94.9%**	0.5%	0.1%	**0.6%**	**4.6%**	**0.0%**

[a] [atoms ^{36}Cl (g target element)$^{-1}$ a^{-1}]
[b] [neutrons (g air)$^{-1}$ a^{-1}]
[c] [μ g^{-1} a^{-1}]

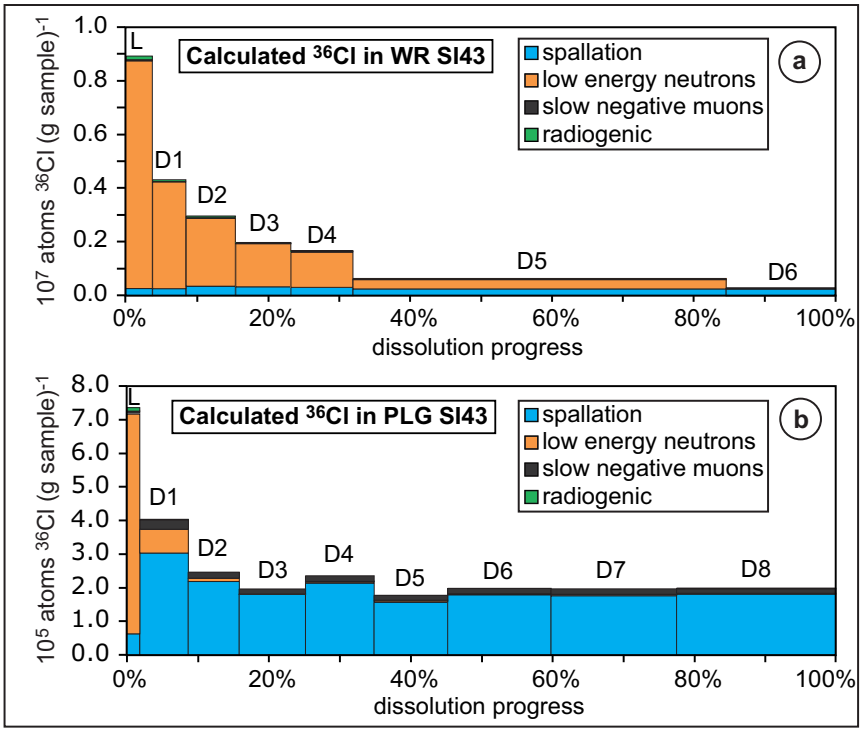

Figure 4.7: *Calculated number of atoms ^{36}Cl per g sample from the different production mechanisms in each extraction step of (a) whole rock and (b) plagioclase of sample SI43. For details on how calculations are done see section 4.3 and the Appendix. Only the fossil component is taken into account.*

Fig. 4.7 and Table 4.6 show the calculated ^{36}Cl contributions from the four production mechanisms (spallation, low-energy neutrons, slow negative muons, and radiogenic) in each extraction step of WR and PLG. Here, we only consider the fossil ^{36}Cl component in order to simplify the discussion. In the case of WR, ^{36}Cl from capture of low-energy neutrons on ^{35}Cl is the dominant production mechanism in the first 85% dissolved. It accounts for 98-66% of the total production. On the contrary, in PLG, after only 9% dissolution, more than 90% of the ^{36}Cl is accounted for spallation.

The same sequential dissolution experiment was performed on the whole rock grains of sample IS9 (Table 4.3, Fig. 4.8). As expected, its ^{36}Cl/^{37}Cl values are close to the blank confirming that this sample has essentially not been exposed to cosmic radiation. Some observations can still be made in terms of how ^{36}Cl and Cl concentrations change through the course of the sequential dissolution. Both decrease following a very similar trend to

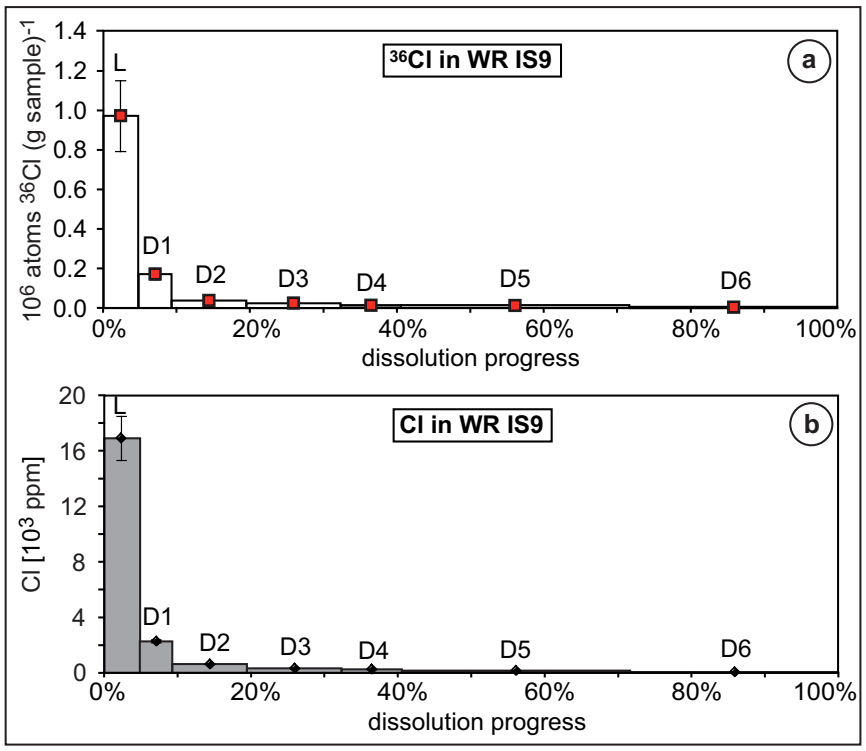

Figure 4.8: *(a) Measured number of atoms ^{36}Cl and (b) Cl concentration in each dissolution step of sample IS9.*

WR SI43, with ^{36}Cl concentrations from 97×10^4 atoms ^{36}Cl (g sample)$^{-1}$ to 0.23×10^4 atoms ^{36}Cl (g sample)$^{-1}$ and Cl concentrations from almost 17000 to 27 ppm. Although 3 times more Cl is released in step L compared to WR SI43, the amount of Cl in the bulk rock of both samples is very similar (section 4.2.3 and Table 4.4). The different amounts of Cl released in the corresponding extraction steps of WR SI43 and IS9 could be due to slightly different grain size fractions (140-400 μm for SI43 and 250-500 μm for IS9) used for processing the two samples. It is interesting to note that Cl is leached faster from IS9, processed with the bigger grain size fractions. Hence, ^{36}Cl concentrations in WR SI43 and IS9 cannot be compared directly but rather it makes sense to look at ^{36}Cl/Cl ratios (Table 4.7). For WR SI43, the ratios are in the range of 13×10^{-14}, where Cl is high (steps L to D5). In the last step (D6), where the Cl concentration is very low, the ratio is one order of magnitude higher. By comparison, the ^{36}Cl/Cl ratios of sample IS9 are in the range of 0.3×10^{-14}.

Table 4.7: *^{36}Cl/Cl ratios in each extraction step of WR SI43 and WR IS9. They were calculated in terms of measured number of atoms of ^{36}Cl and of Cl, both determined from the AMS measurements (see Table 4.3).*

Sample material	Dissol. step	Dissol. progress	^{36}Cl/Cl [10^{-14}]
WR SI43	L	4%	11.99
	D1	9%	13.18
	D2	16%	12.44
	D3	23%	12.76
	D4	32%	13.82
	D5	85%	17.44
	D6	100%	141.04
WR IS9	L	5%	0.34
	D1	9%	0.45
	D2	20%	0.34
	D3	32%	0.42
	D4	41%	0.30
	D5	72%	0.31
	D6	100%	0.51

4.5 Discussion

Why is ^{36}Cl released differently throughout the sequential dissolution of WR and PLG SI43? In WR, capture of low-energy neutrons by ^{35}Cl dominates ^{36}Cl production until 85% of the sample has been dissolved (Fig. 4.7). This production mechanism is directly related to the concentration of Cl: the higher the Cl concentration in the dissolved fraction of the sample the higher the ^{36}Cl production by capture of low-energy neutrons. A Cl concentration as low as 20 ppm would still result in 8% of the ^{36}Cl being derived from low-energy neutrons in the case of WR SI43. In general, the contribution of the low-energy-neutron induced ^{36}Cl to the total ^{36}Cl production will vary from rock to rock, depending on the target element concentrations and on the bulk composition. During the sequential dissolution of WR, the Cl content decreases gradually still being high (334 ppm) even when 85% of the sample had been dissolved. However, in the case of PLG, the Cl concentration diminishes rapidly from a high to very low concentrations (1-3 ppm) after only 16% dissolution.

In order to locate the mineralogical site of high Cl concentrations in the bulk rock, we did an electron microprobe analysis of a thin section of sample SI43 at the University of Nancy, France. This analysis is only qualitative, because detection limits for Cl are high, around 300 ppm. However, Cl concentrations of around 4000 ppm were measured at some spots in the glassy and fine-grained groundmass. Moreover, grain aliquots, taken before and after each extraction step and observed with a scanning electron microscope and a binocular microscope, showed that the groundmass of the whole rock dissolved first, followed by the plagioclase and clinopyroxene phenocrysts (Fig. 4.9). These observations strongly suggest that the release of Cl and ^{36}Cl is associated with the groundmass dissolution.

Previous authors have assumed that most of Cl in rock samples was contained in fluid inclusions (Bierman et al., 1995; Evans et al., 1997). They extracted the Cl by crushing the samples to expose the inclusions and washing them in water. In doing so, Bierman et al. (1995) isolated the ^{36}Cl produced by low-energy neutron capture on ^{35}Cl from granitic whole rocks for erosion rate estimations, and Evans et al. (1997) separated spallogenic from low-energy neutron derived ^{36}Cl in K-feldspars in order to calibrate the K spallation production rate. In our study, the resolution of the electron microprobe analysis is not high enough to determine whether the highest Cl concentrations can be assigned to fluid inclusions. In the PLG phenocrysts no fluid inclusions were observed under the binocular microscope. Moreover, the phenocrysts are practically free from Cl after 16% dissolution implying that minimal Cl is located in the inner part of the minerals. It is not clear whether the higher Cl and ^{36}Cl concentrations observed in the early steps of PLG are due to groundmass powder sticking to the grains or to atmospheric Cl. While only small traces of groundmass could be identified by checking the purity of the separated plagioclase grains under a binocular microscope, the relatively high Fe and Ti concentrations in step L and slightly increased Ca and K concentrations in step D1 can be taken as evidence of groundmass. Subsequent to step D2, the values of the four elements are comparatively stable and therefore represent the composition of the PLG phenocrysts. Slight compositional variations could be due to zoning of the phenocrysts. This explains why the total ^{36}Cl concentrations reach a plateau where, contrary to WR, the dominant production mechanism

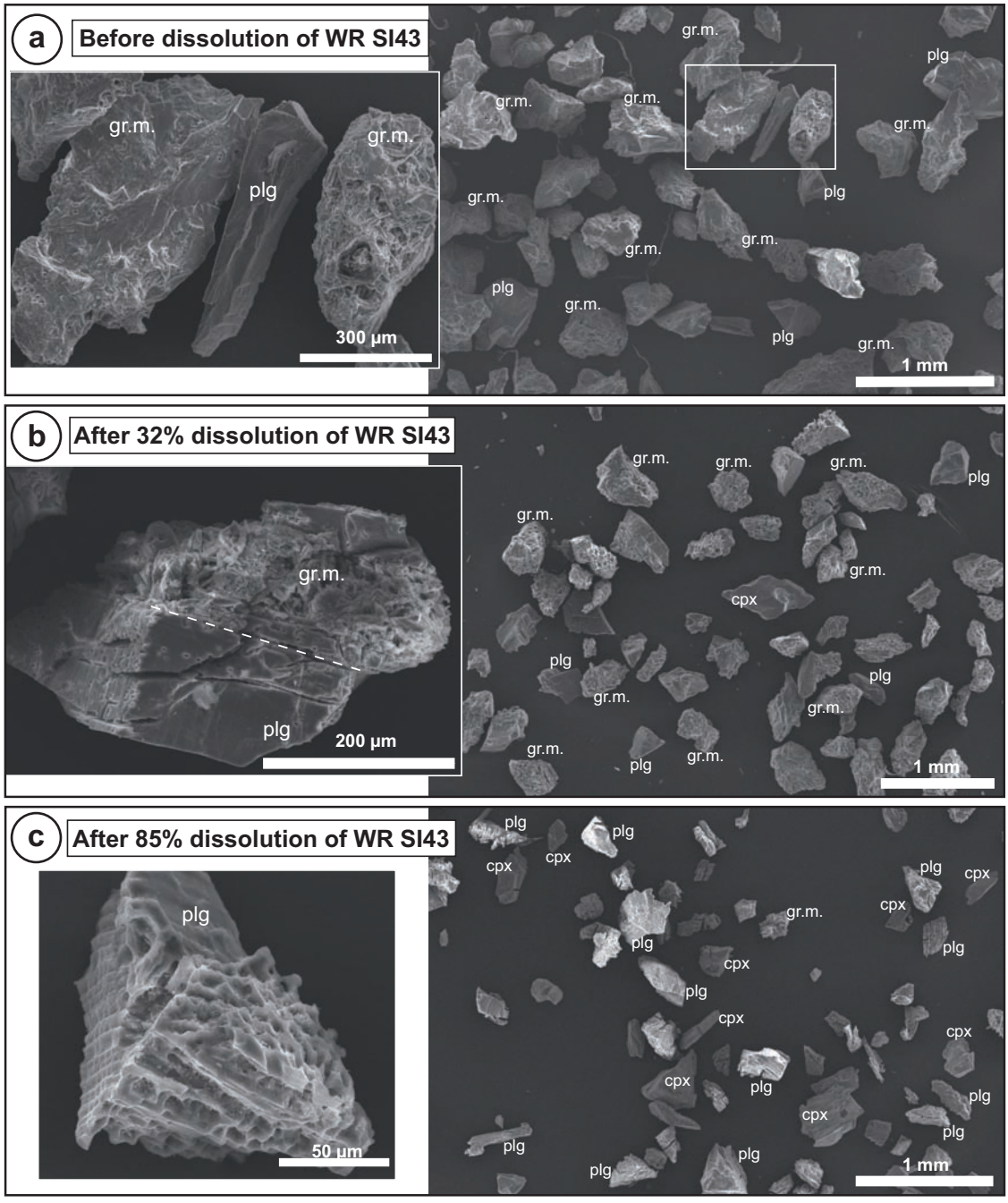

Figure 4.9: *Scanning Electron Microscope pictures of WR SI43 grains (a) before dissolution, (b) after 35% dissolution and (c) after 85% dissolution (gr.m. = groundmass, plg = plagioclase, cpx = clinopyroxene). The fraction of groundmass grains diminishes bit by bit in the course of the dissolution series relative to the phenocrysts.*

is spallation.

Why does whole rock have higher ^{36}Cl exposure ages than plagioclase phenocrysts from the same rock? From the results of the sequential extraction experiments discussed above, we conclude that the high Cl concentrations in the groundmass of the WR are responsible for the overestimation of the exposure age by nearly 30%. Indeed, the exposure age from the Cl-poor PLG is in very good agreement with both K-Ar and ^{3}He ages. Using other published spallation production rates, e.g. PR_{Ca}= 66.8 atoms ^{36}Cl (g Ca)$^{-1}$ a^{-1} (Phillips et al., 2001) instead of 48.8 ± 3.4 atoms ^{36}Cl (g Ca)$^{-1}$ a^{-1} (Stone et al., 1996) would only increase the discrepancy, because the Ca-spallation dominated PLG would have a younger exposure age while the age from the low-energy-neutron dominated WR would only change minimally (PLG: 7.8 ± 0.5 ka, WR: 12.5 ± 0.7 ka according to the exposure age calculations in section 4.4 and Fig. 4.6). Using scaling methods other than Stone (2000) would shift both, WR and PLG, together. Here, we scale the low-energy neutron reactions with the same factors as the spallogenic reactions, as has generally been done (Gosse and Phillips, 2001). However, Desilets et al. (2006b) show that the two production mechanisms require different scaling models, although they do not provide a scaling methodology to take account of this. They state that scaling factors for the low-energy-neutron reactions should be smaller than for spallation above 1500 m. This would, in the case of WR SI43 result in even older exposure ages for WR while not changing the PLG age.

What sources of ^{36}Cl might we have failed to consider? Atmospheric ^{36}Cl comes into consideration. In the atmosphere, ^{36}Cl is produced by spallation on ^{40}Ar and can reach the ground either washed out by precipitation or as dry fallout (Huggle et al., 1996). In order to distinguish absorbed atmospheric from in-situ ^{36}Cl, we cannot directly compare their concentrations but have to normalise to Cl, i.e. look at ^{36}Cl/Cl ratios, because ^{36}Cl behaves physically and chemically together with Cl. Atmospheric ^{36}Cl/Cl ratios range between 10^{-14} and 10^{-12}, depending on the latitude and the distance from the sea (sea salt lowers the atmospheric ^{36}Cl/Cl) (Davis et al., 1998). Since the ^{36}Cl/Cl ratios of WR are on the order of 10^{-13}, an atmospheric contamination with a ratio in the same order or higher could have a significant effect. However, given the hydrophilic nature of Cl, the

atmospheric component should be easily removed in the first extraction steps, because it would be found attached to the grain surfaces. In previous ^{36}Cl studies, samples were usually decontaminated from atmospheric ^{36}Cl by water and dilute $HN0_3$ leaching (e.g. see references in Table 4.1). This was rather done as a precaution, because no atmospheric contamination had ever been proven. Zreda et al. (1991) mention that they did not find any atmospheric Cl contamination after leaching of basalt samples for 2 hours in dilute $HN0_3$, but did not specify how they confirmed this. Stone et al. (1996) conducted a sequential dissolution experiment on limestone and Evans et al. (1997) on K-feldspar, and neither encountered any evidence for atmospheric ^{36}Cl. Recently, Merchel et al. (2008a) compared ^{36}Cl in four replicates of two limestone samples, each pretreated by progressively stronger leaching procedures. They observed a 44% difference between the replicates pretreated with a single water-leach and with two water-leaches. The excess-^{36}Cl was attributed to atmospheric ^{36}Cl. The authors concluded that repeated water-leaching is sufficient to decontaminate limestone from atmospheric ^{36}Cl. However, in the case of WR SI43 the exposure age discrepancies persist until 85% dissolution of the grains and can therefore not be explained by atmospheric ^{36}Cl.

Basalts erupted at Mt. Etna originate from a volatile-rich primitive magma, in which Cl is abundant (Métrich et al., 2004). We hypothesize that ^{36}Cl might be trapped during the rock formation cycle together with Cl from magmatic gases and fluids that already contained ^{36}Cl, e.g. from deep radiogenic production. We call this ^{36}Cl "magmatic" in the following. The in-situ ^{36}Cl/Cl ratio of any sample of magmatic origin would be given by:

$$^{36}Cl_{in-situ}/Cl = {}^{36}Cl_{cosm}/Cl + {}^{36}Cl_{r}/Cl + {}^{36}Cl_{magm}/Cl$$

where Cl is the amount of natural Cl incorporated during rock formation; $^{36}Cl_{in-situ}$ is the total amount of ^{36}Cl being situated in the rock (i.e. excluding atmospheric ^{36}Cl); $^{36}Cl_{cosm}$ is the amount of ^{36}Cl produced by any cosmogenic reaction; $^{36}Cl_{r}$ is the radiogenically produced ^{36}Cl; and $^{36}Cl_{magm}$ is the magmatic ^{36}Cl.

We performed a sequential ^{36}Cl extraction on the shielded sample IS9 to investigate the importance of magmatic ^{36}Cl and to check if it could be another unaccounted-for ^{36}Cl source in sample WR SI43. We assume that ^{36}Cl concentrations in the extraction steps of

sample IS9 are for the most part neither cosmogenic nor radiogenic, because the sample was shielded from cosmic radiation by 2 m rock and because, being less than 400 years old, it is very young with respect to the build-up of radiogenic ^{36}Cl (section 4.2.1). According to the expression given above, this means:

$(^{36}\mathrm{Cl}/\mathrm{Cl})_{IS9} = {}^{36}\mathrm{Cl}_{magm}/\mathrm{Cl}$

where $(^{36}\mathrm{Cl}/\mathrm{Cl})_{IS9}$ is the ratio of measured ^{36}Cl to measured Cl in sample IS9.

Since IS9 and SI43 were both sampled from trachybasaltic pahoehoe lava flows (section 4.2.1, Table 4.4), we assume that $(^{36}\mathrm{Cl}/\mathrm{Cl})_{IS9}$ is also representative for $^{36}\mathrm{Cl}_{magm}/\mathrm{Cl}$ of SI43. The value of $(^{36}\mathrm{Cl}/\mathrm{Cl})_{IS9}$, averaged over all dissolution steps, is 0.4×10^{-14}, which makes up 3% of the mean ^{36}Cl/Cl ratio of WR SI43 being 13.6×10^{-14} (not including extraction step D6 where Cl is very low)(Table 4.7). This magmatic ^{36}Cl is therefore negligible for SI43 and cannot explain the exposure age overestimation of almost 30%. However, for younger samples the fraction of magmatic ^{36}Cl can be much higher, if Cl concentrations are high, and could result in overestimated exposure ages.

Another hypothesis to explain the overestimate of exposure ages for the WR sample is that the calculation of ^{36}Cl production by low-energy-neutron capture on ^{35}Cl gives erroneously low values. In addition to the possibility that the low-energy-neutron production parameter $P_f(0) = 626 \pm 46$ neutrons g^{-1} a^{-1} (Phillips et al., 2001) might be too low, there is the added uncertainty that arises from the fact that the behavior of low-energy neutrons is very complex at the land/atmosphere boundary. This complexity is due to the different composition of the atmosphere and ground surface, resulting in contrasting neutron absorption properties (Phillips et al., 2001; Masarik et al., 2007). As a consequence, the ^{36}Cl production due to Cl is very sensitive to a number of compositional and time dependent external factors that are difficult to estimate accurately for the long time periods in question. The water content of the sample, snow cover and moisture conditions in the rock or in overlying soil have a large influence on the low-energy-neutron flux due to the absorption characteristics and high moderation capacity of hydrogen. For example, Swanson and Caffee (2001) found $P_f(0)$ for "hydrous samples" to be 1166 neutrons (g air)$^{-1}$ a^{-1}, compared to 762 neutrons (g air)$^{-1}$ a^{-1} for samples with low water content. However,

Phillips et al. (2001) conclude in their Fig. 4 that the variation in ^{36}Cl production due to low-energy-neutron capture as a function of water content is small in basalts compared to carbonates. They point out that two mechanisms compete. On the one hand, hydrogen enhances the thermalization of epithermal neutrons due to its high epithermal neutron scattering cross-section. This means that neutrons pass more frequently from the epithermal to the thermal energy range, and that more thermal neutrons can be absorbed by ^{35}Cl to produce ^{36}Cl. On the other hand, hydrogen also absorbs thermal neutrons and thereby reduces ^{36}Cl production. Masarik et al. (2007) calculated numerically that a water content of less than 5% in a rock results in an increase in the neutron flux, whereas higher water contents lead to a decrease. While snow cover has a shielding effect on high-energy neutrons and therefore lowers the spallogenic ^{36}Cl production in a rock (e.g. Schildgen et al., 2005; Benson et al., 2004), as would be the case for the almost Cl-free PLG; it enhances the thermalization of epithermal neutrons, analogous to the effect of water in rock. Masarik et al. (2007) show that snow equivalent to a water cover thickness of up to 20 cm results in a more efficient neutron thermalization just below the rock surface, while a thicker water cover leads to a decrease of the thermal neutron flux at the boundary. In the first case this would result in a higher ^{36}Cl production, hence, disregarding snow cover or external moisture conditions could explain the overestimated exposure age of WR SI43. The PLG fractions, on the other hand, are almost free from Cl. Spallation is therefore the prevailing ^{36}Cl production mechanism (Table 4.6), and should not be affected by these processes.

Ignoring erosion can also lead to misinterpreted ^{36}Cl exposure ages. In a depth profile under the rock surface, the ^{36}Cl production due to low-energy neutrons increases rapidly in the first tens of cm up to a production peak, while spallogenic ^{36}Cl production decreases exponentially (Fig. 4.10a and b). As a consequence, erosion usually results in a higher surface ^{36}Cl contribution from low-energy neutrons but a lower spallogenic ^{36}Cl contribution, compared to non-erosion conditions. Depending on which production mechanism dominates, the total ^{36}Cl concentration at the surface can either increase or decrease. For Cl-rich samples like Mt. Etna lavas, the increase in the ^{36}Cl contribution from low-energy neutrons would prevail as shown in Fig. 4.10c.

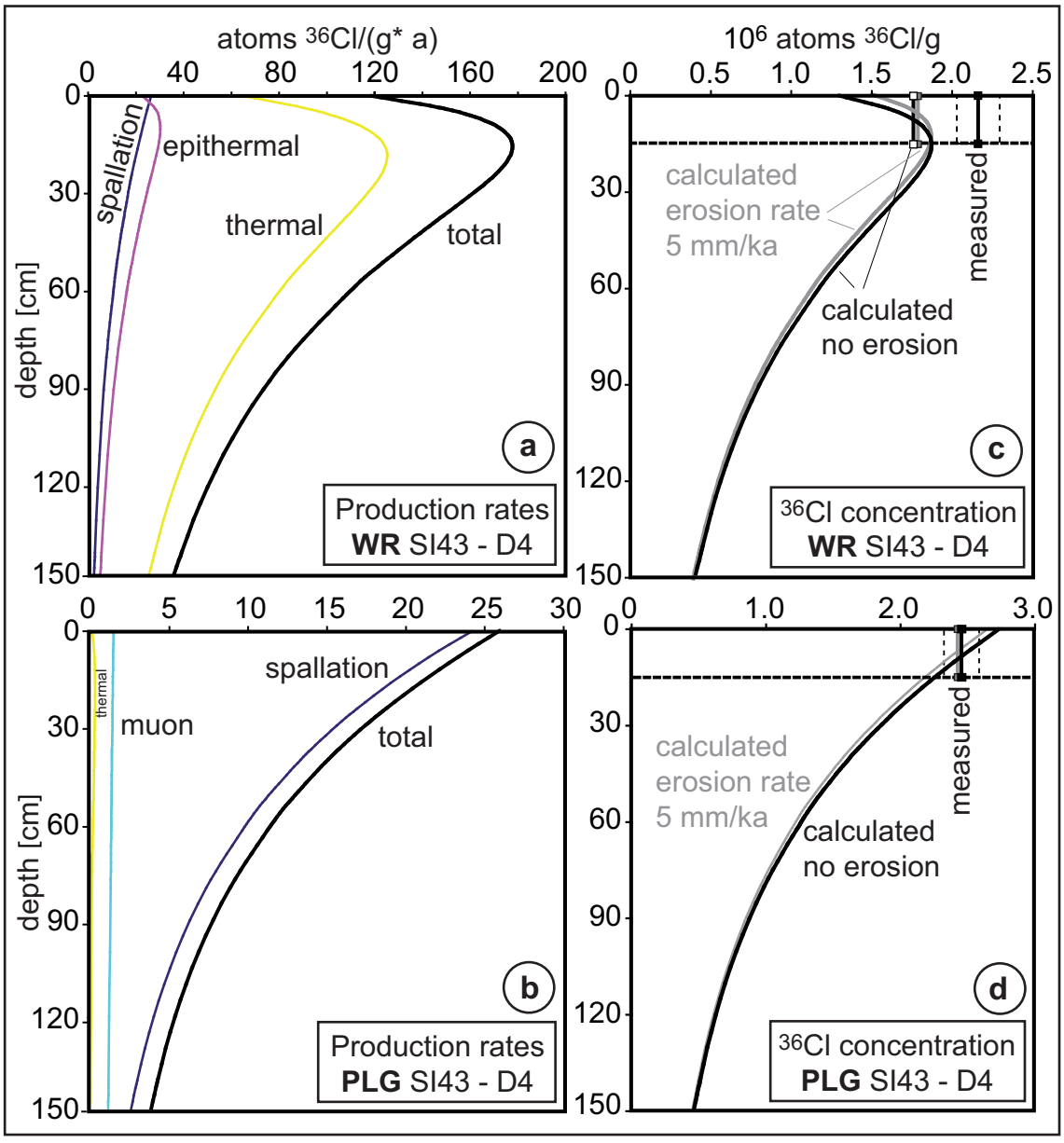

Figure 4.10: *Calculated sample-specific ^{36}Cl production rates versus depth for extraction step D4 of (a) WR SI43 and (b) PLG SI43. The dominant production mechanisms are thermal neutron capture for WR and spallation for PLG. Corresponding ^{36}Cl concentration depth profiles for (c) WR and for (d) PLG without erosion (in black) and with erosion (in grey). Also shown are the measured ^{36}Cl concentrations and the corresponding calculated ^{36}Cl concentrations, integrated over the sample thickness of 15 cm, without erosion (in black) and with erosion (in grey).*

The graphs in Fig. 4.10c and d display the ^{36}Cl concentration pattern below the rock surface for samples WR and PLG SI43, calculated for extraction step D4 of each sample with an exposure age of 10 ka, and integrated over depth. The measured ^{36}Cl concentration in the sample fraction of each is also shown. Two cases are considered, no erosion and a constant erosion rate of 5 mm/ka, which corresponds to a total removal of 5 cm of the initial surface. For WR, for an eroding surface, the peak of maximum ^{36}Cl concentration shifts from 16 cm to 12 cm towards the surface, resulting in a 2% increase in the integrated ^{36}Cl concentration. For PLG, the same erosion rate results in a 1% decrease. Hence, the overestimation in the exposure age from WR cannot be the result of disregarding erosion.

An irregular shape of the surface increases diffusion of low-energy neutrons out of the solid rock into air (neutron leakage) and might lower the low-energy neutron flux below the rock surface by up to 30% according to Zreda et al. (1993) and references therein. Accurate corrections for this effect are difficult to make, especially if lava surface features are very irregular. However, in the case of sample SI43, this would result in an even higher calculated exposure age and increase the discrepancy.

In conclusion, the most probable explanations for the overestimated exposure age from the Cl-rich sample WR SI43 are disregard of snow cover and/or insufficient knowledge of the parameters that constrain ^{36}Cl production by low-energy neutrons, leading to an underestimation of the ^{36}Cl contribution from this mechanism.

4.6 Conclusions

For each extraction step of the 10 ka sample of this study, we calculated the expected ^{36}Cl concentrations including all sources of production. These calculations are compiled in a complete and straightforward Microsoft Excel® spreadsheet (Appendix B). All equations and parameters are presented in Appendix A.

The exposure ages calculated with the measured ^{36}Cl concentrations in the Cl-rich whole rock are systematically almost 30% higher than those in the Cl-low plagioclase. Contamination by an atmospheric ^{36}Cl source can be excluded as an explanation of this discrepancy. The possible existence of a magmatic ^{36}Cl source was also explored and found

to be negligible for this 10 ka sample but should be better constrained in further studies.

We conclude that ^{36}Cl exposure ages from Cl-rich samples can be greatly overestimated due to an underestimation of the sample-specific ^{36}Cl production rates from low-energy neutron capture on ^{35}Cl. Mt. Etna lavas have high concentrations of Cl (around 1000 ppm) associated with the groundmass. But even at 300 ppm Cl a considerable underestimate of the ^{36}Cl production occurs, as shown in the sequential dissolution of the basaltic whole rock. The separated plagioclase phenocrysts, on the contrary, can be decontaminated from Cl by a rigorous pretreatment, so that spallation is by far the dominant ^{36}Cl production mechanism. Therefore, high Cl concentrations in samples that were used for previous ^{36}Cl spallation production rate calibrations could have resulted in underestimated ^{36}Cl contributions from low-energy neutrons and thus in overestimated spallation production rates. This is corroborated by the fact that the lowest spallation production rates from Ca and K were calibrated with Cl-poor samples and the highest ones with Cl-rich samples (Table 4.1): The lowest reported ^{36}Cl spallation production rate from Ca (48.8 atoms ^{36}Cl (g Ca)$^{-1}$ a^{-1}) was calibrated using Ca-feldspars having 2-5 ppm Cl (Stone et al., 1996). In the case of the lowest production rate from K (137 atoms ^{36}Cl (g Ca)$^{-1}$ a^{-1}), the K-richest samples were also the Cl-poorest ones (Phillips et al., 2001) (compositions in Phillips et al. (1996)).

For any type of ^{36}Cl study, exposure age determination or spallation production rate calibration, it is therefore advisable to use separated minerals having low Cl contents instead of magmatic whole rock. Ongoing experiments will determine if other magmatic phenocrysts, e.g. Ca-bearing pyroxene, can also be easily decontaminated from Cl. The major difficulty of avoiding magmatic whole rock for ^{36}Cl studies is that separated minerals are not always available. It remains to be seen if there are effective means to remove Cl, e.g. crushing to very small grain sizes and/or rigorous pretreatments.

Acknowledgments

The contributions of all authors to this work are part of the CRONUS-EU project supported by a Marie-Curie Research Network Contract No: 511927. Aloé Schlagenhauf, Yves

Gaudemer, Silke Merchel, Jurgen Foeken, Luiga Di Nicola and Esmaeil Shabanian helped testing the calculation spreadsheet and gave very useful comments for its improvement. Fred Phillips provided valuable information about the calculations. Devendra Lal gave helpful hints for the discussion. We thank Carmelo Monaco for guiding us during field work. Laure Sevin is acknowledged for compositional measurements at CRPG-SARM. The staff of the LLNL Center for Accelerator Mass Spectrometry assisted greatly with the ^{36}Cl measurements. Thanks to Yves Gally who explained the use of the SEM.

Chapter 5

Calibration of cosmogenic ^{36}Cl production rates by spallation of Ca and K on samples from Mt. Etna (38° N, Italy) and Payun Matru (36° S, Argentina)

Irene Schimmelpfennig[a], Lucilla Benedetti[a], Vincent Garreta[a], Raphaël Pik[b], Pierre-Henri Blard[b], Pete Burnard[b], Didier Bourlès[a], Robert Finkel[a,c], Katja Ammon[d], Tibor Dunai[d]

[a] *CEREGE, UMR 6635 CNRS, Université Paul Cézanne, Europôle de l'Arbois, 13545 Aix en Provence, France*

[b] *CRPG, UPR 2300 CNRS, 15 rue Notre Dame des Pauvres, 54501 Vandoeuvre-lès-Nancy, France*

[c] *Earth and Planetary Science Department, University of California Berkley, CA 94720-4767, USA*

[d] *School of Geosciences, University of Edinburgh, Drummond Street, Edinburgh EH8 9XP, UK*

This chapter will be submitted to *Geochimica Cosmochimica Acta* .

Abstract

Published cosmogenic ^{36}Cl production rates from Ca and K spallation differ by almost 50% (e.g. Gosse and Phillips, 2001). The main difficulty in calibrating ^{36}Cl production rates is to constrain the relative contribution of the various production pathways, which depend on the chemical composition of the rock, particularly on the Cl content. To overcome this difficulty we used separated Ca- and K-rich minerals, very low in Cl to calibrate the production rates from Ca and K. Ca-rich plagioclases and K-feldspars were separated from samples collected on the surfaces of four basaltic lava flows at Mt. Etna (38°N, Italy) and from a trachyte lava flow at Payun Matru volcano (36°S, Argentina), respectively. Their ages were determined by independent methods and range between 0.4 and 32 ka. Sample site elevations range between 500 and 2500 m. Corresponding scaling factors were calculated using five different published scaling models. Four of the scaling methods consider geomagnetic field variations integrated over the respective exposure durations. The resulting five calibration data sets were then analysed using a statistical model in a Bayesian framework. The Bayesian approach allows the major inherent uncertainties to be included in a consistent way. Our best estimate for the spallation production rates from Ca and K, considering all major uncertainties, is 42.2 ± 4.8 atoms ^{36}Cl (g K)$^{-1}$ a^{-1} and 124.9 ± 8.1 atoms ^{36}Cl (g K)$^{-1}$ a^{-1} at SLHL scaled with Stone (2000). Using the other scaling methods results in very similar values. In our study not including the uncertainties in the independent ages results in an increase of the calculated production rate by about 12%, therefore suggesting that inaccurate production rate estimates might result if the main uncertainties are not incorporated in the model.Those results are in agreement with previous production rate estimations both for Ca and K when only low Cl samples are considered. This shows that using samples high in Cl can yield overestimated production rates due to a poorly constrained nature of ^{36}Cl production from low-energy neutrons.

5.1 Introduction

Although in-situ cosmogenic ^{36}Cl is, along with ^{10}Be and ^{26}Al, potentially one of the cosmogenic nuclides most useful for quantifying surface processes in geomorphology (e.g.

review of Gosse and Phillips, 2001), its use is often avoided in preference to ^{10}Be. This even though ^{36}Cl is applicable in a wide range of rock types and minerals (Gosse and Phillips, 2001) while ^{10}Be is almost exclusively measured in quartz. The wide range of applicability of ^{36}Cl arises because ^{36}Cl is produced by a range of production reactions on different target elements (e.g. Fabryka-Martin, 1988; Stone et al., 1998; Gosse and Phillips, 2001). As well as being an advantage, this complexity is also a source of difficulty with ^{36}Cl, because to obtain accurate ^{36}Cl exposure ages all production pathways need to be well quantified. Much progress in ^{36}Cl methodology has been made in recent years. For example, it has been shown that neither contamination by atmospheric ^{36}Cl, nor loss of in situ ^{36}Cl located within the crystal lattices are a problem (Merchel et al., 2008a; Schimmelpfennig et al., 2009). However, a considerable disagreement in published ^{36}Cl production rates (Table 5.1) still exists and significantly degrades the accuracy and reliability of ^{36}Cl dating results. Resolving these discrepancies is one of the goals of the CRONUS-EU and CRONUS-Earth collaborative projects and is the subject of this paper.

The objective of this study is to experimentally calibrate production rates of ^{36}Cl by spallation from Ca and K in such a way that interdependence on competing production mechanisms is avoided and the dependence on scaling models and exposure history is made transparent. For this purpose, ^{36}Cl concentrations were measured in Ca- and K-rich minerals separated from well-preserved lava surfaces of known exposure history and duration. Two volcanoes were studied: Mount Etna in Italy (38°N) and Payun Matru in Argentina (36°S). Lava flows are especially well suited for investigation of cosmogenic nuclide production rates for several reasons. Their exposure history is easily reconstructed, since for the topmost flow, the exposure age is equal to the formation age; there are several non-cosmogenic methods to determine formation ages independently; and erosion conditions can be controlled by close examination of characteristic surface features.

The target element content of the rock material selected plays a crucial role in determining the suitability of a particular lava flow for production rate calibration, since none of the various ^{36}Cl production reactions and/or production rates is yet well constrained. The use of mineral separates allows the isolation of single ^{36}Cl production pathways, which

is essential for minimizing the contribution of unwanted ^{36}Cl production reactions (Stone et al., 1996; Evans et al., 1997). This is in particular a concern for ^{36}Cl production via the ^{35}Cl(n,γ)^{36}Cl pathway, which depends on the Cl content in the sample. This reaction is difficult to parameterize due to the complex factors affecting the distribution of low-energy neutrons at the land/atmosphere interface (Phillips et al., 2001; Schimmelpfennig et al., 2009). Using mineral separates effectively circumvents this difficulty, because the pure minerals used can be selected to have very low Cl contents compared to whole rock samples (Schimmelpfennig et al., 2009). Another advantage of the use of minerals from Mt. Etna and Payun Matru lavas is that the large variation of Ca and K concentrations present makes it possible to derive both production rates in one calibration exercise.

In order to compare production rates determined at different locations in surfaces of different age, it is necessary to scale the results to a common reference place and time, typically sea level, high latitude at the present time (SLHL). The same scaling methods then allow the SLHL reference production rates to be back-scaled to any sample site on earth. Balco et al. (2008) point out that, in use, SLHL reference production rates must be scaled in the same way that they were originally calculated. While in this study we do not seek to assess the validity of the different published scaling methods, we do juxtapose the calibrated spallation production rates normalized with five different published scaling methods (Stone, 2000; Dunai, 2001; Desilets et al., 2006b; Lifton et al., 2005, 2008). The main purpose is to determine how sensitive the SLHL production rate results are to the differences in the scaling methods.

Because of the large number of input parameters required to calculate a production rate, it is challenging to assess the extent to which each of these parameters influences the final production rate and its uncertainty. In this study we developed a Bayesian statistical model to address this issue. This statistical model allows taking account of the major uncertainties in the various input parameters, and provides probability distributions for the resultant production rates, which are governed by the input data and their assigned uncertainties.

After reviewing previous ^{36}Cl production rate studies, we present the methodology with

a detailed description of the sample sites, the chemical protocols, the analytical results and the assigned uncertainties. In the third section we discuss the production rate calculations including all scaling methods and the Bayesian statistical analysis used. The resultant production rates for Ca and K spallation are then presented as well as the recalculated ages for the lava flows. The new production rates are compared with previous published values and the discrepancies discussed.

Table 5.1: *Previous published ^{36}Cl production rate studies and their calculation methods.*

Study	Calibrated SLHL production rates[a]	Sample number	Sample material (and Cl content)	Sample locations and independent ages	Scaling method	Calculation method
Zreda et al. (1991)	PR_{Ca} = 76±5* PR_K = 106±8* $PR(^{35}Cl(n,\gamma)^{36}Cl)$ = 307±24	9	Basaltic whole rock, Microcline, Quartz (94-160 ppm Cl)	Latitude 37°-39°N Longitude 119°-113°W Elevation 1400-3800 m Exposure ages 9.7-14.4 ka	Lal (1991)	For each sample: best estimate of one of the 3 production rates, depending on prevailing target element, iteratively solved for the whole dataset. Global value for each PR by least square algorithm in function of the target element concentrations.
Phillips et al. (1996)	PR_{Ca} = 73±5* PR_K = 154±10* $P_f(0)$ = 586±40	33	Whole silicate rocks (6-350 ppm Cl)	Latitude 20°-80°N Longitude 3-160°W Elevation 20-2600 m Exposure ages 3-55 ka	Lal (1991); corrections for temporal variations according to Nishiizumi (1989)	Based on a small number of selected samples: minimizing the coefficient of variation of the ratios PR_K/PR_{Ca} and $P_f(0)/PR_{Ca}$. For the whole dataset: best estimate for PR_{Ca} by minimizing the reduced χ^2 parameter comparing calculated and independent ages.
Stone et al. (1996)	PR_{Ca} = 48.8±1.7	3	Ca-feldspar (2-5 ppm Cl)	Latitude 38.9° N Longitude 112°W Elevation 1445 m Exposure age 17.3 ka	Lal (1991); corrections for temporal variations similar to Nishiizumi (1989)	PR_{Ca} calculated by a standard χ^2 fitting procedure, minimizing the sum of inverse-error-weighted difference between calculated and measured ^{36}Cl concentrations. Uncertainties derived from a 400 point Monte-Carlo error propagation including full analytical uncertainties, ±20% in P_K, $P(^{35}Cl(n,\gamma)^{36}Cl)$ and ±25% in P_μ.
Evans et al. (1997)	PR_K = 170±25*	11	K-feldspar (9-315 ppm Cl)[c]	Latitudes 38° N, 58°N Longitude 120°W, 4°W Elevation 3000-3600 m, 520 m Exposure ages 13.1 ka, 11.6 ka	Lal (1991)	Not specified
Phillips et al. (2001)	PR_{Ca} = 66.8±4.4 PR_K = 137±9 $P_f(0)$ = 626±46	30	Same as Phillips et al. (1996)	Latitude 35°-80°N Longitude 3-160°W Elevation 20-2600 m Exposure ages 3-49 ka	Same as Phillips et al. (1996)	Same as Phillips et al. (1996)
Swanson and Caffee (2001)	PR_{Ca} = 91±5* PR_K = 228±18* $P_f(0)$ = 762±28	37[b]	Whole silicate rocks (42-290 ppm Cl)	Latitude 48°N Longitude 122°W Elevation 10-140 m Exposure age 15.5 ka	Lal (1991)	For each sample: best estimate of either $P_f(0)$, PR_{Ca} or PR_K, depending on the prevailing target element. Mean value for each production rate.
Licciardi et al. (2008)	PR_{Ca} = 52±5	21	Whole basaltic rock (29-61 ppm Cl)	Latitude 64°N Longitude 21-22°W Elevation 20-460 m Exposure ages 4-10 ka	Lal (1991), Stone (2000)	For each sample: PR_{Ca} is iteratively adjusted until the calculated age matches the independent age. Mean value of each of the four lava flows. Grand mean of the four flows with standard deviation of the grand mean as error.

* Values are not corrected for ^{36}Cl production from slow negative muon capture, the others are production rates only from spallation.

[a] Units for PR_{Ca} and PR_K: [atoms ^{36}Cl (g target element)$^{-1}$ a^{-1}] Unit for $P_f(0)$: [neutrons (g air)$^{-1}$ a^{-1}]. Unit for $PR(^{35}Cl(n,\gamma)^{36}Cl)$: [neutrons (g rock)$^{-1}$ a^{-1}]. PR_{Ca} in Licciardi et al. (2008) is corrected for abnormal pressure effects at their calibration site, Iceland; assuming normal pressure conditions results in 57 ± 5 atoms ^{36}Cl (g target element)$^{-1}$ a^{-1}.

[b] Swanson and Caffee (2001): It is not clear if the dataset contains replicates.

[c] Evans et al. (1997): Cl and associated ^{36}Cl was partly released from fluid inclusions by crushing mineral aliquots in order to quantify the ^{36}Cl contribution due to $^{35}Cl(n,\gamma)^{36}Cl$.

5.2 Previous production rate studies

The published ^{36}Cl production rates from Ca and K both differ by up to a factor two. As shown in the compilation of the previous calibration studies in Table 5.1, the production rates from Ca range between 48.8 ± 1.7 atoms ^{36}Cl (g Ca)$^{-1}$ a^{-1} (Stone et al., 1996) and 91 ± 5 atoms ^{36}Cl (g Ca)$^{-1}$ a^{-1} (Swanson and Caffee, 2001), and those from K range between 106 ± 8 atoms ^{36}Cl (g K)$^{-1}$ a^{-1} (Zreda et al., 1991) and 228 ± 18 atoms ^{36}Cl (g K)$^{-1}$ a^{-1} (Swanson and Caffee, 2001).

A direct comparison, however, is not straightforward since in the various studies the methodological approaches concerning the scaling, the chemical protocol, the sample type and the number of samples can differ. To give a striking example, in the just cited minimum and maximum values, the production rates published by Swanson and Caffee (2001) comprise the ^{36}Cl production from spallation and slow negative muon capture (see section 5.4.1 for details) while those by Stone et al. (1996) and Zreda et al. (1991) are pure spallation production rates corrected for the muogenic ^{36}Cl component.

Swanson and Caffee (2001) and Licciardi et al. (2008) have summarized various possible explanations for these discrepancies. These include potential problems related to characterization of the sample sites, i.e. poorly constrained exposure histories (pre-exposure, erosion) and exposure ages; the sensitivity of the local ^{36}Cl production to the temporal variability of the geomagnetic field (especially important for high elevation and low latitude sites); and uncertainties associated with the scaling method used to normalize the local production rates to the reference point at sea level and high latitude. In addition there are difficulties associated with the method by which total ^{36}Cl production is apportioned between the various production mechanisms. These points are briefly outlined here and will be discussed in more detail when are own data are discussed below.

Spatial and temporal scaling. While the correct interpretation of the exposure history and the accuracy of the independent age constraint are difficult to assess for a reader not intimately familiar with the geologic characteristics of the calibration site, the methods used for the spatial and temporal scaling can be compared. The spatial scaling of all previous

calibration studies is based on the method of Lal (1991). In the studies of Stone et al. (1996) and Phillips et al. (1996, 2001), additional corrections for temporal geomagnetic field fluctuations were applied based on the approach in Nishiizumi et al. (1989). The calibration sites of the various studies are dispersed over the northern hemisphere (between latitudes of 20° and 80°) and are situated at altitudes between 10 m and 3800 m. The exposure durations of all samples range between 3 ka and 55 ka. Therefore it could be possible that inaccuracies in the spatial scaling and the ignorance of temporal geomagnetic fluctuations contribute to the differences in the published calibrated production rates.

Another aspect of the relevance of the geographic location has been emphasized in the study of Licciardi et al. (2008) who recognized that the atmospheric pressure anomalies at their sites in Iceland lead to a relatively higher production rate compared to sites with normal pressure conditions. Further discussion about spatial and temporal scaling and recently developed scaling methods will be addressed to in section 5.4.2.

Calibration sample composition. Licciardi et al. (2008) also discuss the importance in the choice of sample composition for the ^{36}Cl extraction and the related difficulty of modeling the distribution of the ^{36}Cl contributions from the various production reactions in samples of complex composition. The presence of numerous target elements in whole rock samples makes it difficult to isolate individual production reactions, so that an underestimate of the importance of one pathway is likely to show up in an overestimate in the importance of other pathways. Although the simple composition found in separated minerals minimizes the influence of ^{36}Cl contributions via production reactions other than the one being to be calibrated, in most of the calibration studies (Zreda et al., 1991; Phillips et al., 1996, 2001; Swanson and Caffee, 2001; Licciardi et al., 2008), whole silicate rocks of divers compositions were used as calibration samples. In the samples used in these studies not only Ca and K but also Cl were abundantly present (up to 350 ppm). As a consequence, the production rates from Ca and K and the production rate for low-energy neutron capture on ^{35}Cl (^{35}Cl(n,γ)^{36}Cl) had to be calibrated simultaneously. This was not possible in the study of Licciardi et al. (2008) where the narrow compositional range in the Iceland basalts did not allow the calibration of more than one unknown production

rate. In this case, Ca was the most abundant target element in the basalts and the Cl concentrations were considered sufficiently low (29-61 ppm) to that $^{35}Cl(n,\gamma)^{36}Cl$ could be regarded as a minor reaction. Therefore, these authors only calibrated the spallation production rate from Ca, and corrected for the ^{36}Cl contributions from the other production reactions using default production rates from the literature.

Instead of using whole rocks, Stone et al. (1996) and Evans et al. (1997), aware of the problems related to high chlorine concentration samples, calibrated their production rates with separated minerals. In Stone et al. (1996), a Ca-feldspar with low K (0.2%) and Cl concentrations (2-5 ppm) was used to determine the spallation production rate from Ca. The resulting value is the lowest so far observed, 48.8 ± 1.7 atoms ^{36}Cl (g Ca)$^{-1}$ a^{-1}. In Evans et al. (1997), high-K feldspars with Cl contents between 9 and 315 ppm were used to determine the production rate from K. To quantify the ^{36}Cl contribution due to the $^{35}Cl(n,\gamma)^{36}Cl$ reaction in the high-K feldspars, the minerals were crushed to release Cl and the related ^{36}Cl from the fluid inclusions. However, the validity and accuracy of this approach remained uncertain and might have contributed to inaccuracy in correction for the ^{36}Cl production from thermal neutrons, which accounted for up to 60% of the total production. This could explain a possible overestimation of the final production rate from K (170 ± 25 atoms ^{36}Cl (g K)$^{-1}$ a^{-1}).

Calibration sample number. The size of the sample set and the diversity of the calibration sites can be of relevance to the quality of the final result. Published sample sets range widely in sampling density e.g. three samples from one single location (Stone et al., 1996), 37 samples from 2 sites (Swanson and Caffee, 2001) or 33 samples from 14 sites (Phillips et al., 1996). In some cases several samples come from various elevations at the same site (e.g. Swanson and Caffee, 2001). Although, a larger dataset might generally be considered to have a higher statistical robustness, the calibration of cosmonuclide production rates with samples from various geographic locations and with varying exposure durations implies the risk of introducing the inaccuracies of the scaling methods in the SLHL production rate. This problem is raised in Balco et al. (2009) and will be discussed in section 5.5.1.

5.3 Methodology

5.3.1 Sampling strategy and site descriptions

The sampling strategy used in this study was designed to counter, as much as possible, the sources of uncertainty outlined in the previous section. To this end the samples were selected to satisfy three important criteria: (1) erosion of the lava surface could be neglected or determined accurately, (2) the age of the lava flow was known or could be dated, and (3) abundant Ca- or K-rich phenocrysts were present in the lava. The two calibration sites were studied: Mt. Etna on the Italian island Sicily and volcano Payun Matru in the Argentinean province of Mendoza (Fig. 5.1). Both volcanoes are situated at mid-latitudes, Mt. Etna in the northern and Payun Matru in the southern hemisphere, at 38°N and 36°S, respectively.

Mt. Etna is the largest active stratovolcano in Europe. The predominant recent Etnean lava types are the so-called etnates, trachybasalts and trachyandesites with abundant plagioclase, clinopyroxene, olivine, and titanomagnetite phenocrysts (Tanguy et al., 1997, and references therein). Payun Matru is part of a volcanic complex belonging to the back-arc volcanism of the Andean range in Argentina. It is characterized by a large ignimbrite emplacement and trachytic and trachyandesitic lava with sanidine, plagioclase and clinopyroxene phenocrysts (Germa et al., 2009, and references herein). All in all, 13 samples were collected, 9 from pahoehoe lava surfaces of four different flows on Mt. Etna and four from blocks of one aa lava flow on volcano Payun Matru. The characteristic surface features of pahoehoe lava cords and aa lava blocks allow checking the erosion conditions. The geographic locations of the calibration sites and the characteristics of all samples are given in Table 5.2.

Both volcanoes have been tectonically stable for the time considered in this study, which means that ^{36}Cl production rates at the individual sample sites have not been subject to altitudinal variations.

Temporary snow cover cannot be excluded at any of the sampling sites. Since, however, snow cover records do not exist for the exposure durations under consideration and any estimates would have great uncertainties, we do not calculate any snow correction, but do

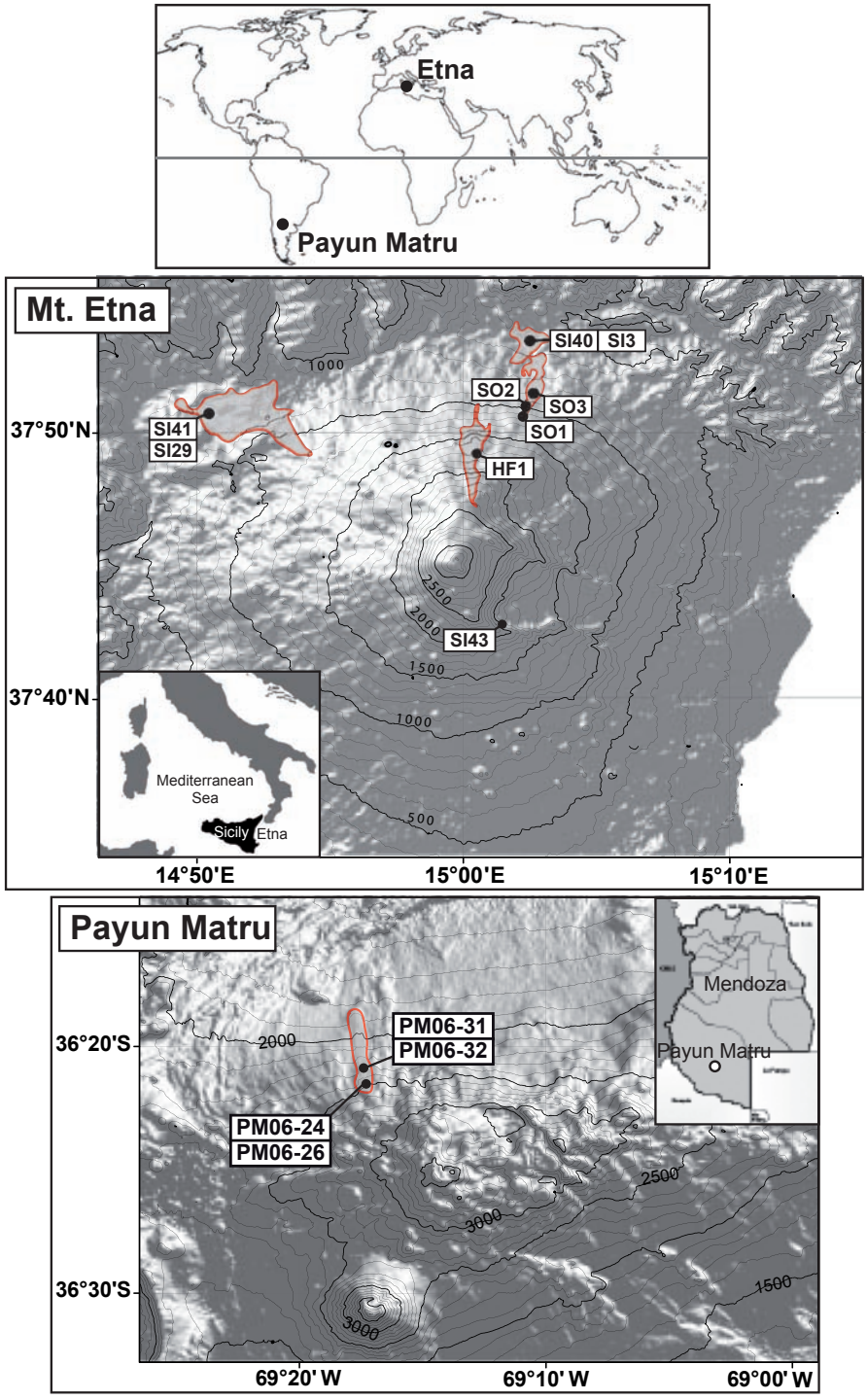

Figure 5.1: *Geographic locations of sample sites at Mt. Etna (38° N) and volcano Payun Matru (36° S).*

discuss the possible implications below.

Sampling sites at Mount Etna:

Historical Flow

The Historical Flow is situated on the northern flank of Mt. Etna between 2300 m and 1000 m altitude. The eruption of this flow is historically recorded from the years 1614-24 A.D. (Tanguy et al., 1997, and references therein). One sample (HF1) was collected in the year 2007, its age thus lies between 383 and 393 years. Due to the very young age the pahoehoe flow tops of its surface are perfectly preserved (Fig. 5.2a).

Solicchiata Flow

Five samples were collected at 4 different altitudes of this flow (SO1, SO2, SO3, SI3, SI40, Fig. 5.2b), which is located on the lower northern flank of Mt. Etna between 1200 m and 500 m. Care was taken to sample only well-preserved surfaces showing minimal indications of erosion. Branca (2003) assigned this flow chronologically to the Il Piano Synthem, whose age is constrained by radiocarbon dates of charred material in tephra layers at 3930 ± 60 years and 15050 ± 70 years (Coltelli et al., 2000). We converted these uncalibrated radiocarbon ages into calibrated calendar ages using the program calib5.0 (Stuiver et al., 2005) yielding 4375 ± 76 (1σ) years for the younger limit and 18350 ± 140 (1σ) years for the older limit.

Piano della Lepre

This site is located at an altitude of 2070 m on the southern shoulder of the "Valle del Bove" collapse structure in the southeastern part of the volcano. Sample SI43 was taken at the top of a 300 m high cliff (sloping at 70°) from a fossil-exposed surface (Fig. 5.2c): it was covered by a younger 250 cm thick overlying flow (Blard et al., 2005; Schimmelpfennig et al., 2009). Pahoehoe features could be distinguished on the covered surface of the fossil-exposed flow, indicating insignificant erosion during exposure. The formation ages of this flow and that of the overlying flow were dated by K-Ar at 20 ± 1 ka and 10 ± 3 ka, respectively (Blard et al., 2005). The exposure time of sample SI43 can be determined by deducing the formation age of the younger flow from the formation age of the older flow,

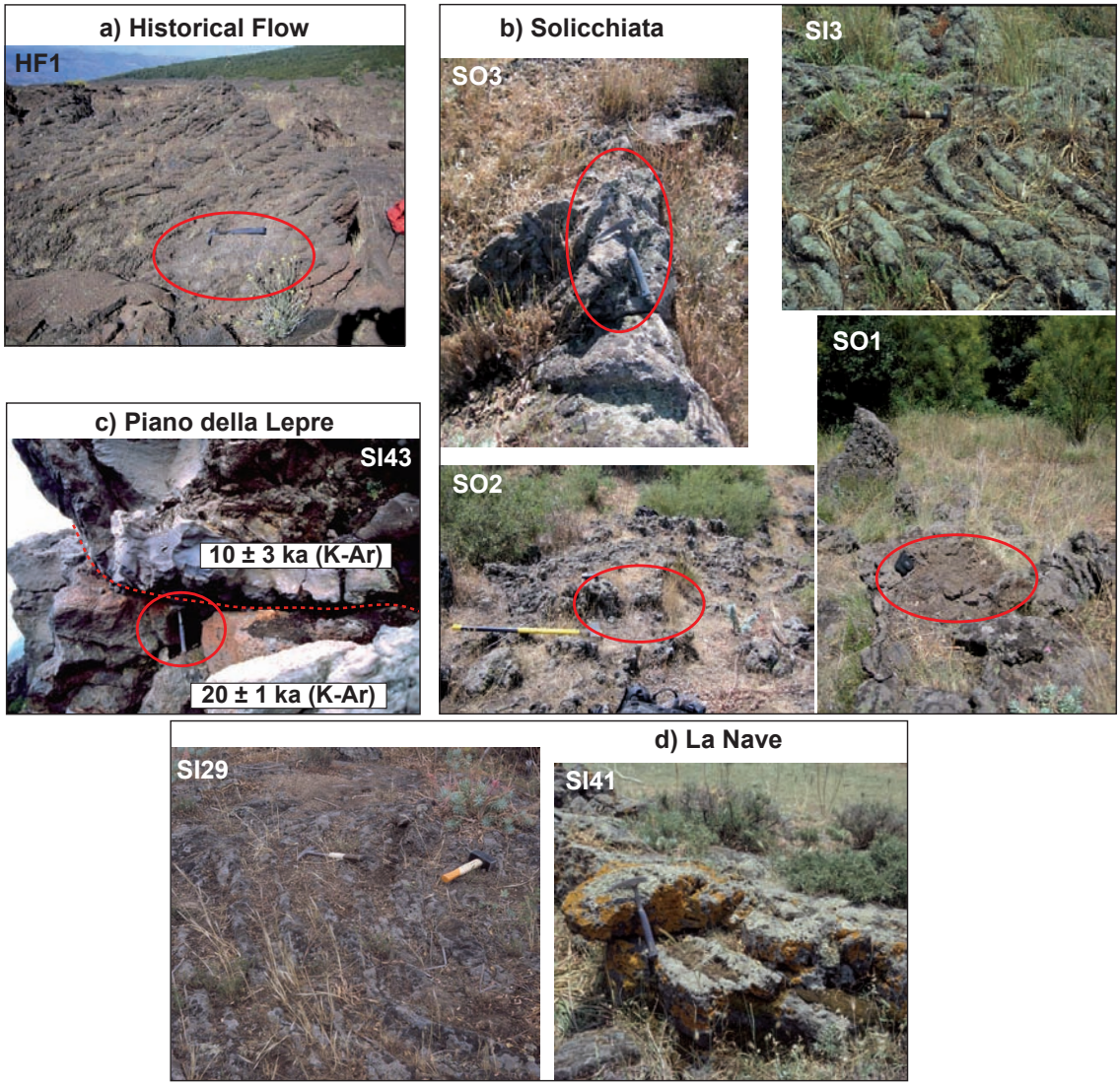

Figure 5.2: *Pictures of sample surfaces at Mt. Etna.*

resulting in 10.0 ± 3.2 ka. ^{3}He was measured in a sample of the cliff some meters below sample SI43, and the cosmogenic component was found to be absent (Blard et al., 2005). This implies a rapid retreat of the cliff wall and therefore negligible recent exposure to cosmic radiation.

La Nave Flow

The La Nave flow is situated at the margin of the northwestern flank of Mt. Etna between 1200 m and 700 m altitude. Two samples (SI41 and SI29) were taken from pahoehoe flow tops (Fig. 5.2d) at altitudes of 820 m and 830 m, respectively. Blard et al. (2005) record

3 age determinations for this flow, 32 ± 4 ka and 33 ± 2 ka from K-Ar dating at two different locations, and 32 ± 2 ka obtained by thermoluminescence. From these three ages, the weighted mean ages by the inverse variances is calculated as follows:

$$\overline{x} = \Big(\frac{x_1}{(\sigma_1)^2} + \frac{x_2}{(\sigma_2)^2} + \frac{x_3}{(\sigma_3)^2}\Big) / \Big(\frac{1}{(\sigma_1)^2} + \frac{1}{(\sigma_2)^2} + \frac{1}{(\sigma_3)^2}\Big) \tag{5.1}$$

with x_1, x_2, x_3 are the individual values and $(\sigma_1)^2$, $(\sigma_2)^2$, $(\sigma_3)^2$ their variances. The standard deviation of the weighted mean is calculated according to

$$\sigma_{\overline{x}} = \sqrt{1/\Big(\frac{1}{(\sigma_1)^2} + \frac{1}{(\sigma_2)^2} + \frac{1}{(\sigma_3)^2}\Big)} \tag{5.2}$$

The resulting age of the La Nave flow is 32.4 ± 1.3 ka.

However, ^{3}He measurements on 2 samples of the flow (Blard et al., 2006) yield significantly younger apparent exposure ages, indicating that this flow has most probably been eroded. Although the surface shows distinguishable pahoehoe cords suggesting erosion is negligible, it is possible that sublayers exist within the lava flow. One of these sublayers could have been removed by erosion, the newly exposed layer underneath appearing pristine. To estimate the erosion rate, the cosmogenic ^{3}He concentration measured in clinopyroxenes of sample SI41 (Blard et al., 2006) was used. Since samples SI29 and SI41 were collected in close proximity (150 m apart from each other) and have indistinguishable ^{3}He (Blard et al., 2005) and ^{36}Cl concentrations (Table 5.4), we assume that both samples experienced the same erosion rate.

The erosion rate ε was obtained by numerical solution of the following equation:

$$N(^3He) = \frac{Q_s\ S_{el,s}\ PR(^3He)\Lambda_f}{\rho\ \varepsilon}(1 - exp\Big(-\frac{\rho\ \varepsilon\ t_{expo}}{\Lambda_f}\Big)) \tag{5.3}$$

where $N(^3He)$ is the measured cosmogenic ^{3}He concentration, (5.27 ± 0.25) × 10^6 atoms ^{3}He g^{-1}; Q_s is the sample thickness integration factor, with a value of 0.89; $S_{el,s}$ is the scaling factor, correcting for spatial and temporal variations of the production rate (Table 5.3); $PR(^3He)$ is the production rate of ^{3}He in olivines and clinopyroxenes normalized to sea level and high latitude, for which the value 128 ± 5 atoms ^{3}He g^{-1} a^{-1} is used (Blard et al., 2006); Λ_f is the apparent fast neutron attenuation length with a value of 177 g cm^{-2}

(Farber et al., 2008); t_{expo} is the independently determined exposure duration [a] of 32.4 ± 1.3 ka; and ρ is the density of the whole basaltic rock sample (2.52 g cm^{-3}).

To calculate the scaling factor $S_{el,s}$, five different scaling methods were applied according to section 5.4.2. The resulting five different erosion rates (Table 5.3) are between 11.1 and 4.1 mm/ka, these values and associated uncertainty (see below) are then used in further calculations for samples SI41 and SI29. Blard et al. (2008) calculated that the erosion rate on a sample of the same flow located 6 km away from our samples would be about 13 mm ka^{-1}, as inferred from the difference between the ^{3}He measurement and the K-Ar age. This value is similar to the one we estimated.

A standard deviation of ±30% (1σ) is estimated for the calculated erosion rates from a sensitivity test, which accounts for the uncertainties in the independent age constraint t_{expo} and in the SLHL production rate $PR(^3He)$ as follows: Values for the erosion rate ε were recalculated replacing t_{expo} and $PR(^3He)$ in Eq. 5.3 with all possible combinations of their confidence interval bound values (x - 2σ and x + 2σ). These bound values are 29.8 ka and 35.1 ka for t_{expo} and 118 and 138 atoms ^{3}He g^{-1} a^{-1} for $PR(^3He)$. The lowest and highest resulting values for ε give an idea of the limits of the confidence interval (2σ) of the mean erosion rate ($\sim \pm 60\%$), from which the standard deviation was derived ($\sim \pm 30\%$).

Sampling sites at volcano Payun Matru:

The four samples were collected from well-preserved aa-block surfaces belonging to a flow located on the northern flank of the volcano, at altitudes of 2290 m and 2490 m. Blocks protrude 50 - 70 cm from the ground. They are about 25 cm wide and a few meters long (Fig. 5.3). Only blocks indicating insignificant erosion were sampled. Given that strong winds are often blowing in that region, a long-term cover of the blocks with ash from later eruptions is not probable.

Germa et al. (2009) performed two K-Ar age determinations on a sample (94AE) of this flow and yielded 15 ± 1 ka and 16 ± 2 ka. Applying Eq. 5.1 and Eq. 5.2 results in a weighted mean of 15.2 ± 0.9 ka.

Payun Matru is located near the Andes, where abnormal atmospheric pressure effects

could have a significant impact on cosmonuclide production. However, mean annual pressure observations at the meteorological station nearest to Payun Matru, Malargue and San Rafael, (http://dss.ucar.edu/datasets/ds570.0) did not show any anomalies. The atmospheric pressure at station San Rafael normalized to sea level and averaged over the years 1971 to 2004 is 1013.7 ± 1.7 mbar. The standard atmospheric at sea level is 1013.25 mbar.

Figure 5.3: *Pictures of sample surfaces at Payun Matru.*

5.3.2 Physical and chemical sample preparation

Physical sample preparation was conducted at CEREGE, Aix en Provence, France, and at the School of Geosciences, University of Edinburgh, UK. Pieces of uncrushed bulk rock from each lava flow were sent to SARM (CRPG, Nancy, France) for bulk composition analysis. Dry rock densities were determined for each sample with pieces of uncrushed bulk rock (Table 5.2). Whole rock samples were then crushed and sieved to select grain

Table 5.2: *Sample locations and description.*

Sample	Altitude [m]	latitude	longitude	Lava morphology	Thickness [cm]	density [g cm^{-3}][a]
Mt. Etna: Historic Flow 1614-24 (between 383 and 393 years)						
HF1	1748	N 37.82°	E 15.01°	Pahoehoe cords	4	2.50
Mt. Etna: Solicchiata (^{14}C between 4.4 ka and 18.4 ka)						
SI3	525	N 37.89°	E 15.09°	Pahoehoe cords	5	2.57
SI40	530	N 37.90°	E 15.07°	Pahoehoe cords	10	2.57
SO3	783	N 37.86°	E 15.07°	Pahoehoe cords	9.5	2.38
SO2	992	N 37.84°	E 15.07°	Pahoehoe cords	8	2.45
SO1	1204	N 37.84°	E 15.06°	Pahoehoe cords	12	2.30
Mt. Etna: Piano della Lepre (K-Ar 10.0 ± 3.2 ka)						
SI43	2070	N 37.71°	E 15.03°	Pahoehoe, fossil-exposed	15	2.37
Mt. Etna: La Nave (K-Ar/TL 32.4 ± 1.3 ka)						
SI41	820	N 37.85°	E 14.84°	Pahoehoe cords, eroded	15	2.52
SI29	830	N 37.85°	E 14.83°	Pahoehoe cords, eroded	10	2.52
Payun Matru (K-Ar 15.2 ± 0.9 ka)						
PM06-31	2293	S 36.35°	W 69.29°	aa-block	4	2.30
PM06-32	2293	S 36.35°	W 69.29°	aa-block	4	2.30
PM06-24	2489	S 36.36°	W 69.29°	aa-block	4	2.30
PM06-26	2490	S 36.36°	W 69.29°	aa-block	4	2.30

[a] Densities were determined using the Archimedes principle.

Table 5.3: *Erosions rates of sample SI41 determined from measured cosmogenic ^{3}He concentration using five different scaling methods (see section 5.3.1 for details).*

Scaling method	Spallation scaling factor	Erosion rate [mm/ka]
St	1.823	11.1 ± 3.3
Du	1.773	9.8 ± 2.9
De	1.776	9.9 ± 3.0
Li05	1.642	6.4 ± 1.0
Li08	1.561	4.1 ± 1.2

size fractions between 100 μm and 1400 μm (Table 5.4). Separation of the feldspar minerals relied exclusively on magnetic methods, since the feldspar phenocrysts are the only non-magnetic components in the lavas. In a first step, the most magnetic grains were taken off with a strong hand magnet. Then, the less magnetic fractions were progressively removed with a Frantz magnetic separator.

The chemical extraction of chloride was conducted at CEREGE. Samples consisting of feldspar grains weighing between 9 g and 325 g were first washed with MQ water in closed HDPE bottles for several hours on a shaker table. Then, they were etched in HDPE bottles shaken overnight with an amount of an HF(40%)/HNO_3(2M) mixture (volume ratio 1:2) calculated to dissolve about 20% of the sample. Samples PM06-24 and PM06-26 were etched with HF and HNO_3 at the School of Geosciences, University of Edinburgh, UK to dissolve 20-30% of the grains. After this first step, any groundmass adhering to the feldspar grains should have been removed. Moreover, potential contamination by atmospheric ^{36}Cl can totally be excluded after this rigorous leaching procedure (Merchel et al., 2008a). An aliquot of 2 g was taken from the etched grains for analysis of the chemical composition at SARM (CRPG, Nancy, France). The remaining sample grains were dissolved with an excess amount of the HF/HNO_3 mixture by shaking overnight. After adding the acid mixture, the sample was spiked with approximately 1.5 mg of chloride enriched in either ^{37}Cl or in ^{35}Cl (OakRidge National Laboratory). After complete dissolution of the grains, the solutions were centrifuged to separate the supernatant from any remaining slurry in suspension and from the fluoric cake formed during the dissolution reaction. AgCl was precipitated by adding $AgNO_3$. This first precipitate was re-dissolved in dilute NH_4OH, and, in order to reduce the isobaric interferences of ^{36}S during the ^{36}Cl AMS measurements, $Ba(NO_3)_2$ was added to precipitate $BaS0_4$/$BaCO_3$. The AgCl was again precipitated from the resulting solution by acidification with HNO_3 and collected by centrifugation. The precipitate was rinsed and dried and finally ^{36}Cl measured at the LLNL-CAMS. AgCl yields, including carrier and natural Cl, accounted for 3 to 7mg.

Several blanks were prepared in order to survey for contamination during the chemical extraction procedure and to correct sample measurements for laboratory sources of ^{36}Cl

and Cl.

Sample SI43 was dissolved in an eight-step sequential dissolution experiment (details in Schimmelpfennig et al., 2009). For the current calibration study, the measurements of steps 4 to 8 are included in the dataset due to their very low Cl content. The first three dissolution steps correspond to a removal of 25% of the initial grain weight and is similar to the etching performed on the other samples. The measurements of steps 4 to 8 are considered as four individual measurements since their ^{36}Cl concentrations depend on the target element concentrations, which vary through the dissolution process (see Table 5.4). The HF used to dissolve sample SI43 (Chimie-Plus Laboratories reagent grade "pure") contains non-negligible amounts of Cl and ^{36}Cl. Blank corrections of the measurements of sample SI43 were therefore done in terms of amount of acid used. For details see Schimmelpfennig et al. (2009).

Replicate analyses were performed for samples SI29 (two different grain sizes), PM06-31 and PM06-32 (two splits of each sample) in order to check the reproducibility of the chemical ^{36}Cl extraction.

Table 5.4: *Results chemical analysis of minerals. ^{36}Cl and Cl concentrations are determined by AMS at LLNL-CAMS and the major element concentrations by ICP-OES at SARM-CRPG.*

Sample	Grain size [μm]	Sample weight dissolved [g]	^{35}Cl/^{37}Cl	^{36}Cl/(stable Cl)[a] [10^{-14}]	Amount carrier [mg Cl][b]	Cl [ppm]	^{36}Cl [10^4 at/g]	Ca [wt%]	K [wt%]	Ti [wt%]	Fe [wt%]
Mt. Etna: Historic Flow 1614-24 (between 383 and 393 years)											
HF1[c]	100-400	341.76	0.5272± 0.0015	6.89± 0.18	1.521	3.5± 0.2	0.50± 0.19	8.2± 0.2	0.36± 0.05	0.05± 0.01	0.48± 0.02
Mt. Etna: Solicchiata (^{14}C between 4.4 ka and 18.4 ka)											
SI3[c]	100-400	35.83	0.1199± 0.0014	7.66± 0.22	1.519	5.6± 0.3	4.52± 0.18	8.4± 0.2	0.30± 0.04	0.05± 0.01	0.52± 0.03
SI40[c]	100-400	40.20	0.1191± 0.0014	9.18± 0.33	1.519	5.0± 0.3	4.98± 0.22	8.3± 0.2	0.29± 0.04	0.05± 0.01	0.51± 0.03
SO3[c]	100-400	37.17	0.0922± 0.0044	8.94± 0.30	1.518	3.9± 0.3	5.16± 0.22	8.2± 0.2	0.29± 0.04	0.05± 0.01	0.50± 0.03
SO2[c]	100-400	32.79	0.0654± 0.0008	9.66± 0.25	1.521	2.7± 0.2	6.34± 0.21	8.4± 0.2	0.29± 0.04	0.05± 0.01	0.50± 0.03
SO1[c]	100-400	21.41	0.0541± 0.0005	6.91± 0.26	1.522	3.1± 0.2	6.50± 0.33	8.2± 0.2	0.29± 0.04	0.05± 0.01	0.50± 0.03
Mt. Etna: Piano della Lepre (K-Ar 10.0 ± 3.2 ka)											
SI43-D4*[f]	140-400	5.03	80.13± 0.51	5.18± 0.16	1.796	2.8± 1.0	23.3± 1.4[g]	8.9± 1.9	0.58± 0.31	0.07± 0.08	0.59± 0.32
SI43-D5*[f]	140-400	4.97	78.91± 0.41	4.48± 0.16	1.792	3.1± 1.0	19.4± 1.4[g]	6.6± 1.7	0.44± 0.27	0.06± 0.07	0.46± 0.28
SI43-D6*[f]	140-400	7.50	56.13± 0.57	6.36± 0.23	1.794	2.5± 1.0	19.6± 1.3[g]	7.5± 0.6	0.46± 0.09	0.06± 0.02	0.50± 0.10
SI43-D7*[f]	140-400	9.77	46.01± 0.59	7.94± 0.21	1.800	2.0± 1.0	19.7± 1.1[g]	7.4± 0.4	0.48± 0.07	0.06± 0.02	0.48± 0.07
SI43-D8*[f]	140-400	13.06	32.32± 0.36	9.83± 0.33	1.792	1.2± 1.0	18.4± 1.3[g]	7.6± 0.2	0.48± 0.02	0.06± 0.01	0.50± 0.03
Mt. Etna: La Nave (K-Ar/TL 32.4 ± 1.3 ka)											
SI41[c]	140-400	8.98	0.0367± 0.0052	7.67± 0.30	1.519	3.4± 1.2	17.44± 0.88	7.4± 0.2	0.45± 0.03	0.06± 0.01	0.45± 0.02
SI29-160[c]	100-160	8.06	0.0327± 0.0004	7.11± 0.24	1.518	2.8± 0.2	17.69± 0.83	7.1± 0.1	0.42± 0.03	0.06± 0.01	0.41± 0.02
SI29-250[c]	160-250	9.91	0.0327± 0.0004	8.54± 0.24	1.522	2.3± 0.2	17.96± 0.67	7.2± 0.1	0.43± 0.03	0.06± 0.01	0.42± 0.02
Payun Matru (K-Ar 15.2 ± 0.9 ka)											
PM06-31[c]	250-1400	5.50	0.0428± 0.0001	13.78± 0.58	1.510	7.7± 0.5	55.5± 2.7	0.54± 0.03	5.4± 0.1	0.03± 0.01	0.19± 0.01
PM06-31-Rep[c]	250-1400	5.28	0.0428± 0.0001	13.18± 0.52	1.516	8.1± 0.5	55.3± 2.5	0.54± 0.03	5.4± 0.1	0.03± 0.01	0.19± 0.01
PM06-32[c]	250-1400	9.59	0.0856± 0.0003	23.56± 0.75	1.521	13.6± 0.7	58.0± 2.0	0.55± 0.03	5.4± 0.1	0.03± 0.01	0.19± 0.01
PM06-32-Rep[c]	250-1400	8.35	0.0749± 0.0002	19.95± 0.48	1.518	12.9± 0.7	55.5± 1.5	0.55± 0.03	5.4± 0.1	0.03± 0.01	0.19± 0.01
PM06-24*[d]	250-1400	7.37	104.49± 0.91	17.46± 0.24	1.470	6.4± 0.4	58.4± 1.2	0.55± 0.03	5.3± 0.1	0.03± 0.01	0.18± 0.01
PM06-26*[e]	250-1400	7.61	74.95± 0.40	17.66± 0.31	1.466	9.2± 0.5	57.6± 1.1	0.52± 0.03	5.2± 0.1	0.03± 0.01	0.19± 0.01
		acid mixture [ml]				Cl [10^{16} atoms]	^{36}Cl [10^5 atoms]				
Blank Bl1		30	0.0214± 0.0001	1.28± 0.10	1.517	10.27±0.5	3.11±0.32				
Blank BLH-D1*		15	171.91± 0.31	1.032± 0.058	1.802	62.8±3.3	3.25±0.18				
Blank BLH-D2*		24	122.98± 0.17	1.32± 0.24	1.802	93.6±4.6	4.17±0.75				
Blank BLH-D3*		30	100.44± 0.45	1.220± 0.073	1.802	118.3±5.9	3.89±0.23				
Blank Bl2*		100	432.0± 4.9	0.969± 0.065	1.465	13.76±0.73	2.45±0.17				
Blank Bl3*		100	482.04± 8.80	0.933± 0.064	1.475	11.31±0.69	2.38±0.16				

[a] The measured ^{36}Cl/(stable Cl) ratio is ^{36}Cl/^{37}Cl for most of the samples and ^{36}Cl/^{35}Cl for those accompanied by an asterisk.

[b],* The Cl carrier is enriched in ^{35}Cl (99.90%) for those accompanied by an asterisk and enriched in ^{37}Cl (98.21%) for the others.

[c] Samples corrected with blank Bl1 in terms of number of atoms ^{36}Cl and Cl (section 5.3.2).

[d] Sample corrected with blank Bl3 in terms of number of atoms ^{36}Cl and Cl (section 5.3.2).

[e] Sample corrected with blank Bl2 in terms of number of atoms ^{36}Cl and Cl (section 5.3.2).

[f] Samples corrected with blanks BLH-D1, BLH-D2, BLH-D3 in terms of number of atoms ^{36}Cl and Cl and according to the amount of acid used (section 5.3.2).

[g] The measured ^{36}Cl concentrations of SI43 were corrected for the calculated non-fossil component, which is the ^{36}Cl production in 250 cm depth since the surface was covered by an superposed flow (for details see Schimmelpfennig et al., 2009). The calculated non-fossil component accounts for about 6% of the total ^{36}Cl inventory.

5.3.3 Chemical measurements

^{36}Cl and Cl concentrations were determined using the Lawrence Livermore National Laboratory FN accelerator mass spectrometer (LLNL-CAMS). Isotope dilution using either ^{37}Cl- or ^{35}Cl-enriched carrier, allowed determination of both concentrations (^{36}Cl and Cl) simultaneously. ^{36}Cl/^{35}Cl and ^{36}Cl/^{37}Cl ratios were normalized to a ^{36}Cl standard prepared by K. Nishiizumi (Sharma et al., 1990). Also the stable ratio ^{35}Cl/^{37}Cl was normalized to this standard assuming the natural ratio of 3.127. Table 5.4 shows the measured ratios and their uncertainties. The precision of the ^{35}Cl/^{37}Cl ratios is 1% or less (standard deviation of repeated measurements), except for samples SO3 (5%) and SI41 (14%). The precision of the ^{36}Cl/^{35}Cl and ^{36}Cl/^{37}Cl ratios ranges between 2% and 4%.

Blank ^{36}Cl/^{35}Cl and ^{36}Cl/^{37}Cl ratios range between 0.9×10^{-14} and 1.3×10^{-14}, being 3 to 19 times lower than the sample ^{36}Cl/^{35}Cl and ^{36}Cl/^{37}Cl ratios (Table 5.4). Blank corrections were done by deducting the number of atoms ^{36}Cl and Cl measured in the blanks from those measured in the samples. In the case of the measurements of sample SI43, the samples were additionally corrected according to the amount of acid used to dissolve the grains, also in terms of number of atoms ^{36}Cl and Cl (section 5.3.2 and Schimmelpfennig et al., 2009). The resulting ^{36}Cl and Cl concentrations for all samples are listed in Table 5.4.

Chemical compositions were analyzed at the Service d'Analyse des Roches et des Minéraux du CNRS (CRPG, Nancy, France). Major elements in the minerals and in the bulk rock were determined by ICP-OES and trace elements in the bulk rock by ICP-MS, except Li (atomic absorption), B (colorimetry), H_20 (Karl Fischer titration) and Cl (spectrophotometry). For the bulk rock analyses, pieces of whole rock were kept aside before crushing the samples (section 5.3.2). Concentrations of the major elements and of H, Li, B, Sm, Gd, U, Th and Cl in the bulk rocks are necessary for calculating the low-energy neutron distributions at the land/atmosphere interface. Aliquots of the etched feldspar grains, taken before their complete dissolution (section 5.3.2), are representative of the sample dissolved for ^{36}Cl extraction and served for the analysis of the corresponding target element concentrations (Ca, K, Ti and Fe). These concentrations and the Cl contents in

the minerals, determined by isotope dilution during AMS measurements, were used to calculate the ^{36}Cl production from all production mechanisms (section 5.4.1) in the dissolved samples. Results of the compositional analysis, including the concentrations of ^{36}Cl and of the target elements Cl, Ca, K, Ti and Fe are listed in Table 5.4.

^{36}Cl concentrations range between 0.5 $\times$ 10^4 and 58 $\times$ 10^4 atoms (g sample)$^{-1}$. Cl concentrations in the Etna minerals range between 1 ppm and 6 ppm, Ca concentrations between 6.6% and 8.9% and K concentrations between 0.29% and 0.58%, while in the Payun Matru minerals Cl accounts for 6 ppm to 14 ppm, Ca for 0.55% and K for 5.2% to 5.4%. Ti does not exceed 0.06% and Fe is a maximum 0.59% in the calibration minerals.

As shown in Fig. 5.4, the large variation in the ^{36}Cl concentrations is most notably due variations in the prevailing target element (compare K-feldspars from Payun Matru with Ca-feldspars from Mt. Etna), the exposure duration, and the elevation of the sample. Replicates on splits of the same sample show very good reproducibility, both in fractions of the same grain size (PM06-31 and PM06-32) and of different grain size (SI29) (section 5.3.2).

5.4 Production rate calibration approach

5.4.1 Calculated in-situ ^{36}Cl production

In-situ ^{36}Cl is produced by various mechanisms in rock, the measured ^{36}Cl concentration in a sample corresponding to the sum of the ^{36}Cl contributions originating from all reactions. The major cosmogenic production reactions are spallation of Ca and K and capture of thermal and epithermal neutron (hereafter low-energy neutrons) by ^{35}Cl (^{35}Cl(n,γ)^{36}Cl). ^{35}Cl(n,γ)^{36}Cl occurrence depends primarily on the Cl concentration, but also on the contents of major elements and of the trace elements H, Li, B, Sm and Gd that influence the low-energy neutrons distribution in the sample. Minor contributions are made by capture of slow negative muons by Ca and K and by spallation of Ti and Fe. Additionally, radiogenic ^{36}Cl results from ^{35}Cl(n,γ)^{36}Cl, the neutrons being produced by spontaneous fission of ^{238}U and as a secondary product during the decay series of U and Th.

In a sample, the ^{36}Cl contribution from each reaction depends mainly on the concentra-

tion of the respective target element. Additionally, other factors affect the sample-specific production rate of ^{36}Cl, such as the geographic location and elevation (see section 5.4.2), the surrounding topography and the geometric position and thickness of the sample.

The composition of our calibration samples (Table 5.4 and Fig. 5.5) indicate that ^{36}Cl is almost exclusively produced from the two target elements Ca and K. The ^{36}Cl contributions from the various production mechanisms were calculated using the ^{36}Cl calculation spreadsheet in Schimmelpfennig et al. (2009) and assuming the ^{36}Cl spallation production rates from Ca and K by Stone et al. (1996) and Evans et al. (1997), respectively, as default values (Table 5.5). Spallation reactions account for at least 87% of production in the Etna minerals and 95% in the Payun Matru minerals. The low Cl concentrations in all minerals result in a small ^{36}Cl contribution from the low-energy-neutron reaction, not exceeding 3.5%. Also due to the low Cl contents, the calculated radiogenic ^{36}Cl contribution accounts for less than 0.1% in all samples and is not listed. The second most important production mechanism is slow negative muon capture on Ca and K, which ranges between 2% and 10% of the total ^{36}Cl inventory in the minerals. Since the ^{36}Cl production due to muons depends on the same target elements as that due to spallation, Ca and K, the ^{36}Cl contributions from these two sources cannot be differentiated in surface samples as simply as can be done to avoid ^{36}Cl contributions due to Cl by using minerals low in Cl.

In the following, we present the calculations on which the calibration is based. Readers are referred to the appendix of Schimmelpfennig et al. (2009) for a detailed compilation of all equations, which were adapted from Gosse and Phillips (2001) and Fabryka-Martin (1988) to the case of ^{36}Cl extraction from separated minerals.

The total measured ^{36}Cl concentration [atoms ^{36}Cl g^{-1}] in a sample corresponds to the total site- and sample-specific ^{36}Cl production from all above-mentioned reaction integrated over the exposure time and can be expressed as:

$$N_{36} = S_{el,s}\ S_T(J_{Q,s}\ d_s\ t_{cosm,s} + J_{Q,eth}\ d_{eth}\ t_{cosm,eth} + J_{Q,th}\ d_{th}\ t_{cosm,th})$$

$$+S_{el,\mu}\ S_T\ J_{Q,\mu}\ d_\mu\ t_{cosm,\mu} + P_r\ t_r \qquad (5.4)$$

with the subscripts s for spallation, eth for epithermal and th for thermal neutron

capture by ^{35}Cl, μ for direct capture of slow negative muons and r for radiogenic production. $S_{el,x}$ are the scaling factors for spallation and slow negative muon reactions, which correct the production rates for the geographic location, elevation and for temporal variations mainly due to fluctuations in the geomagnetic field (section 5.4.2). The scaling factor for spallation reactions $S_{el,s}$ is also applied for the low-energy-neutron reactions. S_T is the correction factor for shielding from the surrounding topography. S_T is 1 for all samples in this study, because no correction for shielding needs to be done.

$J_{Q,x}$ are the production rate coefficients including the sample thickness integration factors Q_x, all composition-dependent variables and the SLHL production rates and parameters of all reactions, and d_x are the depth reference factors for the respective reaction types (see Schimmelpfennig et al., 2009, for the detailed equations). $t_{cosm,x}$ are the time factors for the respective cosmogenic reaction types including the radioactive decay of ^{36}Cl and the erosion rate:

$$t_{cosm,s} = \Big(1 - exp\Big(-t_{expo}\Big(\lambda_{36} + \frac{\rho\ \varepsilon}{\Lambda_f}\Big)\Big)\Big) / \Big(\lambda_{36} + \frac{\rho\ \varepsilon}{\Lambda_f}\Big) \tag{5.5}$$

$$t_{cosm,eth} = \Big(1 - exp\Big(-t_{expo}\Big(\lambda_{36} + \frac{\rho\ \varepsilon}{L_{eth}}\Big)\Big)\Big) / \Big(\lambda_{36} + \frac{\rho\ \varepsilon}{L_{eth}}\Big) \tag{5.6}$$

$$t_{cosm,th} = \Big(1 - exp\Big(-t_{expo}\Big(\lambda_{36} + \frac{\rho\ \varepsilon}{L_{th}}\Big)\Big)\Big) / \Big(\lambda_{36} + \frac{\rho\ \varepsilon}{L_{th}}\Big) \tag{5.7}$$

$$t_{cosm,\mu} = \Big(1 - exp\Big(-t_{expo}\Big(\lambda_{36} + \frac{\rho\ \varepsilon}{\Lambda_\mu}\Big)\Big)\Big) / \Big(\lambda_{36} + \frac{\rho\ \varepsilon}{\Lambda_\mu}\Big) \tag{5.8}$$

where t_{expo} is the exposure duration [a] and λ_{36} the decay constant of ^{36}Cl with a value of 2.303 $\times$ 10^{-6} a^{-1} and ε is the constant erosion rate [cm a^{-1}], ρ the density of the sample [g cm^{-3}], Λ_f the apparent fast neutron attenuation length with a value of 177 g cm^{-2} (Farber et al., 2008), L_{eth} and L_{th} are the epithermal and thermal neutron diffusion lengths [g cm^{-2}], respectively, and Λ_μ is the slow negative muon attenuation length with a value of 1500 g^{-2}.

P_r is the composition-dependent radiogenic ^{36}Cl production rate and t_r is the time factor for the radiogenic reaction including the radioactive decay of ^{36}Cl:

$$t_r = (1 - exp(-t_{form}\lambda_{36}))/\lambda_{36} \tag{5.9}$$

where t_{form} is the formation time of the rock [a], which can be different from the exposure time, e.g. for buried surfaces like sample SI43 in this study (section 5.3.1).

To isolate the two unknowns PR_{Ca} and PR_K, Eq. 5.4 can be written :

$$N_{36} = A\ PR_{Ca} + B\ PR_K + C \tag{5.10}$$

with

$$A = S_{el,s}\ S_T\ Q_s\ [Ca]\ d_s\ t_{cosm,s} \tag{5.11}$$

$$B = S_{el,s}\ S_T\ Q_s\ [K]\ d_s\ t_{cosm,s} \tag{5.12}$$

$$\begin{aligned} C =& S_{el,s}\ S_T\ Q_s\ (P_{Ti} + P_{Fe})\ t_{cosm,s} + S_{el,s}\ S_T\ D\ d_s\ t_{cosm,s} \\ &+ S_{el,s}\ S_T\ J_{Q,eth}\ d_{eth}\ t_{cosm,eth} + S_{el,s}\ S_T\ J_{Q,th}\ d_{th}\ t_{cosm,th} \\ &+ S_{el,s}\ S_T\ E\ d_\mu\ t_{cosm,\mu} + S_{el,\mu}\ S_T\ Q_\mu\ P_\mu\ t_{cosm,\mu} + P_r\ t_r \end{aligned} \tag{5.13}$$

where [Ca] and [K] are the concentrations of Ca and K, respectively, in the dissolved sample [wt%]; P_{Ti} and P_{Fe} are the sample-specific depth-dependent ^{36}Cl production rates from spallation of Ti and Fe [atoms ^{36}Cl (g^{-1} sample) a^{-1}], respectively, D is the second part of the calculation of $J_{Q,s}$ (see for detail Eq. 68 in Schimmelpfennig et al., 2009), and E is the first part of the calculation of $J_{Q,\mu}$ (see for detail Eq. 71 in Schimmelpfennig et al., 2009).

All composition- and depth-dependent variables were calculated using the ^{36}Cl calculation spreadsheet (Schimmelpfennig et al., 2009). Their values are listed for all samples in Table C.2. The production rates of the minor production mechanisms such as P_{mu} were taken from the literature and are presented in Table 5.5.

Since the minerals studied were neither pure Ca- nor pure K-feldspars, there is at each calibration site a small ^{36}Cl contribution from the minor target element: at Mt. Etna

spallation on K accounts for 9% to 16%, and at Payun Matru spallation on Ca accounts for 3% of the total ^{36}Cl. Therefore, the wide range of the Ca/K ratio, with ratios for Etna samples that vary from 15 to 28 and for Payun samples that are about 0.1, allows calibrating the two spallation production rates simultaneously in the same calibration exercise.

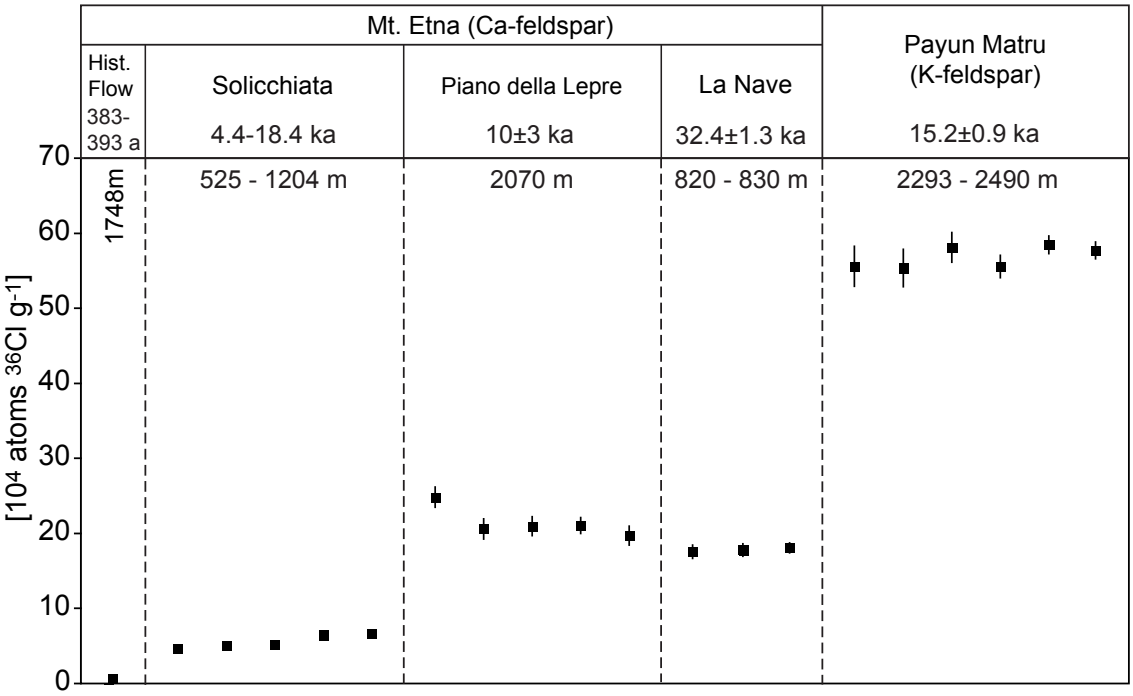

Figure 5.4: ^{36}*Cl concentrations in the calibration samples, determined from AMS isotope dilution measurements.*

5.4.2 Scaling methods

The production rate of any nuclide depends on the cosmic ray flux that varies both in space and time. The geomagnetic field acts as a shield for the incident primary cosmic ray flux allowing only cosmic ray particles above certain energies to penetrate the magnetic field, travel through the atmosphere and reach the earth's surface (Gosse and Phillips, 2001). This shielding effect is usually described by the concept of cutoff rigidity, a measure for the minimum energy a particle must have to penetrate the earth's magnetic field. The cutoff rigidity is generally strongest at the equator and decreases towards high latitudes, therefore mainly depending on the site geomagnetic latitude. Since the geomagnetic and

Table 5.5: *^{36}Cl contribution from the divers production mechanisms in the plagioclases from Mt. Etna and the sanidines from Payun Matru. Calculations were done before the calibration exercise using the ^{36}Cl spreadsheet in Schimmelpfennig et al. (2009) with the listed default values for the SLHL production rates and parameters. Production rates are scaled according to Stone (2000).*

Production mechanism	Default values for ^{36}Cl prod. rates and parameters at SLHL	^{36}Cl Contribution in plagioclases from Mt. Etna	^{36}Cl Contribution in sanidines from Payun Matru
Spallation on Ca, K, Ti and Fe		86.6 - 92.7%	94.8 - 96.7%
Spallation on Ca	48.8±1.7 at (g Ca)$^{-1}$a^{-1} (Stone et al., 1996)	74.3 - 79.9%	2.8 - 2.9%
Spallation on K	162±25 at (g K)$^{-1}$a^{-1} (Evans et al., 1997)	8.9 - 16.4%	91.9 - 93.7%
Spallation on Ti	13±3 at (g Ti)$^{-1}$a^{-1} (Fink et al., 2000)	0.1 - 0.2%	0.04%
Spallation on Fe	1.9 at (g Fe)$^{-1}$a^{-1} (Stone, 2005)	0.2%	0.04%
Low-energy neutron capture by ^{35}Cl	626 neutrons (g air)$^{-1}$a^{-1} (Phillips et al., 2001)	0.9 - 3.1%	1.7 - 3.5%
Slow-negative muon capture by Ca and K	190 μ g^{-1}a^{-1} (Heisinger et al., 2002)	6.3 - 10.2%	1.6 - 1.7%

[a] After Evans et al. (1997) the total production rate from K, including spallation and slow negative muon capture, is 170 ± 25 atoms ^{36}Cl (g K)$^{-1}$a^{-1} with a contribution from muons of about 5%, which results in a spallation production rate of 162 atoms ^{36}Cl (g K)$^{-1}$a^{-1}.

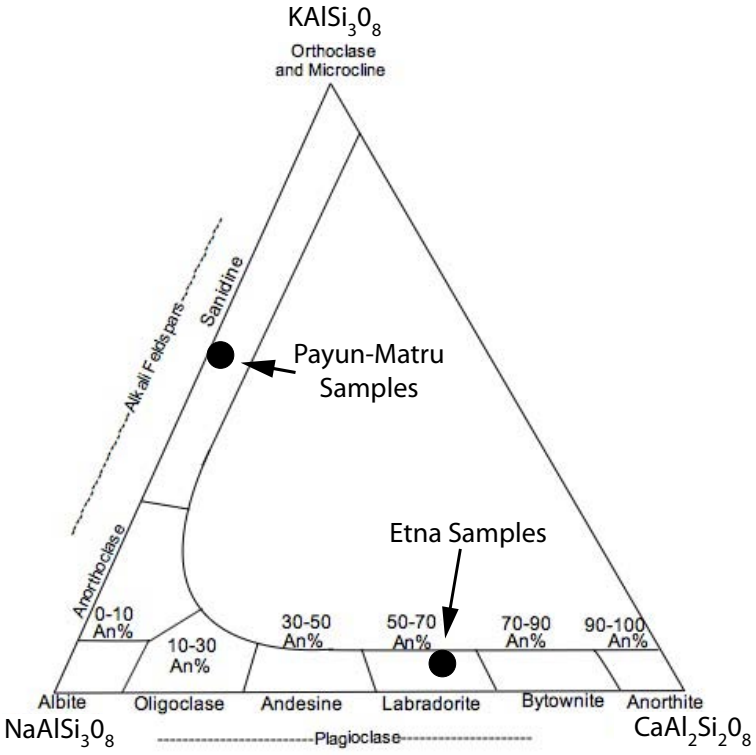

Figure 5.5: *Feldspar ternary diagram with compositional signiture of the calibration minerals. Etna plagioclase have labradorite composition, i.e. Ca is the dominant ^{36}Cl target element, while Payun Matru alkali-feldspars are sanidines, i.e. K is the dominant ^{36}Cl target element.*

geographic poles are not coincident, the geomagnetic latitude differs from the geographic latitude. Temporal fluctuations in the intensity of the geomagnetic field also affect the cutoff rigidity resulting in variations of cosmogenic production rates with time.

Furthermore, in the atmosphere, the nucleon flux diminishes as a function of mass-shielding depth. Incident particles lose energy through nuclear collisions and electromagnetic interactions in the atmosphere, this energy loss being dependent on the mass of air transited and therefore on the site altitude, the cosmogenic nuclide production rates thus increase considerably with increasing elevation.

Consequently, to interpret measured cosmonuclide concentrations correctly, the latitude, elevation and time dependency of production rates need to be quantified accurately. This is accomplished through scaling models, which quantify this variability by calculating scaling factors that integrate the specific site latitude, altitude and time span. Several of

those scaling models have been published. The first method to calculate local production rates as a function of latitude and elevation was published by Lal (1991). Stone (2000) refined Lal's method by expressing the elevation dependence in terms of atmospheric pressure. Later, Dunai (2000, 2001); Desilets and Zreda (2003); Desilets et al. (2006b); Lifton et al. (2005, 2008) developed more complex methods that account for the elevation effect as a function of atmospheric depth, for the latitude effect in terms of cutoff-rigidity, and estimated the temporal fluctuations of the geomagnetic intensity.

For this study, five of these methods were selected to calculate scaling factors for each calibration sample site: Stone (2000) (St), Dunai (2001) (Du), Desilets et al. (2006b) (De), Lifton et al. (2005) (Li05) and Lifton et al. (2008) (Li08). The citations will hereafter be substituted by the abbreviation in brackets. The characteristics of each scaling methods are described in Table 5.6 with their geomagnetic field models and reference sources used. All equations are described in detail in Chapter 1.4.1 of this thesis. It is not in the scope of this paper to discuss the validity of these models, but it is important to stress that mixing different scaling methods can introduce significant bias (Balco et al., 2008). For that reason we have normalized the production rate derived from our data to sea level and high latitude (SLHL) at the present time using each of the five different scaling models. Thus future applications using our reference production rate need not be limited to any particular scaling model. The SLHL reference production rate just needs be chosen to match the scaling scheme selected.

The scaling factors derived for spallation and muon-induced production at each sampling site can be found in detail in Appendix (section C) and are displayed in Fig. 5.6 normalized to the Stone (2000) scaling factor. Absolute values range between 1 and 6 due to the variation in altitude and in exposure duration of the sites (the latitude is for all sites similar, Mt. Etna 38°N, Payun Matru 36°S).

The spallation scaling factors $S_{el,s}$ from the different methods seem to differ most strongly as a function of the time span, over which the scaling factors are integrated, and less as a function of the altitude. Spallation scaling factors for flows younger than 10 ka vary more strongly than for older flows, which is mainly because the geomagnetic field intensity

records and their resolutions differ before and after 10 ka (Table 5.6). The differences are most striking for the historic flow. This arises most probably because for the very short exposure duration of the historic flow (< 400 years) the fluctuations of the geomagnetic field are not effectively averaged.

At Mt. Etna, spallation scaling factors differs by at most 23% between models, while at Payun-Matru the five scaling methods yield more similar scaling factors with a maximum discrepancy of 7% (Fig. 5.6a).

Li05 and Li08 scaling models yield mostly the lowest spallation scaling factor values while for the other scaling methods no systematic tendency is observed.

The muon scaling factors $S_{el,\mu}$, on the other hand, show a systematic offset between St, Du and De. In addition, Li05 and Li08 scaling factors display a different altitude dependency compared to the others models. This can be explained by the fact that in Li05 and Li08 the muon attenuation coefficient in the atmosphere is calculated with a polynomial, fitted on the basis of muon monitor data, while the other methods use linear functions to calculate the muon attenuation coefficient.

It has to be stressed that the $S_{el,\mu}$ are not expected to have a significant influence on the spallation production rate results in contrast to $S_{el,s}$.

Balco et al. (2008) give an overview of the relative differences in calculated cosmogenic ^{10}Be and 26Al exposure ages, when scaled with the different methods, as a function of the latitude, the elevation and the exposure duration. Temporal variations and related differences in the scaling factors for varying exposure durations have the greatest impact at low latitudes, where changes in paleomagnetic field strength are most important. Scaling factors of the different methods are most similar at moderate elevations and diverge most strongly at high elevations but also at very low latitudes. For our study, samples were taken at mid-latitude and at a moderate elevation range (530-2500m), where the scaling is not so much affected by the discrepancies highlighted in Balco et al. (2008).

Table 5.6: *Scaling methods used for the calibration, corresponding geomagnetic field models and database. Calculations, data input and database of each method follow as strictly as possible the respective study.*

Scaling scheme[a]	Geomagnetic field model	Method of calculating R_c	Input for the latitude effect	Input for the elevation effect	Calculation of slow negative muon scaling factor	Comments
St	/	/	Geographic latitude	Atmospheric pressure	Eq. 3 in Stone 2000	- not taking into account temporal variations
Du	<10 ka: non-dipole field with local record of paleoinclination from Brandt et al. (1999) (42.5°N, near Mt. Etna calibration site) >10 ka: GAD[b]	<10 ka: Eq. 2 in Du (dipolar approximation taking into account local paleoinclination and horizontal field strength) - M_c from Ohno and Hamano (1993) >10 ka: Eq.1 in Du - Mc from Yang et al. (2000) (0-11 ka) and SINT800[d] (11-150 ka)	<10 ka: geomagnetic latitude from geographic latitude and longitude[f] and paleopoleposition of northpole from Ohno and Hamano (1993) >10 ka: geographic latitude	Atmospheric depth (g cm-2)	Eq. 8 in Dunai 2000 with Λ_μ = 247 g cm-2 (not taking into account temporal variations)	
De	GAD[b]	Eq. 19 in Desilets and Zreda (2003) (best-fit model based on R_c from trajectory tracing assuming a GAD[b]) - M/M_0 with M_0 from 1950 DGRF[e] - M[c] from Yang et al. (2000) (0-11 ka) and SINT800[d] (11-150 ka)	<10 ka: dipolar geomagnetic latitude from geographic latitude and longitude[g] and paleopoleposition of northpole from Merrill and McElhinny (1983) (0-2 ka) and Ohno and Hamano (1993) (2-10 ka) >10 ka: geographic latitude	Atmospheric depth (g cm-2)	Latitude effect: Eq. 3 in Desilets and Zreda (2003) with α = 38.51 and k =1.03 Elevation effect: Eq. 2 in Desilets and Zreda (2003) with Λ_μ according to Eq. 7 (taking into account temporal variations)	
Li05	GAD[b]	Eq. 6 in Li05 (best-fit model based on R_c from trajectory tracing, averaging current eccentric dipole and non-dipole fields) - M/M_0 with M_0 from 1950 DGRF[e] - M[c] from Yang et al. (2000) (0-11 ka) and SINT800[d] (11-150 ka)	<10 ka: dipolar geomagnetic latitude from geographic latitude and longitude[g] and paleopoleposition of northpole from Merrill and McElhinny (1983) (0-2 ka) and Ohno and Hamano (1993) (2-10 ka) >10 ka: geographic latitude	Atmospheric depth (g cm-2) - standard atmosphere	Eq. 2 in Li05 (taking into account temporal variations)	- Taking into account solar modulation - published spreadsheet in Appendix of Li05 used to integrate the spallation and muon scaling factors over the respective exposure durations
Li08	<7 ka: continuous non-dipole geomagnetic field model (CALS7K.2 from Korte and Constable, 2005) >7 ka: non-dipole field	0-7 ka: R_c from trajectory tracing based on spherical harmonic field model of Korte and Constable (2005) >7 ka: Eq. 4 in Li08 (best-fit model based on the mean CALS7K.2 field over the 0-7 ka period) - M/M_0 with M_0 from 1950 DGRF[e] - M[c] from SINT800[d]	<7 ka: geomagnetic latitude from geographic latitude and longitude[g] and paleopoleposition of northpole from Jackson et al. (2000) (0-0.3 ka) and Korte and Constable (2005) (0.3-7 ka) >7 ka: geographic latitude	Atmospheric depth (g cm-2) variable atmosphere	Eq. 2 in Li05 (taking into account temporal variations)	- Taking into account solar modulation - extended spreadsheet of Li05 (personal communication by N. Lifton) used to find the spallation and muon scaling factors - predicts longitudinal variability

[a] St: Stone (2000), Du: Dunai (2001), De: Desilets et al. (2006b), Li05: Lifton et al. (2005), Li08: Lifton et al. (2008).
[b] GAD: geocentric axial dipole field.
[c] M: dipole moment [Am^2].
[d] Guyodo and Valet (1999).
[e] Definitive Geomagnetic Reference Field.
[f] Positive values for latitude and longitude of Argentinean samples.
[g] Negative values for latitude and longitude of Argentinean samples.

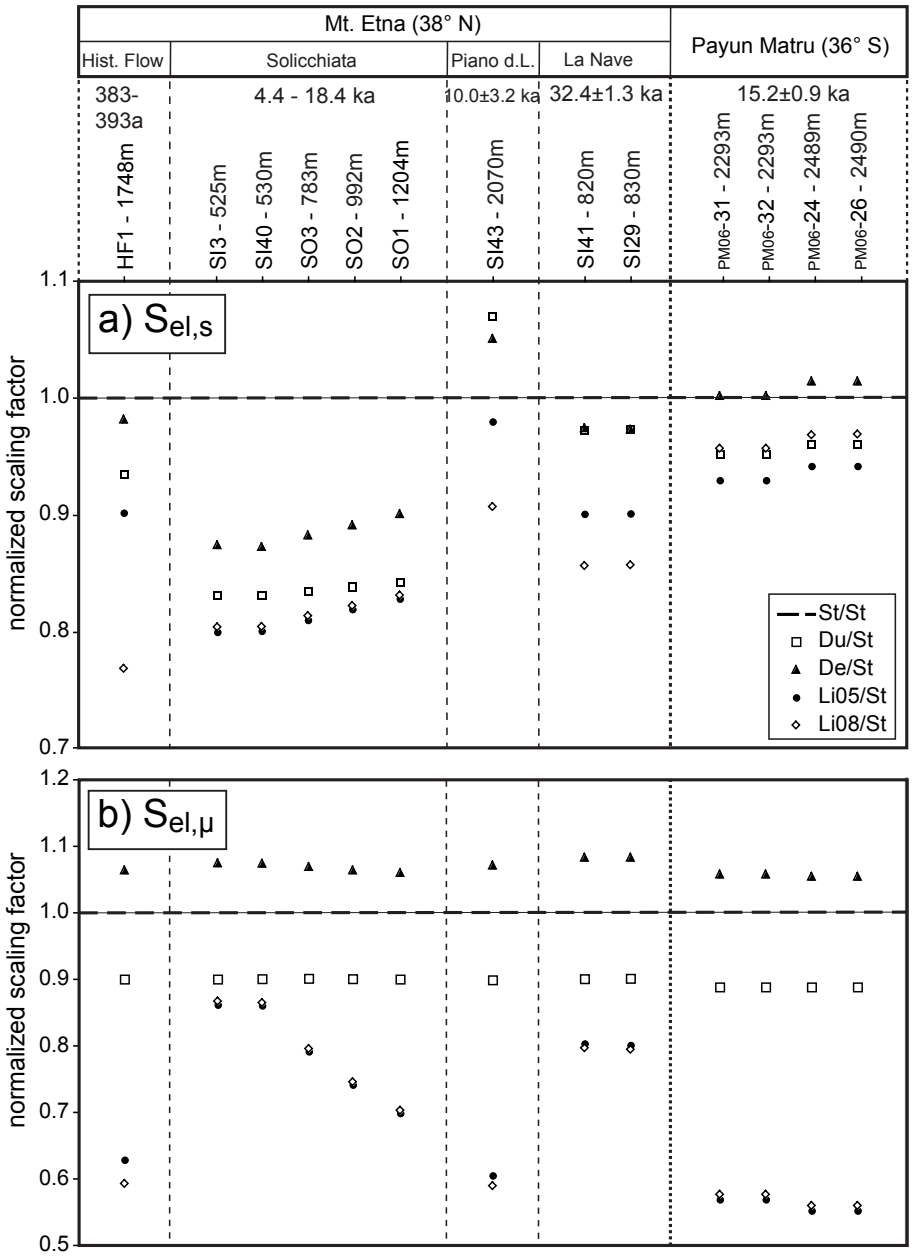

Figure 5.6: *Normalized scaling factors for spallation reactions (a) and slow negative muon capture (b) for each calibration site according to the five different scaling methods. Scaling factors derived from Du, De, Li05 and Li08 are normalized to those derived from St to display the differences between the methods in function of the altitude of the sample site and the exposure duration of the flows. Absolute values are listed in Table C.1. In the case of the four methods that consider temporal variations (Du, De, Li05 and Li08), the scaling factors were integrated over the following time spans: Historical Flow 0-400 years, Solicchiata 0-8 ka, Piano della Lepre 10-20 ka, La Nave 0-32 ka, Payun Matru 0-15 ka.*

5.4.3 Bayesian statistical approach

A fundamental drawback in the numerical and statistical methods of previous calibration studies has been the lack of a consistent approach to incorporation of the uncertainties in the dataset. The Bayesian statistical model (e.g. Gelman et al., 2004) developed in this study allows inclusion of uncertainties in any parameter. We used this model to identify and to take into account the major and most influential uncertainties in the dataset, which are the independently determined exposure ages, the calculated erosion rates of the La Nave flow, the calculated sample-specific ^{36}Cl production due to slow negative capture, P_μ and the analytical uncertainty in the ^{36}Cl concentration. All other parameters are considered to be perfectly known and thus not to contribute significantly to the uncertainty. Although this is not strictly true, only the four listed parameters potentially contribute significantly to the uncertainty in the calibration results. We optimize the production rate independently for each scaling method. This assessment is discussed in the following paragraphs.

Uncertainties in the dataset

Uncertainties in the independent ages

The independent age t_{expo} is a term in the exponent of the time factors $t_{cosm,x}$ (Eqs. 5.5 - 5.8). The time factors are very sensitive to the independent age, as long as the exposure duration is relatively short ($<<$ steady state), as it is the case in this study. Two of the five lava flows have poorly constrained independent exposure durations. The Solicchiata flow erupted sometime between 4.4 ka and 18.4 ka and the Piano della Lepre surface (sample SI43) has a calculated exposure time with 32% uncertainty. The other three flows have age constraints with uncertainties between 1.3% and 6% uncertainty.

Uncertainty in the erosion rate

The time factors $t_{cosm,x}$ also depend on the erosion rate which could play a significant role in the final results. As an example, on a surface exposed for 30 ka, there is a 17% difference in the time factor if considering a constant erosion rate of 10 mm/ka or if ignoring erosion.

However, although the uncertainty in the erosion rate is high (30%) (section 5.3.1), the final calibration results are probably not strongly affected by this uncertainty, since only three measurements of the whole dataset (20 measurements) are subject to erosion.

Uncertainty in the production from slow negative muon capture

The predicted ^{36}Cl contribution from slow negative muon capture accounts for up to 10% of the total ^{36}Cl inventory (Table 5.5). In the calibration model, the total ^{36}Cl inventory is corrected for this contribution to accurately determine the production rates only from spallation (see Eqs. 5.10 - 5.13). The uncertainty in the calculated production rate from muon capture P_μ is estimated at 25%. This is because Gosse and Phillips (2001) associate an error of ±25% to the calculation of the compound factor f_c using the Fermi-Teller Z-law (Charalambus, 1971). f_c is a poorly known factor in the calculation of the ^{36}Cl yield per muon stopped by the target elements (Eq. 3.44 in Gosse and Phillips, 2001). Propagating the uncertainty in f_c and minor uncertainties in other factors into P_μ results in an uncertainty of ∼25% for P_μ.

Analytical and other uncertainties

We also consider the analytical uncertainties in the measured ^{36}Cl concentrations N36 (σ_{analyt}), which range between 2% and 7%.

The uncertainties of the other parameters in the dataset either have much smaller magnitudes than those stated above or will not significantly affect the results of the calibration. Errors in the concentrations of Ca in the Ca-rich samples and of K in the K-rich samples are typically 2% or less (Table 5.4). Only the four measurements of sample SI43 have Ca concentrations with higher uncertainties (5-26%), but this is due to the special dissolution procedure applied to this sample and the mass balance calculations to determine target element concentrations (Schimmelpfennig et al., 2009, for details). The uncertainties in the Cl concentrations can be as high as 83% for samples with Cl contents close to 0 ppm (Table 5.4). However, since the Cl contents in all samples are very low, the calculated ^{36}Cl contributions due to Cl are insignificant in the total ^{36}Cl inventory (max. 3.5%, Table 5.5). The calibration results are therefore insensitive to the uncertainties in the Cl concentrations.

The sensitivity to errors in other components such as the attenuation length for fast

neutrons (Λ_f), the rock density and the sample thickness were tested in the ^{36}Cl calculation spreadsheet using reasonable error estimates ($\sim$10%) and were found to have insignificant impacts in the resulting exposure ages and are therefore expected to have insignificant impacts in the calibration results as well.

Uncertainties in the scaling factors were not calculated for two reasons. Firstly, they are hard to estimate due to the complexity of their determination (e.g. Desilets et al., 2006b) and in the source papers stated uncertainties are often rather rough estimates (e.g. Dunai, 2001).

Theoretical aspects of the Bayesian approach

Bayesian inference is the process of fitting a probability model to a set of data and associated uncertainties and summarizing the result by a probability distribution on the output of the model. This approach has already been successfully applied in archeology and in paleoseismology (e.g. Hilley and Young, 2008). In geochronology the approach has been used to reconcile and combine ages originating from various methods (Muzikar and Granger, 2006). Applied to our problem, the Bayesian approach consists in determining the probability distribution of calculating, for a given set of parameter values, including the production rates PR_{Ca} and PR_K, a value for the ^{36}Cl concentration, which is equal to the measured value N_{36}. The best values for the parameter set will be those, which minimize the discrepancy between the measured and the calculated ^{36}Cl concentrations.

The advantage of using a Bayesian approach is that all uncertainties in the parameters, not just in the measured ^{36}Cl concentrations, can be integrated in the model as probability distributions, which are called prior information. The posterior information are the corresponding probability distributions of the model output. In a Bayesian sense, the question we are trying to answer is therefore: what is the probability distribution for PR_{Ca} and PR_K that will best match the calculated and measured ^{36}Cl (N_{36}) concentrations regarding the whole data set at once?

Bayes rule can be written as:

$$p(a|b) = p(b|a) * \frac{p(a)}{p(b)} \tag{5.14}$$

With p(a|b) the probability distribution of a given b. In our case, a represents the calculated ^{36}Cl concentrations and b the measured ^{36}Cl concentrations, N_{36}, for each sample data. Based on Eq. 5.10, the calculated ^{36}Cl concentration can be written:

$$N_{36,i} = A_i \; PR_{Ca} + B_i \; PR_K + C_i + \zeta_i \tag{5.15}$$

with i = 1, ..., 20 for each of the 20 measurements of the dataset. ζ_i represents for each measurement the divergence of the calculated from the measured ^{36}Cl concentration regarding the whole data set with $p(\zeta) = \mathcal{N}(0, \sigma)$.

The term $p(b|a)$ in Eq. 5.14 is the multivariate Gaussian distribution ($\mathcal{N}_n(M, \Sigma)$) of dimension n with mean vector M and covariance matrix Σ. It can be written as

$$p(\mathbf{^{36}Cl}|\mathrm{PR}_{Ca}, \mathrm{PR}_K, \sigma, \mathrm{t}, \varepsilon, \mathrm{P}_\mu) = \mathcal{N}_{20}(\mathbf{A}\ \mathrm{PR}_{Ca} + \mathbf{B}\ \mathrm{PR}_K + \mathbf{C}, \sigma^2.\mathbf{I}_{20,20}) \tag{5.16}$$

^{36}Cl is the vector of measured $\mathrm{N}_{36,i}$; **A**, **B** and **C** are the vectors created by concatenation of the values A_i, B_i and C_i, which contain the prior information of t_{expo}, ε and P_μ; and $\mathbf{I}_{20,20}$ is the identity matrix (20 dimensional square matrix filled with 0 except 1 on the diagonal).

According to Eq. 5.14, the posterior distribution of all parameters is then written as:

$$p(\mathrm{PR}_{Ca}, \mathrm{PR}_K, \sigma, \mathrm{t}, \varepsilon, \mathrm{P}_\mu|\mathbf{^{36}Cl}) =$$

$$\frac{p(\mathbf{^{36}Cl}|\mathrm{PR}_{Ca}, \mathrm{PR}_K, \sigma, \mathrm{t}, \varepsilon, \mathrm{P}_\mu)p(\mathrm{t})p(\varepsilon)p(\mathrm{P}_\mu)p(1/\sigma^2)p(\mathrm{PR}_{Ca})p(\mathrm{PR}_K)}{p(\mathbf{^{36}Cl})} \tag{5.17}$$

All prior information on the parameters are defined as follows:

- t_{expoFj}: The priors for the exposure durations are considered independent, i.e. $p(t_{expo})$ = $p(t_{expoF1}) * \ldots * p(t_{expoF5})$. Based on the non-cosmogenic age determinations described in section 5.3.1, $p(t_{expoFj})$ for each of the five flows are (here in years):

- Historical flow: $p(t_{expoF1}) = U(383,393)$
- Solicchiata flow: $p(t_{expoF2}) = U(t_{2,1}, t_{2,2})$ with $p(t_{2,1}) = \mathcal{N}(18352, 143)$ and $p(t_{2,2}) = \mathcal{N}(4275,76)$
- Piano della Lepre: $t_{F3} = t_{3,1}$ - $t_{3,2}$ with $p(t_{3,1}) = \mathcal{N}(20000, 1000)$ and $p(t_{3,2}) = \mathcal{N}(1000, 3000)$
- La Nave flow:$p(t_{expoF4}) = \mathcal{N}(32444, 1333)$
- Payun Matru flow: $p(t_{expoF5}) = \mathcal{N}(15200, 894)$

- ε: The priors for the calculated erosion rates of the flow La Nave are centered on the values e_s, which vary depending on the scaling factor used (Table 5.3), and the standard deviation is 30% of e_s (estimated from the sensitivity test described in section 5.3.1): $p(\varepsilon) = \mathcal{N}(e_s, e_s{*}0.3)$.

- P_μ: The priors for the sample-specific ^{36}Cl production rates from muon capture are assumed independent, i.e. $p(P_\mu) = p(P_{\mu 1})$ * ... * $p(P_\mu 5)$. Each $p(P_\mu j)$ is centered on the mean value μj of flow j. Its standard deviation is 25% of the mean value (section 5.3.1): $p(P_\mu) = \mathcal{N}(\mu j, \mu j{*}0.25)$. - PR_{Ca} and PR_K: The priors for the unknown parameters PR_{Ca} and PR_K are chosen conjugated according to Gelman et al. (2004) and quasi non-informative, which means that the values in the set [0, 10000] have roughly the same probability: p(PRCa) = p(PRK) = $\mathcal{N}_{t=0}(0,100000)$.

- ^{36}Cl concentration: The priors for the standard deviations of the ^{36}Cl concentrations are chosen conjugated and quasi non-informative: $p(1/\sigma^2) = \Gamma(0.0001, 0.0001)$.

with $p(x)$ is the probability distribution of the parameter x; $U(a, b)$ is the uniform distribution with the minimum and maximum values a and b; $\mathcal{N}(m, s)$ is the Gaussian distribution with the mean m and the standard deviation s; $\mathcal{N}_{t=a}(m, s)$ is the Gaussian distribution with mean m and standard deviation s, which is left-truncated at a (no value lower than a admitted); $\Gamma(s, r)$ is the Gamma distribution with shape and rate parameters s and r.

The number of evaluations are defined by the dimension number of the joint prior and posterior distributions. Considering that the probability distribution function of each

parameter for each measurement has to be included in the computation, the number of calculations is huge. It can be reduced by decreasing the resolution of the probability distribution function, in other words by discretizing the parameter space into larger increments. But it can also be reduced by limiting the parameter space to be explored. This can be done by using a Markov Chain Monte Carlo algorithm (MCMC, for details see e.g. Robert and Casella, 1999; Gelman et al., 2004). In this method a set of initial randomly selected choices for the (PR_{Ca}, PR_K, P_μ, ε, t_{expo}) are made, and by evaluating these selections using Bayes rule a new set of samples is drawn.

Here we use a stochastic algorithm, the Metropolis-Hastings algorithm (Metropolis et al., 1953; Robert and Casella, 1999), which is a specific MCMC simulation that uses a selection-rejection criteria to guide sampling through the parameter space to mimic the posterior probability distribution. The length of the simulation sequence drives the quality of the posterior distribution of the parameters. In our simulation we used a large sequence of 2.5×10^6 iterations. The algorithm is coded and run using R Development Core Team (2008). We checked the convergence of the sequence by comparing results obtained by initialization at different starting points.

The distributions obtained with this method are shown in Fig. 5.7.

The impacts of the above stated considered uncertainties in the calibration will be tested by running the statistical algorithm several times, first accounting for all selected uncertainties (Fig. 5.7a), then only with the uncertainties in the independent age constraints (Fig. 5.7b) and finally without any uncertainty, taking the mean values of the distributions of each of the five independent ages (Fig. 5.7c).

5.5 Results and discussion

5.5.1 New spallation production rates from Ca and K

Fig. 5.7a shows the posterior distributions of the spallation production rates PR_{Ca} and PR_K resulting from the dataset scaled to SLHL according to all scaling models. The abscissa represents the production rate and the ordinate displays the probability. The highest probability corresponds to the mean value for the production rates that best explains all

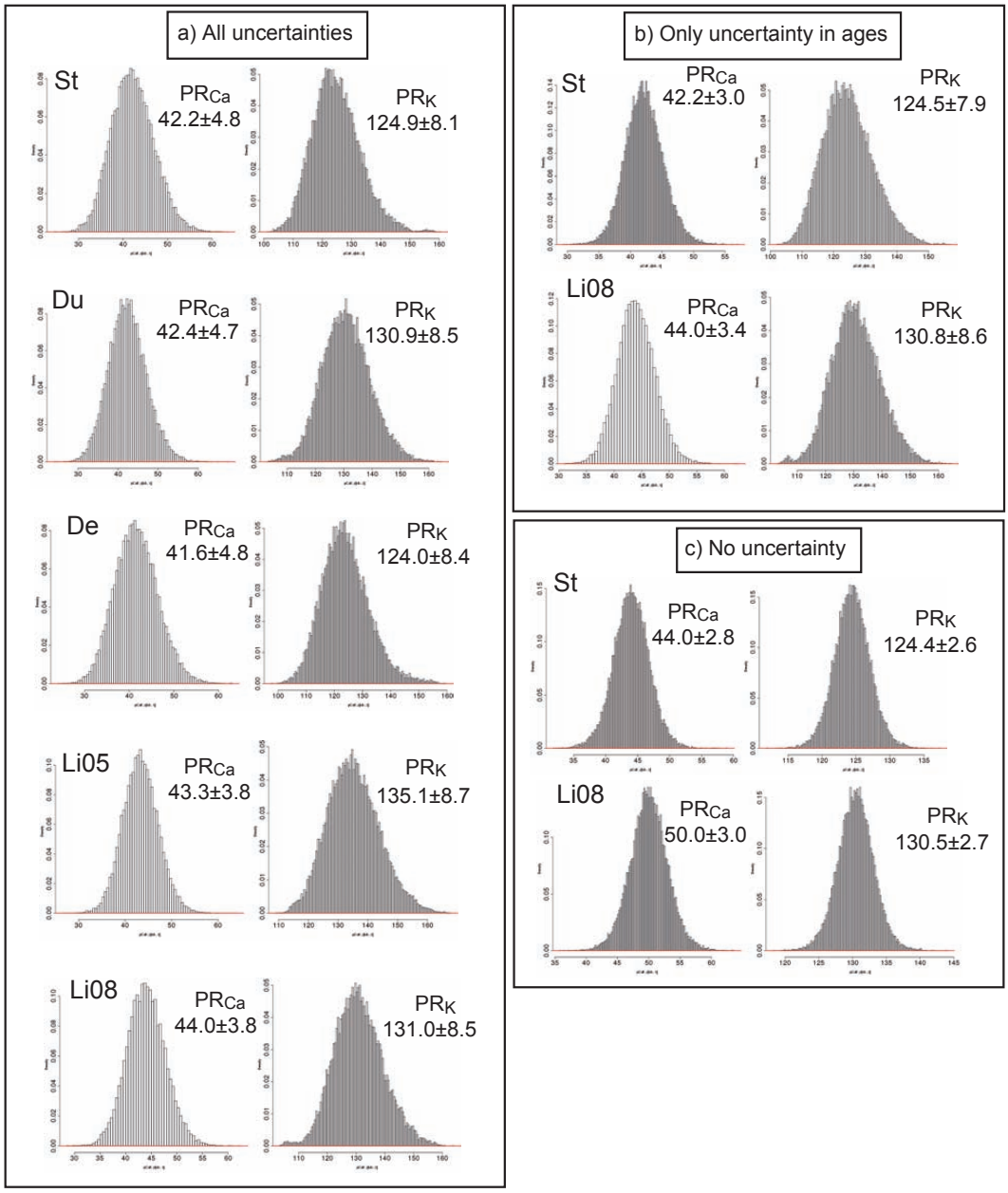

Figure 5.7: *Posterior distributions of PR_{Ca} and PR_K resulting from the Bayesian statistical analysis of the calibration data set. (a) All uncertainties in the selected parameters t_{expo}, P_μ and ε are integrated. (b) Only the uncertainty in t_{expo} of each flow is considered. (c) No uncertainties are assigned to the parameters. In (b) and (c), only the distributions for the results when using the scaling methods of St and Li08 are illustrated. This choice was made because the new "St" production rates are among the lowest mean values, while the new "Li08" production rates are among the highest mean values.*

the data, while the width of the curve at the inflexion point defines its standard deviation.

The geometry of the distributions are in all cases close to normal. Table 5.7 summarizes

the results from all five datasets at SLHL. The mean values of PR_{Ca} are very similar, ranging between 41.6 and 44.0 atoms ^{36}Cl (g Ca)$^{-1}$ a^{-1}, and those of PR_K have a wider range between 124.0 and 135.1 atoms ^{36}Cl (g K)$^{-1}$ a^{-1} with standard deviations on the order of 10% for PR_{Ca} and 7% for PR_K. If the uncertainty in the erosion rate of the flow La Nave ($\pm$30%, 1σ) and the uncertainty on the muon production rate (P_μ) ($\pm$25%, 1σ) are not considered, the means stay the same and standard deviation of PR_{Ca} decreases to about 8% while that on PR_K remains close to 7% (Fig. 5.7b). Therefore, only considering uncertainties in the independent ages, does not change the resulting spallation production rate mean values but reduce their uncertainties by about 2%. When all uncertainties are neglected, the resulting mean values for PR_{Ca} increase between 4% and 12% depending on the scaling model, while PR_K remains similar (Fig. 5.7c). The standard deviations for PR_{Ca} and PR_K are also lowered ($\sim$5% for PR_{Ca} and $\sim$2% for PR_K, Fig. 5.7).

PR_K is primarily constrained by the four Payun Matru sanidine samples with a ^{36}Cl contribution from spallation on K that accounts for about 93% of the total (Table 5.5). However, although the ^{36}Cl contribution due to Ca is dominant in the Etna plagioclases, and thus PR_{Ca} is mainly constrained by these samples, the contribution from K is still significant (9% - 16%). The well-defined independent age of the Payun Matru flow is the reason why ignoring uncertainties on the independent ages does not affect the PR_K value. On the other hand, disregarding those uncertainties clearly yields inaccuracies in the PR_{Ca}. This is probably due to the poor constraint of the independent age of the Solicchiata flow, which constitutes one fourth of the data set. Moreover, while the SLHL PR_{Ca} values with or without uncertainties in the independent ages agree within standard deviations when using the St, Du and De scaling models, this is not the case with Li05 and Li08 models.

Therefore while not taking account of uncertainties in P_μ or in the erosion rate will not significantly change the final results, it is crucial to consider uncertainties in the independent ages. This conclusion is, however, very specific to this study since erosion is only limited to three measurements of the data set and the muon contribution relatively unimportant (max. 10%). This displays the importance for future studies to discuss all uncertainties and to use a calibration model that allows those uncertainties to be accounted

for.

A comparable problem is shown in Balco et al. (2008) where the authors compare a large set of calibration measurements from published and unpublished studies scaled with different scaling models. However, since no uncertainties other than measurement errors could be considered, possible inaccuracies due to the scaling schemes, could not be deconvoluted from errors related to the independent age.

In our case, standard deviations in the production rates mainly originate from the uncertainties in the independant ages. We can therefore assume that mean production rate values from each scaling method can be compared relatively to each other to discuss their relative differences.

PR_{Ca} mean values are very similar with a maximum difference of 5% between the "De" version and the "Li08" version (Table 5.7), although the differences in the spallation scaling factors at Mt Etna reach 23% (section 5.4.2 and Fig. 5.6). On the other hand, while the differences in the scaling factors are much smaller (7%) at Payun Matru, the PR_K mean values differ by almost 8% (between "De" and "Li05").

The observed differences in the scaling factors are almost averaged out in the final PR_{Ca} production rate values over the range of elevations (500 - 2000 m) and exposure durations (388 years 32 ka) encountered, while this is not the case for the PR_K value, mainly constrained by a much smaller number of samples, collected from the same flow at very similar altitudes.

The tendency of the Li05 and Li08 scaling factors to be systematically lower than the others is reflected by higher resulting mean values of the production rates.

5.5.2 Comparison to previous published production rates

The SLHL production rates determined in this study are in the lowest range of the so far calibrated ^{36}Cl spallation production rates. Most of the previously calibrated production rates are significantly higher (Table 5.1). The discrepancies between the various published production rates most probably arise from methodological differences in the manner in which the different calibrations were performed. It can be observed that calibration studies relying on silicate whole rock, which often contain high Cl contents, generally yield higher

Table 5.7: *Calibrated ^{36}Cl spallation production rates from Ca and K, normalised to SLHL with five published scaling schemes: St (Stone, 2000), Du (Dunai, 2001), De (Desilets et al., 2006b), Li05 (Lifton et al., 2005), Li08 (Lifton et al., 2008).*

Scaling method	SLHL PR_{Ca} [atoms ^{36}Cl (g Ca)$^{-1}$ a^{-1}] Mean $\pm\sigma$	SLHL PR_K [atoms ^{36}Cl (g K)$^{-1}$ a^{-1}] Mean $\pm\sigma$
St	42.2 ± 4.8	124.9 ± 8.1
Du	42.4 ± 4.7	130.9 ± 8.5
De	41.6 ± 4.8	124.0 ± 8.4
Li05	43.3 ± 3.8	135.1 ± 8.7
Li08	44.0 ± 3.8	131.0 ± 8.5

production rates (PR_{Ca} in Zreda et al., 1991, Phillips et al., 1996, 2001, Swanson and Caffee, 2001, Licciardi et al., 2008 ignoring corrections for abnormal pressure conditions; PR_K in Phillips et al., 1996, Swanson and Caffee, 2001). The low production rates resulting in this study, on the other hand, are in best agreement with production rates calibrated with low-Cl samples as shown in the next paragraph. An overestimation of spallation production rates calibrated with high-Cl samples could be due to an underestimation of the ^{36}Cl production from the ^{35}Cl(n,γ)^{36}Cl pathway, as shown in Schimmelpfennig et al. (2009).

The production rate from Ca (PR_{Ca}), scaled according to Stone (2000), has a value of 42.2 ± 4.8 atoms ^{36}Cl (g Ca)$^{-1}$a^{-1} (Table 5.7) and is closest to that of Stone et al. (1996) (48.8 ± 1.7 atoms ^{36}Cl (g Ca)$^{-1}$a^{-1}, Table 5.1), scaled with Lal (1991). Stone et al. (1996) used separated Ca-feldspar samples from a basaltic lava flow dated at 17.3 ka, falling in the exposure duration range of this study. The sample site is located at a latitude of 39°N and at an elevation of 1445 m, both very similar to the spatial conditions of the Mt. Etna samples. Also the Cl content in the samples (2-5 ppm) is on the same order as that of the minerals used for this study. These methodological similarities might explain why the results are so close. The difference is that Stone et al. (1996) used only three samples from one single flow and from the same elevation; the SLHL production rate is therefore only controlled by this specific site, as discussed for PR_K in this study (section 5.5.1). In our study, on the other hand, SLHL PR_{Ca} is calibrated from a global dataset with samples

coming from several flows, elevations and exposure durations.

Our spallation production rate PR_K, scaled with St, has a value of 124.5 ± 8.1 atoms ^{36}Cl (g K)$^{-1}$a^{-1} in agreement with that determined by Phillips et al. (2001), 137 ± 9 atoms ^{36}Cl (g K)$^{-1}$a^{-1}, scaled according to Lal (1991) (Table 5.7). The sample set in Phillips et al. (2001) consists of a series of 30 whole rocks of divers compositions, collected at numerous sites from a wide range of latitudes, longitudes, elevations and exposure durations (Phillips et al., 1996) and were used for the calibration of PR_{Ca}, PR_K and $P_f(0)$. However, K concentrations are quite low in all samples, only 3 samples have higher K contents than Ca contents with maximum 4.4% and 2.7% K in two samples. These two samples have the lowest Cl contents in the sample set, with 6 and 18 ppm Cl, and very low Ca (∼0.02%) and probably therefore exert the strongest control on the resulting production rate from K. The exposure duration of these samples is similar (12 ka) to that of the Payun Matru samples (15 ka), but the elevation and the latitude are different (375 m and 52°N).

Evans et al. (1997) on the other hand used a K-feldpar mineral separate with Cl content ranging between 1 to 315 ppm. Samples were collected at various latitudes (38°N, 58°N) with altitude between 500 and 3600 m. The preferred value of Evans et al. (1997) of 170 ± 25 atoms ^{36}Cl (g K)$^{-1}$a^{-1} is supported by 11 samples among which only three had chlorine concentrations lower than 143 ppm. On a closer inspection of Figure 3 in Evans et al. (1997), we observe that two samples yield lower production rate between 110 and 120 atoms ^{36}Cl (g K)$^{-1}$a^{-1}, values that would be in agreement with our proposed production rate. Whether those samples are the ones with lowest chlorine concentration is not clear in the paper, but it is probable that high Cl concentration of all the other samples might have yielded an overestimation of the final production rate.

In this study we made no attempt to correct for potential snow cover because records at Mt Etna show that snow is limited to less than 1 or 2 months per year at the altitudes of the sampling sites and therefore would yield snow correction of less than 5% (e.g. Benson et al., 2004; Schildgen et al., 2005). However, at Payun-Matru it is possible that snow cover is more important and a 6 month coverage per year would yield a higher production

rate by at most 10%.

5.5.3 Recalculated ^{36}Cl ages of the Etna and Payun Matru lava flows

The exposure age of each individual sample and the mean exposure age for each flow are calculated according to the new calibrated ^{36}Cl production rates in two ways. First, the statistical algorithm provides mean ages for each flow (Table 5.8) as posterior distributions. Secondly, the exposure ages of each sample were calculated using the ^{36}Cl calculation spreadsheet of Schimmelpfennig et al. (2009) (Table 5.9). Fig. 5.8a shows these recalculated ages, using the St scaling method, and the independent age constraints for comparison and Fig. 5.8b displays the recalculated ages using Li08 scaling model. This choice was made because the new "St" production rates are among the lowest mean values, while the new "Li08" production rates are among the highest mean values. All ages from the individual samples, the mean values for each flows and the independent age are in good agreement, except for HF1.

When calculated with the spreadsheet, the HF1 exposure age differs significantly with the St scaling model while with Li08 the two values are in agreement. This discrepancy is due to the huge difference between each scaling scheme for the spallation scaling factor (Fig. 5.6), and probably arises from the very young age of the flow. Inaccuracies in the temporal variations of the cosmonuclide production do not average out over such a short period, and the St scaling does not correct for changes in production rate with time. The statistical algorithm, on the other hand, calculates the same exposure age of 388 $\pm$ 3 years for all five scaling schemes. This is because the uniform distribution of the prior for the independent age constraint of this flow prohibits the posterior to go beyond the limits of this closed interval.

For the least well constrained exposure age flow, the Solicchiata flow, the resulting exposure age is 7.2 $\pm$ 1.0 ka using St scaling and 8.5 $\pm$ 1.1 ka using Li08 scaling. Both ages are in agreement and lie close to the younger limit of the independent age interval. Based on field observations of flow superpositions, Branca (2003) estimated that this flow had an eruption age younger than 7 ka (see Fig. 5 in Branca, 2003). This estimate is close to our calculated age.

Table 5.8: *^{36}Cl exposure ages of the Etna and Payun Matru lava flows, resulting as output (posterior distributions) from the stastical algorithm according to the calibration results.*

St	Du	De	Li05	Li08
Mt. Etna: Historic Flow 1614-24 (between 383 and 393 years)				
388 ± 3	388 ± 3	388 ± 3	388 ± 3	388 ± 3
Mt. Etna: Solicchiata (^{14}C between 4.4 ka and 18.4 ka)				
7174 ± 972	8450 ± 1225	8019 ± 1183	8600 ± 1180	8462 ± 1134
Mt. Etna: Piano della Lepre (K-Ar 10 ± 3 ka)				
11691 ± 1056	10946 ± 995	11253 ± 1059	11863 ± 889	12676 ± 927
Mt. Etna: La Nave (K-Ar/TL 32.4 ± 1.3 ka)				
32450 ± 1322	32468 ± 1312	32447 ± 1323	32429 ± 1312	32371 ± 1311
Payun Matru (K-Ar 15.2 ± 0.9 ka)				
15214 ± 886	15276 ± 901	15204 ± 919	15251 ± 894	15255 ± 906

The recalculated mean values of sample SI43 are higher (11.7 ± 1.1 ka St scaling and 12.7 ± 0.9 ka Li08 scaling) than the independent mean value, but lie within one standard deviation (10.0 ± 3.2 ka). For the two flows La Nave and Payun Matru, the recalculated mean values are in excellent agreement with the independent ages.

All our recalculated ages agree within uncertainties with the independent ages regardless of the scaling model, which confirms the internal and external consistency of the whole data set. In addition, we do not see any dependence on latitude or altitude on the resulting exposure ages for any of the scaling models. However, because of the relatively small range of elevation and latitude of our sites, our measurements are relatively insensitive to such effects. This has the advantage of yielding an accurate production rate determination independently of the chosen scaling scheme. On the other hand since we cannot evaluate the effects of the scaling models over a wide range of regional parameters, it is difficult to assess whether our production rate can be extrapolated at high latitude or high altitude and over much longer time span.

Table 5.9: *^{36}Cl exposure ages of the calibration samples, recalculated with the ^{36}Cl calculation spreadsheet (Schimmelpfennig et al.,2009) according to the calibration results. Uncertainties are derived by a standard error propagation, including uncertainties in the chemical analysis, the SLHL spallation production rates, all correction and scaling factors, 10% uncertainty in production from thermal and epithermal neutrons and 25% in the production from slow negative muons. Errors are missing for the exposure ages of the eroding flow La Nave, because the ages were determined by minimizing the difference between measured and calculated ^{36}Cl concentrations, taking into account the erosion rates.*

	St	Du	De	Li05	Li08
Mt. Etna: Historic Flow 1614-24 (between 383 and 393 years)					
HF1	322 ± 30	343 ± 33	330 ± 32	355 ± 35	411 ± 40
Mt. Etna: Solicchiata (^{14}C between 4.4 ka and 18.4 ka)					
SI3	7169 ± 673	8500 ± 818	8103 ± 792	8660 ± 845	8549 ± 830
SI40	8085 ± 783	9586 ± 951	9130 ± 919	9768 ± 981	9643 ± 964
SO3	7019 ± 673	8291 ± 814	7872 ± 785	8463 ± 843	8357 ± 829
SO2	7262 ± 675	8546 ± 815	8089 ± 783	8716 ± 846	8608 ± 831
SO1	6620 ± 665	7758 ± 798	7314 ± 762	7899 ± 826	7803 ± 812
Mt. Etna: Piano della Lepre (K-Ar 10 ± 3 ka)					
SI43-D4	11455 ± 2216	10720 ± 2093	11014 ± 2143	11652 ± 2318	12491 ± 2494
SI43-D5	12809 ± 2859	11984 ± 2695	12313 ± 2757	13028 ± 2984	13972 ± 3216
SI43-D6	11616 ± 1424	10874 ± 1355	11169 ± 1399	11821 ± 1499	12670 ± 1606
SI43-D7	11790 ± 1287	11034 ± 1229	11336 ± 1273	11992 ± 1361	12856 ± 1457
SI43-D8	10791 ± 1189	10100 ± 1134	10377 ± 1176	10976 ± 1253	11764 ± 1340
Mt. Etna: La Nave (K-Ar/TL 32.4 ± 1.3 ka)					
SI41	31575	31760	31697	31652	31550
SI29-160	32518	32660	32615	32483	32335
SI29-250	33200	33320	33280	33075	32887
Payun Matru (K-Ar 15.2 ± 0.9 ka)					
PM06-31	15463 ± 1549	15526 ± 1547	15526 ± 1599	15568 ± 1564	15599 ± 1578
PM06-31-Rep	15379 ± 1519	15442 ± 1517	15441 ± 1569	15485 ± 1534	15515 ± 1548
PM06-32	15843 ± 1477	15922 ± 1475	15905 ± 1528	15976 ± 1495	15997 ± 1508
PM06-32-Rep	15173 ± 1375	15247 ± 1373	15232 ± 1425	15297 ± 1392	15319 ± 1405
PM06-24	14679 ± 1320	14596 ± 1303	14561 ± 1355	14580 ± 1315	14626 ± 1331
PM06-26	14645 ± 1308	14568 ± 1295	14525 ± 1344	14555 ± 1307	14589 ± 1321

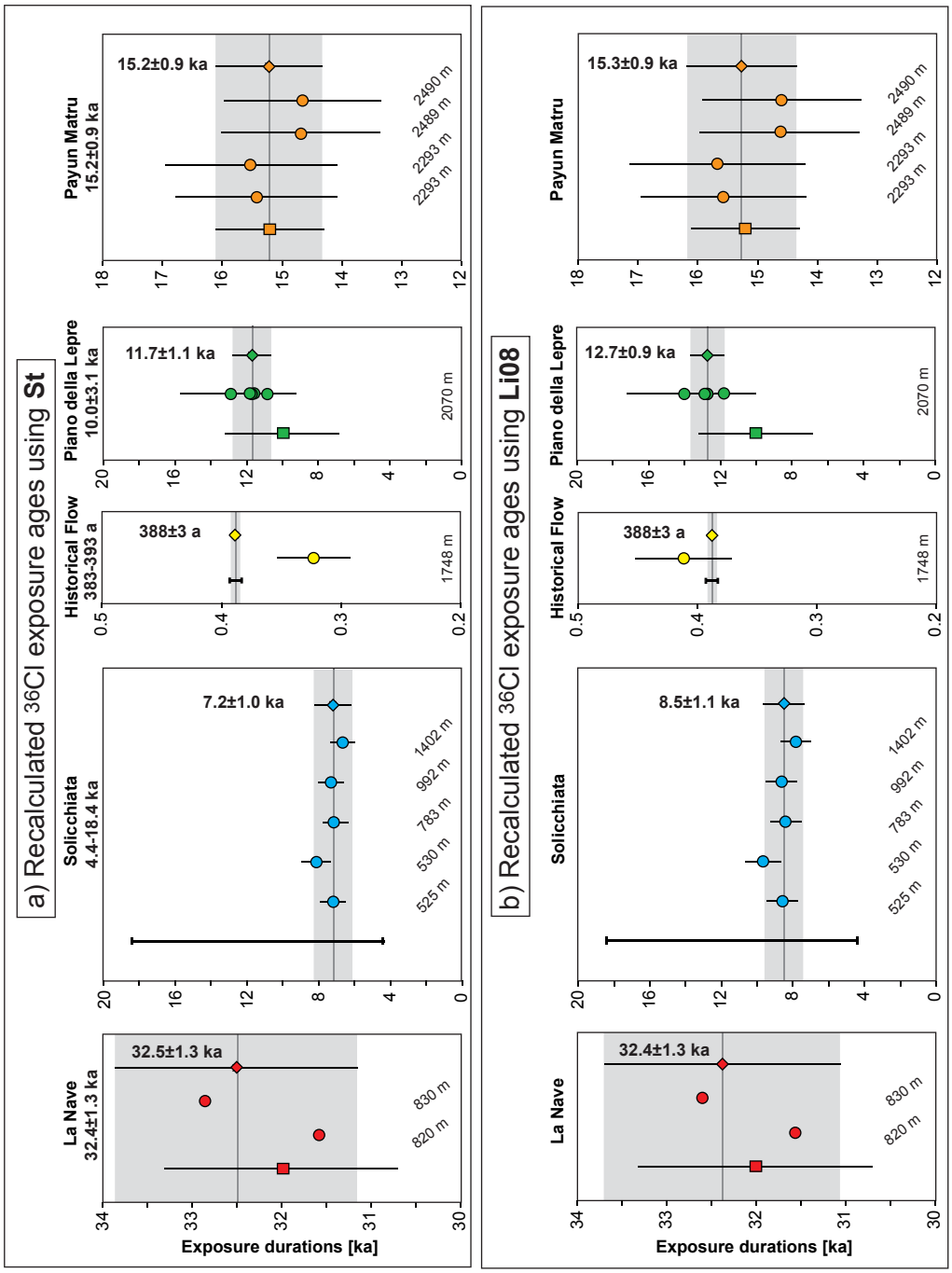

Figure 5.8: *Recalculated ^{36}Cl ages for each calibration site calculated with SLHL PR_{Ca} and PR_K scaled with St (a) and Li08 (b) and using the corresponding scaling factors, in comparison with the independent ages. The plots on the left of each panel show the independent ages (squares with 1σ error bars or black closed intervals representing uniform distributions). Circles are ^{36}Cl exposure ages recalculated with the ^{36}Cl calculation spreadsheet (Schimmelpfennig et al., 2009). Diamonds are exposure ages resulting as model output from the statistical algorithm, also illustrated by the shaded zone.*

5.6 Conclusions

The ^{36}Cl spallation production rates from Ca and K proposed in this study were calibrated with a clear strategy. In order to isolate production from Ca and K volcanic rocks containing Ca and K rich minerals with low Cl contents were sampled from flows with good independent age control. The 13 samples studied were located at latitude 38°N and 36°S, at altitudes between 500 and 2500 m and with ages ranging from 383 to 32.000 years. Each of the five published scaling schemes was applied, generating five versions of the dataset. A Bayesian statistical model developed to calculate the spallation production rates from the dataset includes all inherent major uncertainties in a consistent way. Our best estimate for the spallation production rates from Ca and K are, considering all uncertainties, 42.2 ± 4.8 atoms ^{36}Cl (g Ca)$^{-1}$a^{-1} and 124.9 ± 8.1 atoms ^{36}Cl (g K)$^{-1}$a^{-1} at SLHL scaled with Stone (2000). Production rate values scaled with all other scaling models are presented in Table 5.7. This enables users of these new production rates to calculate exposure ages according to the scaling scheme of their choice.

It is important to stress that Ca and K production rates mean values scaled with Li05 or Li08 differs by almost 6-8% from those scaled with De. Therefore, not considering the specific scaled production rates when calculating exposure ages induce a significant bias in the final result.

The relatively large uncertainties in our derived production rates are mainly due to the uncertainties in the independent age constraints of the sampled lava flows. Ignoring the uncertainty in the independent ages during the inversion of our dataset would lead to a 12% inaccuracy in the resulting production rate. This result emphasizes the importance of performing a statistical analysis of the dataset in which all major uncertainties can be accounted for.

When comparing our production rates with previously published values from samples low in Cl (Phillips et al., 2001; Stone et al., 1996), we find good agreement for both K and Ca production rates. Moreover, although the time spanned by our data (383 years to 32.000 years) is long and the altitude range (500-2500 m) is significant, the ages recalculated with our production rates are mostly in agreement, within uncertainty, with the independent

ages. This therefore suggests that, although there are discrepancies in the scaling methods, for our samples the uncertainties in the independent ages preclude seeing any altitude dependency.

A question that has to be adressed in future studies is whether the spallation ^{36}Cl production from the two target elements Ca and K can be scaled with the same scaling scheme, as done in this study. ^{36}Cl is produced from K at a lower threshold energy than from Ca and therefore the altitudinal dependence on the scaling factors might be different (Desilets et al., 2006b; Michel et al., 1995). In our case, the chemical composition of our samples and their respective altitude do not allow to evaluate this issue.

As an ideal perspective for the future refinement of ^{36}Cl production rates from spallation of Ca and K, the strategy presented in this study provides an firm basis for the combination of numerous measurements from widespread calibration sites. However, as long as scaling is not more accurate, it will not be possible to obtain SLHL ^{36}Cl production rates from a large data set without introducing systematic errors.

Finally this study has enabled us to reconcile all previous published production rates for K and Ca spallation by demonstrating that high Cl content samples over estimated production rates. When using low Cl samples, resulting production rates are in agreement with previous similar studies over various altitudes and time spans.

Chapter 6

Determination of relative cosmogenic production rates for ^{3}He, ^{21}Ne and ^{36}Cl at low latitude (3° S), along an altitude transect on the SE slope of the Kilimanjaro volcano (Tanzania)

This chapter is part of a collaboration between CEREGE, CRPG and GFZ within the CRONUS-EU network. The samples at Kilimanjaro were collected by Alice Williams, Pete Burnard and Raphael Pik. An altitutinal profile has also been sampled at Mt Etna by myself for the purpose of a similar study. However, technical problems on the noble gas mass spectrometer at CRPG prevented us from measuring the cosmogenic ^{3}He concentrations in these samples. The results presented in this chapter will later be integrated in a publication together with the data from Mt Etna.

6.1 Introduction

Accurate application of the surface-exposure dating technique, using terrestrial cosmogenic nuclides (TCN) such as ^{36}Cl, ^{3}He, ^{21}Ne, ^{10}Be or ^{26}Al requires precise knowledge of two aspects: the production rate of the nuclide of interest (the number of atoms produced per gram of target material per year) and how this production rate varies in space and time (scaling). In order to allow the application of the TCN method at any location on Earth, reference production rates have been determined (review in Gosse and Phillips, 2001). They are extrapolated to a particular location using scaling factors, which are calculated using one of the published scaling models (e.g. Stone, 2000; Desilets and Zreda, 2003; Lifton et al., 2005). Calibrations of these reference production rates are made by (1) measuring the concentration of the nuclide of interest in a geological sample from an independently dated surface at a specific geographic location, and (2) scaling the calculated time-integrated local production rate to the traditional reference position at sea-level and high latitude (SLHL) and to the present (see Chapter 5 and the review in Gosse and Phillips, 2001).

It is therefore imperative that the scaling methods used to determine these scaling factors accurately quantify the spatial and temporal variability of TCN production on Earth. Recently, some authors have cast doubt on the understanding of this variability and suggest it could be one of the main causes for inconsistencies between calibrated SLHL production rates, and hence constitute a major source of uncertainty in TCN exposure ages (e.g. Balco et al., 2008, 2009, and Chapter 5).

For example, each of the published scaling methods outlined in Chapter 1.4.1 assume that the scaling factor for a particular type of nuclear-reaction (neutron- or muon-induced) is valid for all TCN and independent of the target element, on which the reaction occurs. Reactions triggering TCN production from various target elements have been shown, however, to have variable threshold energies. Therefore, TCN production is a function of the energy spectra of the incident cosmic ray particles (Michel et al., 1995; Lal, 1987; Desilets et al., 2006b, Fig. 6.1). For example, the threshold energy to produce ^{36}Cl from spallation of K is lower than that from spallation of Ca. The cosmic ray flux is very sensitive to elevation and its energy spectrum increases considerably with increasing altitude and

latitude (by a factor of about 40 from sea level at low latitude to 5000 m at high latitude). It is therefore necessary to evaluate if the various TCN production rates change differently with altitude and latitude. If so, nuclide-specific scaling factors would be required, or even target-element-specific scaling factors for TCN such as ^{36}Cl, whose production rates are strongly dependent on the composition of the target material.

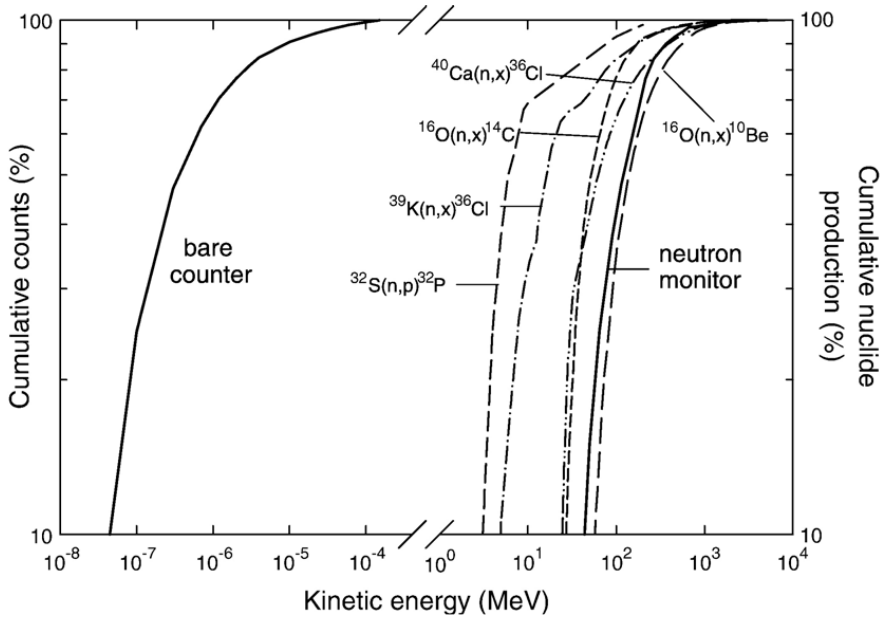

Figure 6.1: *Excitation functions for the commonly used cosmogenic nuclides ^{10}Be, ^{14}C, ^{36}Cl (taken from Desilets et al., 2006b, where these functions are compared to the energy sensitivities of a bare neutron detector and an NM-64 neutron monitor). The threshold energy of ^{36}Cl production by spallation of K is lower than that by spallation of Ca.*

One way of assessing TCN production and the global consistency in scaling is to measure the relative production rates of different TCN in surfaces. These *cross-calibrations* do not require that surfaces be independently dated nor perfectly preserved. Measurements of multiple TCN in different mineral phases from a single sample can be used to refine poorly known SLHL TCN production rates using TCN with well-constrained production rates (e.g. Niedermann et al., 2009; Balco and Shuster, 2009; Amidon et al., 2009). In addition, performing these cross-calibrations over a range of altitudes, latitudes or exposures enables assessment of any spatial and/or temporal dependence in the production of the different TCN. For example, Gayer et al. (2004) measured ^{3}He/^{10}Be in Himalayan garnets over

an altitude transect between 3000 and 4600 m and determined production ratios higher than previously documented (Cerling and Craig, 1994). The ^{3}He overproduction, which seemed to be preponderant at high altitude, was tentatively attributed to a significant difference in the threshold energies for the production of the two nuclides. More recently, Dunai et al. (2007) considered a second significant cosmogenic ^{3}He production mechanism, via low-energy neutron capture on ^{6}Li. Later studies attempted to test the hypothesis of an altitude dependency unique to ^{3}He production but could not confirm it (Blard et al., 2005; Fenton et al., 2009; Vermeesch et al., 2009). In other studies, higher than expected apparent ^{3}He production rates have been documented at high altitudes in the Himalaya (Amidon et al., 2008) and on the Puna plateau (Niedermann et al., 2009, Argentina), and even at lower altitudes in the Coso Volcanic field (Amidon et al., 2009, California, USA).

Are the actual scaling models valid at any altitude and latitude?

Should scaling factors be nuclide or even target element dependent?

Is the higher production rate observed for ^{3}He at high altitudes due to inaccurate scaling?

In this study, we evaluate if relative production rates of TCN change with altitude and if overproduction of ^{3}He at high altitudes occurs. We cross-calibrate production of ^{3}He, ^{21}Ne and ^{36}Cl in lava-flow and glacial surfaces outcropping over an altitude profile between 1000 and 4300 m at a low-latitude site (3°S), on the slopes of Mt. Kilimanjaro, Tanzania. All three nuclides can be measured in clinopyroxene phenocrysts and this mineral phase provides the most complete data set in this study. ^{3}He was measured in olivine phenocrysts in all samples except the lowest, and ^{21}Ne was measured in olivines at two different altitudes.

To the best of our knowledge, this is the first time that ^{36}Cl has been measured in a mafic mineral phase. To validate the method, ^{36}Cl was additionally measured in plagioclase phenocrysts coexisting with pyroxenes in one of the samples.

6.2 Geological setting and sampling

Based on an initial project objective of calibrating absolute and relative production rates of TCN at a low-latitude site and over a large altitude transect, sampling was undertaken in 2005 at Mount Kilimanjaro, Tanzania (3°S) (Fig. 6.2). This large shield volcano, Africa's highest mountain at 5895 m, is located at the eastern end of the Ngorongoro-Kilimanjaro Volcanic Belt, which forms one arm of the triple rift-system that characterises the eastern branch of the East African Rift System. Kilimanjaro consists of three NW-SE aligned volcanic peaks: Shira (3962 m), Mawenzi (5149 m) and Kibo (5895 m) that were constructed in multiple phases (Nonnotte et al., 2008). The first phase took place between 2.5Ma and 1.9 Ma at the Shira vent. A large sector collapse signalled the end of this phase, after which volcanic activity shifted eastwards to the Kibo and Mawenzi peaks, at around 1 Ma. Activity at Mawenzi ceased around 500 ka, but continued at Kibo with two major periods of volcanic activity occurring between 460 ka and 340 ka. The final stages of volcanism at Kilimanjaro consisted of the eruption of basaltic flows and scoria from small parasitic cones located on the volcano flanks, between around 200 ka and 150 ka.

For this study, we principally targeted cones and lava flows from this last volcanic period, located on the south-eastern flank, south of Mawenzi Peak, in a region known as the Rombo Zone (Downie and Wilkinson, 1972). This zone comprises olivine- and pyroxene-rich basanitic and ankaramitic flows erupted from parasitic cones distributed over a large elevation range, from <1500 to >4500 m. However, suitable surface exposure of lava-flows is limited between 1700 and 2500 m due to the presence of the dense tropical rainforest (Fig. 6.3a). Surface flow preservation is also compromised above approximately 3700 m, due to significant glacial activity during the Quaternary (Fig. 6.3b, Shanahan and Zreda, 2000). Thus, while an effort was made to sample pristine flow-top features for absolute calibration of TCN production rates, at many sites this was not possible. Between 2700 and 3200 m, well-preserved ropy tops of lava flows (Fig. 6.4) out-crop at the bases of the parasitic cones, but at these locations it was not possible to access the inner, degassed parts of the flow in order to extract rock suitable for precise Ar/Ar or K/Ar dating. As such, our efforts to obtain independent ages and absolute production rates for two of the

Table 6.1: *Geographic samples locations, scaling factors for neutron induced and slow negative muon induced reactions calculated according to Stone (2000), sample thickness and thickness correction factors for spallation reactions.*

Sample	latitude South	longitude East	altitude [m]	scaling neutrons	scaling muons	thickness [cm]	thickness correction
TZ09	03°23'.740	37°30'.248	1013	1.27	0.95	5.3	0.957
TZ10	03°10'.490	37°31'.180	2740	3.94	1.95	5.8	0.953
TZ12	03°10'.490	37°31'.180	2740	3.94	1.95	5.7	0.953
TZ13	03°09'.319	37°30'.411	3050	4.69	2.19	4.5	0.963
TZ14	03°09'.319	37°30'.411	3050	4.69	2.19	5.1	0.958
TZ17	03°08'.308	37°28'.791	3694	6.56	2.75	6.8	0.945
TZ15	03°07'.020	37°28'.234	4107	8.02	3.16	4.2	0.965
TZ19	03°05'.791	37°25'.240	4331	8.90	3.39	7.2	0.942

sampled flows were unsuccessful. For the parasitic cones erupted in the Rombo Zone, the only precise eruption ages available in the published literature are K/Ar ages of 165 ± 5 ka and 195 ± 5 ka for two basaltic flows (Nonnotte et al., 2008). For the investigation of relative TCN production rates, however, it is possible to use erosion surfaces, such as glacially-polished surfaces, for which the eruption age of the lava-flow is not necessarily equal to the apparent exposure age.

Eight surface samples were collected at six different altitudes between 1000 and 4300 m (Table 6.1 and Fig. 6.4).

6.3 Sample preparation, ^{36}Cl, ^{3}He and ^{21}Ne measurements and compositional analysis

6.3.1 Physical sample preparation

Prior to sample preparation, a few pieces of whole-rock from each surface were set-aside for thin-section preparation and bulk-rock composition analyses. For cosmogenic analyses, the top 5 to 10 cm of each whole rock sample was sawn off then crushed and wet-sieved to remove dust particles and the finest grain sizes (<125μm). A hand-magnet was then passed over the 0.25, 0.5, 0.7, 1.0 and 2.0 mm fractions to remove magnetic groundmass. Using a binocular microscope, olivine and pyroxene phenocrysts were hand-picked to obtain pure mineral separates, with care taken to ensure complete removal of altered crystals and crystals with adhering basalt. For ^{36}Cl analyses, approximately 5 to 10 g of pure pyroxene

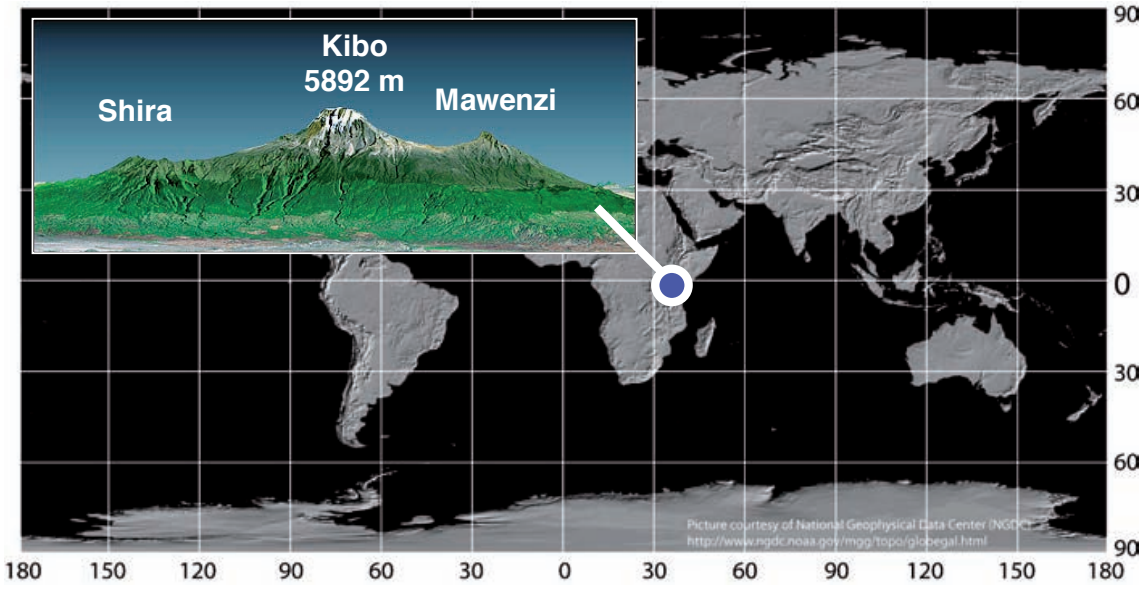

Figure 6.2: *Location map of Mt. Kilimanjaro, Tanzania.*

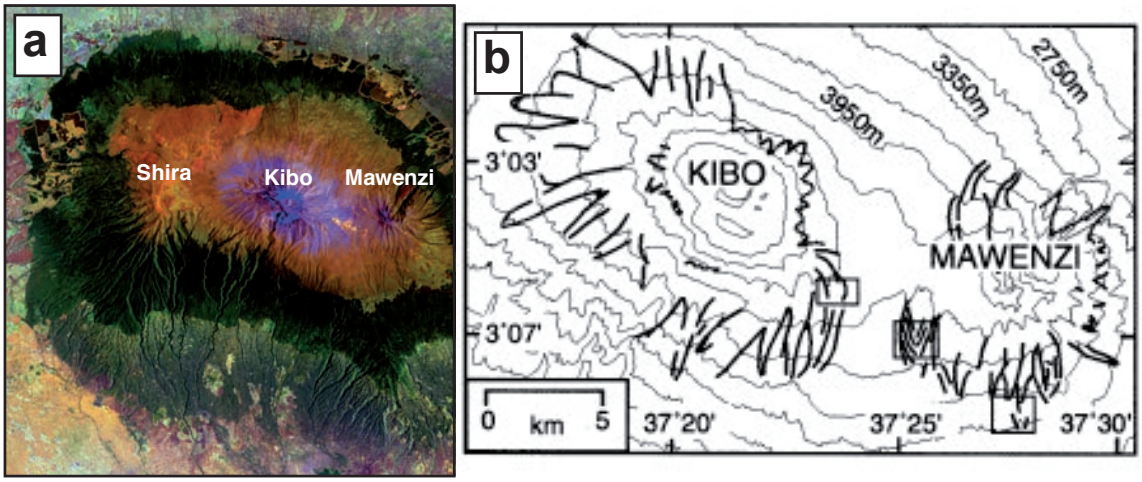

Figure 6.3: *a) Satellite image (Landsat TM) of Mt. Kilimanjaro clearly showing the different altitudinal zones in a ring pattern - cultivated footslopes (green), dense semi-tropical rainforest (dark green), heathlands (pale green), alpine-zone (brown) and the glaciated summit regions (blue). b) Glacial sketch map of Kibo and Mawenzi from Shanahan and Zreda (2000). Solid lines mark glacial moraines.*

phenocrysts were hand-picked from the coarsest fractions. In addition, for sample TZ15, a Frantz magnetic separator was used to separate several grams of 0.5-mm-size plagioclase phenocrysts from the more magnetic mafic minerals. Plagioclases were hand-picked in order to maximize sample purity. For noble gas extractions, approximately 2 g of the coarsest pure fractions were cleaned in acetone and set aside for in vacuo crushing and

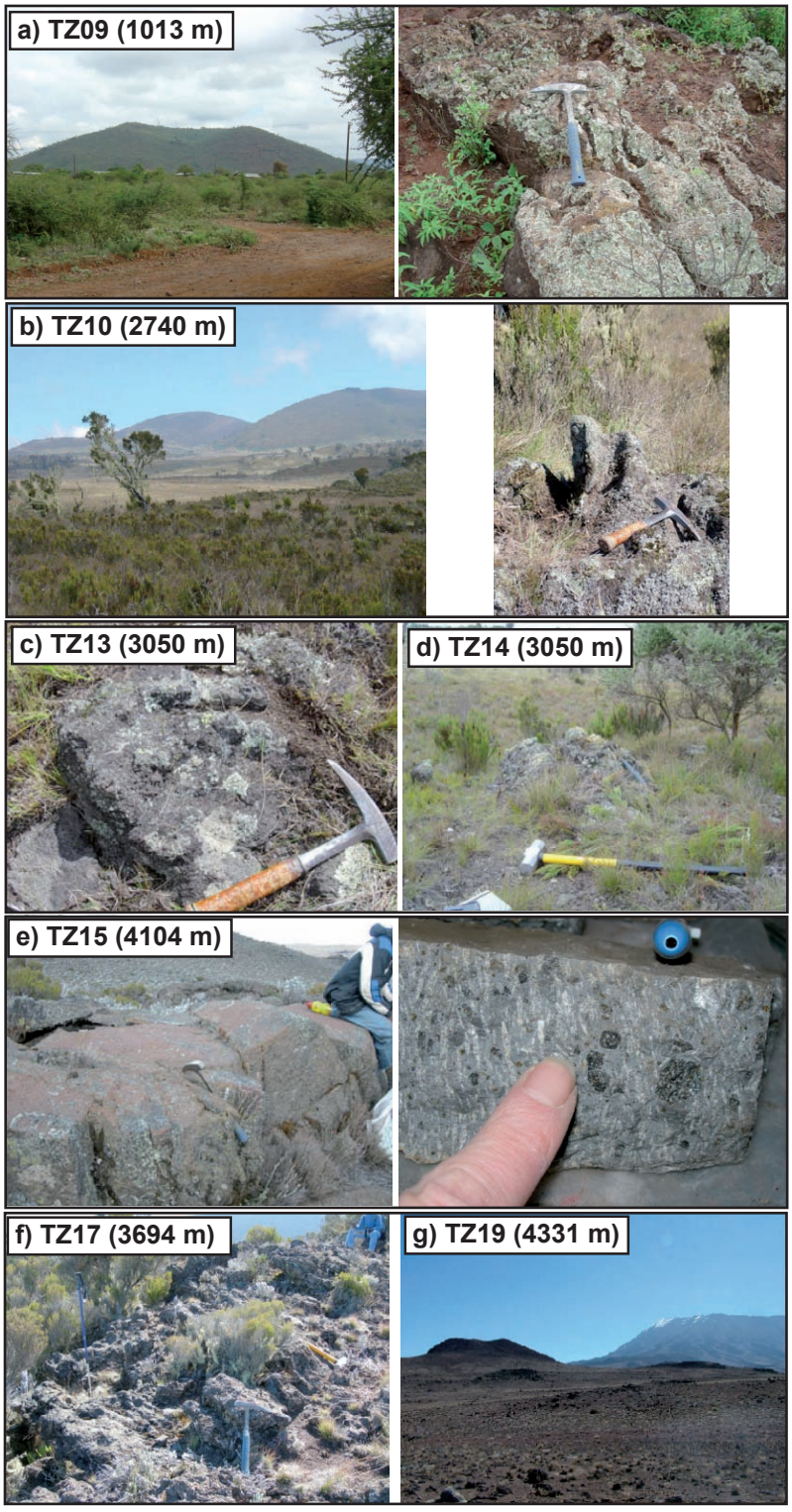

Figure 6.4: *Pictures of sample sites at Kilimanjaro.*

determination of magmatic helium isotope ratios. For the melt extractions, up to 3 g of phenocrysts from the 0.5 to 0.7 mm size fraction were cleaned in acetone, hand-crushed and sieved to 0.1 - 0.3 mm and then re-picked and cleaned once more in acetone, to ensure the highest degree of sample purity.

6.3.2 Chemical ^{36}Cl extraction and measurement

The chemical ^{36}Cl extraction was conducted at CEREGE, following the procedure described in Schimmelpfennig et al. (2009). Initial mineral weights ranged between 3.5 g and 10.5 g. The grains were first washed with MQ water in closed HDPE bottles for several hours on a shaker table, then etched in limited amounts of a HF (48%)/ HNO_3 (2M) mixture (volume ratio 1:2) in order to dissolve about 20% of the grains and ensure total groundmass removal. From the etched grains an aliquot of 1 g was taken for chemical composition analysis at SARM (CRPG, Nancy, France). The rest is dissolved with an excess amount of the HF/HNO_3 mixture by shaking overnight. After adding the acid mixture, approximately 1.5 mg of chloride in the form of a chloride carrier (OakRidge National Laboratory), enriched in ^{35}Cl (99.9%), was added to the solution. After complete dissolution of the grains, the solutions were centrifuged to separate the supernatant from the fluoric cake formed during the dissolution reaction. AgCl was precipitated by adding $AgNO_3$. This first precipitate was re-dissolved in dilute NH_4OH, and, in order to reduce the isobaric interferences of ^{36}S during the ^{36}Cl AMS measurements, $Ba(NO_3)_2$ was added to precipitate $BaSO_4$/$BaCO_3$. The AgCl was again precipitated from the resulting solution by acidification with HNO_3 and collected by centrifuging. Finally, the AgCl precipitates were rinsed and dried in preparation for measurement at LLNL-CAMS. AgCl yields, including carrier and natural Cl, accounted for 4 to 6 g. Several blanks were carried out in order to survey the cleanness during the chemical extraction procedure and to correct sample measurements for laboratory ^{36}Cl and Cl sources.

^{36}Cl and Cl concentrations were determined using the Lawrence Livermore National Laboratory FN accelerator mass spectrometer (LLNL-CAMS). Isotope dilution (addition of a ^{35}Cl-enriched carrier) allows simultaneous determination of ^{36}Cl and Cl concentrations. ^{36}Cl/^{35}Cl ratios were determined by normalizing to a ^{36}Cl standard prepared by

Table 6.2: *^{36}Cl data from AMS measurements at LLNL-CAMS with sample weight, amount of spike-Cl and calculated Cl and ^{36}Cl concentrations in pyroxene separates and in one plagioclase separate (TZ15-plg). Note that replicates were measured for samples TZ10 and TZ12, and that for sample TZ15 ^{36}Cl was measured in both pyroxene separates and plagioclase separates.*

Sample	sample weight dissolved [g]	measured ^{35}Cl/^{37}Cl	measured ^{36}Cl/^{35}Cl [10^{-14}]	Cl content in spike [mg]	[Cl] in sample [ppm]	[^{36}Cl] [10^{5} atoms g^{-1}]
TZ09	4.52	230.2±2.0	11.99±0.28	1.457	2.68±0.25	6.31±0.17
TZ10A	2.63	247.8±1.6	44.03±0.74	1.475	4.60±0.38	42.01±0.83
TZ10B	1.84	341.9±2.4	32.05±0.62	1.473	2.77±0.38	43.1±1.1
TZ12A	2.80	238.3±2.9	46.0±1.1	1.484	4.43±0.40	41.6±1.1
TZ12B	2.79	253.64±0.15	43.1±1.0	1.484	3.86±0.35	39.0±1.0
TZ13	4.17	177.17±0.10	80.2±1.9	1.488	5.21±0.36	49.4±1.2
TZ14	3.75	188.13±0.59	77.3±1.4	1.478	5.18±0.37	52.5±1.0
TZ17	2.01	178.3±2.5	16.88±0.40	1.467	10.06±0.79	20.59±0.59
TZ15	3.41	239.5±4.4	11.27±0.27	1.459	3.18±0.34	7.81±0.21
TZ19	6.42	91.0±7.0	37.5±2.6	1.451	8.41±0.98	14.7±1.0
TZ15-plg	7.52	300.0±5.9	16.08±0.31	1.457	0.74±0.12	5.14±0.11
BL-1		418.6±6.8	0.72±0.10	1.461		
BL-2		412.1±1.9	0.77±0.05	1.460		
BL-3		447.8±1.2	0.85±0.10	1.483		
BL-4		474.78±0.10	0.90±0.06	1.473		

K. Nishiizumi (Sharma et al., 1990). The stable ratio ^{35}Cl/^{37}Cl was also normalized to this standard, assuming the natural ratio of 3.127. Measured ratios and their uncertainties are presented in Table 6.2. The precision of the ^{35}Cl/^{37}Cl ratios accounts for 2% or less (standard deviation of repeat measurements). The precision of the ^{36}Cl/^{35}Cl ratios ranges between 2% and 7%. Blank ^{36}Cl/^{35}Cl ratios range between 7×10^{-15} and 9×10^{-15}, and are one to two orders of magnitude lower than the sample ^{36}Cl/^{35}Cl ratios (Table 6.2). Blank corrections were done by deducing the number of atoms of ^{36}Cl and Cl measured in the blanks from those measured in the samples. The resulting ^{36}Cl and Cl concentrations for all samples are listed in Table 6.2.

6.3.3 Noble gas measurements

Helium and neon extractions and isotope measurements were carried out by Alice Williams at the noble gas laboratories at CRPG, Nancy, France and GFZ, Potsdam, Germany using the GV instruments Helix Split Flight Tube mass spectrometer and Helix Multi-collector

mass spectrometer at CRPG, and a VG-5400 mass spectrometer at GFZ. At CRPG, cross-calibrations of the two mass spectrometers and purification lines were made using the HESJ Helium gas standard (Matsuda et al., 2002), which has a certified ^{3}He/^{4}He of 20.63 $\pm$ 0.10 R/R$_A$. Measurements of the CRONUS pyroxene He standard, "P", were also undertaken at CRPG and GFZ in order to inter-calibrate laboratories. The resulting ^{3}He$_{cos}$ concentrations were 4.95 $\pm$ 0.10 $\times$ 10^9 at g^{-1} at CRPG (mean of 6 analyses), and 4.97 $\pm$ 0.21 $\times$ 10^9 at g^{-1} on the VG5400 at GFZ (mean of three analyses). For inter-laboratory comparisons of neon, aliquots of the 0.25 - 0.5 mm CRONUS CREU-1 quartz neon standard were analysed at GFZ and a cosmogenic ^{21}Ne concentration of 3.24 $\pm$ 0.13 $\times$ 10^8 at g^{-1} was determined.

Crush extractions. In vacuo crushing of phenocrysts releases magmatic He contained within fluid and melt inclusions. Magmatic ^{3}He/^{4}He normally vary little within phenocryst populations of individual lava flows and crushing of single olivine and pyroxene aliquots is considered adequate for determining the magmatic He composition of a flow. All in vacuo crush extractions were undertaken at CRPG using steel tubes containing iron slugs activated by external solenoids. Approximately 1 g of each phenocryst sample were loaded into the crushers, and baked under vacuum at 110°C overnight. After cooling to room temperature, samples were crushed during a 2-minute period (at a rate of 100 strokes/min).

Melt extractions. High-temperature melting of uncrushed phenocryst separates or the powder residues of crushed phenocrysts releases all He contained within a sample: magmatic ^{3}He and ^{4}He present in unruptured inclusions, and cosmogenic ^{3}He and radiogenic ^{4}He contained within the crystal lattice. At CRPG, 0.11 - 0.25 g aliquots of hand-crushed olivine and pyroxene phenocrysts were wrapped in Cu-foil and loaded into the sample carrousel and baked under vacuum at 110°C over a 3-day period. After total degassing of the extraction furnace over several hours, the furnace temperature was maintained at 800°C prior to sample introduction. Each sample was dropped into the Ta-crucible and heated to 1450°C over a 20-minute period, then the furnace temperature was reduced to 800°C before introduction of the gas to the purification line. Repeat extractions ensured total extraction

of He. At GFZ, 0.25 - 1.50 g aliquots of hand-crushed olivine and pyroxene were wrapped in Al foil and placed in the sample carrousel, where they were baked under vacuum for about one week at 100°C. Noble gases were extracted in heating steps of 900°C and 1750°C, in order to partly separate atmospheric and radiogenic from cosmogenic components. More details about the experimental procedure and the methods of data reduction at GFZ can be found in Niedermann et al. (1997).

6.3.4 Major and trace elements

Chemical compositions of the mineral aliquots and the bulk rock were analyzed at the Service d'Analyse des Roches et des Minéraux du CNRS (CRPG, Nancy, France). Major elements were determined by ICP-OES and trace elements by ICP-MS, except Li (atomic absorption), B (colorimetry), and H_20 (Karl Fischer titration) and Cl (spectrophotometry).

In the case of ^{36}Cl, concentrations of the major elements and of H, Li, B, Sm, Gd, U, Th and Cl in the bulk rocks are necessary to calculate the low-energy neutron distributions at the land/atmosphere interface. Aliquots of the etched mineral grains, taken before their complete dissolution (section 5.3.2), are representative for the part of sample dissolved for ^{36}Cl extraction and served for the analysis of the corresponding target element concentrations (Ca, K, Ti and Fe). These concentrations and the Cl contents, determined by isotope dilution during AMS measurements, were used to calculate the ^{36}Cl production from all production mechanisms in the dissolved samples. Results of the compositional analysis are listed in Tables 6.3 and 6.4.

In the case of ^{3}He, whole rock and phenocryst U and Th concentrations are necessary to calculate the implanted or ingrown radiogenic ^{4}He (section 6.4.1).

In the case of ^{21}Ne, the composition of the chemically untreated olivine and pyroxene phenocrysts were determined by electron microprobe (Table 6.5).

6.4 Noble gas data analysis

6.4.1 Determination of cosmogenic ^{3}He and ^{21}Ne concentrations

Determination of magmatic ^{3}He/^{4}He. Magmatic ^{3}He/^{4}He values for the samples were determined either by crushing experiments or, when there was insufficient material

Table 6.3: *Bulk rock composition.*

sample	SiO_2 [%]	Al_2O_3 [%]	Fe_2O_3 [%]	CaO [%]	MgO [%]	Na_2O [%]
TZ09	44.62	11.51	14.51	10.69	8.64	2.12
TZ10	39.16	11.84	13.54	13.50	11.22	2.28
TZ12	39.16	11.84	13.54	13.50	11.22	2.28
TZ13	39.64	11.44	13.98	12.60	12.80	1.79
TZ14	39.64	11.44	13.98	12.60	12.80	1.79
TZ17	40.00	11.67	13.34	12.94	10.71	1.71
TZ15	48.52	14.88	13.08	7.80	6.03	3.56
TZ19	39.25	11.69	14.68	12.97	10.06	2.98

	K_2O [%]	TiO_2 [%]	MnO [%]	P_2O_5 [%]	H_20 [%]	Cl [ppm]
TZ09	0.95	3.07	0.21	0.69	2.01	105
TZ10	0.76	3.85	0.19	0.70	4.02	150
TZ12	0.76	3.85	0.19	0.70	4.02	150
TZ13	0.85	3.52	0.19	0.56	3.25	570
TZ14	0.85	3.52	0.19	0.56	3.25	570
TZ17	1.13	4.00	0.17	0.62	2.90	435
TZ15	1.71	3.01	0.16	0.52	0.33	81
TZ19	1.19	3.89	0.21	0.80	2.23	195

	Li [ppm]	B [ppm]	Sm [ppm]	Gd [ppm]	Th [ppm]	U [ppm]
TZ09	5.8	4.5	8.9	8.0	4.7	0.7
TZ10	6.6	3.4	12.9	9.7	10.7	2.3
TZ12	6.6	3.4	12.9	9.7	10.7	2.3
TZ13	7.5	4.1	11.3	8.6	7.9	1.7
TZ14	7.5	4.1	11.3	8.6	7.9	1.7
TZ17	4.3	3.9	12.2	9.6	9.3	2.1
TZ15	11.1	2.8	9.0	7.7	6.0	0.9
TZ19	7.4	4.8	14.4	10.4	11.2	2.5

Table 6.4: *^{36}Cl target element concentrations in pretreated pyroxene separates and one plagioclase separate (TZ15-plg) before ^{36}Cl extraction. "< D.L." means "under detection limit".*

Sample	CaO [%]	K_2O [%]	TiO_2 [%]	Fe_2O_3 [%]
TZ09	19.40±0.39	< D.L.	1.47±0.07	8.17±0.16
TZ10A	21.97±0.44	< D.L.	2.29±0.11	6.67±0.13
TZ10B	21.94±0.44	< D.L.	2.30±0.12	6.69±0.13
TZ12A	21.76±0.44	< D.L.	2.29±0.11	6.65±0.13
TZ12B	21.65±0.43	< D.L.	2.22±0.11	6.82±0.14
TZ13	21.24±0.42	< D.L.	1.94±0.10	6.64±0.13
TZ14	21.18±0.42	< D.L.	1.85±0.09	6.55±0.13
TZ17	21.29±0.43	0.05±0.01	1.94±0.10	6.54±0.13
TZ15	18.27±0.37	< D.L.	1.63±0.08	10.88±0.22
TZ19	21.60±0.43	< D.L.	2.49±0.12	7.61±0.15
TZ15-plg	10.43±0.21	0.60±0.03	0.16±0.01	0.64±0.01

Table 6.5: *^{21}Ne target element concentrations in chemically untreated pyroxene and olivine separates.*

Sample	Mg [%]	Al [%]	Si [%]	Ca [%]	Fe [%]	Na [%]
TZ10-px	8.06	3.70	22.24	16.23	4.60	0.55
TZ12-px	8.06	3.70	22.24	16.23	4.60	0.55
TZ13-px	8.85	3.03	23.23	15.73	4.20	0.56
TZ14-px	8.85	3.03	23.23	15.73	4.20	0.56
TZ17-px	10.04	1.97	24.32	15.34	3.33	0.51
TZ15-px	9.17	1.65	23.92	14.45	7.03	0.35
TZ10-ol	26.76	0.03	18.97	0.17	12.07	0.04
TZ12-ol	25.49	0.00	18.55	0.30	13.84	0.03
TZ13-ol	26.19	0.02	18.72	0.25	12.71	0.02
TZ14-ol	25.39	0.00	18.56	0.26	14.20	0.00
elemental prod. rates[a]	175.1	62.4	41.7	1.8	0.2	102.0

[a] Elemental production rates for ^{21}Ne according to Masarik (2002) [atoms ^{21}Ne (g element)$^{-1}$ a^{-1}].

for crushing experiments, using isochron intercept values (see section 6.3.3). In vacuo crushing of phenocrysts releases magmatic He contained within fluid and melt inclusions contained in the crystals. Total He released ranged from 0.03 to 11.70 $\times$ 10^{11} atoms g^{-1} and was consistently lower in olivine samples (mean pyroxene = 7.16 $\times$ 10^{11} atoms g^{-1}; mean olivine = 0.12 $\times$ 10^{11} atoms g^{-1}). Because of the low He-yield of olivine samples, possibly indicative of a scarcity of melt/fluid inclusions, the measured olivine $^3He/^4He$ values are associated with large uncertainties (up to 70%). In contrast, calculated $^3He/^4He$ in pyroxenes ranged from 6.2 to 6.6 R_A, with individual measurement uncertainties of 2 to 7 %. Note that this value is consistent with a previous determination of the mantle $^3He/^4He$ signature at Mt. Kilimanjaro (6.7 $\pm$ 0.1 R_A Pik et al., 2006). For calculations of cosmogenic ^3He in the olivine samples we therefore use the pyroxene $^3He/^4He$ values. Magmatic $^3He/^4He$ signatures of pyroxenes usually deviate little from those of co-existing olivines, and in this study, small variations in the magmatic ratio will have a only negligible effect on calculated cosmogenic ^3He since the melt extractions of He from olivines of these four samples also yielded low ^4He concentrations (Table 6.6). For samples TZ17 and TZ19, crushing experiments were not performed and we therefore use isochron intercept values, which have been demonstrated to accurately reflect magmatic ratio (for further details of the isochron method, see section 6.4.1 and Blard and Pik, 2008). For TZ17 and TZ19, these values are 6.1 $\pm$ 0.4 and 6.3 $\pm$ 0.4 R_A, respectively, and are thus equivalent to the values determined by the crush-experiments described above. For samples TZ09 and TZ15, there was an insufficient number of aliquots analysed to construct cosmogenic isochrons. For these samples we therefore use the mean $^3He/^4He$ of the values presented above (6.4 $\pm$ 0.2 R_A). Given the very homogeneous ratios determined for the other samples of this study we consider this approximation to be sufficiently reliable.

Cosmogenic ^{3}He concentrations. Concentrations of cosmogenic ^3He determined in pyroxene and olivine are traditionally calculated from melt and crush measurements using an equation that corrects for the trapped (magmatic) He component (Kurz, 1986b):

$$^3He_{cos} = {}^3He_m - {}^4He_m \times (^3He/^4He)_{mag} \quad (6.1)$$

Table 6.6: *Helium data for pyroxene and olivine separates. Measurements were performed at CRPG Nancy on the GV instruments SFT and Helix mass spectrometers and at GFZ Potsdam on a Vg instrument 5400 mass spectrometer (labelled with *). Data have been corrected for blanks and calibrated against local gas standards that agree for ^{3}He cross calibration within ∼ 3%. Uncertainties correspond to 1σ. Cosmogenic concentrations have been calculated taking into account the radiogenic contribution (4He*) following the "R factor" procedure of Blard and Pik (2008) for non eroded volcanic surfaces or the ingrowth/inplantation correction of Farley et al. (2006) for other samples. Magmatic isotopic ratios of samples TZ10, TZ12, TZ13 and TZ14 were determined by crushing. Isochrone intercepts were used for samples TZ17 and TZ19, and for samples TZ09 and TZ15 the reported value is an estimation (see text for details).*

Sample	Mineral phase	sample weight [mg]	^{4}He (melt) [10^{12} at g^{-1}]	^{3}He (melt) [10^{6} at g^{-1}]	^{3}He/^{4}He (melt) R/R$_A$	^{3}He/^{4}He (crush) R/R$_A$	P ^{4}He [10^{5} at g^{-1}a^{-1}]	R factor	^{3}He$_{cos}$ [10^{6} at g^{-1}]
TZ10	ol	143	0.330±0.020	74.35±7.83	162.5	6.64	3.37	0.994	71.74±7.84
	ol	207	0.041±0.002	67.57±2.22	1176.4	6.64	3.37	0.994	67.60±2.22
	ol*	419	0.027±0.002	67.15±6.07	1813.1	6.64	3.37	0.994	67.31±6.07
	px*	400	1.470±0.074	78.29±6.53	38.4	6.64	7.48	0.987	65.64±6.63
	px	135	0.896±0.002	82.42±2.10	66.4	6.64	7.48	0.987	75.19±2.17
	px	131	2.041±0.018	98.06±2.36	34.7	6.64	7.48	0.987	80.35±2.71
	px	134	1.211±0.003	83.17±1.97	49.6	6.64	7.48	0.987	73.01±2.11
	px	126	2.498±0.004	91.08±1.86	26.3	6.64	7.48	0.987	69.02±2.49
TZ12	ol	173	0.070±0.003	70.39±6.19	728.0	6.61	3.37	0.994	70.17±6.19
	ol	174	0.041±0.001	67.57±2.58	1190.1	6.61	3.37	0.994	67.60±2.58
	ol	186	0.038±0.001	62.18±2.73	1174.7	6.61	3.37	0.994	62.21±2.73
	ol	250	0.036±0.001	67.51±2.70	1371.1	6.61	3.37	0.994	67.59±2.70
	ol	46	0.052±0.007	65.06±7.47	900.6	6.61	3.37	0.994	64.97±7.47
	ol*	401	0.040±0.004	69.56±6.76	1246.0	6.61	3.37	0.994	69.61±6.76
	px*	596	1.823±0.129	85.09±8.80	33.7	6.61	7.48	0.987	69.31±8.92
	px	243	1.054±0.007	75.58±2.73	51.7	6.61	7.48	0.987	66.81±2.78
	px	46	0.683±0.004	64.93±4.71	68.6	6.61	7.48	0.987	59.46±4.72
TZ13	px	161	1.612±0.004	113.46±8.83	50.8	6.24	8.25	0.989	100.67±8.84
	px	201	3.220±0.004	118.93±3.57	26.7	6.24	8.25	0.989	92.14±3.74
	px*	324	2.479±0.124	113.46±8.83	33.0	6.24	8.25	0.989	93.09±8.93
	ol*	451	0.066±0.005	89.76±7.58	982.3	6.24	2.85	0.996	89.55±7.58
	ol	117	0.042±0.004	81.09±5.50	1380.8	6.24	2.85	0.996	81.05±5.50
	ol	254	0.078±0.000	86.48±2.59	801.9	6.24	2.85	0.996	86.14±2.59
	ol	179	0.138±0.001	86.34±3.02	451.3	6.24	2.85	0.996	85.49±3.02
	ol	291	0.105±0.000	84.93±2.55	582.2	6.24	2.85	0.996	84.35±2.55
TZ14	ol*	451	0.088±0.010	98.24±15.49	806.7	6.48	2.85	0.996	97.86±15.49
	px*	504	2.610±0.185	117.53±10.76	32.5	6.48	8.25	0.988	95.22±10.89
	px	387	2.752±0.003	124.22±3.73	32.6	6.48	8.25	0.988	100.70±3.77
	px	154	1.866±0.007	116.24±3.49	44.9	6.48	8.25	0.988	100.68±3.51
TZ09	px	240	0.407±0.003	12.82±0.72	22.7	6.40	3.27	-	10.23±0.78
TZ19	ol	392	0.248±0.001	24.68±0.59	71.9	6.13	3.07	-	22.99±0.59
	ol	272	0.236±0.000	23.92±1.07	73.1	6.13	3.07	-	22.33±1.07
	px	332	1.717±0.002	37.28±1.07	15.7	6.13	9.78	-	24.02±1.48
	px	363	1.806±0.001	36.94±1.18	14.8	6.13	9.78	-	22.92±1.60
TZ15	px	220	0.790±0.002	22.56±0.85	20.6	6.40	6.35	-	18.53±1.20
	px*	1500	0.564±0.040	17.64±2.14	22.6	6.40	6.35	-	15.61±2.23
	ol	292	0.367±0.000	13.76±0.54	27.0	6.40	4.76	-	12.73±0.65
TZ17	ol	172	0.367±0.003	38.10±1.36	75.0	6.30	3.78	-	35.42±1.37
	ol	165	0.297±0.002	42.43±1.14	103.1	6.30	3.78	-	40.37±1.16
	ol	73	0.353±0.005	40.42±1.88	82.5	6.30	3.78	-	37.86±1.90
	ol	358	0.316±0.000	32.31±0.91	73.8	6.30	3.78	-	30.08±0.93
	ol	278	0.241±0.000	32.89±1.04	98.5	6.30	3.78	-	31.31±1.04
	px	854	2.851±0.202	56.71±5.11	14.4	6.30	8.10	-	32.94±5.65
	px	114	3.359±0.002	58.92±2.87	12.7	6.30	8.10	-	30.72±3.52
	px	149	3.172±0.003	59.42±2.69	13.5	6.30	8.10	-	32.85±3.30

where $^3He_{cos}$ is the cosmogenic ^{3}He concentration, ^3He_m and ^4He_m are the concentrations of ^{3}He and ^{4}He measured from melt extractions and $(^3He/^4He)_{mag}$ is the magmatic $^3He/^4He$ value, determined from phenocryst crush extractions. Recently, Blard and Pik (2008) proposed an alternative isochron method for the representation of this system, where in the $(^3He/^4He)_{tot}$ vs $1/^4He_{tot}$ space, the suite of data define a straight line, its intercept representing the magmatic $(^3He/^4He)_{mag}$ ratio, and its slope the cosmogenic ^{3}He concentration. This method has the advantage of avoiding a preliminary crushing step and potential loss of cosmogenic helium (Blard et al., 2006). With an optimised total extraction apparatus, it allows a precise determination of the cosmogenic concentration by increasing the number of measured aliquots. Calculated concentrations should be identical whichever method is used. The isochron method however allows a better assessment of data-set consistency via its graphical output, and also necessitates an increase in the number of replicates, which in turn improves the statistical determination of the cosmogenic concentrations. This is illustrated in Fig. 6.5, where all olivine and pyroxenes analyses of samples TZ10 and TZ12 (same sampling site at 2740 m, Table 6.1) have been plotted, demonstrating a well-defined and precise cosmogenic isochrone. Unfortunately, the helium data acquired in this study were not all measured in line with this recent development, and a preliminary crushing step was performed (Table 6.6). Moreover, for some of the samples, the number of replicates for pyroxenes and olivines is inadequate for isochrone construction. (Table 6.6). For a better homogeneity in the calculations, the cosmogenic concentrations presented in Table 6.6 were all determined using the traditional correction method.

Whichever method is used for determination of cosmogenic ^{3}He, a critical step is the correction for the presence of implanted or ingrown radiogenic ^{4}He (^{4}He*), which may be significant even in very young rocks (e.g. Blard and Farley, 2008; Blard and Pik, 2008). In this study, ^{4}He* is determined from whole-rock and phenocryst U and Th concentrations following Farley et al. (2006). For partially eroded volcanic surfaces (TZ09 and TZ17) and glacially polished surfaces (TZ15 and TZ19), ^{4}He* has been directly subtracted from the ^4He_m abundance before calculation using Eq. 6.1. For the non eroded volcanic surfaces

(TZ10, 12, 13, 14), in which the time-integrated production rates of $^{3}He_{cos}$ and $^{4}He^{*}$ are identical, we applied the R-factor correction of Blard and Pik (2008) (see Table 6.6).

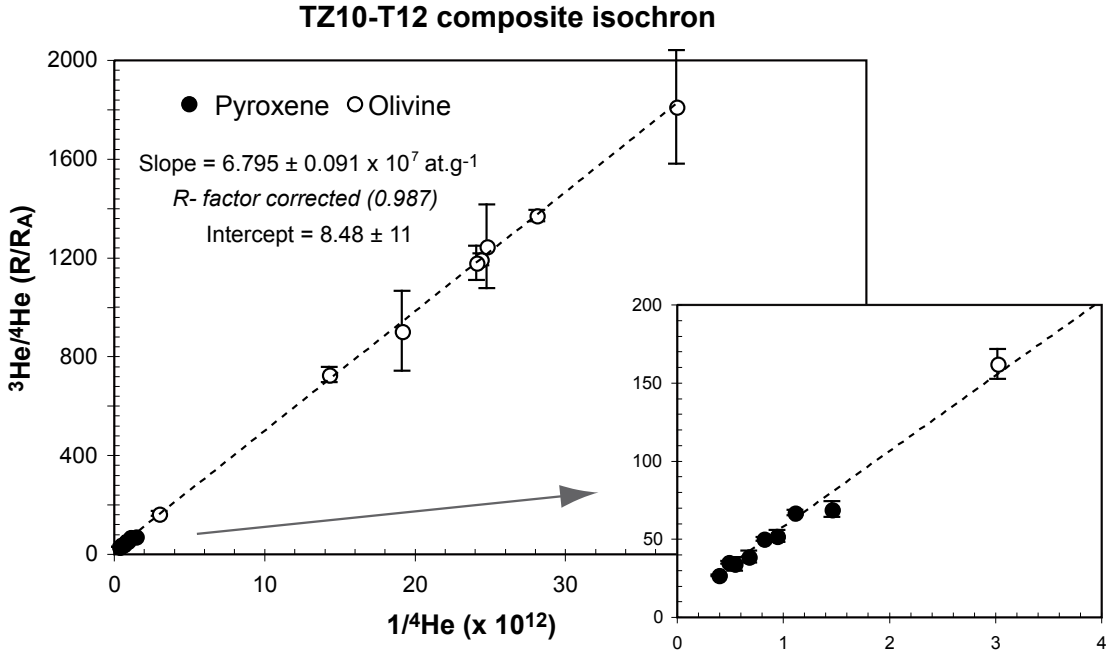

Figure 6.5: *Isochron plot of helium concentrations in olivine and pyroxene of samples TZ10 and TZ12. The intercept represents the magmatic $(^{3}He/^{4}He)_{mag}$ ratio, and the slope the cosmogenic ^{3}He concentration.*

Helium data were systematically obtained for pyroxenes and olivines except for sample TZ09 for which only pyroxenes where available in a sufficient quantity. Full raw data and calculated cosmogenic concentrations are presented in (Table 6.6). $^{3}He_{cos}$ range from 1.27 to 9.79 $\times$ 10^{7} at g^{-1} in olivines and 0.96 to 10.70 $\times$ 10^{7} at g^{-1} in pyroxenes. These cosmogenic concentrations are also plotted in Fig. 6.6 for a better comparison of the relative production of $^{3}He_{cos}$ in the two minerals. For most of the samples the cosmogenic concentrations measured in co-genetic olivines and pyroxenes cannot be distinguished within analytical uncertainty, except for TZ13, where the concentration in olivine is $\sim$11% lower than in pyroxenes and sample TZ15, where a difference of $\sim$25% is observed. The determination of cosmogenic ^{3}He in TZ15 olivine is, however, based on a single aliquot and should be treated cautiously until further aliquots are analysed. Moreover, this sample comes from a polished glacial surface on an old (527 $\pm$ 3 ka, Alice Williams, unpublished data)

dyke at the foot of Mawenzi peak, and is therefore subject to the highest correction for ^{4}He* (42 to 68%), potentially resulting in an imprecise correction for magmatic helium.

Where two samples were taken from a single flow (TZ10 - TZ12, at 2740m and TZ13 - TZ14 at 3000m) results obtained do not differ by more than 4 -7%, which is within the uncertainty of the aliquots dispersion. However, the concentrations determined for olivines of TZ13 are significantly lower than both the cogenetic pyroxenes and concentrations in TZ14 olivines and pyroxenes. For samples TZ10-TZ12, all aliquots from the two surfaces for pyroxenes and olivines lie on a single composite isochron (Fig. 6.5) and allow very precise determination of the $^3He_{cos}$ concentration for this flow.

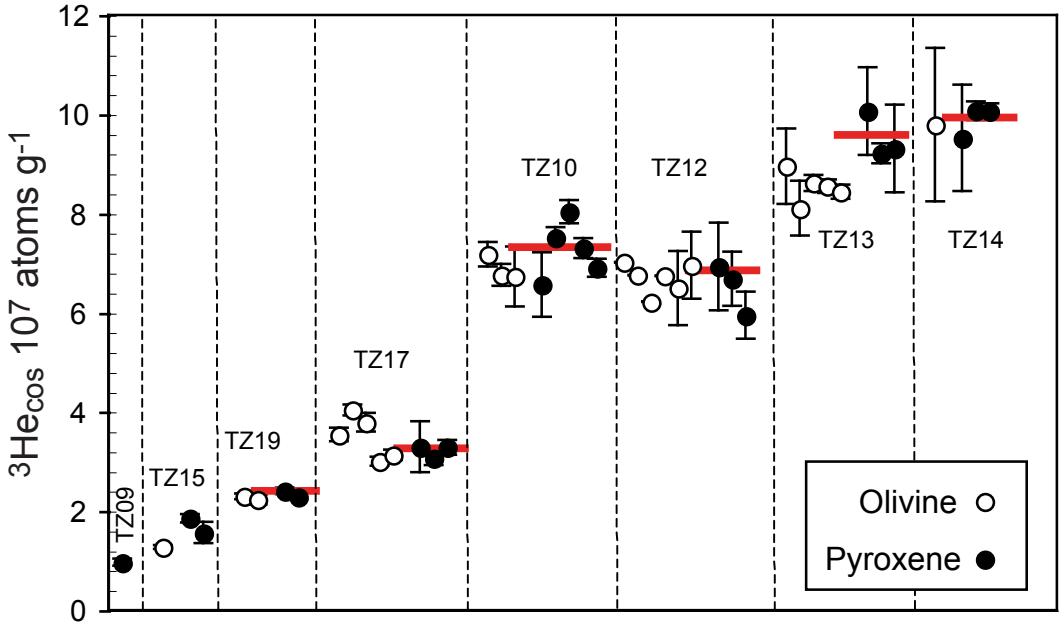

Figure 6.6: *Cosmogenic ^{3}He concentrations in olivine and pyroxene phenocrysts of all samples. The red lines represent the mean values of the concentrations in pyroxene. Sample TZ09 was only measured in pyroxene.*

Three-isotope neon plots and cosmogenic ^{21}Ne concentrations. In young (< 500 ka) basalts, concentrations of cosmogenic ^{21}Ne are calculated using:

$$^{21}Ne_{cos} = [(^{21}Ne/^{20}Ne)_m(^{21}Ne/^{20}Ne)_{tr}] \times ^{20}Ne_m \quad (6.2)$$

(Niedermann, 2002), where $^{21}Ne_{cos}$ are cosmogenic ^{21}Ne concentrations, $(^{21}Ne/^{20}Ne)_m$ and $^{20}Ne_m$ are the measured Ne isotope ratio and concentrations from melt extractions and $(^{21}Ne/^{20}Ne)_{tr}$ is the trapped ^{21}Ne/ ^{20}Ne value. In most basalts, trapped neon components normally have atmospheric compositions (Niedermann, 2002).

Neon isotope data are presented in Table 6.5 and in Fig. 6.7. All isotope data have been corrected for analytical blanks and mass discrimination. Examination of neon measurements on a three-isotope plot enables an assessment of the neon inventory in a sample to be made. In Figure 6.7, olivine and pyroxene data are defined by a linear regression line y = 1.0539x + 0.0994, which is the same, within error, as the Schaefer spallation line for pyroxenes ([1.069 ± 0.035]x + 0.099) (Schaefer et al., 1999). The regression line passes through the air component ($^{21}Ne/^{20}Ne = 0.00296$, $^{22}Ne/^{20}Ne = 0.102$ Niedermann, 2002) and no radiogenic or mantle component is identified in the heating steps. This supports our assumption that the trapped component has an atmospheric composition. Concentrations of $^{21}Ne_{cos}$ are presented in Fig. 6.8 and Table 6.8 and range from 0.28 to 1.90 $\times$ 10^7 at g^{-1} in pyroxenes and 2.48 to 3.49 $\times$ 10^7 at g^{-1} in olivines. In the four samples containing cogenetic olivine and pyroxene, $^{21}Ne_{cos}$(px)/$^{21}Ne_{cos}$(ol) range from 0.51 to 0.54. This is slightly lower than the value calculated from the production rates reported in Fenton et al. (2009) (0.55). Differences in relative production of $^{21}Ne_{cos}$ in the different mineral phases are to be expected since the production rate of cosmogenic ^{21}Ne is a function of mineral composition. In olivines, the principle ^{21}Ne spallation targets are Si, and Mg whereas in pyroxenes a minor component is also derived from spallation of Al. The compositions of Kilimanjaro pyroxenes, determined by electron microprobe, range from En_{41} to En_{44}, overlapping the compositional range of pyroxenes in Fenton et al. (2009) (En_{43-44}). The compositions of Kilimanjaro olivines range from Fo_{81} to Fo_{82}, which is at the upper end of the compositional range of Fenton et al. (2009) (Fo_{77-83}). At 2740 m, where two separate samples (TZ10 and TZ12) were collected from different parts of the same flow, the difference in $^{21}Ne_{cos}$ between the samples is 7% for pyroxenes and 5% for olivines, therefore the same within analytical error. For the two samples (TZ13 and TZ14) from the altitude at 3050 m however, the differences are 12% (pyroxene) and 6% (olivine), therefore within

analytical error of each other for olivines but significantly higher in TZ14 pyroxenes.

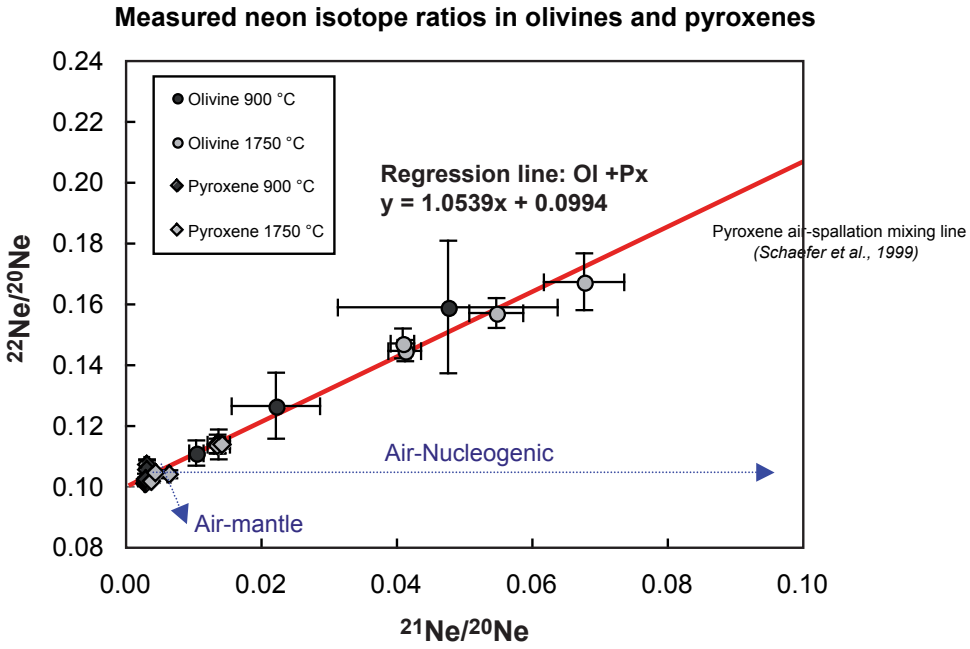

Figure 6.7: *Neon three-isotope diagram showing data from olivines and pyroxenes at two temperature steps. The regression line defines a spallation line, which passes through the air component and is indistinguishable from the air-spallation mixing line from Schaefer et al. (1999).*

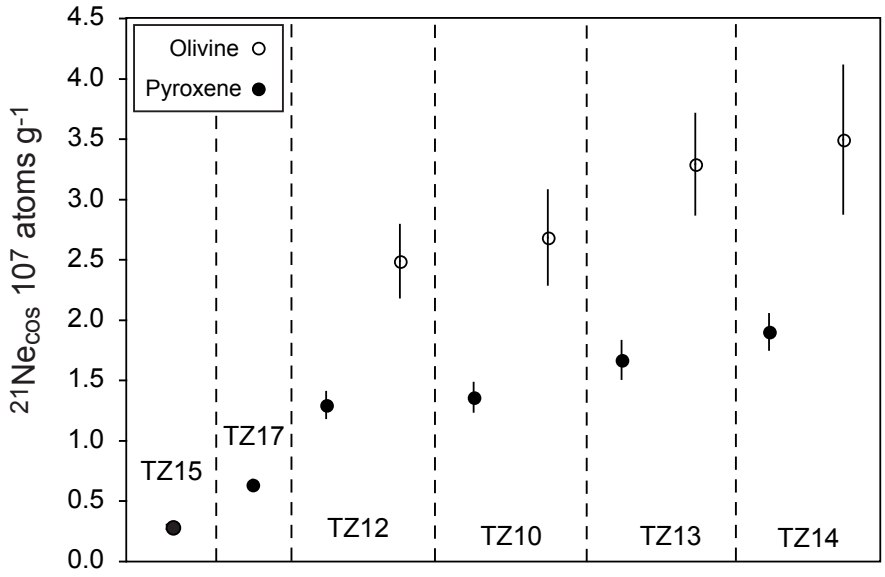

Figure 6.8: *Cosmogenic ^{21}Ne concentrations in olivine and pyroxene phenocrysts.*

Table 6.7: *Neon data for pyroxene and olivine separates. Measurements were performed on the GFZ Potsdam noble gas mass spectrometers by step-wise heating and crushing procedures. Data have been corrected for analytical blanks, isobaric interferences, and mass discrimination effects.*

Sample	sample weight [g]	File n°	Temp [°C]	measured ^{20}Ne [10^{-12} cm^3 g^{-1}]	measured ^{22}Ne [10^{-12} cm^3 g^{-1}]	measured ^{22}Ne/^{20}Ne [10^{-2}]	measured ^{21}Ne/^{20}Ne [10^{-3}]
TZ10 px		0513a	900	24.7±1.8	2.97±0.16	10.70±0.14	3.23±0.32
		0513b	1750	46.6±2.8	5.61±0.33	11.37±0.32	13.61±0.31
	0.40058		Total	71.3±3.3	8.58±0.37	11.14±0.77	10.02±0.76
TZ12 px		p250a	900	42.0±2.5	4.58±0.25	10.22±0.17	3.05±0.30
		p250b	1750	307.8±16.0	32.3±1.7	10.437±0.065	4.51±0.12
	0.5968		Total	349.9±16.2	36.9±1.7	10.41±0.68	4.33±0.31
TZ13 px		0514a	900	35.7±2.5	4.17±0.25	10.53±0.34	3.25±0.52
		0514b	1750	56.9±3.6	6.94±0.39	11.31±0.24	13.66±0.51
	0.32478		Total	92.7±4.4	11.11±0.47	11.01±0.76	9.64±0.80
TZ14 px		p249a	900	72.4±4.0	7.63±0.40	10.173±0.093	3.05±0.21
		p249b	1750	61.8±3.5	7.36±0.39	11.35±0.13	14.28±0.45
	0.50456		Total	134.2±5.3	14.99±0.56	10.71±0.60	8.22±0.56
TZ17 px		p246a	900	175.2±9.1	17.81±0.92	10.074±0.056	2.96±0.12
		p246b	1750	256±13	26.1±1.4	10.160±0.056	3.88±0.13
	0.8542		Total	431±16	43.9±1.6	10.13±0.54	3.50±0.21
TZ15 px		p248a	900	34.7±1.8	3.58±0.19	10.09±0.10	3.02±0.16
		p248b	1750	28.5±1.5	3.01±0.16	10.38±0.13	6.53±0.24
	1.50078		Total	63.2±2.4	6.60±0.25	10.22±0.55	4.61±0.29
TZ10 ol		0515a	900	3.5±1.0	0.739±0.053	12.6±1.1	22.3±6.6
		0515b	1750	24.2±1.9	3.93±0.22	14.44±0.35	41.3±2.4
	0.4192		Total	27.7±2.2	4.67±0.22	14.2±1.6	38.9±4.8
TZ12 ol		p252a	900	6.20±0.37	0.705±0.052	11.37±0.49	13.8±1.6
		p252b	1750	16.5±1.4	2.84±0.16	15.68±0.49	54.8±4.0
	0.40132		Total	22.7±1.5	3.55±0.17	14.5±1.4	43.6±5.3
TZ13 ol		0516a	900	2.55±0.94	0.676±0.046	15.9±2.2	48±16
		0516b	1750	29.1±1.9	4.55±0.28	14.68±0.49	41.0±1.7
	0.45104		Total	31.7±2.1	5.23±0.28	14.8±1.5	41.5±4.5
TZ14 ol		p251a	900	5.77±0.43	0.639±0.053	11.07±0.42	10.6±1.0
		p251b	1750	19.3±2.1	3.65±0.24	16.71±0.93	67.8±5.9
	0.24534		Total	25.1±2.1	4.29±0.25	15.4±2.0	54.7±8.5

6.5 Approaches to TCN cross-calibrations

Comparing cosmogenic ^{36}Cl, ^{3}He and ^{21}Ne concentrations

A common approach for comparing the production rates of different TCN in the same sample is to calculate ratios of cosmogenic concentrations. This approach has been adopted recently to cross calibrate ^{3}He and ^{21}Ne production rates with ^{10}Be (Gayer et al., 2004; Kober et al., 2005; Farley et al., 2006; Amidon et al., 2008, 2009), or to evaluate their relative production rates (Fenton et al., 2009).

In these studies, the compared nuclides are primarily produced by spallation reactions. In the case of the noble gases ^{3}He and ^{21}Ne, nucleogenic and radiogenic contributions are corrected for prior to cross-calibration, so that only cosmogenic components are taken into account. The cosmogenic production of ^{3}He by thermal neutron capture on ^{6}Li has been shown to be potentially significant in Li-rich minerals and rocks ($>\sim$ 100 ppm, Dunai et al., 2007) and should also be corrected for. This approach has not been done in the pioneer paper of Gayer et al. (2004) but is now considered (e.g. Amidon et al., 2009). However, the ^{6}Li concentration in mafic minerals such as olivine and pyroxenes is generally very low ($<$ 10 ppm) and only contributes to the cosmogenic production for a couple of percent ($<$ to the analytical error).

Besides spallation, ^{10}Be is also produced by muon interactions, which is in the case of ^{10}Be, however, only significant at greater depths (Granger and Smith, 2000) and as such is unlikely to be important in cross-calibration studies. Predominantly spallation-produced nuclides such as ^{3}He, ^{21}Ne and ^{10}Be, therefore, should accumulate in a sample with a constant ratio, even for an eroding surface. As a result, comparison of TCN concentration ratios allows simple evaluation of the spatial and temporal dependence of the TCN production rates.

However, if the mentioned nuclides are compared with ^{36}Cl, three issues have to be considered when using this approach.

1) Even though ^{3}He and ^{21}Ne are normally calibrated for a given mineral phase, their production rates depend on the chemical composition of the minerals (Chapters 1.3.7 and 1.3.8). ^{3}He is mainly produced from O and Si, as well as Mg, Fe and Ca. In contrast,

^{21}Ne is produced from Mg, Si, Na and Al but not from O and Ca (e.g. Masarik, 2002). The production rate of ^{21}Ne is therefore more sensitive than ^{3}He to variations in mineral composition. As a consequence, if the composition of a mineral phase varies significantly within an analyzed sample set, calculated ^{3}He/^{21}Ne ratios may also vary significantly. Mineral composition is even more important when comparing noble gas TCN concentrations to those of ^{36}Cl. ^{36}Cl is produced from fewer target elements than ^{3}He and ^{21}Ne, dominantly from Ca, K and ^{35}Cl, making its mineral production rate extremely sensitive to the mineral composition.

2) The noble gases ^{3}He and ^{21}Ne are stable TCN, while ^{10}Be and ^{36}Cl are radioactive. Concentration ratios of a stable and a radioactive nuclide will not remain constant over long exposure durations due to decay of the radionuclide. In the case of ^{10}Be, which has a half-life of ∼1.39 Ma, this becomes significant for exposure ages longer than 100 ka, while in the case of ^{36}Cl, which has a shorter half-life (301 ka), this effect is significant for shorter exposure durations. Therefore, the radioactive decay should be considered when comparing TCN concentrations, especially if the samples have different exposure ages.

3) Cosmogenic ^{36}Cl is not only produced by spallation. A significant ^{36}Cl contribution is also derived from slow negative-muon capture by Ca, and to a lesser degree by K (Chapter 1.3.6). Because the altitude-dependence of the muon flux is weaker than that of the fast neutrons (Chapter 1.4.1), with increasing altitude the production of ^{36}Cl by spallation increases at a higher rate than ^{36}Cl production by muon-capture. Hence, over a given altitude transect, total ^{36}Cl production will not be proportional to the production of TCN derived purely from spallation. ^{36}Cl is also produced by thermal and epithermal neutron capture on the trace element ^{35}Cl, and a significant proportion of ^{36}Cl can result from a high-level of Cl in a sample (Chapter 1.3.6). However, as for ^{3}He production due to ^{6}Li, when Cl concentrations in a sample are low (a few ppm) this mechanism contributes generally insignificantly to the ^{36}Cl production. Cl concentration levels of a few hundred ppm, on the other hand, would mean that most of the ^{36}Cl production in a sample would come from this reaction. Variations in ^{36}Cl concentrations in samples of the same lithology might therefore be a consequence of varying Cl concentrations. ^{36}Cl can have a radiogenic

component, which is also mainly dependent on the Cl concentration in the sample (Chapter 1.3.6).

The favorable chemical composition of the pyroxene phenocrysts in our samples, however, enables us to compare the ratios of the cosmogenic ^{36}Cl, ^{3}He and ^{21}Ne concentrations (Fig. 6.9). The measurements in pyroxene represent the most complete data set documented in this study for a single mineral phase. Production of ^{36}Cl from spallation of Ca is maximized by extraction from a Cl-poor Ca-rich mineral (see Table 6.2). Hence, production from spallation of Ca is the most important production mechanism in pyroxenes, contributing between 86% and 90% of ^{36}Cl in these samples, while the contributions from spallation of K is between 0 and $< 1\%$ and from spallation of Ti and Fe together about 3% (calculated using the ^{36}Cl calculation spreadsheet, Appendix B, Schimmelpfennig et al., 2009). The ^{3}He and ^{36}Cl contributions from thermal and epithermal neutron capture on ^{35}Cl and ^{6}Li in the pyroxenes are 0.04% or less for ^{36}Cl, and $< 1\%$ for ^{3}He (for ^{3}He the contribution is calculated using an equivalent unpublished spreadsheet created by R. Pik and P. Burnard, which is modification of CHLOE (Phillips and Plummer, 1996), adopted for helium production). The ^{36}Cl contributions due to slow negative-muon capture are 10% at 1000 m altitude and decrease to 5% at 4300 m. A slight decrease in ^{36}Cl to noble gas nuclide ratios with increasing altitude might therefore be expected due to the muonic ^{36}Cl contribution.

Since, to our knowledge, ^{36}Cl has never been measured in pyroxene, we validate this method by measuring ^{36}Cl in co-genetic plagioclases in sample TZ15. Plagioclase is now routinely used for ^{36}Cl extraction (e.g. Chapters 4 and 5). The ^{36}Cl concentrations in both mineral phases of TZ15 are given in Table 6.2. Since the Ca concentrations are higher in the pyroxene by almost a factor of two, the ^{36}Cl concentrations cannot be directly compared. We therefore calculated the exposure ages from these two measurements using the above-mentioned ^{36}Cl calculation spreadsheet, which yield 16.4 $\pm$ 2.0 ka for the measurement in pyroxene and 15.9 $\pm$ 1.8 ka for that in plagioclase, being in perfect agreement.

Fig. 6.9 shows the ratios of the cosmogenic nuclide concentrations versus altitude is observed. The mean values of the ratios and their standard deviations are 0.0575 $\pm$

0.0068 (n=8) for ^{36}Cl/^{3}He, 0.183 ± 0.012 (n=6) for ^{21}Ne/^{3}He and 0.301 ± 0.020 (n=6) for ^{36}Cl/^{21}Ne. It should be noted that these ratios are composition dependent, particularly for ^{36}Cl, and ratios should not be expected to be the same in other mineral phases or in pyroxenes with significantly different compositions. For each of the three TCN ratios, all individual measurements lie within the standard deviation of the respective mean values (Fig. 6.9), therefore not showing any altitudinal dependency. Standard deviations are 8% for ^{21}Ne/^{3}He, 13% for ^{36}Cl/^{3}He and 7% for ^{36}Cl/^{21}Ne. Only the ^{36}Cl/^{3}He ratio of sample TZ15 does not lie within the standard deviation of the mean value. However, pyroxenes from this sample (as well as for sample TZ09) do not exhibit exactly the same composition as those of other samples (Table 6.5).

^{21}Ne/^{3}He was also determined in olivines from four of the samples: TZ10 and TZ12 from the 2740 m sample site and TZ13 and TZ14 from the 3000 m site (Table 6.9, Fig. 6.10). ^{36}Cl could not be measured in olivine since there is no target element for this nuclide. A mean ^{21}Ne/^{3}He value of 0.375 ± 0.015 was determined and all four measurements lie within one standard deviation of the mean value. No variation is observed between the two sample localities.

Table 6.8: *Cosmogenic components of the measured ^{36}Cl, ^{3}He and ^{21}Ne concentrations in pyroxene separates and ratios of these concentrations with their mean values and standard deviations. Note that the ^{36}Cl concentrations of samples TZ10 and TZ12 are mean values of the two replicates of each (Table 6.2) with the corresponding standard deviations.*

Sample	$[^{36}Cl]$ (px) $[10^5$ atoms $g^{-1}]$	$[^{3}He]_{cos}$ (px) $[10^6$ atoms $g^{-1}]$	$[^{21}Ne]_{cos}$ (px) $[10^6$ atoms $g^{-1}]$	$[^{36}Cl]/[^{3}He]$ (px)	$[^{21}Ne]/[^{3}He]$ (px)	$[^{36}Cl]/[^{21}Ne]$ (px)
TZ09	6.31±0.17	9.68±0.72		0.0652±0.0052		
TZ10	42.57±0.57	72.6±2.5	13.5±1.2	0.0586±0.0022	0.186±0.018	0.315±0.028
TZ12	40.3±1.2	68.1±3.0	12.9±1.1	0.0592±0.0032	0.190±0.018	0.312±0.028
TZ13	49.4±1.2	95.4±2.7	16.6±1.6	0.0518±0.0020	0.174±0.017	0.297±0.029
TZ14	52.5±1.0	99.0±1.8	19.0±1.5	0.0530±0.0014	0.191±0.015	0.277±0.022
TZ17	20.59±0.59	32.17±0.73	6.29±0.44	0.0640±0.0023	0.196±0.014	0.327±0.025
TZ15	7.81±0.21	17.1±1.5	2.79±0.20	0.0457±0.0041	0.164±0.018	0.279±0.022
TZ19	14.7±1.0	23.47±0.55		0.0628±0.0046		
mean± st.dev				**0.0575±0.0068**	**0.183±0.012**	**0.301±0.020**

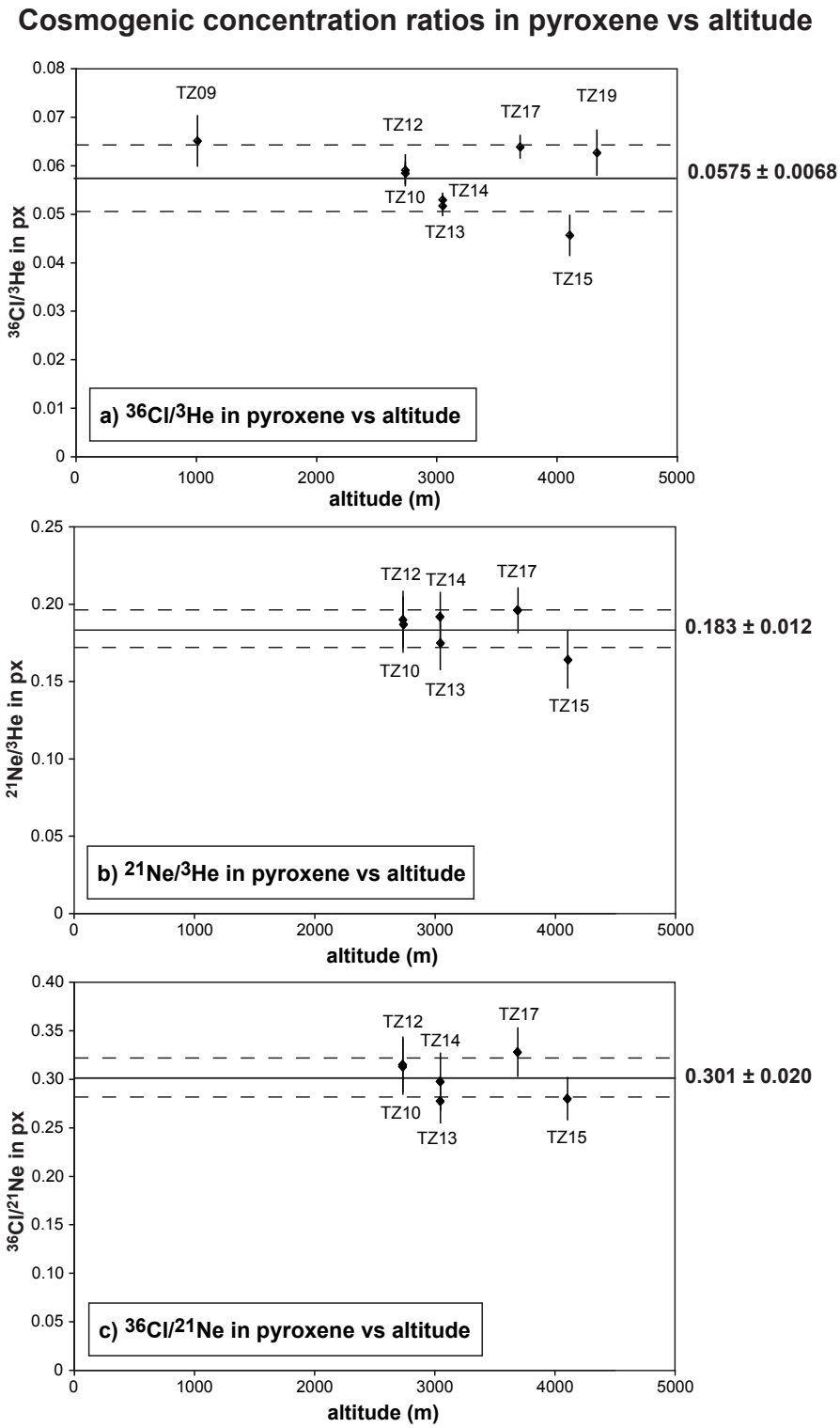

Figure 6.9: *TCN ratios, calculated from the total cosmogenic ^{3}He, ^{21}Ne and ^{36}Cl concentrations in pyroxene, as a function of altitude. Mean values of the ratios and their standard deviations are given on the right of each graph.*

Table 6.9: *Cosmogenic components of the measured ^{3}He and ^{21}Ne concentrations in olivine separates and ratios of these concentrations with their mean value and standard deviation.*

Sample	$[^{3}He]_{cos}$ (ol) $[10^{7}$ atoms $g^{-1}]$	$[^{21}Ne]_{cos}$ (ol) $[10^{7}$ atoms $g^{-1}]$	$[^{21}Ne]/[^{3}He]$ (ol)
TZ10	6.89±0.14	2.68±0.39	0.389±0.057
TZ12	6.71±0.12	2.48±0.30	0.370±0.045
TZ13	8.54±0.14	3.28±0.42	0.385±0.049
TZ14	9.8±1.5	3.49±0.62	0.356±0.084
TZ17	3.50±0.19		
TZ15	1.273±0.042		
TZ19	2.266±0.033		
mean±st.dev			**0.375±0.015**

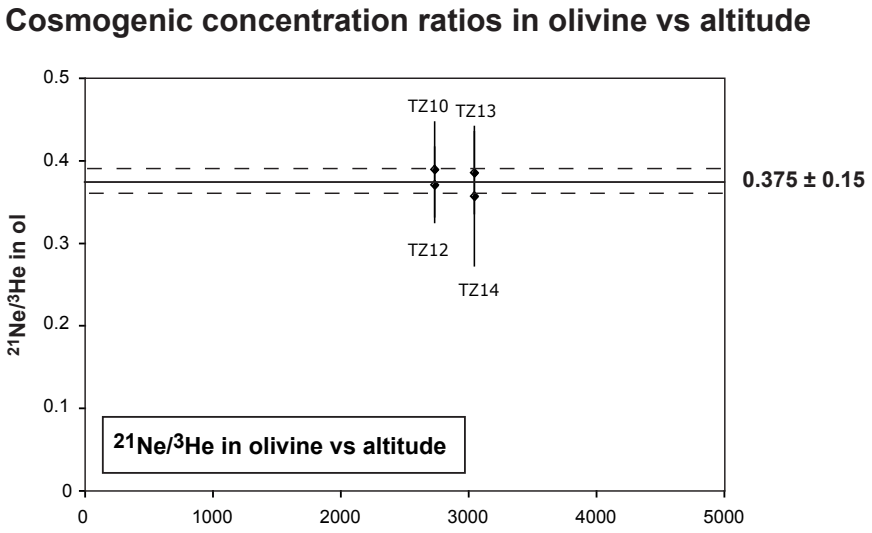

Figure 6.10: *$^{21}Ne/^{3}He$ concentration ratios in olivine as a function of altitude with the mean value of the ratios and its standard deviation.*

Comparing apparent ^{36}Cl, ^{3}He and ^{21}Ne exposure ages

If erosion is negligible, multiple samples collected from a single lava-flow or glacial related surface should yield the same exposure age regardless of which TCN is measured or which mineral phase is used. All composition-, scaling- and decay-related differences between the nuclides are cancelled out in the calculation of the exposure ages. Scaling factors can be disregarded as long as all nuclides are scaled with the same scaling method, so that they cancel down in the nuclide ratios.

In this study, we use the scaling method of Stone (2000) to calculate exposure age ratios for ^{3}He, ^{21}Ne and ^{36}Cl. This method is preferred because all the SLHL production rates considered below were originally scaled according to either Stone (2000) or to Lal (1991). Note that the method of Stone (2000) is derived from that of Lal (1991). Although an additional scaling factor is used for production of ^{36}Cl from muons, differences in the scaling of this reaction between the various scaling methods are expected to have only a minor influence on calculated exposure age ratios, because ^{36}Cl contributions from muons are not higher than 5-10% (see previous paragraph). Moreover, presenting exposure age ratios for each nuclide pair using each of the currently available scaling methods is beyond the scope of this chapter.

The selection of SLHL production rates poses a more serious challenge, because for each nuclide several experimentally calibrated over a quite large range of values (see e.g. Chapters 1.3.6, 1.3.7 and 1.3.8) and modelled production rates exist in addition to different methods of applying element-specific production rates to a given sample. To evaluate all the available production rate combinations for the three nuclide ratios in one exercise, a Bayesian statistical approach would be ideal, since it would allow all uncertainties to be accounted for. At this stage, we will limit our study to select one SLHL production rates for each nuclide and discuss consequences on exposure age ratios. We plan to adopt the Bayesian statistical approach for the future publication of the results.

For ^{36}Cl, production rates are not mineral- but target-element-specific. Production from spallation of Ca is the most important production mechanism in our pyroxenes, contributing between 86% and 90% of ^{36}Cl. We use the production rate for spallation

of Ca with a value of 42.2 ± 4.8 atoms (g Ca)$^{-1}$ a^{-1} (Chapter 5).

For ^{3}He, we use the production rate of 128 ± 5 atoms (g mineral)$^{-1}$ a^{-1} (Blard, 2006). This production rate is assumed to be valid for both pyroxene and olivines.

For ^{21}Ne, both modelled elemental production rates and experimentally-calibrated mineral-specific production rates are currently available. Here, we use the calibrated SLHL production rate of 25 ± 8 atoms (g pyroxene)$^{-1}$ a^{-1} of Fenton et al. (2009). The compositions of pyroxenes in our study (En_{41-43}) overlap those of Fenton et al. (2009) (En_{43-44}), with the exception of TZ09 and TZ15 (both En_{45}).

The resulting exposure ages are listed in Table 6.10. For each nuclide pair, the exposure age ratios are then calculated. These are plotted as a function of the altitude in Fig. 6.11.

The uncertainties in the ratios in Fig. 6.11 do not include the standard deviations of the calibrated production rates, but take into account the uncertainties in the measured nuclide concentrations and those, in the case of ^{36}Cl, in the production reactions other than spallation. This is valid because the ratios of all samples are equally affected by the uncertainties in the production rates.

The distribution of exposure age ratios versus altitude (Fig. 6.11) shows very similar pattern as the concentration plot, indicating that the radioactive decay of ^{36}Cl and its production by slow muon capture have not a significant impact on the concentration ratios in the case of our sample.

Though, in the exposure age ratios a slight decreasing trend of the ratios can visually be observed with relatively higher ratios of sample TZ09 and relatively lower ratios of sample TZ15. Compared to each other, the two samples have an offset of 30% (Fig. 6.11a), their standard deviations not overlapping. However, for TZ15, this trend is not observed for the ^{36}Cl/^{21}Ne comparison, and therefore seems to be related to the calculation of its ^{3}He age. As mentioned in section 6.4.1, from all the samples measured in this study, TZ15 suffered the highest correction for radiogenic ^{4}He*, which affects significantly the determination of the ^{3}He cosmogenic concentration. It also exhibits a significant difference between cosmogenic ^{3}He determined in olivine and pyroxene, which it not the case for the other samples (Table 6.6). Therefore, the helium data of sample TZ15 needs a refinement

before its ^{3}He exposure ages can reliably be compared to those of the other nuclides.

Also, the helium exposure age of sample TZ09 have to be considered with caution, because unlike the other samples its ^{3}He concentration was determined from one single extraction. Measurements of additional aliquots may well identify this single analysis as an anomaly. In addition, the flow-surface of TZ09 was clearly eroded. Erosion can have an effect on ratios in which ^{36}Cl is involved, because the ^{36}Cl contribution from slow negative-muon capture is much less affected by erosion than the ^{36}Cl contribution from spallation due to the longer attenuation length of the muons. Consequently, in the case of erosion, the calculated apparent ^{36}Cl exposure age is higher than the calculated apparent ^{3}He exposure age, and could thus explain the higher ^{36}Cl/^{3}He exposure age ratio. Erosion would not affect the ^{3}He/^{21}Ne ratio, which can, however, not be checked, because insufficient sample material was available to measure ^{21}Ne in sample TZ09.

If TZ09 is excluded, no variation of the exposure age ratios with altitude is apparent from 2700 to 4300 m, regardless of the production rate or nuclide pair examined.

Independent age constraints are not available (section 6.2) for the sampled lava flows, which prevent us from evaluating the SLHL production rates of the three nuclides. Adjusting their values in a way that all three nuclides yield the same exposure ages is not possible at this stage of the study, since the production rates of none of the three nuclides can be considered as definitive, so that infinite possibilities of production rate values for the three nuclides could result in the same exposure ages. As a perspective for the future advancement in this study, we envisage to treat our data set with a similar statistical approach as performed in Chapter 5 to infer the highest probable production rates of the three nuclides.

Table 6.10: *Apparent exposure ages calculated with the cosmogenic ^{36}Cl, ^{3}He and ^{21}Ne concentrations in pyroxene (Table 6.8) with the SLHL production rates detailed in the footnotes. ^{36}Cl exposure ages are calculated with the ^{36}Cl calculation spreadsheet (Schimmelpfennig et al., 2009). Note that the ^{36}Cl exposure ages for samples TZ10 and TZ12 are mean values of the exposure ages of the two replicates of each with the corresponding standard deviations. The uncertainties (1σ) of the exposure ages include the uncertainties in the cosmogenic nuclide concentrations, but not the uncertainties in the SLHL production rates.*

Sample	^{36}Cl (px)[a] [ka]	^{3}He (px)[b] [ka]	^{21}Ne (px)[c] [ka]
TZ09	81.8±6.4	62.2±5.6	
TZ10	181.8±3.8	151.3±6.3	144±13
TZ12	172.8±8.5	141.7±7.4	137±12
TZ13	183±16	165.3±5.6	148±14
TZ14	200±17	172.3±3.8	169±13
TZ17	46.5±3.4	40.5±1.1	40.6±2.8
TZ15	16.4±1.2	17.2±1.8	14.4±1.1
TZ19	23.8±2.3	21.88±0.61	

[a] ^{36}Cl SLHL production for spallation of Ca 42.2±4.8 atoms ^{36}Cl (g Ca)$^{-1}$ a^{-1} according to Chapter 5.
[b] ^{3}He SLHL production for pyroxene 128±5 atoms ^{3}He (g Px)$^{-1}$ a^{-1} according to Blard et al. (2005).
[c] ^{21}Ne SLHL production for pyroxene 25±8 atoms ^{21}Ne (g Px)$^{-1}$ a^{-1} according to Fenton et al. (2009).

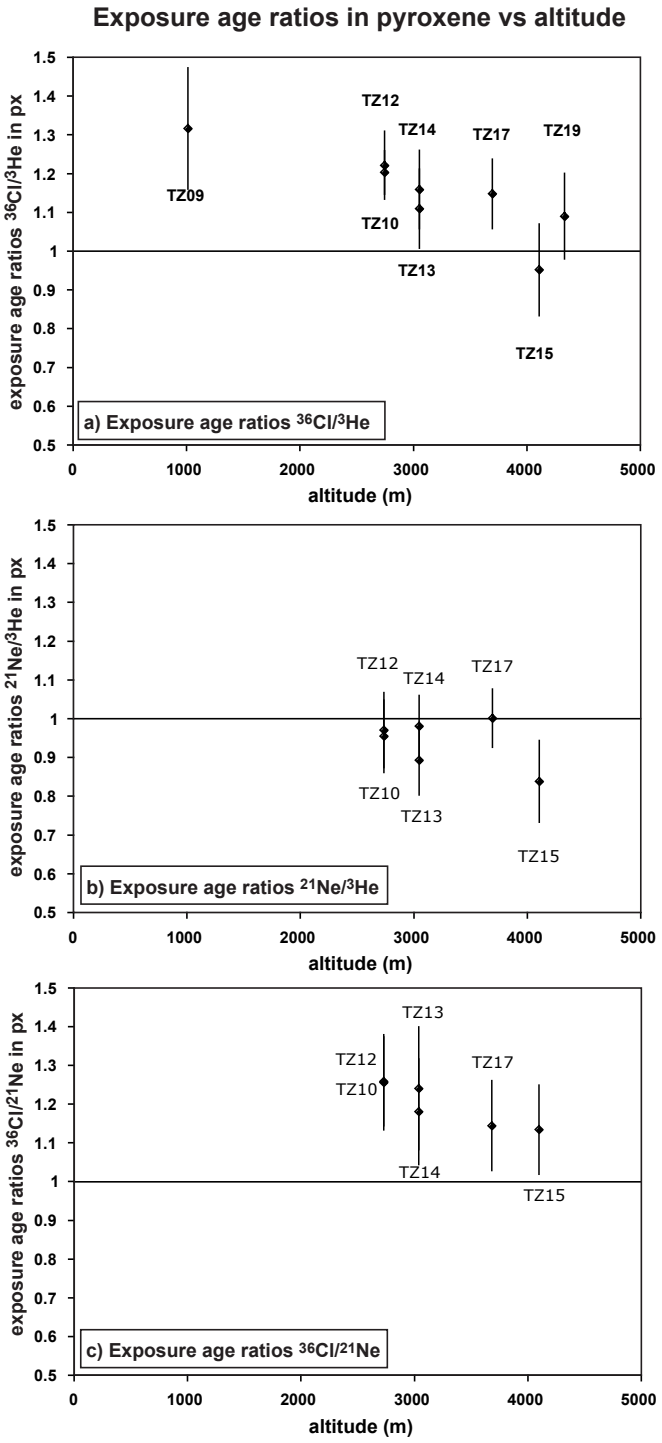

Figure 6.11: *Exposure age ratios calculated from cosmogenic ^{36}Cl, ^{3}He and ^{21}Ne concentrations. Production rates used are: for ^{36}Cl 42.2 ± 4.8 atoms (g Ca)$^{-1}$ a^{-1} (Chapter 5), for ^{3}He 128 ± 5 atoms (g mineral)$^{-1}$ a^{-1} Blard et al. (2006) and for ^{21}Ne 25 ± 8 atoms (g mineral)$^{-1}$ a^{-1} (Fenton et al., 2009). Standard deviations of these production rates are not propagated in the ratios.*

6.6 Comparison with other cross-calibrations

A significant altitudinal dependence of the relative production rates of ^{3}He compared to other nuclides, as was proposed by Gayer et al. (2004) and Amidon et al. (2008), is not documented by the Kilimanjaro data set. Even though the altitude range of samples TZ10 to TZ19 (2700 - 4300 m) is very similar to that of the Himalayan samples (3000 - 4600 m in Gayer et al., 2004, and 3200 - 4800 m in Amidon et al., 2008), the nuclide ratios documented in our study (Fig. 6.9a and b) agree within their standard deviations, not showing any clear relationship with altitude as was documented for ^{3}He/^{10}Be variations (up to 40% difference in the nuclide ratios) by Amidon et al. (2008).

The ^{21}Ne/^{3}He concentration ratios in pyroxene (0.183 ± 0.012) and olivine (0.375 ± 0.015) are in agreement with those of others studies, e.g. in Fenton et al. (2009) (0.204 ± 0.014 in pyroxene and 0.400 ± 0.029 in olivine), Poreda and Cerling (1992) (0.41 ± 0.05 in olivine) and Niedermann et al. (2007) (0.224 +0.022/-0.029 in pyroxene and 0.405 ± 0.034 in olivine), also suggesting that the production rates of ^{3}He and ^{21}Ne in these minerals have no different altitude dependencies.

As discussed in section 6.5, the ^{3}He data in the pyroxenes of sample TZ15 needs to be refined. We expect therefore that the here presented mean value of the ^{21}Ne/^{3}He ratio might slightly increase (compare Fig. 6.9b), if the cosmogenic ^{3}He concentration of sample TZ15 is, as we suspect, overestimated at the moment. The mean value would than be even more similar to the mean values of the above-mentioned previous studies.

To our knowledge, Licciardi et al. (2008) is the only study, in which ^{36}Cl has been co-calibrated with another nuclide, ^{3}He. ^{36}Cl was measured in basaltic whole rock, while ^{3}He was determined in olivine phenocrysts of the same samples (Licciardi et al., 2006). However, concentrations cannot be compared since they are not given for ^{36}Cl in Licciardi et al. (2008). Also, the basalts have varying Cl concentrations (up to 61 ppm), which result in ^{36}Cl contributions from capture of low-energy neutron capture of ^{35}Cl of up to 26%, so that ^{36}Cl/^{3}He concentration ratios could not be expected to be stable from sample to sample (see section 6.5). Finally, all samples come from a narrow range of altitudes (20-460 m) not allowing to evaluate any altitude dependency. The co-calibration is therefore

performed by comparing visually the newly calibrated production rates of both nuclides (^{3}He in olivine and ^{36}Cl from spallation of Ca, see Fig. 5 in Licciardi et al., 2008), which only allowed checking potential external sources of uncertainties in the sample data set. A comparison between the relative production rates of ^{36}Cl and ^{3}He in their study and ours can therefore not be performed.

6.7 Conclusions

This study is the first that deals with the cross-calibration of three cosmogenic nuclides (^{36}Cl, ^{3}He and ^{21}Ne) in minerals over a large altitudinal profile (1000 - 4300 m, on the flanks of the Kilimanjaro volcano). All three nuclides are measured in pyroxene phenocrysts, and ^{3}He and ^{21}Ne are additionally measured in olivine at two elevations. ^{36}Cl is also determined in plagioclase co-existing with pyroxene in one of the samples for the purpose of validating the use of pyroxene for reliable ^{36}Cl measurements. Calculated exposure ages from both minerals yield the same result confirming that ^{36}Cl measurements in pyroxene are valid.

Cosmogenic ^{21}Ne/^{3}He concentration ratios in pyroxene are 0.183 $\pm$ 0.012 and those in olivine are 0.375 $\pm$ 0.015, agreeing with previously determined ratios of these nuclides (Fenton et al., 2009; Poreda and Cerling, 1992; Niedermann et al., 2007). In our samples, the ^{36}Cl/^{3}He and ^{36}Cl/^{21}Ne concentration ratios are 0.0575 $\pm$ 0.0068 and 0.301 $\pm$ 0.020, respectively. These ratios can be very different in other samples, because the ^{36}Cl production rate in a mineral depends strongly on the target element concentrations.

No significant altitude dependence of any of the nuclides can be proved. This is based on nuclide concentration ratios and calculated apparent exposure age ratios plotted versus the elevations of the sample sites. Exposure age ratios compared to concentrations ratios has the advantage that the radioactive decay of ^{36}Cl and the ^{36}Cl contribution from slow negative muons can be accounted for. From 2700 to 4300 m, where the data set is most robust, all reliable data points agree well within standard deviation. The lowest sample, at an altitude of 1013 m, must, at this moment, be considered as an outlier because it is only based on a single ^{3}He determination. Additional ^{3}He replicate measurements on this sample will have to confirm or disprove this assumption.

Hence, the data presented in this study suggests that production of the investigated cosmonuclides is proportional at mid to high altitude, implying that no nuclide-specific scaling factors are needed. However, it will have to be evaluated in future studies if the same is true for nuclides whose production depends strongly on the target elements, like it is the case for ^{36}Cl. It could not be tested in this study if the production rates from spallation of Ca and of K have different altitude-dependencies, since the lava has no phenocrysts containing K. An ideal approach to solve this problem would be to measure ^{36}Cl in co-existing K-rich minerals (e.g. sanidine) and Ca-rich minerals (e.g. Ca-plagioclase) over such a large altitude range as the Kilimanjaro transect.

General conclusions

As part of the CRONUS-EU-objective to advance the cosmogenic nuclide dating method, the key problem of this PhD study lied in improving the accuracy of the SLHL production rates from the most important ^{36}Cl production pathways, spallation of Ca and K.

As a first step towards the solution of this problem, the probably most influential source of discrepancy between the previously published production rates could be detected: the Cl concentrations in the calibration samples. It could be shown that the ^{36}Cl production in samples rich in Cl, such as basaltic whole rocks, can be significantly underestimated, in contrast to that in Ca-rich minerals low in Cl. In the case of exposure age determinations, this leads to an overestimation of the exposure age.

Analogously, in the case of spallation production rate calibrations, high Cl concentrations in the calibration samples might result in underestimation of ^{36}Cl contributions due to Cl and thus in overestimated spallation production rates. This hypothesis is generally concordant with the sample compositions and the resulting production rates of previous calibration studies: The lowest reported ^{36}Cl production rate from Ca (48.8 $\pm$ 1.7 atoms ^{36}Cl (g Ca)$^{-1}$ a^{-1}) was calibrated using Ca-feldspars with 2-5 ppm Cl (Stone et al., 1996), and in the case of the lowest production rate from K (137 $\pm$ 9 atoms ^{36}Cl (g K)$^{-1}$ a^{-1}), the K-richest samples were also the Cl-poorest ones (Phillips et al., 2001, 1996).

We conclude that the use of samples low in Cl yields more accurate ^{36}Cl spallation production rates. In many cases, using separated minerals provides a high probability for low Cl concentrations, in contrast to the use of magmatic whole rock samples. Additionally, within the scope of this PhD, a new chemical protocol for ^{36}Cl extraction from silicate rocks and minerals was established, which includes a rigourous pretreatment for the purpose

of purifying and decontaminating the samples from Cl as much as possible. Finally, as part of the preparatory work before approaching the main objective of this PhD, a new ^{36}Cl calculator was created, including the complete calculations of all ^{36}Cl production mechanisms and being valid for any rock and mineral type.

These findings and efforts thus paved the way for a new and straightforward calibration attempt.

For this purpose, ^{36}Cl was measured in Ca-plagioclases from Mt. Etna lavas (38°N, Italy) and in K-rich feldspars from the Payun Matru volcano (36°S, Argentina), the samples taken from surfaces with independently determined exposure ages. Five different published scaling methods were applied, generating five versions of the data set. Using a Bayesian statistical model allowed including all major uncertainties in the data set. The ^{36}Cl spallation production rates inferred are the so far lowest calibrated values: 42.2 ± 4.8 atoms ^{36}Cl (g Ca)$^{-1}$ a^{-1} and 124.9 ± 8.1 atoms ^{36}Cl (g K)$^{-1}$ a^{-1}, when using the scaling method of Stone (2000). The values when using the other scaling methods (Dunai, 2001; Desilets et al., 2006b; Lifton et al., 2005, 2008) are indistinguable within standard deviation, i.e. significant differences between the various production rates using different scaling methods cannot be observed. The relatively large uncertainties in these production rates are mainly due to the uncertainties in the independent age constraints of the lava flows. Therefore, as a perspective for future studies, the precision of these production rates can still be improved, if appropriate calibration surfaces are found, which can be dated more precisely by an independent method.

Nevertheless, the good agreement between these new ^{36}Cl spallation production rates and those previously calibrated with samples low in Cl (Stone et al., 1996; Phillips et al., 2001) corroborates that the most reliable values are those in the lowest range of all so far published ^{36}Cl spallation production rates.

We suspect, however, that as long as scaling is not more accurate, it will not be possible to obtain SLHL ^{36}Cl production rates and ^{36}Cl exposure ages without introducing systematic errors.

The last part of this PhD study aimed therefore at investigating if the various cosmogenic nuclides feature different altitude dependencies in their production rates, which could explain why the existing scaling methods still fail to describe accurately the spatial variability of these production rates. By cross-calibrating the three nuclides ^{36}Cl, ^{3}He and ^{21}Ne produced in pyroxenes from lava samples taken over an altitude transect between 1000 and 4300 m at Kilimanjaro (3°S, Tanzania), no altitude effect on their production ratios could be observed. This suggests that for the investigated production mechanisms no nuclide-specific factors are needed. However, the question remains open if this is also true for the production of ^{36}Cl from the two target elements Ca and K, their spallation production rates being suspected of having different altitude dependencies due to the different treshold energies of the two spallation reactions.

It could also be shown in this last part that, in addition to feldspar, Ca-rich pyroxene is a silicate mineral suitable for reliable ^{36}Cl measurements. This is not only because it is chemically possible to extract ^{36}Cl from this mineral, but also because the Cl concentrations in the pyroxenes were low enough to obtain a high ^{36}Cl contribution from spallation. It has to be evaluated if this is always the case. This strengthens the assumption that the use of ^{36}Cl is not restricted to certain mineral types, as it is the case for most of the other cosmogenic nuclides, but that it can be applied virtually to any rock type containing at least one of its target elements Ca, K, Ti or Fe.

In summary, the results of this PhD thesis contribute considerably to the improvement of the methodological and analytical aspects of the cosmogenic nuclide ^{36}Cl and therefore facilitate largely its use for the surface exposure dating method. Not only the improvement of the accuracies of the spallation production rates ensures the more accurate quantification of surface processes. Also the new chemical protocol for ^{36}Cl extraction from silicate rocks, the supply of an easily usable and straightforward calculator for ^{36}Cl applications and the validation of an additional mineral, suited for ^{36}Cl extraction, provide a solid basis for the routine application of ^{36}Cl.

Together with the constant improvements in the understanding of cosmogenic nuclide systematics, we are optimistic to go for still more accurate and precise production rates and scaling methods with the perspective to establish the surface exposure dating method with cosmogenic nuclides as a highly reliable geochronometer.

Appendices

Appendix A

Total in-situ ^{36}Cl production calculations

The following equations are for the most part taken and adapted from Gosse and Phillips (2001). If this is not the case the source is cited. The choices of published parameters and calculations are discussed in section 4.3. Note that the equations have been adjusted to account for the fact that ^{36}Cl is not extracted from the bulk rock but from a part of the rock (target fraction). Hence, these calculations can be used if ^{36}Cl is measured in mineral separates or in a leached whole rock. Even if ^{36}Cl is extracted from a leached whole rock, certain elements are preferentially dissolved during leaching, and the composition can change considerably. We therefore make a distinction between the chemical composition of the bulk rock and that of the target fraction. This is indicated by the subscripts *bulk* and *target*, respectively.

The attached Microsoft Excel® spreadsheet includes all these calculations. For an uneroded or eroding sample it calculates the exposure age and the contributions from the various ^{36}Cl production mechanisms. In the case of an eroding sample, either the erosion rate has to be known/estimated to find the exposure age or the exposure age has to be known/estimated to find the erosion rate. Depth profiles showing the vertical distributions of the total calculated ^{36}Cl concentration and the sample-specific production rates are generated automatically from the relevant sample parameters. The calculated ^{36}Cl concentration curve can be fitted to measured ^{36}Cl concentrations in a depth profile by adjusting free parameters such as the exposure age and/or the erosion rate. For further

explanations how to use the spreadsheet, see the worksheet "Legend+Instructions" in the Excel file.

For an uneroded rock sample of finite thickness the total sample-specific in-situ ^{36}Cl production rate [atoms ^{36}Cl g^{-1} a^{-1}] at mass depth z is given by

$$P_{total}(z) = S_{el,s}F_sQ_sP_s(z)+S_{el,s}F_n(Q_{eth}P_{eth}(z)+Q_{th}P_{th}(z))+S_{el,\mu}F_\mu Q_\mu P_\mu(z)+P_r \quad \text{(A.1)}$$

where $P_q(z)$ are the sample-specific depth dependent ^{36}Cl production rates due to the reaction types that are indicated by the subscript: s stands for spallation of Ca, K, Ti and Fe, eth for epithermal neutron capture on ^{35}Cl, th for thermal neutron capture on ^{35}Cl, μ for direct capture of slow negative muons on ^{40}Ca and ^{39}K, and r for radiogenic production.

Q_q are the sample thickness integration factors for the respective reaction types, given the sample-specific production rates of each reaction type referred to a specific mass depth z (section A.5).

$S_{el,s}$ and $S_{el,\mu}$ are the scaling factors for altitude, geographic latitude and temporal geomagnetic variations used to translate production rates from the reference point at sea level and high latitude to the geographic location and elevation of the sample site. F_s, F_n and F_μ include all correction factors for the respective reaction type (s spallation, n low-energy-neutron capture, μ slow negative muon capture), such as topographic shielding, snow shielding or geometry.

The total number of atoms ^{36}Cl that accumulated in an uneroded sample of simple exposure history and finite thickness as a function of depth and time is obtained by multiplying the total production rate by the time factor which includes the radioactive decay of ^{36}Cl:

$$N_{total}(z,t) = P_{total}(z)t_{cosm}(t) \quad \text{(A.2)}$$

with

$$t_{cosm}(t) = (1 - exp^{-t\lambda_{36}})/\lambda_{36} \quad \text{(A.3)}$$

where t is the exposure time [a] and λ_{36} the ^{36}Cl decay constant equal to 2.303×10^{-6}a^{-1}.

If the sample had been exposed to cosmic radiation prior to the exposure event of interest (inheritance) the sample might already have had a significant ^{36}Cl concentration at time $t = 0$. This inherited ^{36}Cl concentration $N_{inher}(0)$ is subject to radioactive decay during the duration of recent exposure. In this case the total number of atoms ^{36}Cl is given by

$$N_{total}(z,t) = N_{inher}(0)exp^{-t\lambda_{36}} + P_{total}(z)t_{cosm}(t) \tag{A.4}$$

A.1 Cosmogenic ^{36}Cl production by spallation of Ca, K, Ti and Fe

The sample-specific cosmogenic ^{36}Cl production rate by spallation of the target elements Ca, K, Ti and Fe [atoms ^{36}Cl g^{-1} a^{-1}] at mass depth z in a target fraction of a rock is given by

$$P_s(z) = \sum_k PR_k(0)\ C_{k,target}\ exp(-z/\Lambda_f) \tag{A.5}$$

where $PR_k(0)$ is the spallation ^{36}Cl production rate by element k at the rock surface and at SLHL [^{36}Cl (g of k)$^{-1}$a^{-1}], $C_{k,target}$ is the mass concentration of element k [%] in the target fraction (k is Ca, K, Fe and Ti). Λ_f is the apparent fast neutron attenuation coefficient with a value of 177 g cm^{-2} according to Farber et al. (2008).

A.2 Cosmogenic ^{36}Cl production by capture of low-energy neutrons on ^{35}Cl

Low-energy (thermal and epithermal) neutrons are generated during various cosmic secondary particle interactions, namely during spallation reactions, slow negative muon capture and fast muon deceleration. In the following equations all these interaction types are considered.

A.2.1 Epithermal neutrons

The sample-specific cosmogenic ^{36}Cl production rate by capture of epithermal neutrons on ^{35}Cl [atoms ^{36}Cl g^{-1} a^{-1}] at mass depth z in a target fraction of a rock close to the land/atmosphere boundary is given by

$$P_{eth}(z) = \frac{f_{eth}}{\Lambda_{eth}} \phi_{eth,total}(z)(1 - p(E_{th})) \tag{A.6}$$

f_{eth} is the fraction of epithermal neutrons absorbed by ^{35}Cl in the target fraction:

$$f_{eth} = \frac{N_{Cl,target} I_{a,Cl}}{I_{eff}} \tag{A.7}$$

Λ_{eth} is the attenuation length for absorption and moderation of the epithermal neutron flux [g cm^{-2}]:

$$\Lambda_{eth} = {\Sigma_{eth}}^{-1} = (\overline{\xi}(I_{eff} + \Sigma_{sc}))^{-1} \tag{A.8}$$

$\phi_{eth,total}(z)$ is the epithermal neutron flux [neutrons cm^{-2} a^{-1}] in the bulk rock at mass depth z:

$$\phi_{eth,total}(z) = \phi^*_{eth} exp(-z/\Lambda_f) + (1 + R_\mu R_{eth})(F\Delta\phi)^*_{eth} exp(-z/L_{eth}) + R_\mu \phi^*_{eth} exp(-z/\Lambda_\mu) \tag{A.9}$$

$p(E_{th})$ is the resonance escape probability of a neutron from the epithermal energy range in the bulk rock:

$$p(E_{th}) = exp\left[-\frac{I_{eff}}{\sum_k \xi_k N_{k,bulk} \sigma_{sc,k}}\right] \tag{A.10}$$

$N_{Cl,target}$ is the atomic concentration of Cl in the target fraction. $I_{a,Cl}$: dilute resonance integral for absorption of epithermal neutrons by Cl [10^{-24} cm^{-2}] (Table A.1).

I_{eff} is the macroscopic epithermal neutron absorption cross section:

$$I_{eff} = \sum_k I_{a,k} N_{k,bulk} \tag{A.11}$$

$I_{a,k}$ is the dilute resonance integral for absorption of epithermal neutrons by element k [10^{-24} cm^{-2}] (Table A.1).

$N_{k,bulk}$ is the atomic concentration of element k in the bulk rock.

Σ_{eth} is the macroscopic absorption and moderation cross-section for epithermal neutrons [cm^{2}g^{-1}].

$\overline{\xi}$ is the macroscopic average logarithmic decrement of energy loss per collision in the bulk rock:

$$\overline{\xi} = \frac{\sum_k \xi_k \sigma_{sc,k} N_{k,bulk}}{\sum_k \sigma_{sc,k} N_{k,bulk}} \tag{A.12}$$

ξ_k is the average logarithmic decrement of energy loss per collision for element k (Table A.1).

$\sigma_{sc,k}$ is the neutron scattering cross section for element k [10^{-24} cm^{-2}] (Table A.1).

Σ_{sc} is the macroscopic neutron scattering cross section [cm^2 g^{-1}]:

$$\Sigma_{sc} = \sum_k N_{k,bulk} \sigma_{sc,k} \tag{A.13}$$

ϕ^*_{eth} is the epithermal neutron flux at land/atmosphere interface that would be observed in the rock if the interface was not present [neutrons cm^{-2}a^{-1}]:

$$\phi^*_{eth} = P_f(0) \frac{R_{eth}}{\Sigma_{eth} - D_{eth}/{\Lambda_f}^2} \tag{A.14}$$

$P_f(0)$ is the production rate of epithermal neutrons from the fast neutron flux in the atmosphere, 626 neutrons (g air)$^{-1}$a^{-1} (Phillips et al., 2001).

R_{eth} is the ratio of epithermal neutron production in the rock to that in the atmosphere:

$$R_{eth} = \sqrt{\overline{A}/A_a} \tag{A.15}$$

A_a=14.5 g mol^{-1} (value according to CHLOE, Phillips and Plummer (1996)) is the average atomic weight of the atmosphere.

$\overline{A}$ is the average atomic weight of the bulk rock:

$$\overline{A} = \frac{\sum_k A_k N_{k,bulk}}{\sum_k N_{k,bulk}} \tag{A.16}$$

A_k is the atomic weight of element k. D_{eth} is the epithermal neutron diffusion coefficient in the rock [g cm^{-2}]:

$$D_{eth} = \frac{1}{3\Sigma_{sc}(1 - 2/(3\overline{A}))} \tag{A.17}$$

R_μ is the ratio of muon production to epithermal neutron production rate:

$$R_\mu = \frac{S_{el,\mu} P_{n\mu 0}}{S_{el,s} P_f(0) R_{eth}} \tag{A.18}$$

$S_{el,\mu}$ is the muon production scaling factor as a function of elevation and latitude. $P_{n\mu 0}$ is the total muon induced neutron production at land surface [neutrons cm^{-2} a^{-1}]

$$P_{n\mu 0} = Y_s \Psi_\mu(0) + 5.8 * 10^{-6} \phi_{\mu f 0} \tag{A.19}$$

$\Psi_\mu(0)$ is the slow negative muon stopping rate at land surface, it has a value of 190 μ g^{-1}a^{-1} according to Heisinger et al. (2002). $\phi_{\mu f 0}$ is the fast muon flux at land surface, its value is 7.9 $\times$ 10^5 μ cm^{-2}a^{-1}.

Y_s is the average neutron yield per stopped negative muon, according to Fabryka-Martin (1988) given by

$$Y_s = \sum_k f_{c,k,bulk} f_{d,k} Y_{n,k} \tag{A.20}$$

$f_{c,k,bulk}$ is the fraction of stopped muons that are captured by element k in the bulk rock (chemical compound factor), approximated by the "Fermi-Teller Z-law" (Charalambus, 1971):

$$f_{c,k,bulk} = \frac{M_{k,bulk} Z_k}{\sum_j M_{j,bulk} Z_j} \tag{A.21}$$

$f_{d,k}$ is the fraction of muons stopped by element k and absorbed by its nucleus before decay of the muon (Table A.1). $Y_{n,k}$ is the average neutron yield per captured muon for element k (Table A.1). $M_{k,bulk}$ and $M_{j,bulk}$ are the molar concentrations of elements k and j, respectively, k refers to the single element whose factor $f_{c,k}$ is to be calculated, and j refers to all elements in the rock. Z_k and Z_j are the respective atomic numbers.

$(F\Delta\phi)^*_{eth}$ is the difference between ϕ^*_{eth} and the actual epithermal neutron flux at the land surface:

$$(F\Delta\phi)^*_{eth} = \frac{\Delta\phi^*_{eth} D_{eth,a}/L_{eth,a} - \Delta\phi^{**}_{eth,a} D_{eth}/\Lambda_f}{D_{eth,a}/L_{eth,a} + D_{eth}/L_{eth}} \tag{A.22}$$

$\Delta\phi^*_{eth}$ is the difference between the hypothetical equilibrium epithermal neutron fluxes in atmosphere and rock [neutrons cm^{-2}a^{-1}]:

$$\Delta\phi^*_{eth} = \phi^*_{eth,a} - \phi^*_{eth} \tag{A.23}$$

$\phi^*_{eth,a}$ is the epithermal neutron flux at the land/atmosphere interface that would be observed in the atmosphere if the interface was not present [neutrons cm^{-2}a^{-1}]:

$$\phi^*_{eth,a} = \frac{P_f(0) R_{eth,a}}{\Sigma_{eth,a} - D_{eth,a}/{\Lambda_f}^2} \tag{A.24}$$

$\Delta\phi^{**}_{eth,a}$ is the adjusted difference between hypothetical equilibrium epithermal neutron fluxes in atmosphere and rock:

$$\Delta\phi^{**}_{eth,a} = \phi^{*}_{eth} - \frac{D_{eth,a}}{D_{eth}}\phi^{*}_{eth,a} \tag{A.25}$$

$D_{eth,a}$ is the epithermal neutron diffusion coefficient in the atmosphere [g cm^{-2}]:

$$D_{eth,a} = \frac{1}{3\Sigma_{sc,a}(1 - 2/(3A_a))} \tag{A.26}$$

$\Sigma_{sc,a}$ is the macroscopic neutron scattering cross section of the atmosphere [cm^2 g^{-1}]. Its value is 0.3773 cm^2 g^{-1} according to CHLOE (Phillips and Plummer, 1996).

$\Sigma_{eth,a}$ is the macroscopic absorption and moderation cross section for epithermal neutrons in the atmosphere. It has a value of 0.0548 cm^2 g^{-1} according to CHLOE (Phillips and Plummer, 1996).

L_{eth} and $L_{eth,a}$ are the epithermal neutron diffusion lengths [g cm^{-2}] in rock and atmosphere, respectively:

$$L_{eth} = (\sqrt{3\Sigma_{sc}\Sigma_{eth}})^{-1} \tag{A.27}$$

$$L_{eth,a} = (\sqrt{3\Sigma_{sc,a}\Sigma_{eth,a}})^{-1} \tag{A.28}$$

The slow muon attenuation length Λ_μ in Eq. A.9 is equal to 1500 g cm^{-2}.

A.2.2 Thermal neutrons

The sample-specific cosmogenic ^{36}Cl production rate by capture of thermal neutrons on ^{35}Cl [atoms ^{36}Cl g^{-1} a^{-1}] at mass depth z in a target fraction of a rock close to the land/atmosphere boundary is given by

$$P_{th}(z) = \frac{f_{th}}{\Lambda_{th}}\phi_{th,total}(z) \tag{A.29}$$

f_{th} is the fraction of thermal neutrons absorbed by ^{35}Cl in the target fraction:

$$f_{th} = \frac{N_{Cl,target}\sigma_{th,Cl}}{\Sigma_{th}} \tag{A.30}$$

Λ_{th} is the attenuation length for absorption the thermal neutron flux [g cm^{-2}]:

$$\Lambda_{th} = {\Sigma_{th}}^{-1} \tag{A.31}$$

Σ_{th} is the macroscopic thermal neutron absorption cross section [cm^2 g^{-1}]:

$$\Sigma_{th} = \sum_k \sigma_{th,k} N_{k,bulk} \tag{A.32}$$

$\phi_{th,total}(z)$ is the thermal neutron flux [neutrons cm^{-2} a^{-1}] in the bulk rock at mass depth z:

$$\phi_{th,total}(z) = \phi^*_{th} exp(-z/\Lambda_f) + (1 + R'_\mu)(\Im\Delta\phi)^*_{eth} exp(-z/L_{eth})$$

$$+(1 + R'_\mu R_{th})(\Im\Delta\phi)^*_{th} exp(-z/L_{th}) + R'_\mu \phi^*_{th} exp(-z/\Lambda_\mu) \tag{A.33}$$

ϕ^*_{th} is the thermal neutron flux at land/atmosphere interface that would be observed in the rock if the interface was not present [neutrons cm^{-2}a^{-1}]:

$$\phi^*_{th} = \frac{p(E_{th})_a R_{th} \phi^*_{eth}}{\Lambda_{eth}(\Sigma_{th} - D_{th}/{\Lambda_f}^2)} \tag{A.34}$$

$p(E_{th})_a$ is the resonance escape probability of a neutron from the epithermal energy range in the atmosphere. It has a value of 0.56 according to CHLOE (Phillips and Plummer, 1996).

R_{th} is the ratio of thermal neutron production in the rock to that in the atmosphere:

$$R_{th} = \frac{p(E_{th})}{p(E_{th})_a} \tag{A.35}$$

D_{th} is the thermal neutron diffusion coefficient in the rock, which is equal to D_{eth} (Eq. A.17).

R'_μ is the ratio of muon production rate to thermal production rate:

$$R'_\mu = \frac{p(E_{th})_a}{p(E_{th})} R_\mu \tag{A.36}$$

$(\Im\Delta\phi)^*_{eth}$ is a parameter describing the difference between ϕ^*_{eth} and the actual flux due to the epithermal flux profile:

$$(\Im\Delta\phi)^*_{eth} = \frac{p(E_{th})_a R_{th} (F\Delta\phi)^*_{eth}}{\Lambda_{eth}(\Sigma_{th} - D_{th}/{L_{eth}}^2)} \tag{A.37}$$

$(\Im\Delta\phi)^*_{th}$ is a parameter describing the difference between ϕ^*_{th} and the actual flux due to the thermal flux profile:

$$(\Im\Delta\phi)^*_{th} = [D_{th,a}\Big(\frac{\phi^*_{th,a}}{\Lambda_f} - \frac{(\Im\Delta\phi)^*_{eth,a}}{L_{eth,a}}\Big) - D_{th}\Big(\frac{\phi^*_{th}}{\Lambda_f} + \frac{(\Im\Delta\phi)^*_{eth}}{L_{eth}}\Big)$$

$$+\frac{D_{th,a}}{L_{th,a}}(\Delta\phi^*_{th}+\Delta(\Im\Delta\phi)^*_{eth})]/\Big(\frac{D_{th}}{L_{th}}+\frac{D_{th,a}}{L_{th,a}}\Big) \tag{A.38}$$

$(\Im\Delta\phi)^*_{eth,a}$ is a parameter describing the difference between $\phi^*_{eth,a}$ and the actual flux due to the epithermal flux profile:

$$(\Im\Delta\phi)^*_{eth,a}=\frac{p(E_{th})_a R_{th,a}(F\Delta\phi)^*_{eth,a}}{\Lambda_{eth,a}(\Sigma_{th,a}-D_{th,a}/{L_{eth,a}}^2)} \tag{A.39}$$

$R_{th,a}$=1 according to CHLOE (Phillips and Plummer, 1996).

$\Sigma_{th,a}$ is the macroscopic thermal neutron absorption cross-section of the atmosphere [cm^2 g^{-1}]. It has a value of 0.0602 cm^{2}g^{-1} according to CHLOE (Phillips and Plummer, 1996).

$(F\Delta\phi)^*_{eth,a}$ is the difference between $\phi^*_{eth,a}$ and the actual epithermal neutron flux at land surface:

$$(F\Delta\phi)^*_{eth,a}=\frac{\Delta\phi^*_{eth,a}D_{eth}/L_{eth}-\Delta\phi^{**}_{eth,a}D_{eth}/\Lambda_f}{D_{eth,a}/L_{eth,a}+D_{eth}/L_{eth}} \tag{A.40}$$

$\Lambda_{eth,a}$ is the attenuation length for absorption and moderation of the epithermal neutron flux [g cm^{-2}] in the atmosphere:

$$\Lambda_{eth,a}={\Sigma_{eth,a}}^{-1} \tag{A.41}$$

$\Delta\phi^*_{th}$ is the difference between hypothetical equilibrium thermal neutron fluxes in atmosphere and rock [neutrons cm^{-2}a^{-1}]:

$$\Delta\phi^*_{th}=\phi^*_{th,a}-\phi^*_{th} \tag{A.42}$$

$\Delta(\Im\Delta\phi)^*_{eth}$ is the difference between $(\Im\Delta\phi)^*_{eth}$ and $(\Im\Delta\phi)^*_{eth,a}$:

$$\Delta(\Im\Delta\phi)^*_{eth}=(\Im\Delta\phi)^*_{eth,a}-(\Im\Delta\phi)^*_{eth} \tag{A.43}$$

$\Delta\phi^*_{eth,a}$ is the difference in equilibrium epithermal neutron fluxes between atmosphere and rock [neutrons cm^{-2}a^{-1}]:

$$\Delta\phi^*_{eth,a}=-\Delta\phi^*_{eth} \tag{A.44}$$

$L_{th,a}$ is the thermal neutron diffusion length in the atmosphere [g cm^{-2}]:

$$L_{th,a}=\sqrt{D_{th,a}/\Sigma_{th,a}} \tag{A.45}$$

L_{th} is the thermal neutron diffusion length in the rock [g cm^{-2}]:

$$L_{th} = \sqrt{D_{th}/\Sigma_{th}} \tag{A.46}$$

A.3 Cosmogenic ^{36}Cl production by direct capture of slow negative muons on ^{40}Ca and ^{39}K

The sample-specific cosmogenic ^{36}Cl production rate by direct capture of slow negative muons on ^{40}Ca and ^{39}K at mass depth z in a target fraction of a rock close to the land/atmosphere boundary is estimated by

$$P_{\mu}(z) = \Psi_{\mu}(z) Y_{\Sigma k} \tag{A.47}$$

$\Psi_{\mu}(z)$ is the slow negative muon stopping rate at mass depth z, which, according to Heisinger et al. (2002), is given by

$$\Psi_{\mu}(z) = \Psi_{\mu}(0) exp^{\frac{-z}{\Lambda_{\mu}}} \tag{A.48}$$

with $\Psi_{\mu}(0) = 190\ \mu$ g^{-1}a^{-1} (Heisinger et al., 2002).

$Y_{\Sigma k}$ is the ^{36}Cl yield per muon stopped by element k in the target fraction (k = ^{40}Ca and ^{39}K):

$$Y_{\Sigma k} = \sum_{k} f_{c,k,target} f_{i,k} f_{d,k} f_{n,k} \tag{A.49}$$

$f_{c,k,target}$ is the fraction of stopped muons that are captured by element k in the bulk rock (chemical compound factor), approximated by the "Fermi-Teller Z-law" (Charalambus, 1971):

$$f_{c,k,target} = \frac{M_{k,target} Z_k}{\sum_j M_{j,bulk} Z_j} \tag{A.50}$$

$f_{i,k}$ is the abundance of the isotope of element k that produces ^{36}Cl subsequent to slow muon capture, with values of $f_{i,^{40}Ca} = 0.969$ and $f_{i,^{39}K} = 0.933$. $f_{d,k}$ is the fraction of muons stopped by element k and absorbed by its nucleus before decay of the muon, with values of $f_{d,Ca} = 0.864$ (Fabryka-Martin, 1988) $f_{d,K} = 0.83$ (Fabryka-Martin, 1988).

$f_{n,k}$ is the fraction of slow muon captures by element k that produce ^{36}Cl ("branching ratio"), with values of $f_{n,Ca} = 0.045 \pm 0.005$ and $f_{n,K} = 0.035 \pm 0.005$ (Heisinger et al., 2002).

A.4 Radiogenic ^{36}Cl production

The following equations are according to Fabryka-Martin (1988) Fabryka-Martin (1988) except Eqs. A.51, A.52 and A.53 which are taken from CHLOE (Phillips and Plummer, 1996).

The sample-specific radiogenic ^{36}Cl production rate [atoms ^{36}Cl g^{-1} a^{-1}] is given by

$$P_r = P_{eth,r} f_{eth} + P_{th,r} f_{th} \tag{A.51}$$

$P_{eth,r}$ is the total radiogenic epithermal neutron production [neutrons g^{-1} a^{-1}]:

$$P_{eth,r} = (P_{n,\alpha} + P_{n,sf})(1 - p(E_{th})) \tag{A.52}$$

$P_{th,r}$ is the total radiogenic thermal neutron production [neutrons g^{-1} a^{-1}]:

$$P_{th,r} = (P_{n,\alpha} + P_{n,sf}) p(E_{th}) \tag{A.53}$$

$P_{n,\alpha}$ is the neutron production rate [neutrons g^{-1} a^{-1}] due to α,n-reaction resulting from the U and Th α-decay series, estimated by

$$P_{n,\alpha} = X[U] + Y[Th] \tag{A.54}$$

where [U] and [Th] are the concentrations of U and Th, respectively, in the bulk rock in [ppm] and X and Y is the neutron yield in [neutrons g^{-1} a^{-1}] per [ppm] U and Th, respectively:

$$X = \frac{\sum_k S_k F_{k,bulk} Y_n^U}{\sum_k S_k F_{k,bulk}} \tag{A.55}$$

$$Y = \frac{\sum_k S_k F_{k,bulk} Y_n^{Th}}{\sum_k S_k F_{k,bulk}} \tag{A.56}$$

S_k is the mass stopping power of element k for α-particles of a given energy (Table A.2). $F_{k,bulk}$ is the fractional abundance of element k in [ppm] in the bulk rock. Y_n^U and Y_n^{Th} is the neutron yield of element k per [ppm] U and Th, respectively, in radioequilibrium (Table A.2). $P_{n,sf}$ is the neutron production rate [neutrons g^{-1} a^{-1}] due to spontaneous fission of ^{238}U

$$P_{n,sf} = 0.429 \times [U] \tag{A.57}$$

A.5 Sample thickness integration factors

The ^{36}Cl production varies with depth and has therefore to be integrated over the sample thickness to calculate the ^{36}Cl concentration in the sample. Q_s, Q_{eth}, Q_{th} and Q_μ are, as a function of the sample thickness, the correction factors relative to the ^{36}Cl production at a certain depth reference. The Q-factors are calculated according to Schlagenhauf et al. (2009). They are valid for deeper samples and eroded surfaces. The mass depth reference z [g cm^{-2}] refers to the center of the sample and is given by the depth of the top of the sample [g cm^{-2}] plus half of the sample thickness z_s [g cm^{-2}].

Q_s is the sample thickness integration factor for spallation:

$$Q_s = 1 + \frac{1}{6}\Big(\frac{z_s/2}{\Lambda_f}\Big)^2 \tag{A.58}$$

Q_{eth} is the sample thickness integration factor for epithermal neutron capture:

$$\begin{aligned} Q_{eth} = \frac{1}{P_{eth}}[&\phi^*_{eth}\frac{f_{eth}}{\Lambda_{eth}}(1-p(E_{th}))exp(\frac{-z}{\Lambda_f})(1+\frac{1}{6}\Big(\frac{z_s/2}{\Lambda_f}\Big)^2) \\ &+(1+R_\mu R_{eth})(F\Delta\phi)^*_{eth}\frac{f_{eth}}{\Lambda_{eth}}(1-p(E_{th}))exp(\frac{-z}{L_{eth}})(1+\frac{1}{6}\Big(\frac{z_s/2}{L_{eth}}\Big)^2) \\ &+R_\mu\phi^*_{eth}\frac{f_{eth}}{\Lambda_{eth}}(1-p(E_{th}))exp(\frac{-z}{\Lambda_\mu})(1+\frac{1}{6}\Big(\frac{z_s/2}{\Lambda_\mu}\Big)^2)] \end{aligned} \tag{A.59}$$

Q_{th} is the sample thickness integration factor for thermal neutron capture:

$$\begin{aligned} Q_{th} = \frac{1}{P_{th}}[&\phi^*_{th}\frac{f_{th}}{\Lambda_{th}}exp(\frac{-z}{\Lambda_f})(1+\frac{1}{6}\Big(\frac{z_s/2}{\Lambda_f}\Big)^2) \\ &+(1+R'_\mu)(\Im\Delta\phi)^*_{eth}\frac{f_{th}}{\Lambda_{th}}exp(\frac{-z}{L_{eth}})(1+\frac{1}{6}\Big(\frac{z_s/2}{L_{eth}}\Big)^2) \\ &(1+R'_\mu R_{th})(\Im\Delta\phi)^*_{th}\frac{f_{th}}{\Lambda_{th}}exp(\frac{-z}{L_{th}})(1+\frac{1}{6}\Big(\frac{z_s/2}{L_{th}}\Big)^2) \\ &R'_\mu\phi^*_{th}\frac{f_{th}}{\Lambda_{th}}exp(\frac{-z}{\Lambda_\mu})(1+\frac{1}{6}\Big(\frac{z_s/2}{\Lambda_\mu}\Big)^2)] \end{aligned} \tag{A.60}$$

Q_μ is the sample thickness integration factor for slow negative muon capture:

$$Q_\mu = 1 + \frac{1}{6}\Big(\frac{z_s/2}{\Lambda_\mu}\Big)^2 \tag{A.61}$$

A.6 Eroded surfaces

If the surface is eroding at a constant rate, the total number of atoms ^{36}Cl in a sample of simple exposure history and finite thickness as a function of depth, time and erosion rate is given by:

$$N_{total}(z,t,\varepsilon) = S_{el,s}S_T(J_{Q,s}d_s(z)t_{cosm,s}(t,\varepsilon) + J_{Q,eth}d_{eth}(z)t_{cosm,eth}(t,\varepsilon) + J_{Q,th}d_{th}(z)t_{cosm,th}(t,\varepsilon) + J_{Q,\mu}d_\mu(z)t_{cosm,\mu}(t,\varepsilon)) + P_r t_r \quad \text{(A.62)}$$

S_T is the topographic shielding correction factor.

$J_{Q,q}$ are the production rate coefficients including the sample thickness integration factors for the respective reaction types:

$$J_{Q,s} = Q_s S_{shape} S_{snow} \sum_k PR_k(0)\, C_{k,target} + Q_{eth}(1-p(E_{th}))\frac{f_{eth}}{\Lambda_{eth}}\phi^*_{eth} + Q_{th}\frac{f_{th}}{\Lambda_{th}}\phi^*_{th} \quad \text{(A.63)}$$

where S_{shape} is the geometric correction factor for spallogenic ^{36}Cl production and S_{snow} is the correction factor for snow shielding for spallogenic reactions.

$$J_{Q,eth} = (F\Delta\phi)^*_{eth}[Q_{eth}(1+R_\mu R_{eth})(1-p(E_{th}))\frac{f_{eth}}{\Lambda_{eth}}] + (\Im\Delta\phi)^*_{eth}[Q_{th}\frac{f_{th}}{\Lambda_{th}}(1+R'_\mu)] \quad \text{(A.64)}$$

$$J_{Q,th} = Q_{th}(1+R'_\mu R_{th})\frac{f_{th}}{\Lambda_{th}}(\Im\Delta\phi)^*_{th} \quad \text{(A.65)}$$

$$J_{Q,\mu} = Q_{eth}R_\mu(1-p(E_{th}))\frac{f_{eth}}{\Lambda_{eth}}\phi^*_{eth} + Q_{th}R'_\mu\frac{f_{th}}{\Lambda_{th}}\phi^*_{th} + Q_\mu\frac{S_{el,\mu}}{S_{el,s}}Y_{\Sigma k}\Psi_\mu(0) \quad \text{(A.66)}$$

$d_q(z)$ are the depth reference factors for the respective reaction types:

$$d_s(z) = exp(-\frac{z}{\Lambda_f}) \quad \text{(A.67)}$$

$$d_{eth}(z) = exp(-\frac{z}{L_{eth}}) \quad \text{(A.68)}$$

$$d_{th}(z) = exp(-\frac{z}{L_{th}}) \tag{A.69}$$

$$d_{\mu}(z) = exp(-\frac{z}{\Lambda_{\mu}}) \tag{A.70}$$

Note that to conform with the calculations for the thickness integration factors (section A.5) the mass depth reference z [g cm^{-2}] refers to the center of the sample according to Schlagenhauf et al. (2009).

$t_{cosm,q}(t, \varepsilon)$ are the time factors for the respective cosmogenic reaction types including the radioactive decay of ^{36}Cl and the erosion rate:

$$t_{cosm,s}(t, \varepsilon) = (1 - exp(-t\Big(\lambda_{36} + \frac{\rho\varepsilon}{\Lambda_f}\Big)))/\Big(\lambda_{36} + \frac{\rho\varepsilon}{\Lambda_f}\Big) \tag{A.71}$$

$$t_{cosm,eth}(t, \varepsilon) = (1 - exp(-t\Big(\lambda_{36} + \frac{\rho\varepsilon}{L_{eth}}\Big)))/\Big(\lambda_{36} + \frac{\rho\varepsilon}{L_{eth}}\Big) \tag{A.72}$$

$$t_{cosm,th}(t, \varepsilon) = (1 - exp(-t\Big(\lambda_{36} + \frac{\rho\varepsilon}{L_{th}}\Big)))/\Big(\lambda_{36} + \frac{\rho\varepsilon}{L_{th}}\Big) \tag{A.73}$$

$$t_{cosm,\mu}(t, \varepsilon) = (1 - exp(-t\Big(\lambda_{36} + \frac{\rho\varepsilon}{\Lambda_{\mu}}\Big)))/\Big(\lambda_{36} + \frac{\rho\varepsilon}{\Lambda_{\mu}}\Big) \tag{A.74}$$

where ε is the constant erosion rate [cm a^{-1}] and ρ the density of the sample [g cm^{-3}].

t_r is the time factor for the radiogenic reaction including the radioactive decay of ^{36}Cl:

$$t_r = \frac{1 - exp(-t_{form}\lambda_{36})}{\lambda_{36}} \tag{A.75}$$

where t_{form} is the formation time of the rock [a]. The formation age can be different from the exposure time, e.g. for buried surfaces. In this case even for uneroded samples N_r has to be calculated separately from the cosmogenic ^{36}Cl concentrations.

Table A.1: *Elemental constant parameters for calculations of the low-energy-neutron field and slow negative muon capture, from Fabryka-Martin (1988) except $f_{n,k,^{36}Cl}$, from Heisinger et al. (2002). See text for explanation of symbols.*

k	$I_{a,k}$ $[10^{-24}cm^2]$	ξ_k	$\sigma_{sc,k}$ $[10^{-24}cm^2]$	$\sigma_{a,k}$ $[10^{-24}cm^2]$	$f_{d,k}$	$Y_{n,k}$	$f_{i,k}$	$f_{n,k,^{36}Cl}$
H	0	1	20.5	0.33				
Li	0	0.264	0.95	70.5				
B	1722	0.174	4.27	767				
C	0.0016	0.158	4.74	0.0034	0.090	0.76		
O	0.0004	0.12	3.76	0.0002	0.223	0.8		
Na	0.311	0.084	3.025	0.53	0.432	1.0		
Mg	0.038	0.08	3.42	0.063	0.538	0.6		
Al	0.17	0.072	1.41	0.23	0.582	1.26		
Si	0.127	0.07	2.04	0.17	0.671	0.86		
Cl	13.7	0.055	15.8	33.5				
K	1	0.05	2.04	2.15	0.83	1.25	0.933	0.035
Ca	0.235	0.049	2.93	0.43	0.864	0.75	0.969	0.045
Ti	3.1	0.041	4.09	6.1				
Cr	1.6	0.038	3.38	3.1				
Mn	14	0.036	2.2	13.3				
Fe	1.39	0.035	11.35	2.56	0.906	1.125		
Sm	1400	0.013	38	9640				
Gd	390	0.013	172	41560				
P			5	0.2				

Table A.2: *Elemental constant parameters for calculations of radiogenic low-energy production, from Fabryka-Martin (1988). See text for explanation of symbols.*

	S_k [MeV (g cm^{-2})$^{-1}$] at 8.0 MeV	Y_n^U [neutrons g^{-1}a^{-1} (ppm U)$^{-1}$]	Y_n^{Th} [neutrons g^{-1}a^{-1} (ppm Th)$^{-1}$]
Li	548	21.1	9.6
B	527	62.3	19.2
C	561	0.45	0.18
O	527	0.23	0.079
Na	456	14.5	6.8
Mg	461	5.8	2.6
Al	444	5.1	2.6
Si	454	0.69	0.335
K	414	0.45	0.305
Ca	428	0	0
Ti	375	0	0
Fe	351	0.19	0.205
Be	529	265	91.2
F	472	30.8	11.8
P	433	0	0
S	439	0	0

Appendix B

Spreadsheet for in situ ^{36}Cl production calculations

This Microsoft Excel® spreadsheet can be found in the online version of the paper Schimmelpfennig et al. (2009), at http://dx.doi.org/doi:10.1016/j.quageo.2009.06.003

Appendix C

Supplementary information for Chapter 5

Table C.1: *Scaling factors for spallation reactions ($S_{el,s}$) and slow negative muon reactions ($S_{el,\mu}$) according to five different scaling schemes. Locations of the sample sites see Table 5.2*

Sample	$S_{el,s}$					$S_{el,\mu}$				
	St	Du	De	Li05	Li08	St	Du	De	Li05	Li08
Mt. Etna: Historic Flow (integrated over exposure duration 0-400 years)										
HF1	3.649	3.409	3.582	3.290	2.805	2.024	1.820	2.152	1.271	1.199
Mt. Etna: Solicchiata (integrated over exposure duration 0-8 ka)										
SI3	1.440	1.197	1.259	1.152	1.158	1.176	1.058	1.263	1.013	1.019
SI40	1.446	1.202	1.262	1.158	1.163	1.179	1.061	1.266	1.014	1.019
SO3	1.771	1.478	1.563	1.435	1.441	1.325	1.193	1.416	1.048	1.053
SO2	2.088	1.751	1.861	1.711	1.717	1.459	1.313	1.552	1.081	1.087
SO1	2.451	2.065	2.208	2.030	2.037	1.602	1.441	1.697	1.119	1.125
Mt. Etna: Piano della Lepre (integrated over exposure duration 10-20 ka)										
SI43	4.553	4.869	4.783	4.460	4.129	2.308	2.073	2.471	1.395	1.359
Mt. Etna: La Nave (integrated over exposure duration 0-32 ka)										
SI41	1.823	1.773	1.776	1.642	1.561	1.348	1.213	1.459	1.082	1.073
SI29	1.838	1.788	1.788	1.656	1.575	1.354	1.219	1.466	1.084	1.075
Payun Matru (integrated over exposure duration 0-15 ka)										
PM06-31	5.122	4.874	5.131	4.761	4.900	2.486	2.207	2.629	1.413	1.431
PM06-32	5.122	4.874	5.131	4.761	4.900	2.486	2.207	2.629	1.413	1.431
PM06-24	5.820	5.590	5.902	5.480	5.635	2.685	2.384	2.830	1.482	1.501
PM06-26	5.824	5.594	5.906	5.484	5.642	2.686	2.384	2.831	1.482	1.502

Table C.2: *Calculated sample-specific production rates for all production mechanisms, correction factors and time factor.*

	Q_s	Q_μ	d_s	d_{eth}	d_{th}	d_μ	P_{Ti}	P_{Fe}	P_μ	P_r	D	E	$J_{Q,eth}$	$J_{Q,th}$	L_{th}	L_{eth}
Mt. Etna: Historic Flow 1614-24 (between 383 and 393 years)																
HF1	1.000	1.000	0.972	0.757	0.792	0.997	0.007	0.009	0.602	0.003	0.183	0.010	-0.250	0.134	21.49	17.98
Mt. Etna: Solicchiata (^{14}C between 4.4 ka and 18.4 ka)																
SI3	1.000	1.000	0.964	0.632	0.729	0.996	0.007	0.009	0.612	0.006	0.279	0.020	-0.240	0.063	20.33	14.02
SI40	1.001	1.000	0.930	0.400	0.531	0.992	0.007	0.009	0.614	0.005	0.243	0.017	-0.209	0.054	20.33	14.02
SO3	1.001	1.000	0.938	0.439	0.572	0.993	0.006	0.009	0.605	0.004	0.189	0.012	-0.158	0.039	20.26	13.75
SO2	1.001	1.000	0.946	0.493	0.617	0.994	0.006	0.009	0.616	0.003	0.133	0.008	-0.112	0.028	20.29	13.85
SO1	1.001	1.000	0.925	0.363	0.506	0.991	0.006	0.009	0.603	0.003	0.149	0.009	-0.122	0.029	20.23	13.62
Mt. Etna: Piano della Lepre (K-Ar 10.0 ± 3.2 ka)																
SI43-D4	1.002	1.000	0.904	0.259	0.421	0.988	0.009	0.010	0.661	0.003	0.138	0.006	-0.108	0.022	20.57	13.16
SI43-D5	1.002	1.000	0.904	0.259	0.421	0.988	0.007	0.008	0.487	0.004	0.153	0.007	-0.120	0.024	20.57	13.16
SI43-D6	1.002	1.000	0.904	0.259	0.421	0.988	0.007	0.009	0.552	0.003	0.124	0.005	-0.097	0.019	20.57	13.16
SI43-D7	1.002	1.000	0.904	0.259	0.421	0.988	0.007	0.008	0.546	0.002	0.099	0.004	-0.077	0.015	20.57	13.16
SI43-D8	1.002	1.000	0.904	0.259	0.421	0.988	0.007	0.009	0.560	0.002	0.059	0.003	-0.046	0.009	20.57	13.16
Mt. Etna: La Nave (K-Ar/TL 32.4 ± 1.3 ka)																
SI41	1.002	1.000	0.899	0.246	0.393	0.988	0.007	0.008	0.547	0.004	0.162	0.010	-0.132	0.030	20.23	13.47
SI29-160	1.001	1.000	0.931	0.392	0.536	0.992	0.007	0.007	0.530	0.003	0.136	0.009	-0.111	0.025	20.23	13.47
SI29-250	1.001	1.000	0.931	0.392	0.536	0.992	0.007	0.007	0.531	0.003	0.111	0.007	-0.091	0.020	20.23	13.47
Payun Matru (K-Ar 15.2 ± 0.9 ka)																
PM06-31B	1.000	1.000	0.974	0.700	0.798	0.997	0.003	0.003	0.312	0.004	0.349	0.015	-0.256	0.048	20.36	12.89
PM06-31B-Rep	1.000	1.000	0.974	0.700	0.798	0.997	0.003	0.003	0.312	0.006	0.366	0.016	-0.268	0.050	20.36	12.89
PM06-32	1.000	1.000	0.974	0.700	0.798	0.997	0.004	0.004	0.313	0.006	0.614	0.027	-0.451	0.084	20.36	12.89
PM06-32-Rep	1.000	1.000	0.974	0.700	0.798	0.997	0.004	0.004	0.313	0.005	0.584	0.026	-0.429	0.080	20.36	12.89
PM06-24	1.000	1.000	0.974	0.700	0.798	0.997	0.003	0.003	0.307	0.003	0.288	0.012	-0.211	0.040	20.36	12.89
PM06-26	1.000	1.000	0.974	0.700	0.798	0.997	0.004	0.003	0.300	0.003	0.415	0.017	-0.303	0.057	20.36	12.89

Table C.3: *Calibrated ^{36}Cl spallation production rates from Ca and K, normalised to SLHL with five published scaling schemes: St (Stone, 2000), Du (Dunai, 2001), De (Desilets et al., 2006b), Li05 (Lifton et al., 2005), Li08 (Lifton et al., 2008). Only the uncertainties in the independent age constraints are included in the calculations.*

Scaling method	SLHL PR_{Ca} [atoms ^{36}Cl (g Ca)$^{-1}$ a^{-1}] Mean $\pm\sigma$	SLHL PR_K [atoms ^{36}Cl (g K)$^{-1}$ a^{-1}] Mean $\pm\sigma$
St	42.2 ± 3.0	124.5 ± 7.9
Du	42.4 ± 3.2	131.4 ± 8.3
De	41.6 ± 3.3	124.0 ± 8.7
Li05	43.4 ± 3.4	135.2 ± 8.7
Li08	44.0 ± 3.4	130.8 ± 8.6

Table C.4: *Calibrated ^{36}Cl spallation production rates from Ca and K, normalised to SLHL with five published scaling schemes: St (Stone, 2000), Du (Dunai, 2001), De (Desilets et al., 2006b), Li05 (Lifton et al., 2005), Li08 (Lifton et al., 2008). No uncertainty in the parameters of the data set is included in the calculations.*

Scaling method	SLHL PR_{Ca} [atoms ^{36}Cl (g Ca)$^{-1}$ a^{-1}] Mean $\pm\sigma$	SLHL PR_K [atoms ^{36}Cl (g K)$^{-1}$ a^{-1}] Mean $\pm\sigma$
St	44.0 ± 2.8	124.4 ± 2.6
Du	43.9 ± 2.0	131.0 ± 2.0
De	43.5 ± 2.3	123.4 ± 2.1
Li05	47.5 ± 2.4	134.8 ± 2.4
Li08	50.0 ± 3.0	130.4 ± 2.7

Appendix D

Supplementary information for Chapter 6

Sample site descriptions:

- **Sample TZ09: 1013 m altitude, 03°23.740' S**

  Ropey but eroded tumuli surface of a pyroxene-rich ($\sim$ 3 mm) "red" basalt flow on Mui Crater in the Kilemo Zone on the southern slopes of Kilimanjaro (Fig. 6.4a).

- **Sample TZ10: 2740 m altitude, 03°10.490' S**

  30 cm-high well-preserved hornito on the surface of an ankaramitic lava flow at the edge of the rainforest in the Rombo Zone (Fig. 6.4b).

- **Sample TZ12: 2740 m altitude, 03°10.490' S**

  Sample from a pressure ridge taken a few meters from TZ10.

- **Sample TZ13: 3050 m altitude, 03°09.319' S**

  Set of three preserved pahoehoe ropes of an ankaramitic lava flow in the Rombo Zone containing large olivines and pyroxenes (Fig. 6.4c).

- **Sample TZ14: 3050 m altitude, 03°09.319' S**

  Flat edge of small, 1 m-wide tumulus a few meters from TZ13 on the same ankaramitic flow (Fig. 6.4d).

- **Sample TZ15: 4107 m altitude, 03°07.020' S**

Surface of a 3 m-wide, glacially polished doleritic dyke (Fig. 6.4e). Contains large plagioclase laths and pyroxene phenocrysts and minor olivine (<2 mm). $^{39}Ar/^{40}Ar$ age of the dyke is 527 ± 3 ka (Alice Williams, unpublished data).

- **Sample TZ17: 3694 m altitude, 03°08.308' S**

  Vesicular but fresh sample taken from the ropey surface of a rubbly ankaramitic lava flow near the top of a small parasitic cone in the Rombo Zone (Fig. 6.4f).

- **Sample TZ19: 4331 m altitude, 03°05.791' S**

  Surface of an ankaramitic pressure-ridge exhibiting weathering polish. Low vesicularity. Contains abundant fresh olivine and pyroxene phenocrysts (Fig. 6.4g).

Bibliography

Ackert, R., Singer, B., Guillou, H., Kaplan, M., Kurz, M., 2003. Long-term cosmogenic ^{3}He production rates from ^{40}Ar/^{39}Ar and K-Ar dated Patagonian lava flows at 47°S. Earth and Planetary Science Letters 210 (1-2), 119–136.

Amidon, W., Farley, K., Burbank, D., Prattsitaula, B., 2008. Anomalous cosmogenic ^{3}He production and elevation scaling in the high Himalaya. Earth and Planetary Science Letters 265 (1-2), 287–301.

Amidon, W. H., Rood, D. H., Farley, K. A., 2009. Cosmogenic ^{3}He and ^{21}Ne production rates calibrated against ^{10}Be in minerals from the Coso volcanic field. Earth and Planetary Science Letters 280 (1-4), 194 – 204.

Balco, G., Briner, J., Finkel, R. C., Rayburn, J. A., Ridge, J. C., Schaefer, J. M., 2009. Regional beryllium-10 production rate calibration for late-glacial northeastern North America. Quaternary Geochronology 4 (2), 93 – 107.

Balco, G., Shuster, D. L., 2009. Production rate of cosmogenic ^{21}Ne in quartz estimated from ^{10}Be, ^{26}Al, and ^{21}Ne concentrations in slowly eroding Antarctic bedrock surfaces. Earth and Planetary Science Letters 281 (1-2), 48 – 58.

Balco, G., Stone, J., Lifton, N., Dunai, T., 2008. A complete and easily accessible means of calculating surface exposure ages or erosion rates from ^{10}Be and ^{26}Al measurements. Quaternary Geochronology 3 (3), 174–195.

Benedetti, L., Finkel, R., King, G., Armijo, R., Papanastassiou, D., Ryerson, F. J., Flerit, F., Farber, D., Stavrakakis, G., 2003. Motion on the Kaparelli fault (Greece) prior to

the 1981 earthquake sequence determined from ^{36}Cl cosmogenic dating. Terra Nova 15, 118–124.

Benson, L., Madole, R., Phillips, W., Landis, G., Thomas, T., Kubik, P., 2004. The probable importance of snow and sediment shielding on cosmogenic ages of north-central Colorado Pinedale and pre-Pinedale moraines. Quaternary Science Reviews 23 (1-2), 193–206.

Bentley, H. W., Phillips, F. M., Davis, S. N., 1986. Chlorine-36 in the Terrestrial Environment. In: Fritz, P., Fontes, J. C. (Eds.), Handbook of Environmental Isotope Geochemistry. Vol. 2. Elsevier, Amsterdam, Ch. 10, pp. 427 – 480.

Bierman, P., Gillespie, A., Caffee, M., Elmore, D., 1995. Estimating erosion rates and exposure ages with ^{36}Cl produced by neutron activation. Geochimica et Cosmochimica Acta 59 (18), 3779–3798.

Bierman, P. R., 1994. Using in situ produced cosmogenic isotopes to estimate rates of landscape evolution: A review from the geomorphic perspective. Journal of Geophysical Research 99 (B7), 13885–13896.

Blard, P. H., 2006. Les isotopes cosmogéniques ^{3}He et ^{10}Be dans les minéraux maphiques : développements analytiques, calibration et nouvelles applications. Ph.D. thesis, Université Paul Cézanne - Aix-Marseille III, France.

Blard, P. H., Bourlès, D., Pik, R., Lavé, J., 2008. In situ cosmogenic ^{10}Be in olivines and pyroxenes. Quaternary Geochronology 3 (3), 196–205.

Blard, P. H., Farley, K. A., 2008. The influence of radiogenic ^{4}He on cosmogenic ^{3}He determinations in volcanic olivine and pyroxene. Earth and Planetary Science Letters 276 (1-2), 20 – 29.

Blard, P. H., Lavé, J., Pik, R., Quidelleur, X., Bourlès, D., Kieffer, G., 2005. Fossil cosmogenic He record from K-Ar dated basaltic flows of Mount Etna volcano (Sicily, 38 °N): Evaluation of a new paleoaltimeter. Earth and Planetary Science Letters 236 (3-4), 613–631.

Blard, P. H., Pik, R., 2008. An alternative isochron method for measuring cosmogenic ^{3}He in lava flows. Chemical Geology, 13.

Blard, P. H., Pik, R., Lavé, J., Bourlès, D. L., Burnard, P., Yokochi, R., Marty, B., Trusdell, F., 2006. Cosmogenic ^{3}He production rates revisited from evidences of grain size dependent release of matrix-sited helium. Earth and Planetary Science Letters 247 (3-4), 222–234.

Bonforte, A., Puglisi, G., 2006. Dynamics of the eastern flank of Mt. Etna volcano (Italy) investigated by a dense GPS network. Journal of Volcanology and Geothermal Research 153, 357–369.

Bradley, R. S., 1999. Paleoclimatology. Reconstructing Climates of the Quaternary, 2nd Edition. Vol. 64 of International Geophysics Series. Harcourt Academic Press.

Branca, S., 2003. Geological and geomorphological evolution of the Etna volcano NE flank and relationships between lava flow invasions and erosional processes in the Alcantara Valley (Italy). Geomorphology 53, 247–261.

Brandt, U., Nowaczyk, N. R., Ramrath, A., Brauer, A., Mingram, J., Wulf, S., Negendank, J. F. W., 1999. Palaeomagnetism of Holocene and Late Pleistocene sediments from Lago di Mezzano and Lago Grande di Monticchio (Italy): initial results. Quaternary Science Reviews 18 (7), 961 – 976.

Braucher, R., Blard, P. H., Benedetti, L., Bourlès, D. L., 2006. Extending ^{10}Be applications to carbonate rich and mafic environments. In: Siame, L., Bourlès, D., Brown, E. (Eds.), In Situ-produced cosmogenic Nuclides and Quantification of geological processes. Special Paper 415. The Geological Society of America, Boulder, Colorado, USA, pp. 17–28.

Braucher, R., DelCastillo, P., Siame, L., Hidy, A. J., Bourlès, D. L., 2009. Determination of both exposure time and denudation rate from an in situ-produced ^{10}Be depth profile: A mathematical proof of uniqueness. Model sensitivity and applications to natural cases. Quaternary Geochronology 4 (1), 56 – 67.

Brook, E. J., Kurz, M. D., Ackert, R. P., Denton, G. H., Brown, E. T., Raisbeck, G. M., Yiou, F., 1993. Chronology of Taylor glacier advances in Arena Valley, Antarctica, using in situ cosmogenic ^{3}He and ^{10}Be. Quaternary Research 39 (1), 11 – 23.

Cerling, T. E., Craig, H., 1994. Cosmogenic ^{3}He production rates from 39°N to 46°N latitude, western USA and France. Geochimica et Cosmochimica Acta 58, 249–255.

Charalambus, S., 1971. Nuclear transmutation by negative stopped muons and the activity induced by the cosmic-ray muons. Nuclear Physics A166, 145–161.

Chmeleff, J., von Blanckenburg, F., Kossert, K., Jakob, D., 2009. Determination of the ^{10}Be half-life by multicollector ICP-MS and liquid scintillation counting. Nuclear Instruments and Methods in Physics Research Section B, in press.

Coltelli, M., Carlo, P. D., Vezzoli, L., 2000. Stratigraphic constraints for explosive activity in the past 100 ka at Etna Volcano, Italy. International Journal of Earth Sciences 89, 665–677.

Davis, R. J., Schaeffer, O. A., 1955. Chlorine-36 in Nature. Annals New York Academy of Science 62, 105–122.

Davis, S. N., Cecil, D., Zreda, M., Sharma, P., 1998. Chlorine-36 and the initial value problem. Hydrogeology Journal 6, 104–114.

Desilets, D., Zreda, M., 2001. On scaling cosmogenic nuclide production rates for altitude and latitude using cosmic-ray measurements. Earth and Planetary Science Letters 193 (1-2), 213 – 225.

Desilets, D., Zreda, M., 2003. Spatial and temporal distribution of secondary cosmic-ray nucleon intensities and applications to in situ cosmogenic dating. Earth and Planetary Science Letters 206, 21–42.

Desilets, D., Zreda, M., Almasi, P., Elmore, D., 2006a. Determination of cosmogenic ^{36}Cl in rocks by isotope dilution: innovations, validation and error propagation. Chemical Geology 233 (3-4), 185–195.

Desilets, D., Zreda, M., Prabu, T., 2006b. Extended scaling factors for in situ cosmogenic nuclides: New measurements at low latitude. Earth and Planetary Science Letters 246 (3-4), 265–276.

Dockhorn, B., Neumaier, S., Hartmann, F. J., Petitjean, C., Faestermann, H., Korschinek, G., Morinaga, H., Nolte, E., 1991. Determination of erosion rates with cosmic ray produced ^{36}Cl. Zeitschrift für Physik A - Hadrons and Nuclei 341, 117–119.

Dorman, L. I., Villoresi, G., Iucci, N., Parisi, M., Tyasto, M. I., Danilova, O. A., Ptitsyna, N. G., 2000. Cosmic ray survey to antarctica and coupling functions for neutron component near solar minimum (1996-1997) 3. geomagnetic effects and coupling functions. Journal of Geophysical Research 105, 21047–21056.

Downie, C., Wilkinson, P., 1972. The Geology of Kilimanjaro. The Department of Geology, The University of Sheffield, Sheffield, 253 pp.

Dunai, T. J., 2000. Scaling factors for production rates of in situ produced cosmogenic nuclides: a critical reevalution. Earth and Planetary Science Letters 176, 157–169.

Dunai, T. J., 2001. Influence of secular variation of the geomagnetic field on production rates of in situ produced cosmogenic nuclides. Earth and Planetary Science Letters 193, 197–212.

Dunai, T. J., López, G. A. G., Juez-Larré, J., 2005. Oligocene-Miocene age of aridity in the Atacama Desert revealed by exposure dating of erosion-sensitive landforms. Geology 33, 321–324.

Dunai, T. J., Stuart, F. M., Pik, R., Burnard, P., Gayer, E., 2007. Production of ^{3}He in crustal rocks by cosmogenic thermal neutrons. Earth and Planetary Science Letters 258 (1-2), 228 – 236.

Dunne, J., Elmore, D., Muzikar, P., 1999. Scaling factors for the rates of production of cosmogenic nuclides for geometric shielding and attenuation at depth on sloped surfaces. Geomorphology 27 (1-2), 3 – 11.

Easterbrook, D. J., 2003. Comment on the paper "Determination of ^{36}Cl production rates from the well-dated deglaciation surfaces of Whidbey and Fidalgo Islands, Washington" by T.W. Swanson and M.C. Caffee. Quaternary Research 59 (1), 132 – 134.

Elmore, D., Phillips, F. M., 1987. Accelerator mass spectrometry for measurement of long-lived radioisotopes. Science 236, 543–550.

Elsasser, W., Ney, E. P., Winckler, J. R., 1956. Cosmic-ray intensity and geomagnetism. Nature 178, 1226–1227.

Evans, J. M., Stone, J. O., Fifield, L. K., Cresswell, R. G., 1997. Cosmogenic ^{36}Cl production in K-feldspar. Nuclear Instruments and Methods in Physics Research Section B: Beam Interactions with Materials and Atoms 123, 334–340.

Fabryka-Martin, J. T., 1988. Production of radionuclides in the earth and their hydrogeologic significance, with emphasis on chlorine-36 and iodine-129. Ph.D. thesis, University of Arizona, Tucson.

Farber, D. L., Mériaux, A.-S., Finkel, R. C., 2008. Attenuation length for fast nucleon production of ^{10}Be derived from near-surface production profiles. Earth and Planetary Science Letters 274 (3-4), 295 – 300.

Farley, K. A., Libarkin, J., Mukhopadhyay, S., Amidon, W., 2006. Cosmogenic and nucleogenic ^{3}He in apatite, titanite, and zircon. Earth and Planetary Science Letters 248 (1-2), 451 – 461.

Fenton, C. R., Niedermann, S., Goethals, M. M., Schneider, B., Wijbrans, J., 2009. Evaluation of cosmogenic ^{3}He and ^{21}Ne production rates in olivine and pyroxene from two Pleistocene basalt flows, western Grand Canyon, AZ, USA. Quaternary Geochronology, in press.

Fink, D., Vogt, S., Hotchkis, M., 2000. Cross-sections for ^{36}Cl from Ti at E_p = 35-150 MeV: Applications to in-situ exposure dating. Nuclear Instruments and Methods in Physics Research Section B 172, 861–866.

Finkel, R. C., Suter, M., 1993. AMS in the earth sciences: Technique and applications. Advances in Analytical Geochemistry 1, 1–114.

Gayer, E., Pik, R., Lavé, J., France-Lanord, C., Bourlès, D., Marty, B., 2004. Cosmogenic ^{3}He in Himalayan garnets indicating an altitude dependence of the ^{3}He/^{10}Be production ratio. Earth and Planetary Science Letters 229 (1-2), 91 – 104.

Gelman, A., Carlin, J. B., Stern, H. S., Rubin, D. B., 2004. Bayesian Data Analysis, 2nd Edition. Texts in Statistical Science. Chapman & Hall/CRC, Boca Raton.

Germa, A., Quidelleur, X., Gillot, P. Y., Tchilinguirian, P., 2009. Volcanic evolution of the back-arc Pleistocene Payun Matru Volcanic Field (Argentina). Journal of South American Earth Sciences, in press.

Gillespie, A. R., Bierman, P. R., 1995. Precision of terrestrial exposure ages and erosion rates estimated from analysis of cosmogenic isotopes produced in situ. Journal of Geophysical Research 100 (B12), 24637–24649.

Gosse, J. C., Phillips, F. M., 2001. Terrestrial in situ cosmogenic nuclides: theory and application. Quaternary Science Reviews 20, 1475–1560.

Graf, T., Kohl, C. P., Marti, K., Nishiizumi, K., 1991. Cosmic-ray produced neon in Antarctic rocks. Geophysical Research Letters 18, 203–206.

Granger, D. E., Smith, A. L., 2000. Dating buried sediments using radioactive decay and muogenic production of ^{26}Al and ^{10}Be. Nuclear Instruments and Methods in Physics Research Section B 172, 822–826.

Guyodo, Y., Valet, J. P., 1999. Global changes in intensity of the Earth's magnetic field during the past 800 kyr. Nature 399, 249–252.

Heisinger, B., Lal, D., Jull, A. J. T., Kubik, P., Ivy-Ochs, S., Knie, K., Nolte, E., 2002. Production of selected cosmogenic radionuclides by muons: 2. Capture of negative muons. Earth and Planetary Science Letters, 357–369.

Hilley, G. E., Young, J. J., 2008. Deducing paleoearthquake time and recurrence from paleoseismic data, Part II: Analysis of paleoseismic excavation data and earthquake behavior along the Central and Southern San Andreas Fault. Bulletin of the Seismological Society of America, 407–439.

Huggle, D., Blinov, A., Stan-Sion, C., Korschinek, G., Scheffel, C., Massonet, S., Zerle, L., Beer, J., Parrat, Y., Gaeggeler, H., Hajdas, W., Nolte, E., 1996. Production of cosmogenic ^{36}Cl on atmospheric argon. Planetary and Space Science 44 (2), 147–151.

Ivy-Ochs, S., Synal, H.-A., Roth, C., Schaller, M., 2004. Initial results from isotope dilution for Cl and ^{36}Cl measurements at the PSI/ETH Zurich AMS facility. Nuclear Instruments and Methods in Physics Research Section B: Beam Interactions with Materials and Atoms 223-224, 623 – 627, proceedings of the Ninth International Conference on Accelerator Mass Spectrometry.

Jackson, A., Jonkers, A. R. T., Walker, M. R., 2000. Four centuries of geomagnetic secular variation from historical records. Philosophical Transactions of the Royal Society of London, Series A. 358, 957–990.

Kober, F., Ivy-Ochs, S., Leya, I., Baur, H., Magna, T., Wieler, R., Kubik, P. W., 2005. In situ cosmogenic ^{10}Be and ^{21}Ne in sanidine and in situ cosmogenic ^{3}He in Fe-Ti-oxide minerals. Earth and Planetary Science Letters 236 (1-2), 404 – 418.

Kohl, C. P., Nishiizumi, K., 1992. Chemical isolation of quartz for measurement of in-situ -produced cosmogenic nuclides. Geochimica et Cosmochimica Acta 56 (9), 3583 – 3587.

Korschinek, G., Bergmaier, A., Faestermann, T., Gerstmann, U. C., Knie, K., Rugel, G., Wallner, A., Dillmann, I., Dollinger, G., von Gostomski, C. L., Kossert, K., Maiti, M., Poutivtsev, M., Remmert, A., 2009. A new value for the half-life of ^{10}Be by Heavy-Ion Elastic Recoil Detection and liquid scintillation counting. Nuclear Instruments and Methods in Physics Research Section B, in press.

Korte, M., Constable, C. G., 2005. Continuous geomagnetic field models for the past 7 millennia: 2. CALS7K. Geochemistry Geophysics Geosystems 6, Q02H16.

Kurz, M. D., 1986a. Cosmogenic helium in a terrestrial igneous rock. Nature 320, 435–439.

Kurz, M. D., 1986b. In situ production of terrestrial cosmogenic helium and some applications to geochronology. Geochimica et Cosmochimica Acta 50, 2855–2862.

Laj, C., Kissel, C., Beer, J., 2004. High resolution global paleointensity stack since 75 kyr (GLOPIS-75) calibrated to absolute values. In: Channell, J. E. T., Kent, D. V., Lowrie, W., Meert, J. G. (Eds.), Timescales of the Geomagnetic Field. Geophysical Monograph. American Geophysical Union, Washington D.C., pp. 255 – 265.

Lal, D., 1987. Production of ^{3}He in terrestrial rocks. Chemical Geology: Isotope Geoscience section 66 (1-2), 89 – 98.

Lal, D., 1991. Cosmic ray labeling of erosion surfaces: in situ nuclide production rates and erosion models. Earth and Planetary Science Letters 104, 424–439.

Lal, D., Peters, B., 1967. Cosmic ray produced radioactivity on the earth. In: Sitte, K. (Ed.), Handbuch der Physik. Springer-Verlag, New York, pp. 551–612.

Licciardi, J., Denoncourt, C., Finkel, R., 2008. Cosmogenic ^{36}Cl production rates from Ca spallation in Iceland. Earth and Planetary Science Letters 267 (1-2), 365–377.

Licciardi, J., Kurz, M., Curtice, J., 2006. Cosmogenic ^{3}He production rates from Holocene lava flows in Iceland. Earth and Planetary Science Letters 246 (3-4), 251 – 264.

Licciardi, J. M., Kurz, M. D., Clark, P. U., Brook, E. J., 1999. Calibration of cosmogenic ^{3}He production rates from Holocene lava flows in Oregon, USA, and effects of the Earth's magnetic field. Earth and Planetary Science Letters 172 (3-4), 261 – 271.

Licciardi, J. M., Schaefer, J. M., Taggart, J. R., Lund, D. C., 2009. Holocene glacier fluctuations in the Peruvian Andes indicate northern climate linkages. Science, in press.

Lifton, N., Bieber, J., Clem, J., Duldig, M., Evenson, P., Humble, J., Pyle, R., 2005. Addressing solar modulation and long-term uncertainties in scaling secondary cosmic rays for in situ cosmogenic nuclide applications. Earth and Planetary Science Letters 239 (1-2), 140–161.

Lifton, N., Smart, D. F., Shea, M. A., 2008. Scaling term time-integrated in situ cosmogenic nuclide production rates using a continuous geomagnetic model. Earth and Planetary Science Letters 268, 190–201.

Liu, B., Phillips, F. M., Fabryka-Martin, J. T., Fowler, M. M., Stone, W. D., 1994. Cosmogenic ^{36}Cl accumulation in unstable landforms 1. Effects of the thermal neutron distribution. Water Resources Research 30 (11), 3115–3125.

Masarik, J., 2002. Numerical simulation of in-situ production of cosmogenic nuclides. Goldschmidt Conference Abstract A491.

Masarik, J., Kim, K., Reedy, R., 2007. Numerical simulations of in situ production of terrestrial cosmogenic nuclides. Nuclear Instruments and Methods in Physics Research Section B: Beam Interactions with Materials and Atoms 259 (1), 642–645.

Masarik, J., Reedy, R. C., 1996. Monte Carlo simulation of in-situ-produced cosmogenic nuclides. Radiocarbon 38, 163–164.

Masarik, J., Wieler, R., 2003. Production rates of cosmogenic nuclides in boulders. Earth and Planetary Science Letters 216 (1-2), 201–208.

Matsuda, J., Matsumoto, T., Sumino, H., Nagao, K., Yamamoto, J., Miura, Y., Kaneoka, I., Takahata, N., Sano, Y., 2002. The ^{3}He/^{4}He ratio of the new internal He Standard of Japan (HESJ). Geochemical Journal 36, 191–195.

Matthes, S., 1996. Mineralogie: Eine Einführing in die spezielle Mineralogie, Petrologie und Lagerstättenkunde, 5th Edition. Springer, Berlin Heidelberg New York.

Merchel, S., Arnold, M., Aumaître, G., Benedetti, L., Bourlès, D. L., Braucher, R., Alfimov, V., Freeman, S., Steier, P., Wallner, A., 2008a. Towards more precise ^{10}Be and ^{36}Cl data from measurements at the 10^{-14} level: Influence of sample preparation. Nuclear Instruments and Methods in Physics Research Section B.

Merchel, S., Braucher, R., Benedetti, L., Grauby, O., Bourlès, D., Feb 2008b. Dating carbonate rocks with in-situ produced cosmogenic ^{10}Be: Why it often fails. Quaternary Geochronology, 27.

Merrill, R. T., McElhinny, M. W., 1983. The Earth's magnetic field: Its history, origin and planetary perspective. Academic Press, London, 401 pp.

Merrill, R. T., McElhinny, M. W., McFadden, P. L., 1996. The magnetic field of the Earth: Paleomagnetism, the Core, and the Deep Mantle. Academic Press, London, 531 pp.

Métrich, N., Allard, P., Spilliaert, N., Andronico, D., Burton, M., 2004. 2001 flank eruption of the alkali- and volatile-rich primitive basalt responsible for Mount Etna's evolution in the last three decades. Earth and Planetary Science Letters 228 (1-2), 1–17.

Metropolis, N., Rosenbluth, A. W., Rosenbluth, M. N., Teller, A. H., 1953. Equation of state calculations by fast computing machines. Journal of Chemical Physics 21, 1087–1092.

Michel, R., Lüpke, M., Herpers, U., Rösel, R., Suter, M., Dittrich-Hannen, B., Kubik, P. W., Filges, D., Cloth, P., 1995. Simulation and modelling of the interaction of galactic protons with stony meteoroids. Planetary and Space Science 43 (3-4), 557 – 572, small Bodies in the Solar System - Origin, Evolution, and Significance for the Formation of Planets.

Monaco, C., Tapponnier, P., Tortorici, L., Gillot, P. Y., 1997. Late Quaternary slip rates on the Acireale-Piedimonte normal faults and tectonic origin of Mt. Etna (Sicily). Earth and Planetary Science Letters 147, 125–139.

Moysey, S., Davis, S. N., Zreda, M., Cecil, L. D., 2003. The distribution of meteoric ^{36}Cl/Cl in the United States: a comparison of models. Hydrogeology Journal 11 (6), 615–627.

Muzikar, P., Elmore, D., Granger, D. E., 2003. Accelerator mass spectrometry in geologic research. Geological Society of America Bulletin 115 (6), 643–654.

Muzikar, P., Granger, D., 2006. Combining cosmogenic, stratigraphic, and paleomagnetic information using a Bayesian approach: General results and an application to Sterkfontein. Earth and Planetary Science Letters 243, 400–408.

Niedermann, S., 2000. The ^{21}Ne production rate in quartz revisited. Earth and Planetary Science Letters 183 (3-4), 361 – 364.

Niedermann, S., 2002. Cosmic-ray-produced noble gases in terrestrial rocks: Dating tools for surface processes. Reviews in Mineralogy and Geochemistry 47 (1), 731–784.

Niedermann, S., Bach, W., Erzinger, J., 1997. Noble gas evidence for a lower mantle component in MORBs from the southern East Pacific Rise: Decoupling of helium and neon isotope systematics. Geochimica et Cosmochimica Acta 61 (13), 2697 – 2715.

Niedermann, S., Goethals, M. M., Pilz, P., 2009. Evidence for a high ^{3}He or low ^{10}Be production rate from cosmogenic nuclide cross-calibration. Goldschmidt Conference Abstract A940.

Niedermann, S., Graf, T., Kim, J. S., Kohl, C. P., Marti, K., Nishiizumi, K., 1994. Cosmic-ray-produced ^{21}Ne in terrestrial quartz: the neon inventory of Sierra Nevada quartz separates. Earth and Planetary Science Letters 125 (1-4), 341 – 355.

Niedermann, S., Pilz, P., Goethals, M., 2007. Assessing the relative production rates of cosmogenic ^{3}He and ^{21}Ne in olivine, pyroxene and quartz. Goldschmidt Conference Abstract A717.

Nishiizumi, K., Kohl, C. P., Arnold, J. R., Klein, J., Fink, D., Middleton, R., 1991. Cosmic ray produced ^{10}Be and ^{26}Al in Antarctic rocks: exposure and erosion history. Earth and Planetary Science Letters 104 (2/4), 440–454.

Nishiizumi, K., Lal, D., Klein, J., Middleton, R., Arnold, J. R., 1986. Production of ^{10}Be and ^{26}Al by cosmic rays in terrestrial quartz in situ and implications for erosion rates. Nature 319, 134–136.

Nishiizumi, K., Winterer, E. L., Kohl, C. P., Klein, J., Middleton, R., Lal, D., Arnold, J. R., 1989. Cosmic ray production rates of ^{10}Be and ^{26}Al in quartz from glacially polished rocks. Journal of Geophysical Research 94 (B12), 17907–17915.

Nonnotte, P., Guillou, H., Gall, B. L., Benoit, M., Cotten, J., Scaillet, S., 2008. New K-Ar age determinations of Kilimanjaro volcano in the North Tanzanian diverging rift, East Africa. Journal of Volcanology and Geothermal Research 173 (1-2), 99 – 112.

O'Brien, K., Sandmeier, H. A., Hansen, G. E., Campbell, J. E., 1978. Cosmic ray induced neutron background sources and fluxes for geometries of air over water, ground, iron, and aluminum. Journal of Geophysical Research 83, 114–120.

Ohno, M., Hamano, Y., 1993. Global analysis of the geomagnetic field: Time variation of the dipole moment and the geomagnetic pole in the Holocene. Journal of Geomagnetism and Geoelectricity 45, 1455–1466.

Phillips, F. M., Plummer, M. A., 1996. CHLOE: A program for interpreting in-situ cosmogenic nuclide data for surface exposure dating and erosion studies. Abstracts of the 7th international conference on Accelerator mass spectrometry, 98–99.

Phillips, F. M., Stone, W. D., Fabryka-Martin, J. T., 2001. An improved approach to calculating low-energy cosmic-ray neutron fluxes near the land/atmosphere interface. Chemical Geology 175, 689–701.

Phillips, F. M., Zreda, M. G., Flinsch, M. R., 1996. A reevaluation of cosmogenic ^{36}Cl production rates in terrestrial rocks. Geophysical Research Letters 23 (9), 949–952.

Pigati, J., Lifton, N., 2004. Geomagnetic effects on time-integrated cosmogenic nuclide production with emphasis on in situ ^{14}C and ^{10}Be. Earth and Planetary Science Letters 226 (1-2), 193–205.

Pik, R., Marty, B., Hilton, D., 2006. How many mantle plumes in Africa? The geochemical point of view. Chemical Geology 226 (3-4), 100 – 114, special Issue in Honour of R.K. O'Nions.

Poreda, R. J., Cerling, T. E., 1992. Cosmogenic neon in recent lavas from the western United States. Geophysical Research Letters 19, 1863–1866.

R Development Core Team, 2008. R: A Language and Environment for Statistical Computing. R Foundation for Statistical Computing, Vienna, Austria, ISBN 3-900051-07-0.

Robert, C. P., Casella, G., 1999. Monte Carlo Statistical Methods. Springer Texts in Statistics. Springer-Verlag, New York.

Rothwell, P., 1958. Cosmic rays in the Earth's magnetic field. Philosophical Magazine 3, 961–970.

Schaefer, J. M., Denton, G. H., Kaplan, M., Putnam, A., Finkel, R. C., Barrell, D. J. A., Andersen, B. G., Schwartz, R., Mackintosh, A., Chinn, T., Schluechter, C., 2009. High-frequency Holocene glacier fluctuations in New Zealand differ from the northern signature. Science 324, 622–625.

Schaefer, J. M., Ivy-Ochs, S., Wieler, R., Leya, I., Baur, H., Denton, G. H., Schluechter, C., 1999. Cosmogenic noble gas studies in the oldest landscape on earth: surface exposure ages of the Dry Valleys, Antarctica. Earth and Planetary Science Letters 167 (3-4), 215 – 226.

Schildgen, T., Phillips, W., Purves, R., 2005. Simulation of snow shielding corrections for cosmogenic nuclide surface exposure studies. Geomorphology 64 (1-2), 67–85.

Schimmelpfennig, I., Benedetti, L., Finkel, R., Pik, R., Blard, P.-H., Bourlès, D., Burnard, P., Williams, A., 2009. Sources of in-situ ^{36}Cl in basaltic rocks. Implications for calibration of production rates. Quaternary Geochronology, in press.

Schlagenhauf, A., Gaudemer, Y., Benedetti, L., Manighetti, I., Palumbo, L., Schimmelpfennig, I., Finkel, R., Pou, K., 2009. Using in-situ chlorine-36 cosmonuclide to recover past earthquake histories on limestone normal fault scarps: A reappraisal of methodology and interpretations. Geophysical Journal International submitted, –.

Seidl, M. A., Finkel, R. B., Caffee, M. W., Hudson, G. B., Dietrich, W. E., 1997. Cosmogenic isotope analyses applied to river longitudinal profile evolution: Problems and interpretations. Earthe Surface Processes and Landforms 22, 195–209.

Shabanian, E., Siame, L., Bellier, O., Benedetti, L., Abassi, M. R., 2009. Quaternary slip rates along the northeastern boundary of the Arabia-Eurasia collision zone (Kopeh Dagh Mountains, Northeast Iran). Geophysical Journal International 178, 1055–1077.

Shanahan, T. M., Zreda, M., 2000. Chronology of Quaternary glaciations in East Africa. Earth and Planetary Science Letters 177 (1-2), 23 – 42.

Sharma, P., Kubik, P. W., Fehn, U., Gove, H. E., Nishiizumi, K., Elmore, D., 1990. Development of ^{36}Cl standards for AMS. Nuclear Instruments and Methods in Physics Research Section B 52, 410–415.

Shea, M. A., Smart, D. F., McCall, J. R., 1968. A five degree world grid of trajectory-determined vertical cutoff rigidities. Canadian Journal of Physics 46, S1098–S1101.

Shea, M. A., Smart, D. F., McCracken, K. G., 1965. A study of vertical cutoff rigidities using sixth degree simulations of the geomagnetic field. Journal of Geophysical Research 70, 4117–4130.

Siame, L., Bellier, O., Braucher, R., Sèbrier, M., Cushing, M., Bourlès, D., Hamelin, B., Baroux, E., de Voogd, B., Raisbeck, G., Yiou, F., 2004. Local erosion rates versus active tectonics: cosmic ray exposure modelling in Provence (south-east France). Earth and Planetary Science Letters 220 (3-4), 345 – 364.

Siame, L., Bourlès, D., Brown, E. (Eds.), 2006. In Situ-produced cosmogenic Nuclides and Quantification of Geological Processes. Special Paper 415. The Geological Society of America, Boulder, Colorado, USA.

Smart, D. F., Shea, M. A., 2003. Geomagnetic cutoff rigidity calculations at 50-year intervals between 1600 and 2000. In: Kajita, T., Asaoka, Y., Kawachi, A., Matsubara, Y., Sasaki, M. (Eds.), 28th International Cosmic Ray Conference. Universal Academic Press, Tsukuba, Japan, pp. 4201–4204.

Solanki, S. K., Usoskin, I. G., Kromer, B., Schüssler, M., Beer, J., 2004. Unusual activity of the sun during recent decades compared to the previous 11,000 years. Nature 431, 1084–1087.

Stone, J. O., 2000. Air pressure and cosmogenic isotope production. Journal of Geophysical Research 105 (B10), 7.

Stone, J. O., September 2005. Terrestrial chlorine-36 production from spallation of iron. Abstract of 10th International Conference on Accelerator Mass Spectrometry.

Stone, J. O., Allan, G. L., Fifield, L. K., Cresswell, R. G., 1996. Cosmogenic ^{36}Cl from calcium spallation. Geochimica et Cosmochimica Acta 60 (4), 679–692.

Stone, J. O., Evans, J. M., Fifield, L. K., Allan, G. L., Cresswell, R. G., 1998. Cosmogenic ^{36}Cl production in calcite by muons. Geochimica et Cosmochimica Acta 62 (3), 433–454.

Stormer, C., 1935. On the trajectories of electric particles in the field of a magnetic dipole with applications to the theory of cosmic radiation: fourth communication. Astrophysica Norvegica 1 (4), 115–184.

Stuiver, M., Reimer, P. J., Reimer, R., 2005. Calib 5.0. [WWW programm and documentation].

Swanson, T., 2005. Reply to comment by D.J. Easterbrook (Quaternary Research 2003, 59, 132-134) on "Determination of ^{36}Cl production rates from the well-dated deglaciation surfaces of Whidbey and Fidalgo Islands, Washington". Quaternary Research 63 (2), 228–230.

Swanson, T. W., Caffee, M. L., 2001. Determination of ^{36}Cl production rates derived from the well-dated deglaciation surfaces of Whidbey and Fidalgo Islands, Washington. Quaternary Research 56 (3), 366–382.

Tanguy, J.-C., Condomines, M., Goff, M., Chillemi, V., Delfa, S., Patanè, G., 2007. Mount Etna eruptions of the last 2,750 years: revised chronology and location through archeomagnetic and ^{226}Ra-^{230}Th dating. Bulletin of Volcanology 70 (1), 55–83.

Tanguy, J.-C., Condomines, M., Kieffer, G., 1997. Evolution of the Mount Etna magma: Constraints on the present feeding system and eruptive mechanism. Journal of Volcanology and Geothermal Research 75 (3-4), 221 – 250.

Taylor, J. R., 1997. An Introduction to Error Analysis. The Study of Uncertainties in Physical Measurements. University Science Books, Sausalito, USA.

Trull, T. W., Kurz, M. D., Jenkins, W. J., 1991. Diffusion of cosmogenic ^{3}He in olivine and quartz: implications for surface exposure dating. Earth and Planetary Science Letters 103 (1-4), 241 – 256.

Vermeesch, P., 2007. Cosmocalc: An Excel add-in for cosmogenic nuclide calculations. Geochemistry Geophysics Geosystems 8 (8), 1525–2027.

Vermeesch, P., Baur, H., Heber, V. S., Kober, F., Oberholzer, P., Schaefer, J. M., Schlüchter, C., Strasky, S., Wieler, R., 2009. Cosmogenic ^{3}He and ^{21}Ne measured in quartz targets after one year of exposure in the Swiss Alps. Earth and Planetary Science Letters 284 (3-4), 417 – 425.

Yang, S., Odah, H., Shaw, J., 2000. Variations in the geomagnetic dipole moment over the last 12 000 years. Geophysical Journal International 140, 158–162.

Zreda, M. G., Phillips, F. M., 1994. Cosmogenic ^{36}Cl accumulation in unstable landforms 2. Simulations and measurementson eroding moraines. Water Resources Research 11, 3127–3136.

Zreda, M. G., Phillips, F. M., Elmore, D., Kubik, P. W., Sharma, P., Dorn, R. I., 1991. Cosmogenic chlorine-36 production rates in terrestrial rocks. Earth and Planetary Science Letters 105, 94–109.

Zreda, M. G., Phillips, F. M., Kubik, P. W., Sharma, P., Elmore, D., 1993. Cosmogenic ^{36}Cl dating of a young basaltic eruption complex, Lathrop Wells, Nevada. Geology 21, 57–60.

Abstract in English

Published cosmogenic ^{36}Cl SLHL production rates from Ca and K spallation differ by almost 50% (Gosse and Phillips, 2001). The main difficulty in calibrating ^{36}Cl production rates is to constrain the relative contribution of the various production pathways, which depend on the chemical composition of the rock, particularly on the Cl content.
Whole rock ^{36}Cl exposure ages were compared with ^{36}Cl exposure ages evaluated in Ca-rich plagioclases in the same independently dated 10 ± 3 ka lava sample taken from Mt. Etna (Sicily, 38° N). Sequential dissolution experiments showed that high Cl concentrations in plagioclase grains could be significantly reduced after 16% dissolution yielding ^{36}Cl exposure ages in agreement with the independent age. Stepwise dissolution of whole rock grains, on the other hand, is not as effective in reducing high Cl concentrations as it is for the plagioclase. 330 ppm Cl still remains after 85% dissolution. The ^{36}Cl exposure ages are systematically about 30% higher than the ages calculated from the plagioclase. We could exclude contamination by atmospheric or magmatic ^{36}Cl as an explanation for this overestimate. High Cl contents in the calibration samples used for several previous production rate studies are most probably the reason for overestimated spallation production rates from Ca and K. This is due to a poorly constrained nature of ^{36}Cl production from low-energy neutrons.
We used separated minerals, very low in Cl, to calibrate the production rates from Ca and K. ^{36}Cl was measured in Ca-plagioclases collected from 4 lava flows at Mt. Etna (38° N, Italy, altitudes between 500 and 2000 m), and in K-feldspars from one flow at Payun Matru volcano (36° S, Argentina, altitudes 2300 and 2500 m). The flows were independently dated between 0.4 and 32 ka. Scaling factors were calculated using five different published scaling models resulting in five calibration data sets. Using a Bayesian statistical model allowed including the major inherent uncertainties. The inferred SLHL spallation production rates from Ca and K are 42.2 ± 4.8 atoms ^{36}Cl (g Ca)$^{-1}$ a^{-1} and 124.9 ± 8.1 atoms ^{36}Cl (g K)$^{-1}$ a^{-1} scaled with Stone (2000). Using the other scaling methods results in very similar values. These results are in agreement with previous production rate estimations both for Ca and K calibrated with low Cl samples. Moreover, although the exposure durations of our samples are very different and the altitude range is large, the ages recalculated with our production rates are mostly in agreement, within uncertainties, with the independent ages no matter which scaling method is used.
However, scaling factors derived from the various scaling methods differ significantly. Cosmic ray flux is sensitive to elevation and its energy spectrum increases considerably with increasing altitude and latitude. To evaluate whether various TCN production rates change differently with altitude and latitude and if nuclide-specific or even target-element-specific scaling factors are required, cosmogenic ^{36}Cl, ^{3}He and ^{21}Ne concentration were determined in pyroxenes over an altitude transect between 1000 and 4300 m at Kilimanjaro volcano (3° S). No altitude-dependency of the nuclide ratios could be observed, suggesting that no nuclide-specific scaling factors be needed for the studied nuclides.

Key words: *Cosmogenic-nuclide exposure dating, in situ ^{36}Cl, silicate minerals, basaltic whole rock, Mt. Etna, ^{36}Cl calculator, production rate calibration, scaling methods, cosmogenic noble gases, cross-calibration*